Dissertation
submitted to the
Combined Faculties of the Natural Sciences and Mathematics
of the Ruperto-Carola-University of Heidelberg, Germany
for the degree of
Doctor of Natural Sciences

put forward by

Dipl.-Phys. Jonas Friedrich Gunst

born in Heidelberg, Germany
Oral examination: December 14$^{\text{th}}$, 2015

Mutual control of x-rays and nuclear transitions

Referees: Honorarprof. Dr. Christoph H. Keitel
Prof. Dr. Jörg Jäckel

Zusammenfassung

In dieser Arbeit wird die gegenseitige Wechselwirkung von Röntgenstrahlung und Kernen theoretisch untersucht. Im ersten Teil betrachten wir die Anregung von Kernübergängen mit den hochbrillianten und kohärenten Röntgen-Freie-Elektronen-Lasern. Neben der verstärkten resonanten Kernanregung, können durch die hohe Laserintensität auch neue Materiezustände, wie kalte, dichte Plasmen, erzeugt werden, in denen sekundäre Kernprozesse, z.B. Kernanregung durch Elektroneneinfang, zu Tage kommen. Unsere Ergebnisse zeigen, dass im Falle von ^{57}Fe-Kernen diese sekundäre Kernanregung durch Elektroneneinfang verschwindend klein ist, wohingegen sie bei der Aktivierung von $^{93\mathrm{m}}$Mo-Isomeren die dominierende Rolle spielt verglichen zur direkten Laseranregung. Anhand dieser Fallstudien leiten wir allgemeingültige Kriterien zur Identifizierung des dominanten Anregungskanals ab, welche von großer Relevanz für künftige Kernresonanzstudien an Röntgen-Freie-Elektronen-Lasern sind. Im zweiten Teil dieser Arbeit wird die Kontrolle einzelner Röntgenphotonen mithilfe von resonanten Kernübergängen thematisiert. Wir zeigen, dass durch abrupte Magnetfeldrotationen die Polarisation von Röntgenquanten im Zuge der Kernvorwärtsstreuung an ^{57}Fe-Targets bewusst manipuliert werden kann, wodurch Bool'sche Operationen im Röntgenbereich möglich werden. Neben möglichen Anwendungen in der Informationswissenschaft, weisen unsere Ergebnisse darauf hin, dass es durch Polarisationskodierung möglich ist, Streupfade der Röntgenphotonen gezielt zu markieren, so dass deren Interferenz kontrolliert ab- und angeschaltet werden kann. Die vorgeschlagenen Schemata bringen Zeit-Energie-Komplementaritätstests in den bislang unerforschten Parameterbereich der Röntgenstrahlung voran.

Abstract

In the course of this Thesis the mutual control between x-rays and nuclear transitions is investigated theoretically. In the first Part, we study the nuclear photoexcitation with the highly brilliant and coherent x-ray free-electron lasers (XFELs). Apart from amplifying the direct resonant interaction with nuclear transitions, the super-intense XFEL can produce new states of matter like cold, high-density plasmas where secondary nuclear excitation channels may come into play, e.g., nuclear excitation by electron capture (NEEC). Our results predict that in the case of ^{57}Fe targets secondary NEEC can be safely neglected, whereas it is surprisingly the dominating contribution (in comparison to the direct photoexcitation) for the XFEL-induced $^{93\mathrm{m}}$Mo isomer triggering. Based on these case studies, we elaborate a general set of criteria to identify the prevailing excitation channel for a certain nuclear isotope. These criteria may be most relevant for future nuclear resonance experiments at XFEL facilities. On the opposite frontier, the interplay between single x-ray photons and nuclear transitions offer potential storage and processing applications for information science in their most compact form. In the second Part of this Thesis, we show that nuclear forward scattering off ^{57}Fe targets can be employed to process polarization-encoded single x-rays via timed magnetic field rotations. Apart from the realization of logical gates with x-rays, the polarization encoding is used to design an x-ray quantum eraser scheme where the interference between scattering paths can be switched off and on in a controlled manner. Such setups may advance time-energy complementarity tests to so far unexplored paramater regimes, e.g., to the domain of x-ray quanta.

In the course of this Thesis, the following article has been published in a peer-reviewed journal:

- Jonas Gunst, Yuri A. Litvinov, Christoph H. Keitel, Adriana Pálffy
  Dominant Secondary Nuclear Photoexcitation with the X-ray Free Electron Laser
  Phys. Rev. Lett. **112**, 082501 (2014)
    - Highlighted as Viewpoint in Physics, Physics **7**, 20 (2014)
    - Editor's suggestion

Moreover, the following articles have been submitted for publication in peer-reviewed journals:

- Jonas Gunst, Christoph H. Keitel, Adriana Pálffy
  Logical operations with single x-ray photons via dynamically-controlled nuclear resonances
  arXiv:1506.00517 (2015)
- Jonas Gunst, Yuanbin Wu, Naveen Kumar, Christoph H. Keitel, Adriana Pálffy
  Direct and secondary nuclear excitation with x-ray free-electron lasers
  arXiv:1508.07264 (2015)

In addition, the following unrefereed research report has been published:

- Jonas Gunst, Yuri A. Litvinov, Christoph H. Keitel, Adriana Pálffy
  Dominant secondary nuclear photoexcitation with the XFEL
  GSI scientific report 2013

Contents

Introduction **1**

I Nuclear excitations induced by high-intensity x-ray lasers **9**

1 X-ray free-electron lasers & their potential for nuclear physics **11**
- 1.1 The x-ray free-electron laser 11
- 1.2 Nuclear photoexcitation 14
- 1.3 Plasma-mediated nuclear processes 17

2 Light-induced resonant nuclear excitation **21**
- 2.1 Basic quantum dynamics 21
- 2.2 Interaction matrix elements 24
  - 2.2.1 Magnetic transitions 24
  - 2.2.2 Electric transitions 26
- 2.3 The collective nuclear decay rate 26

3 Nuclear excitation by electron capture **29**
- 3.1 Decomposition of Fock space 31
- 3.2 The system's Hamiltonian 32
  - 3.2.1 Magnetic interaction 33
  - 3.2.2 Nuclear model 34
- 3.3 Total NEEC cross section 35
- 3.4 Excitation rate via NEEC 37
  - 3.4.1 Electric transitions 38
  - 3.4.2 Magnetic transitions 39

4 Direct and secondary nuclear excitation with the XFEL **41**
- 4.1 Theoretical treatment 42
  - 4.1.1 NEEC reaction rates in the plasma environment 42
  - 4.1.2 Plasma expansion model 44
  - 4.1.3 Nuclear targets 45
- 4.2 Direct photoexcitation 45
- 4.3 Secondary NEEC in a stationary plasma 47
- 4.4 Secondary NEEC in an expanding plasma 50
  - 4.4.1 Initial plasma conditions 50
  - 4.4.2 Atomic effects in plasma expansion 51

4.4.3 Total NEEC excitation 54
4.5 Comparison between direct and secondary excitation 57

II Single x-rays controlled by nuclear transitions 61

5 Nuclear forward scattering 63
5.1 Wave equation 66
5.2 Nuclear current density 67
5.3 General solution 69
5.4 Static hyperfine interactions 71
5.5 Instantaneous rotations of the magnetic field 73
5.6 Fast switchings of the magnetic field 74

6 Polarization control of hard x-rays 77
6.1 Polarization effects in static NFS 77
6.2 Dynamical control of nuclear polarization response 79
6.2.1 90°-Voigt rotation: from z to x 82
6.2.2 Effect of multiple scattering 87
6.3 Control beyond the single scattering approximation 88

7 Logical gates with polarization-encoded single x-rays 93
7.1 The universal platform for single x-ray manipulations 94
7.2 Unary logical operations 95
7.3 Boolean algebra with x-rays 100

8 Quantum eraser with x-ray quanta 105
8.1 Interference mechanisms in NFS 106
8.2 Which-way information and quantum eraser 109
8.2.1 Scheme 1: Two-target scenario 109
8.2.2 Scheme 2: Interferometer-like setup 112

Summary & Outlook 119

Appendix 123

A Supplement for NEEC theory 123

B ^{93}Mo isomer production 129

C Supplement for NFS theory 133

D NFS off ^{57}Fe targets under 90°-Voigt rotations 137

Bibliography **143**

Acknowledgements **167**

Introduction

Many groundbreaking scientific discoveries have been triggered by light. Bunsen and Kirchhoff used spectroscopic methods for the discovery of chemical elements like caesium and rubidium. Planck's law of black-body radiation and Einstein's theory of the photoelectric effect have been the historical starting point of modern quantum theory. The gravitational redshift has given insights into the expansion of the universe and laid the foundation for Einstein's theory of relativity. Observations with the Hooker telescope by Hubble have altered our view of the universe forever. The double-helix structure of DNA has first been seen via an x-ray diffraction image. The best observational evidence for black holes has been provided by the detection of x-rays with the Hubble space telescope. To say it with the words of Martin Luther King Jr. : "Darkness cannot drive out darkness; only light can do that." [1]

It was also the invention of the laser in 1960 [2,3] engaging a key role in the development of modern quantum dynamics which had a big stake in revolutionizing our view on nature. Many quantum phenomena could be investigated and understood by exploiting the laser's monochromaticity, directionality and coherence. The establishment of quantum optics led furthermore to many schemes for coherently controlling atomic degrees of freedom with light, and vice versa [4–6]. The control of light and matter resulted in a vast amount of applications nowadays present in everyday life.

In quantum optics, mostly photons in the microwave, infrared or optical regime are used. Extending the ideas of quantum optical control to shorter wavelengths, e.g., to x-ray energies [7] brings new, basically different aspects into the field. X-rays, for instance, overcome the diffraction limit of optical photons potentially resolving spectral information with a high spatial accuracy [8, 9]. Because of the short wavelengths, x-rays can be much better focused than visible light potentially down to the sub-Å regime. Recent experiments have already demonstrated a focal spot diameter of several nm [10–12] which renders physical research on the nanoscale feasible. In the future, it may be even possible to address single atoms by x-rays opening interesting perspectives for quantum information and quantum communication. In contrast to visible light, keV photons primarily interact with inner-shell electrons instead of the valence shell. In this manner, exotic systems, e.g., atoms with inner-shell vacancies can be prepared and studied under unique conditions. Moreover, x-rays are typically able to penetrate deep into materials leading to a uniform irradiation not only restricted to the surface.

The main reason why x-ray wavelengths have been neglected in the quantum optical domain for a long time is the lack of a proper coherent x-ray source [13]. However, already the commissioning of the third generation synchrotron light sources has boosted the development in many fields of physics concerned with x-rays including light-nucleus interaction experiments [14]. In comparison to former x-ray sources, synchrotrons are able to produce x-ray beams with much higher intensities and much better collimation properties. The new fourth generation light sources like x-ray free-electron lasers (XFELs) offer an even better beam quality characterized by partially coherent pulses with an eight orders of magnitude higher brilliance in comparison to synchrotron radiation (SR) [15]. Currently there are two XFELs operating in the hard x-ray regime [16,17] and several under construction [18–20]. The application of seeding schemes [21–23] or the construction of an x-ray oscillator [24,25] based on high-reflectivity x-ray mirrors [26,27] are expected to bring us closer to the long-time goal of fully coherent x-ray pulses. The concept of self-seeded free-electron lasers could be recently demonstrated in the soft [28] and hard x-ray regime [29]. The realization of two-color double-pulse XFELs [30, 31] further improves the flexibility of x-ray light sources. These new x-ray lasers along with x-ray detection efficiencies close to 100% render x-ray quantum optics a rich, promising and timely research field [7].

Although the transfer of quantum optical schemes to x-ray wavelengths seems at first glance to be straightforward, the situation one encounters in reality often calls for new ideas. The drawbacks which require complementary approaches are, for instance, the poor temporal coherence of current x-ray sources [32], the existence of only a single beam line with a single x-ray photon energy in typical experimental setups and the compression of the photons into short pulses instead of continuous waves. A peculiar circumstance is that x-rays are no longer resonant to valence-electron transitions in atoms. The corresponding resonant systems are either inner-shell electron transitions in highly charged ions [33–38], or alternatively transitions in atomic nuclei [39, 40].

Nuclear transitions present a clean, well-isolated system with long coherence times. In comparison to highly charged ions, nuclei are in many aspects beneficial. First of all, the interaction with nuclear transitions is reversible in the considered energy range, whereas in the interaction with electrons inside ions x-rays may ionize inner-shell electrons changing the system. Moreover, atomic nuclei can be embedded into high-density, solid-state targets. No external trapping mechanisms are required like it is the case for highly charged ions. Due to the placement inside solids, atomic nuclei are much less sensitive to small distortions of their environment than trapped ions whose state may crucially depend on collisions with surrounding particles. Instead, nuclear transitions can be addressed almost decoherence-free [41]. The limitation coming from the small cross sections of the light-nucleus interaction [42] can be overcome by using high-density targets.

Driving nuclear transitions in a controlled manner involves also practical purposes like the process of isomer triggering or isomer depletion [43–47]. Isomers are long-lived nuclear excited states capable of storing the excitation energy over a long time. This entails potential applications, e.g., nuclear batteries. The basic idea of isomer triggering is to retrieve the energy initially stored in a metastable isomeric state via the excitation to an above-lying triggering level which is connected to freely radiating states. Belic and co-workers were able to demonstrate the triggering of the $^{180\mathrm{m}}$Ta isomer [48, 49] which has a lifetime of approx. 10^{15} years, longer than the expected lifetime of the universe. They used 6 MeV bremsstrahlung photons to couple the isomeric state to a bunch of triggering levels. The efficiency of the incoherent coupling is however rather low. For triggering transitions in the keV range, the usage of coherent XFEL pulses instead of incoherent electromagnetic waves promises a strong increase in the depletion efficiency.

Apart from the burst in isomer triggering applications, the XFEL is further expected to strongly promote the establishment of quantum optical schemes in the x-ray domain. The unique radiation properties of the XFEL offer for the first time the possibility to study the light-nucleus interaction beyond the weak nuclear excitation regime where more than one nucleus is excited per pulse [50]. The hopes are to observe nonlinear effects like Rabi oscillations [39], to gain the direct quantum control of nuclear excitations [51] or to coherently manipulate nuclear state populations with x-ray pulses [52, 53]. The question is what qualitative and quantitative changes can be expected for nuclear quantum optics experiments to be performed at XFEL sources in the near future?

While in SR experiments the electronic response only acted as background, the XFEL intensity can reach values where the electronic interaction may additionally influence nuclear excitation channels. The increase of the electric field strength leads to drastic changes not only in the nuclear interaction, but also in the interaction between photons and electrons [54]. For photon energies of approximatively 10 keV and middle-range atomic number Z materials, the photoelectric effect dominates the electronic processes. The unique interplay between the super-intense XFEL and matter stimulated many applications and beautiful experiments in a broad spectrum of research fields. To be mentioned here are imaging in structural biology [55–57], nanochrystallography [58, 59], time-resolved observation of bond formation in solution [60], x-ray spectroscopy and diffraction of the photosystem II crucial for photosynthesis [61–63], double-core-hole creation [64, 65], nonlinear x-ray two-photon absorption [66], x-ray and optical wave mixing [67], controlling x-rays with light [68], stimulated x-ray emission [69] and atomic inner-shell x-ray lasing [70, 71].

The light-matter interaction with the super-intense XFEL is of nonlinear nature since multiple x-ray photons are absorbed [72]. There is a variety of works studying the behavior of matter, in particular due to photoionization, under these extreme conditions [73–78]. In experiments with neon [74, 75] and xenon gases [76, 79], for instance, researchers could follow and analyze the formation of highly charged ions during a single XFEL pulse. Nagler and co-workers have moreover shown that solid-state aluminum targets turn transparent for soft x-rays during the photoionization by the intense photon beam [73]. If the XFEL intensity is high enough even new states of matter like cold, high-density plasmas can be produced [80]. In 2012, the Linac Coherent Light Source (LCLS) beam has been applied with an intensity of around 10^{17} W/cm^2 to solid-state aluminum foils. Vinko and co-workers were able to create a solid-density plasma at temperatures in excess of 10^6 K induced by the XFEL [77].

In such plasma environments, secondary nuclear processes from the coupling to the atomic shell are rendered possible by the presence of free electrons and atomic vacancies. For instance, in the process of nuclear excitation by electron capture (NEEC) a free electron is captured into a bound state simultaneously transferring the capture energy to the atomic nucleus [81]. Such processes at the interface between atomic and nuclear physics may give insights into nuclear structure difficult to obtain in conventional scattering experiments and give direct information about nuclear transition energies and reduced transition probabilities. Moreover, secondary nuclear processes in the XFEL-induced plasma open new channels of nuclear excitation which could be neglected in SR experiments so far, but may be essential in nuclear photoexcitation studies with the XFEL.

Depending on the goal of the nuclear quantum optics experiment, the plasma-mediated excitation channels might be of advantage, for instance if the maximization of nuclear excitation is desired, or of disadvantage, if coherence-based enhancement of nonlinear interaction between x-rays and nuclei is envisaged.

So far the investigation of NEEC as nuclear excitation mechanism in plasma environments has been confined to hot astrophysical plasmas [82–86] or plasmas generated by optical lasers [87]. In these studies no equivalent of the direct photoexcitation exists. For the first time, the potential competition of the **Direct and secondary nuclear excitation with the XFEL** is discussed in Part I of this Thesis. Note that this is also a new and diametrically opposed situation compared to photonuclear studies involving petawatt optical lasers [88–92].

We investigate the secondary effect of NEEC at two explicit case studies: (i) the depletion of the $^{93\mathrm{m}}$Mo isomer via a 4.85 keV triggering transition to an above-lying level; and (ii) the resonant driving of the famous 14.4 keV Mössbauer transition in ^{57}Fe important for a large class of experiments. For both cases it is vital to know whether also additional plasma effects may play an important role for the nuclear excitation or for the sought-for coherence effects. In order to take time-dependent dynamics of the plasma into account the plasma expansion is parameterized by means of a hydrodynamical model [93, 94] in the quasi-neutral limit. Atomic processes in the plasma are included with the help of the population kinetics model implemented in the FLYCHK code [95]. Following a fair comparison between direct photoexcitation via the XFEL and secondary NEEC in the occurring plasma, our results show that for the case of isomer triggering in ^{93}Mo secondary nuclear excitation via NEEC dominates by several orders of magnitude. This is not at all the case for ^{57}Fe, where the secondary excitation can be safely neglected. Based on our findings, we work out criteria related to the nuclear transition energy, the atomic structure and plasma conditions that can be used to identify whether for a particular nuclear species, the secondary processes can be dominant compared to the direct photoexcitation channel. This knowledge is then applied to the present nuclear transition candidates starting from stable or metastable ground states and energies in the operation range of the XFEL. These results are most relevant for the layout of future nuclear quantum optics experiments at the XFEL.

Having investigated the control over nuclear transitions by means of x-ray lasers, it is natural to ask whether nuclear transitions can be in turn used to coherently manipulate x-rays. The capabilities to store and release single x-rays on demand [96–98], to manipulate the group velocity of γ-ray bursts [99], to control the Mössbauer spectra in a coherent way and to modify the time behavior of x-ray photons [100] have already been proven with nuclear iron samples. The ^{57}Fe nucleus is one among few nuclear species which may absorb and emit radiation recoil-free inside solid-state samples. This process has been first demonstrated by R. Mössbauer in 1958 [101, 102] and is known today as the Mössbauer effect. Depending on the sample properties, the 14.4 keV Mössbauer transition in ^{57}Fe can be strongly enhanced via cooperative effects [103, 104] and has been intensively investigated. Along with the developed instrumentation and optical elements for 14.4 keV photons, the distinct properties of ^{57}Fe seem to make it the perfect candidate for nuclear quantum optics experiments. The ^{57}Fe nucleus is furthermore the present candidate for x-ray quantum optics using nuclear transitions in thin film x-ray planar cavities [104, 105]. Within this geometry, effects like the collective Lamb shift [106], electromagnetically induced transparency [107], spontaneously generated coherences [41], subluminal light propagation [108] and Fano resonance control [109] could be demonstrated at x-ray energies.

Experiments performed with Mössbauer targets at SR facilities significantly boosted the studies of the resonant light-nucleus interaction, although these investigations are limited to the linear regime where at most one nucleus is excited per pulse [104]. In particular the pioneering work of Shvyd'ko [96], where the storage of single photons by dynamically controlling the nuclear response has been achieved, inspired several works proposing control schemes in nuclear forward scattering setups. Worth mentioning are, for instance, the nuclear "cage" for x-rays [110] and the field control of single x-ray photons [111]. Single photon entanglement in the x-ray regime [112, 113] and the entanglement between macroscopic nuclear samples [114] have also been discussed on the basis of nuclear forward scattering. These control procedures operated at single-photon nuclear interfaces along with the recent development of x-ray optics elements [26, 27, 115–119] and x-ray waveguides [120–124] open the perspective to extend fields like quantum information and quantum communication to photon energies in the keV range.

The elementary building block of all quantum information protocols is the information carrier, the so-called qubit [125]. So far, mostly microwaves or optical photons are used as information carriers. X-ray photonic qubits potentially have sub-Å spatial resolution [126], drastically reducing the fundamental limitation on nanoscale photonic circuits. A promising way to encode information in single x-rays is to employ orthogonal polarization states like it is accomplished in the optical regime [127–130]. X-ray linear polarization can be measured with precision up to 0.3° using polarimeters based on the Compton effect [131, 132], and Bragg reflections on crystals can filter polarizations states as good as $10^{-6}\%$ [133, 134]. However, such information encoding requires precise control and processing schemes for the polarization of individual x-rays so far not addressed.

In Part II of this Thesis the possibility to implement **Logic gates with polarization-encoded single x-rays** by means of resonant nuclear interactions is therefore investigated. A broadband x-ray pulse resonant to a nuclear transition impinges on a target in the presence of a hyperfine magnetic field and produces a single nuclear excitation. Fast rotations of the hyperfine field [96] are used to actively manipulate the polarization of the single-photon response of the nuclear target. We show that it is feasible to implement single-input logical gates via such magnetic field rotations, and even binary gates by introducing in addition a second, temporally synchronized control photon. Possible x-ray photonic realizations of logical operations involving two input states like the destructive controlled NOT (CNOT) gate are put forward.

Polarization-encoding can be also used to mark individual interference paths in order to obtain the *which-way* information, e.g., in the course of a scattering process. In general, interference occurs whenever a system has the possibility to choose between different interaction paths to reach the same final state. The most famous interference setup is probably Young's double slit where the indistinguishability of two spatial paths leads to an interference pattern in the momentum distribution. Quantum interference is closely related to the principle of complementarity [135], referring to the inability of revealing all information about a quantum system within a single experimental setup.

In quantum systems it is, for instance, possible to coherently obtain the *which-way* information in a double-slit setup which can be erased again later on, recovering the interference ability. This scheme proposed in Ref. [136] is known as the "quantum eraser". The basic elements of a quantum eraser, so enumerated in Ref. [137] are individual interfering quantum systems, a method of introducing which-path information, and a method of subsequently erasing this information in order to restore the interference. Various realizations of the quantum eraser in more or less traditional systems have been reported so far. First experiments in this direction employed entangled optical photon pairs for the study of interference [137] and momentum-position complementarity [138–140], while later on also more exotic systems have been employed or envisaged, for instance, mesoscopic systems [141, 142], kaons [143], nuclear spins [144], continuous-variable quantum erasing using field quadrature amplitude and phases [145] or ultrafast quantum emitters in microcavities [146]. We note that most of these setups address the position-momentum complementarity, with few exceptions [137, 143, 145].

As a further application of the single-photon polarization control in Part II, we propose a **Quantum eraser with x-ray quanta**, extending time-energy complementarity tests into a so far unexplored parameter range, the domain of x-ray photons. Considering the setup of nuclear forward scattering with synchrotron radiation, typically more than one hyperfine transition can be driven at once. The interference between the different frequency components results in the characteristic quantum beat pattern. The idea is to mark these scattering paths with orthogonal polarizations, e.g., right- and left-circular, in order to gain the *which-way* information. Once we know the scattering channel of the x-ray photon, the quantum beat pattern disappears in the intensity spectrum. However, projecting on a linear polarization basis recovers the quantum interference by erasing the *which-way* information. We put forward two schemes how to realize such a quantum eraser setup with x-ray quanta.

Structure of the Thesis

This Thesis is organized into two parts. Part I is about **Nuclear excitations induced by high-intensity x-ray lasers**. It starts with an introduction to the physics of x-ray free-electron lasers where the basic working principle is explained. The main goal of Chapter 1 is however to work out the prospects for nuclear physics opened by the XFEL. Afterwards in Chapter 2, the fundamental theory of the light-nucleus interaction is discussed. We follow a semiclassical approach where the nucleus is described as two-level system and the radiation field classically. Chapter 3 is devoted to the theoretical treatment of nuclear excitation by electron capture. The microscopic description builds the basis for treating NEEC as secondary excitation channel in an XFEL-induced plasma. Chapter 4 closes then the first Part. It delivers our numerical results for the competition between direct and secondary nuclear processes in nuclear photoexcitation setups with the XFEL. Here, the theoretical model for the plasma expansion is derived as well.

Part II of this Thesis treats the topic of **Single x-rays controlled by nuclear transitions**. In Chapter 5, we give a comprehensive description of nuclear forward scattering. We employ a theoretical approach which solves the problem directly in space and time. In Chapter 6, the possibility to dynamically manipulate the polarization response of nuclear targets by applying timed rotations of a magnetic field is discussed. Furthermore, it is shown how to extend present control schemes beyond the single scattering approximation. Our results for the implementation of logical operations for polarization-encoded x-rays is topic of Chapter 7. In Chapter 8, we propose a quantum eraser scheme employing nuclear forward scattering which enables time-energy complementarity tests in so-far unexplored parameter regimes.

Finally, the main findings are summarized and an outlook for future investigations is given.

Part I

Nuclear excitations induced by high-intensity x-ray lasers

Chapter 1

X-ray free-electron lasers & their potential for nuclear physics

Optical lasers have engaged a key role in the investigation of quantum dynamics in atomic systems over the last decades. While their success story is in particular based on non-linear effects, quantum phenomena and coherence, these are still difficult to achieve in the x-ray energy domain. In contrast to optical photons, x-rays are not longer resonant to valence-electron transitions, but rather inner-shell electrons in highly charged ions or low-lying nuclear transitions in the keV regime can be addressed. In particular in the nuclear realm, the advent and commissioning of the x-ray free-electron laser (XFEL) promise significant progress in nuclear quantum optical experiments with x-rays. This Chapter is therefore devoted to XFELs and their potential applications for nuclear physics. In Sec. 1.1, first the basic working principle of the XFEL is explained. Particular emphasis is put on the properties of the produced x-ray pulses which make them attractive for studying the resonant laser-nucleus interaction. Afterwards, in Sec. 1.2 we stress how the XFEL can be used to go beyond the weak nuclear excitation regime. Furthermore, the principle of isomer triggering is discussed. Sec. 1.3 is then devoted to possible plasma-mediated nuclear processes which occur under very characteristic plasma conditions due to the unique light-matter interaction of the XFEL.

1.1 The x-ray free-electron laser

Crystals, liquid dye or gases are the most common gain media for conventional lasers. In the latter light amplification is realized via the stimulated emission of electronic transitions inside the gain medium. In order to turn stimulated emission dominant over resonant absorption, the number of atoms in the excited state needs to be larger than the number of atoms in the ground state. This kind of population inversion is reached via an external energy source, the so-called pump. Establishing the population inversion for the lasing transition transforms the gain medium into an optical amplifier. This amplification process is further enhanced by using a resonator which directs the photons many times through the gain medium before extraction. The output laser light is finally characterized by a high degree of coherence, a narrow (diffraction-limited) beam collimation and a single frequency typically in the optical, ultraviolet or infrared regime.

The wish to build a coherent x-ray source exists nearly since the invention of the optical laser in 1960 [2, 3]. However, it has been quickly realized that the crossover from the visible to the x-ray domain has some fundamental obstacles resulting in the dilemma

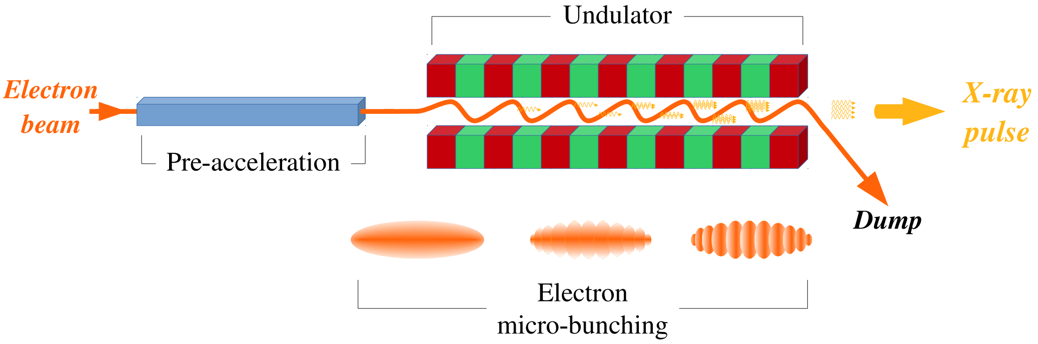

Figure 1.1: Working principle of the XFEL. After entering the undulator the pre-accelerated electrons start to oscillate and emit radiation into the forward direction. By passing the undulator, the electron beam becomes longitudinally modulated, a phenomenon called micro-bunching. The modulation leads to a collective emission which is exponentially amplified along the undulator passage.

of the γ-ray laser based on nuclear transitions [13]. On the one hand, a sufficient number of nuclei needs to be accumulated in order to obtain population inversion, on the other hand, the γ-ray emission must be operated at its natural line width to achieve the maximal possible stimulated emission rate. The antagonism is that the high pump intensity required for population inversion is either not achievable with available sources or leads to heating and destruction effects of the gain medium resulting in inhomogeneous broadening of the lasing transition [147, 148]. Since the cross section of stimulated emission ($\propto \lambda^2$) is anyway strongly suppressed in the case of x-ray wavelengths (more than 8 orders of magnitude in comparison to optical photons) [147], this dilemma makes it nearly impossible to build an x-ray laser in the conventional sense; rather a new, radically different approach is required.

In order to bypass this dilemma much effort has been put into the development of a coherent x-ray source which finally peaked out in the commissioning of the x-ray free-electron lasers. Instead of using bound transitions in crystals, liquid dye or gases, the gain medium of the XFEL is made up of free electrons. The basic idea relies on the fact that the acceleration of charged particles to relativistic velocities leads to a strong emission of electromagnetic waves. Unlike in conventional lasers, the amplification process of the XFEL happens only in a single pass through the gain medium.

The working principle of the XFEL is illustrated in Fig. 1.1. Pre-accelerated electrons typically via a linear accelerator (LINAC) enter a long array of periodically arranged magnetic dipoles, the so-called undulator. Due to the Lorentz force of the periodic magnetic field, the electrons start to oscillate leading to the emission of electromagnetic waves. Since the electrons move with relativistic velocities close to the speed of light, the emitted radiation is strongly collimated into the forward direction [149]. Moreover, the usage of free electrons as gain medium has the advantage that the photon energy is not restricted to a certain atomic transition. This makes the radiation typically tunable over a wide wavelength spectrum depending on the properties of the incoming electron beam [149].

A key feature of the XFEL mechanism is the micro-bunching [15] of the electron cloud as illustrated in Fig. 1.1. During the propagation through the undulator the electron beam experiences a longitudinal modulation caused by the interaction with the self-emitted electromagnetic waves. The transverse B-field of these waves and the transverse velocity component of the electrons results in a Lorentz force which pushes the electron beam into micro-bunches. This modulation has two important consequences [149, 150]: (i) the total emitted intensity is proportional to N^2 instead of N where N is the number of electrons; (ii) the radiation power is exponentially amplified along the passage through the undulator, a process called self-amplified spontaneous emission (SASE). Moreover, the wavelength of the emitted radiation pulse is directly connected to the periodicity of the micro-bunching [150]. In contrast to common optical lasers, XFELs are operated in a single-SASE setup where the x-ray pulse traverses only once the undulator.

Characteristic for this new kind of radiation sources are the small wavelengths in the x-ray regime, high power, high brilliance, narrow bandwidths ($\sim$ eV), pure polarization and good coherence properties. The pulse duration lies usually in the range of hundreds of fs. The brilliance is determined by the spectral photon flux divided by the divergence and the rms radius of the photon beam. In comparison to synchrotron radiation (SR) sources, XFEL facilities are able to provide x-ray pulses with an eight orders of magnitude higher brilliance [15].

In addition to the brightness of the XFEL radiation, the coherence properties are substantially improved in comparison to broad-band synchrotron radiation. However, while the XFEL pulses are fully spatial coherent, their temporal coherence is poor because of random fluctuations in the electron charge density at the start-up of the SASE process [32]. In general, the quality of the x-ray pulse is critically dependent on the quality of the incoming electron beam. Since the electrons are typically produced by the emission of a cathode, the random distribution at the start-up leads to XFEL wave packets consisting of many statistically distributed spikes. Each individual radiation spike is fully coherent, spatially as well as temporally, but without fixed phase relation among each other.

Until now, there are mainly two ideas on how to tackle the problem of the poor temporal coherence. The first idea is to load the undulator with an already seeded light pulse which can reduce shot-to-shot fluctuations at the start-up (seeded XFEL) [21–23]. The two-stage SASE free-electron laser proposed by Feldhaus in 1997 [21] has already been demonstrated in the soft [28] and hard x-ray regime [29]. The design consists of a sequence of two undulators with a monochromator in between. Operating the first undulator in the linear regime results in a seeded radiation pulse at the entrance of the second undulator. A monochromatic x-ray pulse close to the Fourier limit and a significant reduction of shot-to-shot fluctuations in the energy spectral density can be expected.

The second idea to improve the temporal coherence of the XFEL radiation is to construct an x-ray oscillator (XFEL oscillator, XFELO) [24]. Key ingredients for the XFELO are electron bunches of ultralow emittance and a low-loss optical cavity. The cavity directs the light pulse several times through the undulator such that it meets a new, fresh electron bunch each time when entering the undulator. In this manner, the initially incoherent x-rays evolve into a coherent pulse. In order to obtain an exponential increase of the pulse intensity along with the round-trip number, a low-loss x-ray cavity based on high-reflectivity crystals [26] is required. For instance, a 0.2 mm thick sapphire crystal shows a reflectivity of 0.96 for 14.4 keV photons while keeping the heat load minimal [24]. Diamond mirrors with a reflectivity at normal incidence close to 100% are even more preferable [27]. Apart of the good coherence properties, the XFELO output radiation is anticipated to comprise a narrow spectral bandwidth (more than 3 orders of magnitude narrower in comparison to the XFEL) and a high repetition rate. Although a lower peak intensity is expected in comparison to the XFEL, the peak brilliance should be of the same order of magnitude while the average spectral brightness should increase by a factor of one thousand in the case of the XFELO [25].

Currently, there are two operating XFEL facilities worldwide, the LCLS [151] at SLAC in Stanford and the SACLA [152] in Japan. The LCLS provides photons with an energy of approximatively 10 keV and an average spectral brightness up to 2.7×10^{22} photons/(s mrad^2 mm^2 0.1%bandwidth). The SACLA facility in Japan delivered the so-far highest photon energy of 19.5 keV. In addition, several XFEL machines are in construction like the European XFEL [18] at DESY in Hamburg, the SwissFEL [19] at the Paul Scherrer Institute in Switzerland, and MaRIE [20] at the Los Alamos National Laboratory in the United States. The European XFEL, for instance, is expected to achieve photon energies up to 24.8 keV [18]. The XFEL higher harmonics may even provide photon pulses with energies above 25 keV.

In Table 1.1, we summarize the parameters of the currently running XFELs, the LCLS and the SACLA, and of the European XFEL which is still under construction at DESY. Additionally, we also provide expected characteristics for the XFELO. We assume a moderate laser focusing on a spot of 10 μm^2, although a focal length of 7 nm has for instance already been achieved in Ref. [10]. While the peak intensities of the considered lasers are all on the order of 10^{17} W/cm^2, the XFELO has an outstanding long coherence time (1 ps) and also an expected repetition rate of 10^6 Hz [24] which is about 1-2 orders of magnitude higher than the other facilities. In Chap. 4, we will explicitly show that the coherence properties and the repetition rate play a crucial role in the XFEL nuclear photoexcitation.

1.2 Nuclear photoexcitation

The advent and commissioning of the XFEL promise significant progress in the field of nuclear quantum optics. It offers in particular the possibility to investigate the direct laser-nucleus interaction in solid-state targets with coherent, highly brilliant x-ray pulses resonant to nuclear transitions in the few keV regime. In the optical domain there is a multitude of methods successfully applied to understand and manipulate the dynamical behavior of electronic states in atoms. The idea of nuclear quantum optics is to transfer these methods to the nuclear realm in order to explore and control the electromagnetic interaction of nuclei on the most fundamental level [39]. The controlled preparation, manipulation and detection of nuclear states would, for instance, offer the possibility to measure nuclear properties like transition frequency or dipole moment independent of any nuclear model.

A general hindrance in the laser-induced nuclear excitation is that only a small fraction

Parameter	LCLS	SACLA	Eur. XFEL	XFELO
E_{max} (eV)	10332	19556	24800	25000
BW	2×10^{-3}	2.2×10^{-3}	8×10^{-4}	1.6×10^{-7}
T_{pulse} (fs)	100	100	100	1000
T_{coh} (fs)	2	–[1]	0.2	1000
P_{peak} (W)	1.5–4×10^{10}	10^{10}	2×10^{10}	4.1×10^{9}
I_{peak} (W/cm^2)	3.9×10^{17}	9.8×10^{16}	2.0×10^{17}	4.0×10^{16}
f_{rep} (Hz)	30	10	4×10^{4}	10^{6}

[1] In our calculations we assumed 10% of the pulse duration, i.e., 10 fs.

Table 1.1: The maximal achievable photon energy E_{max}, bandwidth BW, pulse duration T_{pulse}, coherence time T_{coh}, peak power P_{peak}, peak intensity I_{peak} and pulse repetition frequency f_{rep} for the four considered XFEL facilities: LCLS [16,153,154], SACLA [17,155], Eur. XFEL [18] and XFELO [24]. A focal spot of 10 μm^2 is assumed.

of the laser photons really fulfills the nuclear resonance condition due to the usually small nuclear transition widths. This has two major consequences. First, since only a small number of nuclei is excited per pulse, the repetition rate of the XFEL facility is a key ingredient for an effective driving of nuclear transitions. The repetition rates of the LCLS and the SACLA have with 30 Hz and 10 Hz, respectively, the same order of magnitude (see Table 1.1). The future European XFEL is expected to provide light pulses with a repetition rate of 4×10^4 Hz and the XFELO even with a frequency of 10^6 Hz, which is 3 and respectively 4-5 orders of magnitude higher than the corresponding values of the already operational XFELs.

The second consequence is that we need to introduce an effective laser intensity which accounts for the mismatch between photon and nuclear transition energy [156], namely

$$I_{\mathrm{eff}} = \frac{\Gamma_{\mathrm{nucl}}}{\Gamma_{\mathrm{laser}}} I \ . \tag{1.1}$$

Thereby, Γ_{nucl} denotes the nuclear transition width and Γ_{laser} the bandwidth of the laser pulse. The effective field amplitude E_{eff} experienced by the corresponding nuclear transition is proportional to $\sqrt{I_{\mathrm{eff}}}$.

So far, experiments concerning the direct light-nucleus interaction are mostly performed with incoherent, broadband SR light [157]. In particular the interaction of x-ray light with Mössbauer nuclei in the few keV transition energy range has gained considerable momentum, both theoretically [105,110–114,148,158–163] and experimentally [41,96–98,100,104,106–109,164]. In all these experiments only weak nuclear excitations can be achieved due to the low degeneracy of SR and the small nuclear transition widths (typically $\sim 10^{-8}$ eV). The high brilliance of XFELs drastically changes this situation, making the step from one to a few or maybe many resonant photons per pulse. Recently, the first nuclear resonance scattering experiment at an XFEL has been performed with FeBO$_3$ crystals [50]. Chumakov and co-workers have demonstrated multiple nuclear excitations of ^{57}Fe. Using a high-monochromatization scheme for the x-ray beam at SACLA, up to 70 excited nuclei per pulse could be achieved.

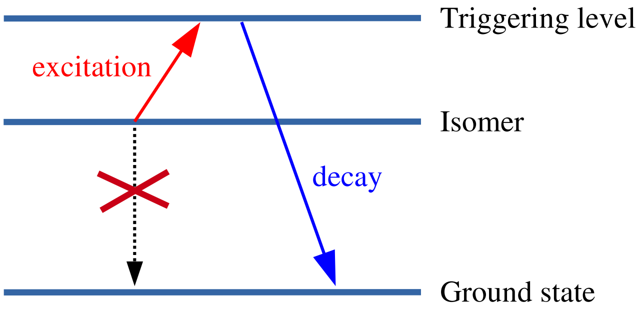

Figure 1.2: The process of isomer triggering. The decay of the metastable isomeric state to the ground state is highly forbidden. The excitation to an above lying triggering level which is connected to the ground state can efficiently depopulate the isomer releasing the initially stored excitation energy.

Apart of reaching the multiple excitation regime, the coherence properties of the self-seeded XFEL in development today [29] are expected to further promote quantum optical effects [7, 39, 156] in the nuclear realm. For instance, when coherent population transfer in nuclear systems becomes feasible [52, 53], nuclear reactions can be studied in systems initially prepared in excited states. The controlled excitation of nuclei entails further potential applications like fully coherent γ-ray lasers [13, 158, 164], a new nuclear frequency standard based on the isomeric state in ^{229}Th [165] or a nuclear energy storage solution founded on the principle of isomer triggering [43–47].

Isomers are long-lived nuclear excited states whose decay to the ground state is fundamentally supressed (see Fig. 1.2). In general, one needs to distinguish between shape, spin and K isomers [43]. In shape isomers a metastable state occurs due to a second potential minimum for large elongation of the nucleus. Such isomers typically decay by fission into two smaller parts and only in a few cases the γ-decay channel is able to compete. In the case of spin and K isomers the decay to the ground state is highly forbidden because of angular momentum conservation. A large change in either the nuclear spin quantum number or the spin projection quantum number (K represents the spin projection onto the nuclear symmetry axis) requires the emission of photons with high multipolarity which is strongly suppressed.

The isomeric lifetimes can range from ms ($^{242\mathrm{m}}$Am: $\tau \approx 14$ ms, shape isomer) over hours ($^{180\mathrm{m}}$Hf: $\tau \approx 5.5$ h, K isomer) up to millions of years ($^{180\mathrm{m}}$Ta: $\tau \approx 10^{15}$ y, spin isomer). The study of isomers has several incentives [44]: (i) they are expected to play a crucial role in the creation of elements in the universe which is important for nuclear astrophysics; (ii) understanding the formation process of isomers would gain new insights into the nuclear structure; (iii) the process of isomer triggering makes them to a “clean” energy storage solution.

The idea of isomer triggering is to connect the metastable isomer with an above lying triggering level in order to release the initially stored excitation energy on demand. The triggering level needs to be linked to freely radiating states in order to efficiently depopulate the isomer. The basic principle of isomer triggering is illustrated in Fig. 1.2.

Triggering via the coherent XFEL radiation is expected to lead to a strong enhancement of the depletion efficiency in comparison to the incoherent excitation mechanisms so far employed [48, 49].

In Chap. 4, we investigate the XFEL-induced depletion of the isomeric state in molybdenum. The 6.85 h long-lived $^{93\mathrm{m}}$Mo isomer is particularly attractive for an XFEL-induced activation, since the isomeric energy of 2.5 MeV can be retrieved by a 4.85 keV triggering transition accessible by today's XFEL facilities. Because of the advantageous energy ratio, 4.85 keV to 2.5 MeV, isomer depletion in ^{93}Mo opens interesting applications for energy storage solutions. Advantageous is furthermore that the long-lived excited state $^{93\mathrm{m}}$Mo can be produced by $^{93}_{41}$Nb(p,n)$^{93\mathrm{m}}_{42}$Mo reactions. In this way, the isomers are directly embedded into solid-state niobium foils which makes it possible to employ solid-state target scenarios beneficial for an XFEL activation. Surprisingly, it is not the direct photoexcitation which dominates the $^{93\mathrm{m}}$Mo isomer triggering in such a scenario, instead secondary processes from the coupling to the atomic shell play the crucial role. How such secondary excitation channels come into play is discussed in the next Section.

1.3 Plasma-mediated nuclear processes

The step from broadband synchrotron sources to coherent XFEL facilities is expected to bring nuclear photoexcitation experiments from the regime of weak excitation into a region where a few nuclei can be excited at once, as motivated in the previous Section. In the same manner the high XFEL intensity enhances the light-nucleus interaction, also the interaction with the electrons is directed into nonlinear regimes where sequential, multi-photon absorption processes are prevalent [72]. XFEL experiments with gaseous samples like neon [74] or xenon [76] have for instance proven the production of high charge states during a single pulse. It was even possible to follow the sequence of the individual ionization processes. In the case of neon for instance, 2 keV photons have produced charge states up to fully ionized neon cores via a repeated sequence of inner-shell photon absorption and subsequent Auger decay [74]. The photoionization of valence electrons only plays a role at the end of the ionization chain for highly charged ions or in the case of lower photon energies where inner-shell photoionization is energetically no longer possible.

In scenarios with solid-state targets, photoionization via the XFEL can also play an important role. For instance in Ref. [73] it has been shown that the absorption of intense x-ray pulses with a photon energy of 92 eV turns solid aluminum transparent for the impinging x-rays in a timescale shorter than the pulse duration. By increasing the intensity further, XFELs have moreover the potential to create new states of matter. In 2012, the creation of an aluminum plasma with an XFEL has been experimentally demonstrated [77]. Laser light with a photon energy up to 1.8 keV and an intensity larger than 10^{17} W/cm^2 has been used. Plasma states at solid-state density with temperatures in excess of 10^6 K could be created due to the unique light-matter interaction in this wavelength regime and the characteristic XFEL properties.

The light-matter interaction between keV radiation and mid-Z materials is predomi-

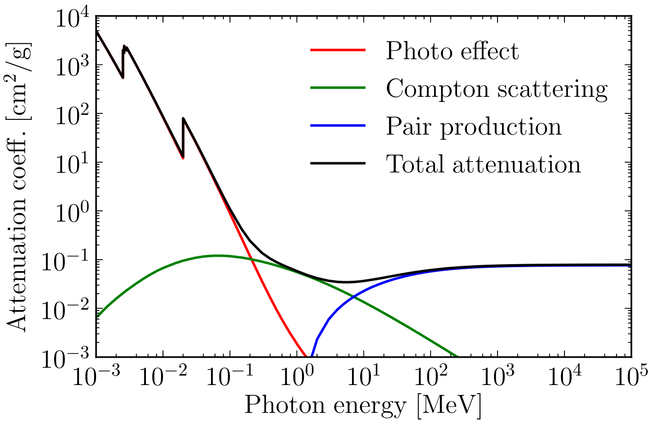

Figure 1.3: Attenuation coefficient for molybdenum. The contributions from the photoelectric effect (red curve), Compton scattering (green curve) and pair production (blue curve) are shown in dependence of the photon energy. The data is taken from [166].

nantly dictated by the photoelectric effect as shown in Fig. 1.3 for the example of molybdenum. Compton scattering is in this case orders of magnitude smaller and pair production is energetically forbidden for photon energies below 1.022 MeV. The photoelectric effect prefers the interaction with deeply bound electrons which leads to inner-shell photoionization if the photon energy is higher than the corresponding ionization potential. At the small energy tail of the red curve in Fig. 1.3, the so-called ionization edges can be seen. This stepwise increase of the attenuation coefficient is caused by reaching the ionization energy of a new shell. In Fig. 1.3, the L-shell edge at a photon energy of around 2.5 keV and the K-shell edge at approx. 20 keV are visible. Generally, the probability of interaction via the photoelectric effect decreases exponentially with increasing photon energy.

In contrast to optical or infrared photons, x-rays are not only able to produce directly inner-shell holes by photoionization, but also penetrate much further into the material leading to a very uniform energy deposition of the XFEL pulse inside the target. Moreover, the heating of the solid-state sample by a laser pulse with a duration around 100 fs occurs very rapidly. On this time scale the ionic motion is negligible, resulting in a plasma with near to solid-state density. This rapid, isochoric heating of the plasma (the volume is nearly unaffected during the formation process) leads to uniform temperature and density distributions immediately after the interaction with the XFEL pulse. The plasma expansion after the creation process evolves hydrodynamically along isentropes [149]. The ability to vary the initial temperature over a wide range while keeping the initial density at its solid-state value offers the possibility to gain insights into the plasma creation and evolution in so far unexplored temperature-density regions [149].

In such plasma environments, nuclear effects can engage an important role. For instance, the presence of free electrons and atomic vacancies renders the occurrence of exotic nuclear processes from the coupling to the atomic shell possible. In the case of XFEL-induced plasmas, such secondary nuclear excitation processes can potentially

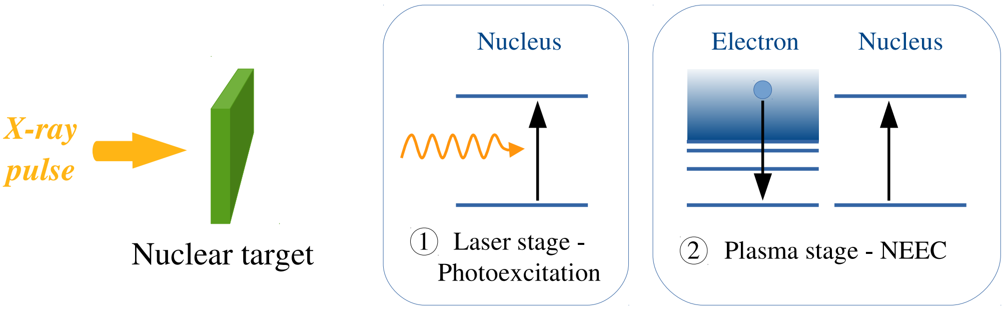

Figure 1.4: Competition of direct and secondary nuclear excitation. The super-intense XFEL is able to resonantly drive low-lying nuclear transitions in the keV regime via photoexcitation (laser stage). If the laser intensity is high enough, a plasma can be created where secondary nuclear excitation channels come into play, e.g., NEEC (plasma stage).

compete with the direct photoexcitation via the laser pulse. Possible secondary nuclear excitation channels are:

- Photoexcitation via secondary photons present in the plasma.
- Coulomb excitation (inelastic electron scattering).
- Nuclear processes coupled to the atomic shell:
  - Nuclear Excitation by Electron Capture (NEEC).
  - Nuclear Excitation by Electron Transition (NEET).

These plasma-mediated nuclear excitation mechanisms have already been investigated in hot, dense astrophysical [82–86] and optical laser-produced plasmas [87]. The excitation of low-lying nuclear transitions as well as the enhanced nuclear level decay of isomers like $^{235\mathrm{m}}$U, $^{201\mathrm{m}}$Hg and $^{93\mathrm{m}}$Mo has been analyzed under local thermal equilibrium and non-local thermal equilibrium conditions. Typically, the microscopic excitation mechanism is treated independently of the thermodynamic plasma environment. More advanced approaches treating the nuclear excitation mechanism in contact with the thermodynamic environment are rather seldom [167, 168].

In the case of cold, high-density plasmas, nuclear processes coupling to the atomic shell are expected to engage a dominant role among the secondary excitation channels. In this Thesis, we restrict ourselves to the process of NEEC. In the resonant process of NEEC, a free electron is captured into a bound atomic state by the simultaneous excitation of the nucleus as illustrated in Fig. 1.4. NEEC is investigated as plasma-mediated, secondary nuclear excitation channel in a scenario initially designed for the observation of the direct, resonant nuclear photoexcitation via the XFEL. In distinction to previous works, the XFEL not only grants access to parameter regimes of unexplored temperatures and densities, but also offers the possibility to study the competition between direct and secondary excitation mechanisms not available in laboratory plasmas generated by optical lasers [88–92].

The evaluation of possible secondary effects in nuclear photoexcitation studies with the XFEL is the topic of Part I of this Thesis. The XFEL-induced excitation in solid-state nuclear targets can be split into two stages. In the time period when the XFEL pulse is present (a typical value for the pulse duration is 100 fs), the nuclei inside the solid-state target can be resonantly driven by the laser-nucleus interaction which is referred to as laser stage in Fig. 1.4. The theoretical treatment of the resonant nuclear photoexcitation by the XFEL is presented in Chap. 2. During the laser stage, the interaction with the electrons may lead to the formation of a plasma. In the plasma stage (in principle also during but mostly after the laser interaction) secondary processes like NEEC become possible. The microscopic NEEC process is presented in Chap. 3. Both the laser-induced photoexcitation and the plasma-mediated NEEC channels contribute to the final nuclear excitation rate. In Chap. 4, it is exactly this competition between the direct excitation in the laser stage and the secondary NEEC channel in the plasma stage that is investigated. The specific examples of $^{93\mathrm{m}}$Mo isomer triggering and the driving of ^{57}Fe from the ground to the first excited state are discussed. It turns out that secondary NEEC gives the dominant contribution in the case of the $^{93\mathrm{m}}$Mo depletion, whereas it can be safely neglected for ^{57}Fe targets.

Chapter 2

Light-induced resonant nuclear excitation

The study of the resonant laser-nucleus interaction is considered to be strongly promoted by the development of the fourth generation x-ray sources like super-intense XFEL. Although the XFEL-photon energies allow to employ solid-state target scenarios, the available frequency range is still limited ($\lesssim 25$ keV) such that the list of suitable nuclear transitions is short. In particular, low-lying electric dipole ($\mathcal{E}1$) transitions which are mainly used in atomic quantum optics, are hard to find in the nuclear domain. However, in Ref. [156] it has been shown that in nuclear systems electric dipole-forbidden transition can have matrix elements of comparable magnitude with those of electric dipole-allowed transitions. Especially, $\mathcal{M}1$ and $\mathcal{E}2$ transitions are mostly found in the energy range where resonant photons are accessible by today's x-ray sources.

In order to describe the direct, resonant light-nucleus interaction we use the density matrix formalism well known from quantum optics [4]. Within this formalism the dynamics of the nuclear system is determined in dependence of the considered interaction Hamiltonian including all relaxation channels. Here, a semiclassical approach is applied where the nuclear quantum system interacts with a classical radiation field. Furthermore, the theoretical approach is introduced on the example of a two-level system since the x-ray field is nearly resonant with a single nuclear transition.

This Chapter mainly follows the approach presented in Refs. [40] and [156], and references therein. The general framework of the density matrix formalism applied to quantum optical systems can also be found in standard textbooks like for instance Ref. [4]. In particular Sec. 2.1 introducing the basic equations describing the quantum dynamics of the nuclear system follows Ref. [4]. Afterwards the calculation of the interaction matrix elements is presented in Sec. 2.2. Therein, the multipole expansion of the electromagnetic field is applied which allows to go beyond electric dipole transitions. The final Sec. 2.3 follows the work published in Ref. [161] where collective effects and their influence on the laser-induced nuclear excitation are studied. Atomic units $\hbar = m_{\mathrm{e}} = e = 4\pi\varepsilon_0 = 1$ are used throughout this Chapter.

2.1 Basic quantum dynamics

The natural and most convenient way to describe the direct laser-nucleus interaction is via the well-established density matrix formalism. In this formalism the time evolution

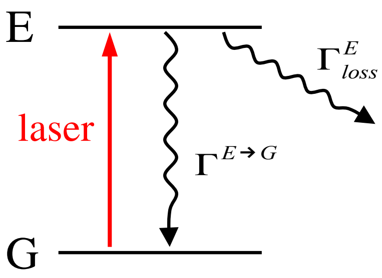

Figure 2.1: Nuclear two-level system resonantly driven by a laser field. The ground state G is considered to be stable, whereas the width of the excited state is composed of two parts: the decay back to the ground state $\Gamma^{E\rightarrow G}$ and a loss channel $\Gamma^{E}_{\mathrm{loss}}$ which removes nuclear state population from the system.

of the density matrix ρ is determined by the master equation [4]

$$\mathrm{i}\frac{\partial}{\partial t}\rho = [H_0 + H_{\mathrm{I}}, \rho] + \mathcal{L}\rho \; . \tag{2.1}$$

The so-called Lindblad operator $\mathcal{L}$ includes decoherent relaxation processes of the system like spontaneous decay or dephasing of the laser field.

Since we are interested here only in the interaction between the nuclear degrees of freedom and the electromagnetic field, the total Hamiltonian can be split into an unperturbed part H_0 and a part H_{I} describing the laser-nucleus interaction which can be written as

$$H_I = -\frac{1}{c}\int \mathrm{d}^3r\, \boldsymbol{j}_{\mathrm{n}}(\boldsymbol{r}) \cdot \boldsymbol{A}(\boldsymbol{r}, t) \; . \tag{2.2}$$

Here, c stands for the speed of light and $\boldsymbol{j}_{\mathrm{n}}$ represents the nuclear current density. The vector potential of the electromagnetic field denoted by $\boldsymbol{A}$ is described classically. In the Coulomb gauge it is given by [156]

$$\boldsymbol{A}(\boldsymbol{r}, t) = \frac{c}{\omega_k} E_k \mathrm{e}^{-\mathrm{i}\omega_k t} \mathrm{e}^{-\mathrm{i}\boldsymbol{k}\cdot\boldsymbol{r}} \boldsymbol{e}^{*}_{\boldsymbol{k}\sigma} + \text{c.c.} \; , \tag{2.3}$$

where E_k represents the electric field amplitude, $\boldsymbol{k}$, ω_k and σ are the photonic wave vector, frequency and transversal polarization, respectively, and $\boldsymbol{r}_{\mathrm{n}}$ denotes the nuclear spatial coordinates. Here, we exemplarily consider polarization vectors $\boldsymbol{e}^{*}_{\boldsymbol{k}\sigma}$ with $\sigma = \pm 1$ which refers to circularly polarized light. The generalization to arbitrary polarizations is straightforward.

For the considered scenario of resonant or near-resonant photoexcitation it is adequate to describe the nucleus as a two-level quantum system consisting of the states $|G\rangle$ and $|E\rangle$ as shown in Fig. 2.1. Each of these states is composed of a set of hyperfine levels characterized by their total angular momentum I_l and projection $M_l = -I_l, \ldots, I_l$, with $l \in \{g, e\}$ referring to the states $|G\rangle$ and $|E\rangle$, respectively. The unperturbed Hamiltonian of the considered two-level system can be represented by

$$H_0 = \omega_g |G\rangle\langle G| + \omega_e |E\rangle\langle E| \; . \tag{2.4}$$

Furthermore, the laser is assumed to be nearly resonant to the nuclear transition energy $\omega_0 = \omega_e - \omega_g$ in order to drive the nuclear population from the ground to the excited level. The ground state $|G\rangle$ is thereby assumed to be stable, whereas the excited level $|E\rangle$ has a natural transition width Γ_0 which can be written as

$$\Gamma_0 = \Gamma^{E\to G} + \sum_{F\neq G} \Gamma^{E\to F} = \Gamma^{E\to G} + \Gamma^{E}_{\mathrm{loss}} \ , \tag{2.5}$$

where the contribution $\Gamma^{E}_{\mathrm{loss}}$ integrates possible loss channels removing occupation from the considered two-level system for instance by decay paths not reaching $|G\rangle$. This contribution is in particular important for the cases where the initial state $|G\rangle$ does not coincide with the ground state of the nucleus.

The main purpose of this Section is to derive the optical Bloch equations which fully determine the dynamics of the considered system. Therefore, the master equation (2.1) is projected onto the states $|G\rangle$ and $|E\rangle$ which results in a system of differential equations for the density matrix elements ρ_{ab} with $a, b \in \{g, e\}$,

$$\begin{aligned}
\frac{\partial}{\partial t}\rho_{\mathrm{gg}}(M_{\mathrm{g}}) &= -2\,\mathrm{Im}\left(\sum_{M_{\mathrm{e}}} \rho_{\mathrm{ge}}(M_{\mathrm{g}}, M_{\mathrm{e}}) \mathrm{e}^{\mathrm{i}\omega_k t} \langle I_{\mathrm{e}} M_{\mathrm{e}} | H_{\mathrm{I}} | I_{\mathrm{g}} M_{\mathrm{g}} \rangle \right) \\
&\quad + \sum_{M_{\mathrm{e}}} \gamma^{E\to G}(M_{\mathrm{g}}, M_{\mathrm{e}}) \rho_{\mathrm{ee}}(M_{\mathrm{e}}) \ , \\
\frac{\partial}{\partial t}\rho_{\mathrm{ge}}(M_{\mathrm{g}}, M_{\mathrm{e}}) &= -\mathrm{i}\Delta \rho_{\mathrm{ge}}(M_{\mathrm{g}}, M_{\mathrm{e}}) + \mathrm{i}\left(\rho_{\mathrm{gg}}(M_{\mathrm{g}}) - \rho_{\mathrm{ee}}(M_{\mathrm{e}})\right) \mathrm{e}^{-\mathrm{i}\omega_k t} \langle I_{\mathrm{g}} M_{\mathrm{g}} | H_{\mathrm{I}} | I_{\mathrm{e}} M_{\mathrm{e}} \rangle \\
&\quad - \frac{\gamma^{E\to G}(M_{\mathrm{g}}, M_{\mathrm{e}})}{2} \rho_{\mathrm{ge}}(M_{\mathrm{g}}, M_{\mathrm{e}}) - \gamma_{\mathrm{dec}} \rho_{\mathrm{ge}}(M_{\mathrm{g}}, M_{\mathrm{e}}) \ , \\
\frac{\partial}{\partial t}\rho_{\mathrm{ee}}(M_{\mathrm{e}}) &= 2\,\mathrm{Im}\left(\sum_{M_{\mathrm{g}}} \rho_{\mathrm{ge}}(M_{\mathrm{g}}, M_{\mathrm{e}}) \mathrm{e}^{\mathrm{i}\omega_k t} \langle I_{\mathrm{e}} M_{\mathrm{e}} | H_{\mathrm{I}} | I_{\mathrm{g}} M_{\mathrm{g}} \rangle \right) \\
&\quad - \rho_{\mathrm{ee}}(M_{\mathrm{e}}) \sum_{M_{\mathrm{g}}} \gamma^{E\to G}(M_{\mathrm{g}}, M_{\mathrm{e}}) - \gamma^{E}_{\mathrm{loss}}(M_{\mathrm{e}}) \rho_{\mathrm{ee}}(M_{\mathrm{e}}) \ .
\end{aligned} \tag{2.6}$$

In the derivation of Eqs. (2.6), a transformation to a rotating frame was applied in order to eliminate the rapidly oscillating terms from the equations of motion. Moreover, the detuning Δ is defined by the difference of the transition frequency ω_0 and the photon frequency ω_k. The limited coherence time of the laser pulse is described as decay of the nuclear coherences ρ_{ge} with decay rate γ_{dec}. The partial decay rates $\gamma^{E\to G}(M_{\mathrm{g}}, M_{\mathrm{e}})$ of the upper level $|E\rangle$ are given by [156]

$$\gamma^{E\to G}(M_{\mathrm{g}}, M_{\mathrm{e}}) = \frac{2I_{\mathrm{e}} + 1}{2L + 1} C\big(I_{\mathrm{g}} \ I_{\mathrm{e}} \ L; M_{\mathrm{g}} \ -M_{\mathrm{e}} \ M\big)^2 \, \Gamma^{E\to G} \ , \tag{2.7}$$

where L and M are the multipolarity and projection quantum numbers of the decay photon and $C(j_1 \ j_2 \ j_3; m_1 \ m_2 \ m_3)$ stand for the Clebsch-Gordan coefficients. Summing the partial decay rates $\gamma^{E\to G}(M_{\mathrm{g}}, M_{\mathrm{e}})$ over all possible projections M_{g} and M_{e} recovers the total rate $\Gamma^{E\to G}$. Similarly, the contribution from the loss channel $\gamma^{E}_{\mathrm{loss}}(M_{\mathrm{e}})$ may depend on the projection quantum number M_{e}. The optical Bloch equations (2.6) can be solved numerically once the interaction matrix elements $\langle I_{\mathrm{e}} M_{\mathrm{e}} | H_{\mathrm{I}} | I_{\mathrm{g}} M_{\mathrm{g}} \rangle$ are known.

2.2 Interaction matrix elements

In atomic physics the electromagnetic field is usually described in terms of plane waves as shown in Eq. (2.3). The photons are characterized by their wave vector $\boldsymbol{k}$ and the polarization σ. In nuclear systems, it is often more convenient to use the angular momentum L with projection M and the transition parity to define the photonic states. Therefore, the electromagnetic field is expanded in terms of its electric and magnetic multipoles $\boldsymbol{A}^{\mathcal{E}}_{LM}$ and $\boldsymbol{A}^{\mathcal{M}}_{LM}$ [169],

$$\boldsymbol{A}(\boldsymbol{r},t) = \frac{c}{\omega_k} E_k \mathrm{e}^{-\mathrm{i}\omega_k t} \sum_{LM} \sqrt{2\pi(2L+1)}(-\mathrm{i})^L \mathcal{D}^L_{M\,-\sigma}(\hat{\boldsymbol{k}}) \left(\boldsymbol{A}^{\mathcal{M}}_{LM}(\boldsymbol{r}) + \mathrm{i}\sigma \boldsymbol{A}^{\mathcal{E}}_{LM}(\boldsymbol{r}) \right) \ , \tag{2.8}$$

where $\mathcal{D}^L_{M\,-\sigma}(\hat{\boldsymbol{k}})$ represents the Wigner rotation matrix [170] turning the quantization axis (z-axis) into the direction of $\hat{\boldsymbol{k}} = \boldsymbol{k}/k$. The electric and magnetic multipole fields $\boldsymbol{A}^{\mathcal{E}}_{LM}$ and $\boldsymbol{A}^{\mathcal{M}}_{LM}$ are eigenfunctions of both $\boldsymbol{L}^2$ and L_z and are themselves solutions of the field-free Maxwell equations. According to Ref. [169] they are given by

$$\begin{aligned} \boldsymbol{A}^{\mathcal{M}}_{LM}(\boldsymbol{r}) &= j_L(kr)\boldsymbol{Y}^M_{LL}(\theta,\varphi) \ , \\ \boldsymbol{A}^{\mathcal{E}}_{LM}(\boldsymbol{r}) &= \sqrt{\frac{L+1}{2L+1}} j_{L-1}(kr)\boldsymbol{Y}^M_{LL-1}(\theta,\varphi) - \sqrt{\frac{L}{2L+1}} j_{L+1}(kr)\boldsymbol{Y}^M_{LL+1}(\theta,\varphi) \\ &= -\frac{\mathrm{i}}{k}\nabla \times \left(j_L(kr)\boldsymbol{Y}^M_{LL}(\theta,\varphi) \right) \ , \end{aligned} \tag{2.9}$$

where j_L represent the spherical Bessel functions and $\boldsymbol{Y}^M_{JL}$ stand for the vector spherical harmonics defined by [170]

$$\boldsymbol{Y}^M_{JL}(\theta,\varphi) = \sum_\nu \sum_q C(L\ 1\ J; \nu\ q\ M) Y_{L\nu}(\theta,\varphi)\boldsymbol{\varepsilon}_q \ . \tag{2.10}$$

Here, $Y_{L\nu}$ represent the spherical harmonics [170] and $\boldsymbol{\varepsilon}_q$ ($q = 0, \pm 1$) stand for the spherical unit vectors which can be expressed in terms of the Cartesian unit vectors as follows

$$\begin{aligned} \boldsymbol{\varepsilon}_0 &= \boldsymbol{e}_z \ , \\ \boldsymbol{\varepsilon}_{\pm 1} &= \mp \frac{1}{\sqrt{2}} \left(\boldsymbol{e}_x \pm \mathrm{i}\boldsymbol{e}_y \right) \ . \end{aligned} \tag{2.11}$$

The vector spherical harmonics are irreducible tensors of rank J with components $M = -J, \ldots, J$. Thereby, J is subject to $L-1 \leq J \leq L+1$ due to the Clebsch-Gordan coefficient $C(L\ 1\ J; \nu\ q\ M)$.

2.2.1 Magnetic transitions

First, we consider the case of nuclear transition with magnetic multipolarity. Inserting the magnetic part of Eq. (2.8) into Eq. (2.2) leads to

$$H_{\mathrm{I}} = -\frac{E_k}{\omega_k} \mathrm{e}^{-\mathrm{i}\omega_k t} \sqrt{2\pi} \sum_{LM} (-\mathrm{i})^L \sqrt{2L+1} \mathcal{D}^L_{M\,-\sigma}(\hat{k}) \int \mathrm{d}^3 r\, j_L(kr) \boldsymbol{j}_{\mathrm{n}}(\boldsymbol{r}) \cdot \boldsymbol{Y}^M_{LL}(\theta,\varphi) \ . \tag{2.12}$$

In the following, the photons are assumed to move along the z-axis which reduces the Wigner rotation matrix to $\mathcal{D}^L_{M\,-\sigma}(\hat{k}) = \delta_{M,-\sigma}$. The Kronecker delta $\delta_{M,-\sigma}$ is 1 for $M = -\sigma$ and 0 otherwise.

In nuclear physics, it is usually the case that the wavelength of the radiation is much longer than the nuclear dimension, $kR_0 \ll 1$ such that the long-wavelength approximation is applicable. In this case the spherical Bessel function $j_L(kr)$ can be expanded in terms of the small parameter kr. Following the procedure presented in Appendix B of Ref. [171] it is possible to connect the interaction Hamiltonian with the magnetic multipole moments $\mathcal{M}_{LM}$ by expanding up to first order,

$$H_{\mathrm{I}} = E_k \mathrm{e}^{-\mathrm{i}\omega_k t}\sqrt{2\pi}\sum_L (-\mathrm{i})^{L+1}\sqrt{\frac{(2L+1)(L+1)}{L}}\frac{k^{L-1}}{(2L+1)!!}\mathcal{M}_{L\,-\sigma}\ . \tag{2.13}$$

Here, !! stands for the double factorial giving $n!! = n(n-2)(n-4)\cdots\kappa_n$ with $\kappa_n = 1$ for odd n and $\kappa_n = 2$ for even n. The magnetic multipole moment is defined by [171]

$$\mathcal{M}_{LM} = -\frac{\mathrm{i}}{c}\sqrt{\frac{L}{L+1}}\int \mathrm{d}^3r\, r^L \mathbf{Y}^M_{LL}(\theta,\varphi)\cdot \boldsymbol{j}_{\mathrm{n}}(\boldsymbol{r})\ . \tag{2.14}$$

According to Eq. (2.13), the calculation of the magnetic interaction matrix elements reduces to the evaluation of $\langle I_{\mathrm{e}}M_{\mathrm{e}}|\mathcal{M}_{LM}|I_{\mathrm{g}}M_{\mathrm{g}}\rangle$. Since $\mathcal{M}_{LM}$ is a spherical tensor it is possible to apply the Wigner-Eckart theorem [170] which isolates the dependence on the projection quantum numbers from the dynamics of the system,

$$\langle I_{\mathrm{e}}M_{\mathrm{e}}|\mathcal{M}_{LM}|I_{\mathrm{g}}M_{\mathrm{g}}\rangle = \frac{(-1)^{I_{\mathrm{g}}-M_{\mathrm{g}}}}{\sqrt{2L+1}}C(I_{\mathrm{e}}\ I_{\mathrm{g}}\ L; M_{\mathrm{e}}\ -M_{\mathrm{g}}\ M)\langle I_{\mathrm{e}}\|\mathcal{M}_L\|I_{\mathrm{g}}\rangle\ . \tag{2.15}$$

After utilizing the Wigner-Eckart theorem the angular dependence of the matrix element is now only included in the factor containing the Clebsch-Gordan coefficient $C(I_{\mathrm{e}}\ I_{\mathrm{g}}\ L; M_{\mathrm{e}}\ -M_{\mathrm{g}}\ M)$. The radial dependence has been separated into the reduced matrix element $\langle I_{\mathrm{e}}\|\mathcal{M}_L\|I_{\mathrm{g}}\rangle$ which is independent of any projection quantum numbers. The latter can be related to the so-called reduced transition probability $\mathcal{B}$ [171],

$$\mathcal{B}(\mathcal{M}L, I_{\mathrm{g}}\to I_{\mathrm{e}}) = \frac{1}{2I_{\mathrm{g}}+1}\left|\langle I_{\mathrm{e}}\|\mathcal{M}_L\|I_{\mathrm{g}}\rangle\right|^2\ . \tag{2.16}$$

Inserting this definition into Eq. (2.15) leads to

$$\langle I_{\mathrm{e}}M_{\mathrm{e}}|\mathcal{M}_{LM}|I_{\mathrm{g}}M_{\mathrm{g}}\rangle = (-1)^{I_{\mathrm{g}}-M_{\mathrm{g}}}\sqrt{\frac{2I_{\mathrm{g}}+1}{2L+1}}C(I_{\mathrm{e}}\ I_{\mathrm{g}}\ L; M_{\mathrm{e}}\ -M_{\mathrm{g}}\ M)\sqrt{\mathcal{B}(\mathcal{M}L, I_{\mathrm{g}}\to I_{\mathrm{e}})}\ . \tag{2.17}$$

Instead of constructing nuclear wave functions which are typically strongly model dependent, measured data of the reduced transition probabilities is used for the evaluation of the nuclear transition amplitudes. For a specific multipolarity L we obtain the following interaction matrix element

$$\begin{aligned}\langle I_{\mathrm{e}}M_{\mathrm{e}}|H_{\mathrm{I}}|I_{\mathrm{g}}M_{\mathrm{g}}\rangle &\propto E_k\mathrm{e}^{-\mathrm{i}\omega_k t}C(I_{\mathrm{e}}\ I_{\mathrm{g}}\ L; M_{\mathrm{e}}\ -M_{\mathrm{g}}\ -\sigma)\\ &\times\sqrt{2\pi}\sqrt{\frac{L+1}{L}}\frac{k^{L-1}}{(2L+1)!!}\sqrt{2I_{\mathrm{g}}+1}\sqrt{\mathcal{B}(\mathcal{M}L, I_{\mathrm{g}}\to I_{\mathrm{e}})}\ .\end{aligned} \tag{2.18}$$

2.2.2 Electric transitions

In the same manner as for magnetic transitions, the interaction Hamiltonian for electric transitions can be expressed in terms of the electric multipole moments $\mathbb{Q}_{LM}$ as follows

$$H_{\mathrm{I}} = E_k \mathrm{e}^{-\mathrm{i}\omega_k t}\sqrt{2\pi}\sum_L (-\mathrm{i})^L \sqrt{\frac{(2L+1)(L+1)}{L}}\frac{\sigma k^{L-1}}{(2L+1)!!}\mathbb{Q}_{L\,-\sigma} \; . \tag{2.19}$$

The multipole moment $\mathbb{Q}_{LM}$ is defined by [171]

$$\mathbb{Q}_{LM} = \int \mathrm{d}^3 r\, r^L Y_{LM}(\theta,\varphi)\rho_{\mathrm{n}}(\boldsymbol{r}) \; , \tag{2.20}$$

where ρ_{n} represents the nuclear charge density. The current density $\boldsymbol{j}_{\mathrm{n}}$ and charge density ρ_{n} are connected via the standard continuity equation [172].

In order to express the matrix element $\langle I_{\mathrm{e}} M_{\mathrm{e}}|\mathbb{Q}_{LM}|I_{\mathrm{g}} M_{\mathrm{g}}\rangle$ in terms of the reduced transition probabilities, the Wigner-Eckart theorem is again utilized resulting in

$$\langle I_{\mathrm{e}} M_{\mathrm{e}}|\mathbb{Q}_{LM}|I_{\mathrm{g}} M_{\mathrm{g}}\rangle = (-1)^{I_{\mathrm{g}}-M_{\mathrm{g}}}\sqrt{\frac{2I_{\mathrm{g}}+1}{2L+1}}C\big(I_{\mathrm{e}}\ I_{\mathrm{g}}\ L; M_{\mathrm{e}}\ -M_{\mathrm{g}}\ M\big)\sqrt{\mathcal{B}(\mathcal{E}L, I_{\mathrm{g}}\to I_{\mathrm{e}})} \tag{2.21}$$

with

$$\mathcal{B}(\mathcal{E}L, I_{\mathrm{g}}\to I_{\mathrm{e}}) = \frac{1}{2I_{\mathrm{g}}+1}\left|\langle I_{\mathrm{e}}\|\mathbb{Q}_L\|I_{\mathrm{g}}\rangle\right|^2 \; . \tag{2.22}$$

Using Eq. (2.21) we obtain the following expression for the interaction matrix elements of electric multipolarity L

$$\begin{aligned}\langle I_{\mathrm{e}} M_{\mathrm{e}}|H_{\mathrm{I}}|I_{\mathrm{g}} M_{\mathrm{g}}\rangle &\propto E_k \mathrm{e}^{-\mathrm{i}\omega_k t} C\big(I_{\mathrm{e}}\ I_{\mathrm{g}}\ L; M_{\mathrm{e}}\ -M_{\mathrm{g}}\ -\sigma\big)\\ &\times \sqrt{2\pi}\sqrt{\frac{L+1}{L}}\frac{k^{L-1}}{(2L+1)!!}\sqrt{2I_{\mathrm{g}}+1}\sqrt{\mathcal{B}(\mathcal{E}L, I_{\mathrm{g}}\to I_{\mathrm{e}})} \; .\end{aligned} \tag{2.23}$$

2.3 The collective nuclear decay rate

The nuclear transition width Γ_0 introduced in Eq. (2.5) is usually composed of two parts: (i) the radiative decay A_{r} where the nuclear excitation energy is released in form of a photon, and (ii) internal conversion (IC) which accelerates a bound electron into the continuum due to the nuclear de-excitation. The radiative decay rate A_{r} can be again expressed in terms of the reduced transition probabilities analogously to the previous Section. For a given multipolarity L, A_{r} is determined by [171]

$$A_{\mathrm{r}}^{E\to G} = \frac{8\pi(L+1)}{L[(2L+1)!!]^2}\left(\frac{E_{\mathrm{n}}}{c}\right)^{2L+1}\mathcal{B}(\lambda L, I_{\mathrm{e}}\to I_{\mathrm{g}}) \; , \tag{2.24}$$

where the parameter λ determines whether the transition type is electric ($\lambda = \mathcal{E}$) or magnetic ($\lambda = \mathcal{M}$) and $E_{\mathrm{n}} = \omega_0$ represents the nuclear transition energy. Moreover, using the principle of detailed balance the transition probabilities corresponding to either down or up conversion can be related via [156]

$$\mathcal{B}(\lambda L, I_\mathrm{e} \to I_\mathrm{g}) = \frac{2I_\mathrm{g}+1}{2I_\mathrm{e}+1}\mathcal{B}(\lambda L, I_\mathrm{g} \to I_\mathrm{e}) \; . \tag{2.25}$$

Typically, Γ_0 is in the range of 10^{-5} to 10^{-10} eV in the case of nuclear transitions. The large discrepancy between the nuclear width Γ_0 and the XFEL bandwidths currently in the order of several eV is one of the main limiting factors for the direct laser-nucleus interaction. However, if solid-state targets are considered there can be a third decay channel, the collective or coherent decay, strongly enhancing the nuclear transition width and hence the laser-induced nuclear excitation. This collective decay relies on the fact that in solid-state targets with Mössbauer nuclei photons can be absorbed and re-emitted recoillessly. The photon momentum is then rather transferred to the whole crystal lattice than to a single nucleus. The probability of recoilless scattering is described by the Lamb-Mössbauer factor f_LM which in the Debye-model is given by [173]

$$f_\mathrm{LM} = \exp\left[-\frac{2E_\mathrm{R}}{k_\mathrm{B}\theta_\mathrm{D}}\left(1+4\frac{T^2}{\theta_\mathrm{D}^2}\int_0^{\theta_\mathrm{D}/T}\frac{x\,\mathrm{d}x}{\mathrm{e}^x-1}\right)\right] \; . \tag{2.26}$$

In this expression k_B stands for the Boltzmann constant, θ_D is the material-specific Debye temperature and E_R denotes the recoil energy depending on E_n. We will always assume the sample to be at room temperature $T = 300$ K.

Due to the recoilless scattering it is impossible to distinguish which nucleus has been excited such that a collective excitation also known as nuclear exciton is created [103]. Any process like IC, nuclear recoil or spin-flip leaving a trace of nuclear excitation immediately destroys the collective nature at the nucleus where it took place. The origin of the excitonic state is explained in much more detail in Chap. 5. Here, it is at first only important to know that the collective excitation predominantly decays by emitting a photon into the forward direction with an enhanced decay rate Γ [103]. For instance, by considering a laser pulse δ-like in time and $\Gamma^E_\mathrm{loss} = 0$, the time dependence of the scattered intensity immediately after the interaction with the laser pulse can be approximated by [103, 174]

$$I(t) \propto \mathrm{e}^{-(\xi+1)\Gamma_0 t} \; , \tag{2.27}$$

where $\xi = \frac{1}{4}\sigma_\mathrm{R} n_0 L$ stands for the dimensionless thickness parameter with n_0 denoting the number density of nuclei in a sample of length L. The radiative nuclear resonance cross section σ_R is given by

$$\sigma_\mathrm{R} = 2\pi\frac{2I_\mathrm{e}+1}{2I_\mathrm{g}+1}\left(\frac{c}{E_\mathrm{n}}\right)^2\frac{1}{1+\alpha_\mathrm{ic}}f_\mathrm{LM} \; . \tag{2.28}$$

Here, α_ic represents the so-called IC coefficient which gives the ratio of the internal conversion and radiative decay rate. Including the collective decay channel the following formula for the total transition width is obtained

$$\Gamma \simeq (\xi+1)\Gamma_0 \; . \tag{2.29}$$

This enhancement is of course only valid as long as it is possible to build up the excitonic state. According to Ref. [161], there are two length scales limiting the extension of the collective excitation: (i) the photoabsorption length $1/\mu$ describing incoherent scattering and absorption from electrons, and (ii) the focal length of the laser L_{foc} over which a resonant photon can be shared by the nuclear sample. The smaller one of these two always dictates the upper limit of ξ. In the case of ^{57}Fe, for instance, the photoabsorption length lies around 22 μm for photons resonant to the nuclear transition from the ground to the first excited state ($\sim$ 14.4 keV) [161]. The focal length L_{foc} is determined by the focal diameter d_{foc} and the laser wavelength λ via $L_{\mathrm{foc}} = \frac{2\pi}{\lambda}(d_{\mathrm{foc}}/2)^2$ which gives twice the Rayleigh length. For a photon energy of 14.4 keV and moderate laser focusing of $d_{\mathrm{foc}} \approx 100$ nm, L_{foc} is always larger than $1/\mu$ leading to a total transition width for the first excited state maximally enhanced by a factor of up to $\xi \approx 87$ [161].

Chapter 3

Nuclear excitation by electron capture

Over the last decades the process of electron-ion recombination has been studied extensively in theory as well as in experiments. It is one of the fundamental atomic processes which plays an important role in many branches of physics. For instance, in semiconductor physics the carrier-hole recombination builds the basis for many semiconductor electronic devices like photodiodes, LEDs, transistors, solar cells to name a few. Or, in non-equilibrium plasmas the recombination is the main counterpart to ionization and excitation processes whose interplay determines the ionization balance and the atomic state populations. Moreover, electron-ion recombination followed by the emission of a photon gives one of the major contributions to the radiation field emitted by plasmas. In particular in plasmas that are not accessible by direct probes, the detection of the emitted light is the principal way to analyze the prevailing plasma conditions which again requires a good understanding of the recombination processes.

The case when the capture of the initially free electron into a bound state of the ion is followed by the emission of a photon is the so-called photo recombination (PR). The direct, non-resonant channel of PR is called radiative recombination (RR). In this process the electron recombination involves the emission of a photon ensuring energy and momentum conservation. The process of RR not only plays an important role in plasma physics as already pointed out above, but also takes the responsibility for the main background in ion trap or electron-ion collision experiments. RR has been the subject of many theoretical and experimental studies in a broad spectrum of fields of physics.

Instead of emitting a photon, the capture energy (the energy difference between the free electron and the bound state) can also be transferred to an initially bound electron by stimulating a bound-bound transition. This process is referred to as dielectronic recombination (DR) and when followed by radiative decay of the excited electronic state in a second step, provides an indirect, resonant contribution to PR. The interference between the RR and the DR channel has already been under investigation in Refs. [175, 176]. Moreover, DR is expected to give the dominant contribution to PR especially in hot astrophysical plasmas. Note that DR is a resonant process because the capture energy and the electronic transition energy need to match in order for the recombination to take place.

The nuclear analog to DR is nuclear excitation by electron capture, short NEEC. In the process of NEEC the initially free electron is captured into a bound state and simultaneously transfers its capture energy to the nucleus. In Fig. 3.1, NEEC is illustrated for the example of an *L*-shell capture with a fully occupied *K* shell ($1s^2$) followed by the

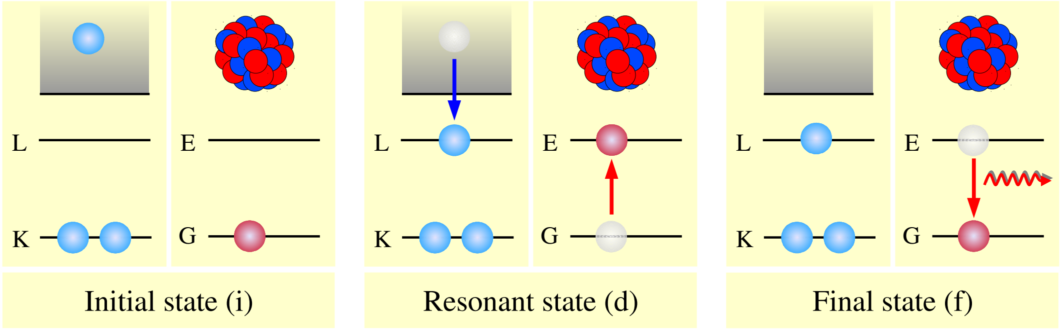

Figure 3.1: NEEC followed by radiative decay. An initially free electron is captured by a He-like ion into the L shell. This capture energy is simultaneously transfered to the nucleus which is driven into an excited state. The created resonant state subsequently decays back to the nuclear ground state by emitting a photon.

radiative decay of the nuclear excited level. It is again important to note that the energy difference between the free and the bound electronic state needs to coincide with the nuclear transition energy in order for NEEC to take place (see middle part of Fig. 3.1). Analogously to DR, the process of NEEC followed by radiative decay of the nucleus gives an additional channel to PR. The interference between NEEC followed by the emission of a photon and RR has been studied theoretically in Ref. [177].

The process of NEEC has been first proposed theoretically by Goldanskii and Namiot in 1976 [178]. Since then NEEC has been subject to a number of theoretical studies in plasma environments [82, 84, 85, 87, 179] as well as in solid targets [180–183]. Although there have been efforts to verify the existence of NEEC experimentally, no NEEC signal has been measured yet. The main obstacle seems to be the large background created by RR [184, 185]. In contrast, the time reversed process of NEEC called internal conversion (IC) where the nuclear de-excitation kicks out a bound electron, is a well established nuclear decay mechanism. Moreover, related processes like nuclear excitation by electron transition (NEET) [186] and its time reversal, bound internal conversion (BIC) [187], have already been demonstrated in experiments. In the process of NEET the nuclear excitation is driven by a bound-bound electronic transition instead of free-bound like in the case of NEEC. Based on these achievements, there is no disbelief that the process of NEEC exists and it may be only a question of overcoming the large RR background until the first NEEC signal is detected.

This Chapter is devoted to the theoretical treatment of NEEC which follows the approach developed by Pálffy [81, 188]. In order to derive the cross section for NEEC followed by radiative decay of the nucleus, Pálffy uses a perturbation expansion of the transition operator analogously as it has been done for RR and DR [189, 190]. Moreover, a Feshbach projection operator method is applied [176, 191] which allows to separate the subspaces of initial, intermediate and final states. In Ref. [81], the capture into bare nuclei or He-like ions has been considered which makes it possible to reduce the electronic part into a one-electron problem. Here, we extend the formalism to many electron wave functions analogously to how it has been performed for NEET in Ref. [192]. However, we do not go into the details of the perturbation expansion or of the projection method which have been given elsewhere [81, 188].

In Sec. 3.1, we first discuss the decomposition of the Fock space into initial, intermediate and final states as illustrated in Fig. 3.1. In Sec. 3.2 the Hamilton operator of the system is introduced. Moreover, we sketch the nuclear model used for describing the nuclear degrees of freedom. Sec. 3.3 is solely devoted to the derivation of the total NEEC cross section. Explicit formulas for the electric and magnetic NEEC rates in terms of reduced transition probabilities and electronic wave functions are derived in Sec. 3.4. Atomic units $\hbar = m_\mathrm{e} = e = 4\pi\varepsilon_0 = 1$ are employed throughout this Chapter.

3.1 Decomposition of Fock space

The initial state of the system consists of the nucleus in its ground state, an electronic configuration with a free electron and the radiation field in the vacuum state. The composed state vector can be written as a direct product of nuclear, electronic and photonic degrees of freedom,

$$|\Psi_\mathrm{i}\rangle = |I_\mathrm{i}M_\mathrm{i}, \Psi_\mathrm{i}^\mathrm{el}, 0\rangle \equiv |I_\mathrm{i}M_\mathrm{i}\rangle \otimes |\Psi_\mathrm{i}^\mathrm{el}\rangle \otimes |0\rangle \ . \tag{3.1}$$

Thereby, the initial electronic wave function is given by

$$|\Psi_\mathrm{i}^\mathrm{el}\rangle = |\alpha_\mathrm{i} J_\mathrm{i} \mu_\mathrm{i}, \boldsymbol{p} m_\mathrm{s}\rangle \ , \tag{3.2}$$

where the electronic configuration α_i and the total angular momentum J_i with projection μ_i represent the initial state of the bound electrons. The free electron is characterized by its momentum $\boldsymbol{p}$ and spin projection quantum number m_s. The nuclear ground state is determined by the total angular momentum I_i and its projection M_i.

The resonant or intermediate state produced via NEEC is composed of the excited nucleus, the electronic capture state and the radiation field still in vacuum as illustrated in Fig. 3.1. The direct product is given by

$$|\Psi_\mathrm{d}\rangle = |I_\mathrm{d}M_\mathrm{d}, \Psi_\mathrm{d}^\mathrm{el}, 0\rangle \equiv |I_\mathrm{d}M_\mathrm{d}\rangle \otimes |\Psi_\mathrm{d}^\mathrm{el}\rangle \otimes |0\rangle \ , \tag{3.3}$$

where the quantum numbers I_d and M_d determine the nuclear excited state. Since the free electron is captured into a bound level during the process of NEEC, the electronic state can be written as

$$|\Psi_\mathrm{d}^\mathrm{el}\rangle = |\alpha_\mathrm{d} J_\mathrm{d} \mu_\mathrm{d}\rangle \tag{3.4}$$

with α_d representing the electronic configuration, J_d the total angular momentum and μ_d the projection quantum number of the NEEC capture level.

In the second step shown in Fig. 3.1, the nuclear excited state decays back to the ground state by emitting a photon. The electronic state remains unchanged. Therefore, the final state is given by

$$|\Psi_\mathrm{f}\rangle = |I_\mathrm{f}M_\mathrm{f}, \Psi_\mathrm{d}^\mathrm{el}, \lambda k L M\rangle \equiv |I_\mathrm{f}M_\mathrm{f}\rangle \otimes |\Psi_\mathrm{d}^\mathrm{el}\rangle \otimes |\lambda k L M\rangle \ . \tag{3.5}$$

Again, the quantum numbers I_f and M_f describe the nucleus in the final state. Moreover, the nuclear radiative decay creates a photon with wave number k, total angular momentum L and projection M. The parameter λ determines whether an electric ($\lambda = \mathcal{E}$) or magnetic ($\lambda = \mathcal{M}$) wave is produced. This production process can be expressed in terms of the photon creation operator applied to the vacuum state,

$$|\lambda kLM\rangle = a^\dagger_{\lambda kLM}|0\rangle \ . \tag{3.6}$$

The corresponding annihilation operator is denoted by $a_{\lambda kLM}$.

3.2 The system's Hamiltonian

The total Hamilton operator of the considered system is composed of nuclear, electronic and photonic degrees of freedom,

$$H = H_\mathrm{n} + H_\mathrm{e} + H_\mathrm{r} + H_\mathrm{en} + H_\mathrm{er} + H_\mathrm{nr} \ . \tag{3.7}$$

Within our framework, the nucleus is described by a collective model. The main purpose of using this kind of model is to relate the nuclear matrix elements with available experimental data in order to stay independent of any nuclear wave function constructions (see Sec. 3.2.2). For the case of an even-even nucleus (even number of protons and even number of neutrons) the free nuclear Hamiltonian can be written as [188]

$$H_\mathrm{n} = \sum_{\ell m} \omega_\ell \left(\beta^\dagger_{\ell m} \beta_{\ell m} + \frac{1}{2} \right) \ , \tag{3.8}$$

where $\beta^\dagger_{\ell m}$ and $\beta_{\ell m}$ are the phonon creation and annihilation operators of the collective modes with frequency ω_ℓ.

The relativistic Dirac Hamiltonian is given by

$$H_\mathrm{e} = \sum_{i=1}^{N} \left[c\boldsymbol{\alpha} \cdot \boldsymbol{p}_i + (\beta - 1)c^2 \right] + \frac{1}{2} \sum_{i \neq j} \frac{1}{|\boldsymbol{r}_i - \boldsymbol{r}_j|} \ . \tag{3.9}$$

Here, N is the number of electrons, $\boldsymbol{p}_i$ stands for the momentum of the i^th electron, $\boldsymbol{\alpha}$ denotes the vector composed of the Dirac matrices $(\alpha_x, \alpha_y, \alpha_z)$ and β represents the fourth Dirac matrix. Furthermore, the rest mass energy c^2 has been subtracted. Note that H_e also contains the electron-electron interactions which are given by the second summation in Eq. (3.9). Here, the Breit interaction is not taken into account.

The Hamiltonian of the quantized radiation field is expressed in terms of the photon creation and annihilation operators with frequency ω_k, namely

$$H_\mathrm{r} = \sum_{\lambda kLM} \omega_k a^\dagger_{\lambda kLM} a_{\lambda kLM} \ . \tag{3.10}$$

The remaining Hamiltonians describe the interactions between the subspaces: H_en – electron-nucleus interaction, H_er – electron-radiation interaction and H_nr – nucleus-radiation interaction. For the electron-nucleus interaction we apply the Coulomb gauge which renders it possible to split up the dominant Coulomb interaction,

$$H_{\mathrm{en}} = \sum_{i=1}^{N} h_{\mathrm{en}}(i) = \sum_{i=1}^{N} \int \mathrm{d}^3 r_{\mathrm{n}} \, \frac{\rho_{\mathrm{n}}(\boldsymbol{r}_{\mathrm{n}})}{|\boldsymbol{r}_i - \boldsymbol{r}_{\mathrm{n}}|} \ . \tag{3.11}$$

Thereby, $\boldsymbol{r}_{\mathrm{n}}$ and $\boldsymbol{r}_i$ stand for the spatial coordinates of the nucleus and the i^{th} electron, respectively. The nuclear charge density is represented by ρ_{n}. The Coulomb-type Hamiltonian H_{en} describes the electric interaction between the electron and the nucleus and will be responsible for electric NEEC transitions.

By using the multipole expansion of the electromagnetic vector potential the interaction between the electron and the quantized radiation field can be written as

$$H_{\mathrm{er}} = -\sum_{i=1}^{N} \boldsymbol{\alpha} \cdot \boldsymbol{A}(\boldsymbol{r}_i) = \sum_{i=1}^{N} \sum_{\lambda k L M} \left(a^{\dagger}_{\lambda k L M} \boldsymbol{\alpha} \cdot \boldsymbol{A}_{\lambda k L M}(\boldsymbol{r}_i) + \mathrm{H.c.} \right) \ , \tag{3.12}$$

where $\boldsymbol{A}_{\lambda k L M}$ with $\lambda = \mathcal{E}$ and $\lambda = \mathcal{M}$ represent the electric and magnetic multipole fields, respectively. Both are eigenfunctions of $\boldsymbol{L}^2$ and L_z and fulfill the field-free Maxwell equations. Taking a spherical quantization volume of radius R they are given by [171]

$$\begin{aligned} \boldsymbol{A}_{(\mathcal{M})kLM}(\boldsymbol{r}) &= \sqrt{\frac{4\pi c k}{R}} j_L(kr) \boldsymbol{Y}_{LL}^{M}(\theta, \varphi) \ , \\ \boldsymbol{A}_{(\mathcal{E})kLM}(\boldsymbol{r}) &= \frac{\mathrm{i}}{k} \sqrt{\frac{4\pi c k}{R}} \nabla \times \left(j_L(kr) \boldsymbol{Y}_{LL}^{M}(\theta, \varphi) \right) \ , \end{aligned} \tag{3.13}$$

closely related to the semiclassical case [see Eq. (2.9)] where the normalization due to a finite quantization volume was not required. The term j_L represents the spherical Bessel function and $\boldsymbol{Y}_{JL}^{M}$ stands for the vector spherical harmonics defined in Eq. (2.10).

By making use of the multipole expansion of the electromagnetic field, H_{nr} can be analogously expressed in terms of the electric and magnetic multipole fields,

$$H_{\mathrm{nr}} = -\frac{1}{c} \sum_{\lambda k L M} \left(a^{\dagger}_{\lambda k L M} \int \mathrm{d}^3 r_{\mathrm{n}} \, \boldsymbol{j}_{\mathrm{n}}(\boldsymbol{r}_{\mathrm{n}}) \cdot \boldsymbol{A}_{\lambda k L M}(\boldsymbol{r}_{\mathrm{n}}) + \mathrm{H.c.} \right) \ , \tag{3.14}$$

where $\boldsymbol{j}_{\mathrm{n}}$ is the nuclear current density. Likewise in Eq. (3.11), the integration is performed over the complete nuclear volume. Note that according to the chosen normalization in Eq. (3.13) we obtain the following commutation relations for the photon creation and annihilation operators [171]

$$\begin{aligned} [a_{\lambda k L M}, a_{\lambda' k' L' M'}] &= 0, \\ [a_{\lambda k L M}, a^{\dagger}_{\lambda' k' L' M'}] &= \delta_{\lambda\lambda'} \delta_{kk'} \delta_{LL'} \delta_{MM'} \ . \end{aligned} \tag{3.15}$$

3.2.1 Magnetic interaction

The total Hamiltonian presented in Eq. (3.7) can be split into an unperturbed part H_0 and an interaction part V by making use of the Feshbach projection operator method.

For instance, the interaction part V can be written as a sum whose terms exactly describe transitions between the subspaces defined in Sec. 3.1. Applying further an infinite perturbation expansion to the transition operator T known from scattering theory, it is possible to include energy corrections due to Coulomb nuclear polarization, nuclear self-energy and electronic one-loop self energy [188]. Moreover, transition widths caused by radiative decay or internal conversion are introduced. In many electron systems it is also possible to account for Breit interactions between the electronic currents in this way [188].

Apart of these energy corrections, in the second-order term one can identify the Hamiltonian responsible for the magnetic interaction between the electronic and nuclear currents. According to Ref. [188], the magnetic Hamiltonian reads

$$H_{\text{magn}} = \sum_{i=1}^{N} \hbar_{\text{magn}}(i) = -\sum_{i=1}^{N} \frac{1}{c}\boldsymbol{\alpha} \cdot \int \mathrm{d}^3 r_{\text{n}} \, \frac{\boldsymbol{j}_{\text{n}}(\boldsymbol{r}_{\text{n}})}{|\boldsymbol{r}_i - \boldsymbol{r}_{\text{n}}|} \ . \tag{3.16}$$

This term describes the magnetic interaction between the electron and the nucleus by the exchange of a transverse photon. In other words, electrons interact with the vector potential produced by the nuclear current. For us, H_{magn} is specifically important for the magnetic NEEC transitions discussed in Sec. 3.4.

3.2.2 Nuclear model

We describe the nucleus by using a collective model whose underlying physical picture is that of a classical charged liquid drop [171,172]. In this model the interior structure, i.e., the composition of the nucleus by individual nucleons is totally neglected. The nucleus is considered as a liquid drop with a sharp surface which is filled with homogeneous nuclear matter with constant density. This kind of description is only applicable if the size of the individual nucleons is much smaller than the total size of the nucleus. Hence, the validity of the collective model increases with the weight of considered nuclei. Excitations of the nucleus can be described in this framework as vibrations and rotations of the nuclear surface.

Using the collective model it can be shown that the nuclear charge density ρ_{n} can be split up into two terms, a static one which describes the nuclear ground state and a term responsible for nuclear excitations. Following Ref. [188], these are given by

$$\begin{aligned} \rho_{\text{n}}^{\text{st}}(\boldsymbol{r}) &= \rho_0 \Theta(R_0 - r) \ , \\ \rho_{\text{n}}^{\text{exc}}(\boldsymbol{r}) &= \rho_0 \delta(R_0 - r) R_0 \sum_{\ell m} \alpha_{\ell m}^{*} Y_{\ell m}(\theta, \varphi) \ , \end{aligned} \tag{3.17}$$

where R_0 represents the radius of the liquid drop and the time-dependent amplitudes $\alpha_{\ell m}^{*}$ describe fluctuations of the nuclear surface. The parameter ρ_0 is given by $\frac{3Z}{4\pi R_0^3}$. Inserting the explicit form of ρ_{n} into Eq. (3.11), the interaction Hamiltonian h_{en} splits up in the same manner into a static part $\hbar_{\text{en}}^{\text{st}}$ and a dynamical part $\hbar_{\text{en}}$ which is responsible for the electron-nucleus interaction describing excitations of electric type. For $r_{\text{e}} > r_{\text{n}}$ the static part evaluates to the well-known spherical Coulomb potential $V_C = -\frac{Z}{|\boldsymbol{r}_{\text{e}} - \boldsymbol{r}_{\text{n}}|}$. Since we are dealing with single-particle Hamiltonians we drop the particle index i and replace

$\boldsymbol{r}_i$ by $\boldsymbol{r}_\mathrm{e}$ in order to clearly differentiate between nuclear and electronic coordinates. Whenever using the single-particle Hamiltonians $\mathscr{h}_\mathrm{en}$ or $\mathscr{h}_\mathrm{magn}$ in the following these replacement rules apply.

The collective model is specifically important for our theoretical treatment of NEEC because it allows to relate the electric and magnetic interaction Hamiltonians with the nuclear multipole moments. Following the procedure presented Chap. 2 of Ref. [188], the following expressions can be obtained for $\mathscr{h}_\mathrm{en}$ and $\mathscr{h}_\mathrm{magn}$,

$$\begin{aligned}\mathscr{h}_\mathrm{en} &= \sum_{LM} \frac{\mathbb{Q}_{LM}}{R_0^L} \int d^3 r_\mathrm{n} \, \frac{\delta(R_0 - r_\mathrm{n}) Y^*_{LM}(\theta_\mathrm{n}, \varphi_\mathrm{n})}{|\boldsymbol{r}_\mathrm{e} - \boldsymbol{r}_\mathrm{n}|} \ , \\ \mathscr{h}_\mathrm{magn} &= -\mathrm{i} \sum_{LM} \frac{4\pi}{2L+1} \sqrt{\frac{L+1}{L}} r_\mathrm{e}^{-(L+1)} \mathscr{M}_{LM} \boldsymbol{\alpha} \cdot \boldsymbol{Y}^{M*}_{LL}(\theta_\mathrm{e}, \varphi_\mathrm{e}) \ , \end{aligned} \tag{3.18}$$

where the electric and magnetic multipole moments $\mathbb{Q}_{LM}$ and $\mathscr{M}_{LM}$ are the ones defined in Eqs. (2.20) and (2.14). Analogously to the previous Chapter, the matrix elements between the nuclear multipole moments can be expressed in terms of the reduced transition probabilities $\mathcal{B}(\mathcal{E}(\mathcal{M})L, I_\mathrm{i} \to I_\mathrm{d})$ whose definitions can be found in Eqs. (2.22) and (2.16). This means ultimately that the nuclear part of the NEEC transition amplitudes can be related to $\mathcal{B}$ values for which experimental data is available. We use experimental values for the reduced transition probabilities in order to evaluate the nuclear matrix elements as it was shown in the previous Chapter.

3.3 Total NEEC cross section

For the calculation of the NEEC cross section we assume that the projection quantum numbers of $|\Psi_\mathrm{i}\rangle$ and $|\Psi_\mathrm{d}\rangle$ are not resolved in the experiment. This is done by averaging over M_i, μ_i and m_s and summing over M_d and μ_d. Furthermore, we integrate over the solid angle $\Omega_{\boldsymbol{p}}$ of the incoming electrons. For the general case of both electric and/or magnetic transitions, the NEEC cross section reads [81,188]

$$\sigma^{\mathrm{i}\to\mathrm{d}}_\mathrm{neec}(E) = \frac{2\pi}{F_\mathrm{i}} \frac{1}{2(2I_\mathrm{i}+1)(2J_\mathrm{i}+1)} \sum_{M_\mathrm{i}\mu_\mathrm{i}m_\mathrm{s}} \sum_{M_\mathrm{d}\mu_\mathrm{d}} \frac{1}{4\pi} \int d\Omega_{\boldsymbol{p}} \, \frac{\left|\langle\Psi_\mathrm{d}|H_\mathrm{N}|\Psi_\mathrm{i}\rangle\right|^2 \Gamma_\mathrm{d}/2\pi}{(E-E_\mathrm{d})^2 + \Gamma_\mathrm{d}^2/4} \ , \tag{3.19}$$

where F_i stands for the incoming electron flux. Here, the isolated resonance approximation has been applied where only a single resonant state $|\Psi_\mathrm{d}\rangle$ with resonance energy E_d and natural width Γ_d is taken into account. The interaction Hamiltonian H_N describes transitions of both electric and magnetic multipolarity induced by the electron-nucleus interaction and is defined by

$$H_\mathrm{N} = \sum_{i=1}^{N} \left[\mathscr{h}_\mathrm{en}(i) + \mathscr{h}_\mathrm{magn}(i)\right] \ . \tag{3.20}$$

In order to write $\sigma^{\mathrm{i}\to\mathrm{d}}_\mathrm{neec}$ in a more compact form the NEEC rate $Y^{\mathrm{i}\to\mathrm{d}}_\mathrm{neec}$ is introduced,

$$Y^{\mathrm{i}\to\mathrm{d}}_\mathrm{neec} = \frac{2\pi}{2(2I_\mathrm{i}+1)(2J_\mathrm{i}+1)} \sum_{M_\mathrm{i}\mu_\mathrm{i}m_\mathrm{s}} \sum_{M_\mathrm{d}\mu_\mathrm{d}} \int d\Omega_{\boldsymbol{p}} \left|\langle\Psi_\mathrm{d}|H_\mathrm{N}|\Psi_\mathrm{i}\rangle\right|^2 \rho_\mathrm{i} \ . \tag{3.21}$$

Using that the incoming electron flux F_i and the initial density of continuum electron states ρ_i are related by $F_\mathrm{i}\rho_\mathrm{i} = \frac{p^2}{(2\pi)^3}$, the NEEC cross section can be written in terms of $Y^{\mathrm{i}\to\mathrm{d}}_{\mathrm{neec}}$ as

$$\sigma^{\mathrm{i}\to\mathrm{d}}_{\mathrm{neec}} = \frac{2\pi^2}{p^2} Y^{\mathrm{i}\to\mathrm{d}}_{\mathrm{neec}} L_\mathrm{d}(E - E_\mathrm{d}) \ , \tag{3.22}$$

where p is the absolute value of the free electron momentum $\boldsymbol{p}$. The function L_d represents the well-known normalized Lorentz profile occurring in resonant systems,

$$L_\mathrm{d}(E - E_\mathrm{d}) = \frac{\Gamma_\mathrm{d}/2\pi}{(E - E_\mathrm{d})^2 + \Gamma_\mathrm{d}^2/4} \ . \tag{3.23}$$

For arbitrary capture levels $|\Psi_\mathrm{d}\rangle$ the width Γ_d is composed of an electronic and a nuclear part, $\Gamma_\mathrm{d} = \Gamma^{\mathrm{el}}_\mathrm{d} + \Gamma^{\mathrm{nucl}}_\mathrm{d}$. The nuclear width itself can be split into a radiative term and a contribution via IC,

$$\Gamma^{\mathrm{nucl}}_\mathrm{d} = \sum_{\mathrm{f}'} \left(A^{\mathrm{d}\to\mathrm{f}'}_\mathrm{r} + A^{\mathrm{d}\to\mathrm{f}'}_{\mathrm{ic}}\right) \ , \tag{3.24}$$

where the index f′ stands for an arbitrary final state $|\Psi_{\mathrm{f}'}\rangle$. In the case of IC this state can generally be written as

$$|\Psi_{\mathrm{f}'}\rangle = |I_{\mathrm{f}'} M_{\mathrm{f}'}, (\alpha_{\mathrm{f}'} J_{\mathrm{f}'} \mu_{\mathrm{f}'}, \mathbf{p}' m'_\mathrm{s}), 0\rangle \ , \tag{3.25}$$

where the state notation exactly follows that of Sec. 3.1. The IC transition rate $A^{\mathrm{d}\to\mathrm{f}'}_{\mathrm{ic}}$ can be related to $Y^{\mathrm{f}'\to\mathrm{d}}_{\mathrm{neec}}$ using the principle of detailed balance,

$$A^{\mathrm{d}\to\mathrm{f}'}_{\mathrm{ic}} = \frac{2(2I_{\mathrm{f}'}+1)(2J_{\mathrm{f}'}+1)}{(2I_\mathrm{d}+1)(2J_\mathrm{d}+1)} Y^{\mathrm{f}'\to\mathrm{d}}_{\mathrm{neec}} \ . \tag{3.26}$$

Consequently, IC rates are highly dependent on the electronic structure of the considered atom and can be hence modified by removing or adding electrons from or to the atomic shells. A bare nucleus, for instance, can only decay radiatively. Moreover, it is important to note that IC can only take place if the nuclear excitation energy is above the ionization threshold of the bound electrons present.

In contrast, the radiative decay rate $A^{\mathrm{d}\to\mathrm{f}'}_\mathrm{r}$ is independent of the electronic structure. $A^{\mathrm{d}\to\mathrm{f}'}_\mathrm{r}$ is completely determined by the nuclear matrix elements of H_{nr}. The nuclear radiative decay of $|\Psi_\mathrm{d}\rangle$ leads in general to a final state which has the form of $|\Psi_\mathrm{f}\rangle$ defined in Eq. (3.5). The corresponding decay rate $A^{\mathrm{d}\to\mathrm{f}}_\mathrm{r}$ can be expressed as

$$A^{\mathrm{d}\to\mathrm{f}}_\mathrm{r} = \frac{2\pi}{2I_\mathrm{d}+1} \sum_{M_\mathrm{f} M} \sum_{M_\mathrm{d}} \left|\langle\Psi_\mathrm{f}|H_{\mathrm{nr}}|\Psi_\mathrm{d}\rangle\right|^2 \rho_\mathrm{f} \ . \tag{3.27}$$

Following the procedure in Ref. [171], the matrix elements of H_{nr} can be connected to the reduced transition probabilities $\mathcal{B}$ leading to the expression of A_r already given in Eq. (2.24).

Typically, the nuclear width takes values between 10^{-5} and 10^{-10} eV which makes it often very hard to fulfill the nuclear resonance condition. However, the peak value on resonance $E = E_\mathrm{d}$ can be very large. Therefore, it is often more reasonable to speak about the integrated cross section, the so-called resonance strength. Integrating Eq. (3.22) over the continuum energy E and considering p^2 and $Y_{\mathrm{neec}}^{\mathrm{i}\to\mathrm{d}}$ constant over the region Γ_{d} leads to the following resonance strength expression for NEEC

$$S_{\mathrm{neec}}^{\mathrm{i}\to\mathrm{d}} = \frac{2\pi^2}{p^2} Y_{\mathrm{neec}}^{\mathrm{i}\to\mathrm{d}} \; . \tag{3.28}$$

Here, it was used that the integral of the Lorentz function L_{d} is normalized to unity.

So far we only discussed the population of the nuclear excited state via NEEC. In order to incorporate the second step, the nuclear decay, the so-called branching ratio can be employed [172]. In general, the two-step cross section for NEEC followed by the nuclear decay can be written as

$$\sigma_{\mathrm{neec}}^{\mathrm{i}\to\mathrm{d}\to\mathrm{f}} = \sigma_{\mathrm{neec}}^{\mathrm{i}\to\mathrm{d}} B^{\mathrm{d}\to\mathrm{f}} \; , \tag{3.29}$$

where the branching ratio $B^{\mathrm{d}\to\mathrm{f}}$ describes the probability of the considered decay channel. For instance, in the case of NEEC followed by radiative decay as illustrated in Fig. 3.1, $B^{\mathrm{d}\to\mathrm{f}}$ evaluates to

$$B^{\mathrm{d}\to\mathrm{f}} = \frac{A_{\mathrm{r}}^{\mathrm{d}\to\mathrm{f}}}{\Gamma_{\mathrm{d}}^{\mathrm{nucl}}} \; . \tag{3.30}$$

Since we are later on only interested in the relative probability of a certain nuclear decay channel, the nuclear part $\Gamma_{\mathrm{d}}^{\mathrm{nucl}}$ has been used in Eq. (3.30) instead of the full width Γ_{d} which may also have electronic contributions.

3.4 Excitation rate via NEEC

For the calculation of the NEEC rate $Y_{\mathrm{neec}}^{\mathrm{i}\to\mathrm{d}}$ given in Eq. (3.21) it is helpful to first reduce the many-electron matrix elements to matrix elements of the "active" electron only (the electron which undergoes the capture process) by employing the single-active electron approximation [192]. Therefore, we use the theory of angular momentum coupling [170] in order to compose the electronic capture level $|\alpha_{\mathrm{d}} J_{\mathrm{d}} \mu_{\mathrm{d}}\rangle$ into a many-electron part determined by α_{i}, J_{i} and μ_{i} and an active-electron part characterized by the set of quantum numbers n_{d}, κ_{d} and m_{d},

$$|\Psi_{\mathrm{d}}^{\mathrm{el}}\rangle = |\alpha_{\mathrm{d}} J_{\mathrm{d}} \mu_{\mathrm{d}}\rangle = \sum_{\mu_{\mathrm{i}} m_{\mathrm{d}}} C(J_{\mathrm{i}}\ j_{\mathrm{d}}\ J_{\mathrm{d}}; \mu_{\mathrm{i}}\ m_{\mathrm{d}}\ \mu_{\mathrm{d}}) |\alpha_{\mathrm{i}} J_{\mathrm{i}} \mu_{\mathrm{i}}, n_{\mathrm{d}} \kappa_{\mathrm{d}} m_{\mathrm{d}}\rangle \; . \tag{3.31}$$

The coupling weights of the superposition are given by the Clebsch-Gordan coefficients $C(J_{\mathrm{i}}\ j_{\mathrm{d}}\ J_{\mathrm{d}}; \mu_{\mathrm{i}}\ m_{\mathrm{d}}\ \mu_{\mathrm{d}})$. The total and orbital angular momentum of $|n_{\mathrm{d}} \kappa_{\mathrm{d}} m_{\mathrm{d}}\rangle$ are denoted as $j_{\mathrm{d}} = |\kappa_{\mathrm{d}}| - \frac{1}{2}$ and l_{d}, respectively. Furthermore, it is possible to write the interaction Hamiltonian H_{N} occurring in Eq. (3.21) as a direct product of a part only acting on the nuclear degrees of freedom and an electronic part, $H_{\mathrm{N}} = H_{\mathrm{N}}^{\mathrm{nucl}} \otimes H_{\mathrm{N}}^{\mathrm{el}}$. The matrix elements of $H_{\mathrm{N}}^{\mathrm{el}}$ evaluate in our case to

$$\begin{aligned}\langle \Psi_{\mathrm{d}}^{\mathrm{el}} | H_{\mathrm{N}}^{\mathrm{el}} | \Psi_{\mathrm{i}}^{\mathrm{el}} \rangle &= \sum_{\mu_{\mathrm{i}}' m_{\mathrm{d}}} C(J_{\mathrm{i}}\ j_{\mathrm{d}}\ J_{\mathrm{d}}; \mu_{\mathrm{i}}'\ m_{\mathrm{d}}\ \mu_{\mathrm{d}}) \langle \alpha_{\mathrm{i}} J_{\mathrm{i}} \mu_{\mathrm{i}}', n_{\mathrm{d}} \kappa_{\mathrm{d}} m_{\mathrm{d}} | H_{\mathrm{N}}^{\mathrm{el}} | \alpha_{\mathrm{i}} J_{\mathrm{i}} \mu_{\mathrm{i}}, \boldsymbol{p} m_{\mathrm{s}} \rangle \\ &= \sum_{m_{\mathrm{d}}} C(J_{\mathrm{i}}\ j_{\mathrm{d}}\ J_{\mathrm{d}}; \mu_{\mathrm{i}}\ m_{\mathrm{d}}\ \mu_{\mathrm{d}}) \langle n_{\mathrm{d}} \kappa_{\mathrm{d}} m_{\mathrm{d}} | \boldsymbol{\hbar}_{\mathrm{N}}^{\mathrm{el}} | \boldsymbol{p} m_{\mathrm{s}} \rangle \; . \end{aligned} \tag{3.32}$$

Here, the single-active electron approximation [192] was applied in order to derive the second line of Eq. (3.32) where we assume that the initial bound electronic wave function does not change by adding an additional electron.

The further calculation of the single-electron matrix elements requires the continuum electron states with definite asymptotic momentum $\boldsymbol{p}$ and spin projection m_{s} to be expanded in terms of partial waves $|\varepsilon\kappa m\rangle$ [193],

$$|\boldsymbol{p}m_{\mathrm{s}}\rangle = \sum_{\kappa m} \mathrm{i}^{l} \mathrm{e}^{\mathrm{i}\Delta_{\kappa}} \sum_{m_l} Y^{*}_{l m_l}(\theta_{\boldsymbol{p}}, \varphi_{\boldsymbol{p}}) C(l\ \frac{1}{2}\ j; m_l\ m_{\mathrm{s}}\ m) |\varepsilon\kappa m\rangle \ , \tag{3.33}$$

where ε represents the kinetic energy, $\varepsilon = \sqrt{p^2c^2 + c^4} - c^2$ and κ the eigenvalue of the relativistic spin-orbit operator (analogously to κ_{d}). The total and orbital angular momentum of the partial wave are defined as j and l. Δ_{κ} is the so-called Coulomb phase which ensures the correct boundary conditions. In the case of electron capture, the electronic boundary condition consists of an incoming plane wave and an outgoing spherical wave. The further derivation of the NEEC transition rates is divided into the special cases of electric and magnetic multipolarity.

3.4.1 Electric transitions

By considering NEEC transitions of electric multipolarity and using Eq. (3.32), Eq. (3.21) simplifies to

$$\begin{aligned} Y^{\mathrm{i}\to\mathrm{d}}_{\mathrm{neec}} = & \frac{2\pi(2J_{\mathrm{d}}+1)}{2(2I_{\mathrm{i}}+1)(2J_{\mathrm{i}}+1)(2j_{\mathrm{d}}+1)} \\ & \times \sum_{M_{\mathrm{i}} m_{\mathrm{s}}} \sum_{M_{\mathrm{d}} m_{\mathrm{d}}} \int d\Omega_{\boldsymbol{p}} \left| \langle I_{\mathrm{d}} M_{\mathrm{d}}, n_{\mathrm{d}}\kappa_{\mathrm{d}} m_{\mathrm{d}}, 0 | \boldsymbol{\hbar}_{\mathrm{en}} | I_{\mathrm{i}} M_{\mathrm{i}}, \boldsymbol{p} m_{\mathrm{s}}, 0\rangle \right|^2 \rho_{\mathrm{i}} \ , \end{aligned} \tag{3.34}$$

where only the Coulomb interaction $\boldsymbol{\hbar}_{\mathrm{en}}$ contributes. In order to calculate the occurring matrix element we make use of the multipole expansion [170]

$$\frac{1}{|\boldsymbol{r}_{\mathrm{e}} - \boldsymbol{r}_{\mathrm{n}}|} = \sum_{L=0}^{\infty} \sum_{M=-L}^{L} \frac{4\pi}{2L+1} Y_{LM}(\theta_{\mathrm{n}}, \varphi_{\mathrm{n}}) Y^{*}_{LM}(\theta_{\mathrm{e}}, \varphi_{\mathrm{e}}) \frac{r_{<}^{L}}{r_{>}^{L+1}} \ , \tag{3.35}$$

where the following notation has been introduced: $r_{<} = r_{\mathrm{n}}$ and $r_{>} = r_{\mathrm{e}}$ if $r_{\mathrm{n}} < r_{\mathrm{e}}$; $r_{<} = r_{\mathrm{e}}$ and $r_{>} = r_{\mathrm{n}}$ if $r_{\mathrm{n}} > r_{\mathrm{e}}$. Inserting the multipole expansion into the definition of $\boldsymbol{\hbar}_{\mathrm{en}}$ [Eqs. (3.18)] and integrating over the angular coordinates leads us to the following expression

$$\begin{aligned} \langle \Psi_{\mathrm{d}} | \boldsymbol{\hbar}_{\mathrm{en}} | \Psi_{\mathrm{i}} \rangle = & \sum_{LM} \frac{1}{R_0^{L+2}} \frac{4\pi}{2L+1} \langle I_{\mathrm{d}} M_{\mathrm{d}} | \mathbb{Q}_{LM} | I_{\mathrm{i}} M_{\mathrm{i}} \rangle \\ & \times \langle n_{\mathrm{d}}\kappa_{\mathrm{d}} m_{\mathrm{d}} | Y^{*}_{LM}(\theta_{\mathrm{e}}, \varphi_{\mathrm{e}}) \int_0^{\infty} \mathrm{d}r_{\mathrm{n}}\, r_{\mathrm{n}}^2 \frac{r_{<}^{L}}{r_{>}^{L+1}} \delta(R_0 - r_{\mathrm{n}}) | \boldsymbol{p} m_{\mathrm{s}} \rangle \ . \end{aligned} \tag{3.36}$$

Since the multipole operator $\mathbb{Q}_{LM}$ is a spherical tensor, the nuclear matrix element occurring in Eq. (3.36) can be related to the reduced transition probabilities by applying the Wigner-Eckart theorem [analogously to Eq. (2.21)].

The calculation of the electronic matrix element appearing in Eq. (3.36) is shown in App. A. Putting everything together and by making use of some Clebsch-Gordan algebra, we finally obtain

$$Y_{\mathrm{neec}}^{(\mathcal{E}L)} = \frac{4\pi^2\rho_{\mathrm{i}}}{(2L+1)^2} R_0^{-2(L+2)} \mathcal{B}(\mathcal{E}L, I_{\mathrm{i}} \to I_{\mathrm{d}}) \frac{2J_{\mathrm{d}}+1}{2J_{\mathrm{i}}+1} \sum_{\kappa} C(j_{\mathrm{d}}\ L\ j; \frac{1}{2}\ 0\ \frac{1}{2})^2 \left| R_{L,\kappa_{\mathrm{d}},\kappa}^{(\mathcal{E})} \right|^2 . \tag{3.37}$$

The occurring radial integral $R_{L,\kappa_{\mathrm{d}},\kappa}^{(\mathcal{E})}$ has to be evaluated numerically and is defined by

$$\begin{aligned} R_{L,\kappa_{\mathrm{d}},\kappa}^{(\mathcal{E})} = \frac{1}{R_0^{L-1}} & \int_0^{R_0} \mathrm{d}r_{\mathrm{e}}\, r_{\mathrm{e}}^{L+2} \Big(f_{n_{\mathrm{d}}\kappa_{\mathrm{d}}}(r_{\mathrm{e}}) f_{\varepsilon\kappa}(r_{\mathrm{e}}) + g_{n_{\mathrm{d}}\kappa_{\mathrm{d}}}(r_{\mathrm{e}}) g_{\varepsilon\kappa}(r_{\mathrm{e}}) \Big) \\ & + R_0^{L+2} \int_{R_0}^{\infty} \mathrm{d}r_{\mathrm{e}}\, r_{\mathrm{e}}^{-L+1} \Big(f_{n_{\mathrm{d}}\kappa_{\mathrm{d}}}(r_{\mathrm{e}}) f_{\varepsilon\kappa}(r_{\mathrm{e}}) + g_{n_{\mathrm{d}}\kappa_{\mathrm{d}}}(r_{\mathrm{e}}) g_{\varepsilon\kappa}(r_{\mathrm{e}}) \Big) , \end{aligned} \tag{3.38}$$

with the relativistic continuum wave function

$$\Psi_{\varepsilon\kappa m}(\boldsymbol{r}) = \begin{pmatrix} g_{\varepsilon\kappa}(r)\Omega_{\kappa}^{m}(\theta,\varphi) \\ \mathrm{i} f_{\varepsilon\kappa}(r)\Omega_{-\kappa}^{m}(\theta,\varphi) \end{pmatrix} \tag{3.39}$$

and the relativistic bound wave function

$$\Psi_{n_{\mathrm{d}}\kappa_{\mathrm{d}}m_{\mathrm{d}}}(\boldsymbol{r}) = \begin{pmatrix} g_{n_{\mathrm{d}}\kappa_{\mathrm{d}}}(r)\Omega_{\kappa_{\mathrm{d}}}^{m_{\mathrm{d}}}(\theta,\varphi) \\ \mathrm{i} f_{n_{\mathrm{d}}\kappa_{\mathrm{d}}}(r)\Omega_{-\kappa_{\mathrm{d}}}^{m_{\mathrm{d}}}(\theta,\varphi) \end{pmatrix} . \tag{3.40}$$

Here, $g_{\varepsilon\kappa}$ and $f_{\varepsilon\kappa}$ denote the large and small radial components of the continuum Dirac spinor, $g_{n_{\mathrm{d}}\kappa_{\mathrm{d}}}$ and $f_{n_{\mathrm{d}}\kappa_{\mathrm{d}}}$ the corresponding quantities for the bound spinor and Ω_{κ}^{m} are the so-called spin-angular functions, respectively.

3.4.2 Magnetic transitions

In the case of magnetic transitions the NEEC rate is given by Eq. (3.34) with the Coulomb interaction $\mathscr{H}_{\mathrm{en}}$ being replaced by the magnetic Hamiltonian $\mathscr{H}_{\mathrm{magn}}$. The occurring matrix element $\langle \Psi_{\mathrm{d}} | \mathscr{H}_{\mathrm{magn}} | \Psi_{\mathrm{i}} \rangle$ is explicitly given by

$$\begin{aligned} \langle \Psi_{\mathrm{d}} | \mathscr{H}_{\mathrm{magn}} | \Psi_{\mathrm{i}} \rangle = 4\pi\mathrm{i} \sum_{LM} (-1)^M \sqrt{\frac{L+1}{L}} \frac{1}{2L+1} & \\ \times \langle I_{\mathrm{d}} M_{\mathrm{d}} | \mathscr{M}_{LM} | I_{\mathrm{i}} M_{\mathrm{i}} \rangle \langle n_{\mathrm{d}}\kappa_{\mathrm{d}} m_{\mathrm{d}} | r_{\mathrm{e}}^{-(L+1)} & \boldsymbol{\alpha} \cdot \boldsymbol{Y}_{LL}^{-M}(\theta_{\mathrm{e}}, \varphi_{\mathrm{e}}) | \boldsymbol{p} m_{\mathrm{s}} \rangle , \end{aligned} \tag{3.41}$$

where the following relation was used

$$\boldsymbol{Y}_{JL}^{M*} = (-1)^{L+J+M+1} \boldsymbol{Y}_{JL}^{-M} . \tag{3.42}$$

Analogously to electric transitions, the nuclear part can be again expressed in terms of the reduced transition probabilities $\mathcal{B}$, see Eq. (2.17). The remaining task is to calculate the electronic free-bound transition amplitude. The derivation is presented in App. A. By furthermore using the definition of the Wigner $3j$-symbols in terms of Clebsch-Gordan coefficients [170]

$$C(j_1\;j_2\;j;m_1\;m_2\;m) = (-1)^{m+j_1-j_2}\sqrt{2j+1}\begin{pmatrix} j_1 & j_2 & j \\ m_1 & m_2 & -m \end{pmatrix}\ , \tag{3.43}$$

the final result for the magnetic NEEC transition rate with fixed multipolarity L is obtained

$$\begin{aligned} Y_{\mathrm{neec}}^{(\mathcal{M}L)} &= \frac{4\pi^2\rho_{\mathrm{i}}}{L^2(2L+1)^2}\mathcal{B}(\mathcal{M}L, I_{\mathrm{i}}\to I_{\mathrm{d}}) \\ &\quad\times\frac{2J_{\mathrm{d}}+1}{2J_{\mathrm{i}}+1}\sum_{\kappa}(2j+1)(\kappa_{\mathrm{d}}+\kappa)^2\begin{pmatrix} j_{\mathrm{d}} & j & L \\ \frac{1}{2} & -\frac{1}{2} & 0 \end{pmatrix}^2\left|R_{L,\kappa_{\mathrm{d}},\kappa}^{(\mathcal{M})}\right|^2\ . \end{aligned} \tag{3.44}$$

The radial integral $R_{L,\kappa_{\mathrm{d}},\kappa}^{(\mathcal{M})}$ is defined by

$$R_{L,\kappa_{\mathrm{d}},\kappa}^{(\mathcal{M})} = \int_0^\infty \mathrm{d}r_{\mathrm{e}}\, r_{\mathrm{e}}^{-L+1}\Big(g_{n_{\mathrm{d}}\kappa_{\mathrm{d}}}(r_{\mathrm{e}})f_{\varepsilon\kappa}(r_{\mathrm{e}}) + f_{n_{\mathrm{d}}\kappa_{\mathrm{d}}}(r_{\mathrm{e}})g_{\varepsilon\kappa}(r_{\mathrm{e}})\Big)\ , \tag{3.45}$$

and requires a numerical approach to be solved analogously to $R_{L,\kappa_{\mathrm{d}},\kappa}^{(\mathcal{E})}$ in Eq. (3.38).

Chapter 4

Direct and secondary nuclear excitation with the XFEL

Photon energies accessible with the new x-ray free-electron laser (XFEL) facilities open a way for the resonant driving of low-lying nuclear transitions in the keV range. In particular, the high brilliance and coherence features of the XFEL light promise an increase in magnitude of nuclear excitations in comparison to synchrotron radiation experiments as pointed out in Chap. 1. While in the latter the electronic response only acted as background, the unique interaction between the super-intense XFEL pulses and matter can lead to new states of matter, like cold, high-density plasmas [77] where secondary nuclear processes from the coupling to the atomic shell are rendered possible, for instance, NEEC.

We investigate and quantify the direct and secondary nuclear excitations in a normal incidence setup for two species of nuclei: (i) ^{93}Mo isomer triggering where the isomeric state IS is depopulated via a 4.85 keV transition to an above lying triggering level T, as depicted in Fig. 4.1; and (ii) the resonant driving of the 14.4 keV transition in ^{57}Fe from the ground state G to the first excited level E. The latter nucleus has been the "working horse" of the nuclear resonance scattering community at synchrotron sources [96, 104] and it is also the present candidate for x-ray quantum optics using nuclear transitions in thin film x-ray planar cavities [41, 106, 107]. Many of the present studies at synchrotron sources have extensions envisaged with the XFEL as source of stronger, nonlinear nuclear excitation. In the case of ^{93}Mo isomer triggering, the super-intense XFEL is a priori desirable in order to efficiently depopulate the isomeric state. For these studies it is therefore vital to know whether also additional plasma effects may play an important role for the nuclear excitation or for the sought-for coherence effects.

In the following we address in more detail the XFEL parameter choice and present our photoexcitation and NEEC numerical results for the competing excitation channels. A theoretical approach for describing NEEC inside a plasma environment as well a hydrodynamic model for the plasma expansion is set up in Sec. 4.1. There, we also give a short overview about the considered nuclear targets. Afterwards, we investigate independently of each other the direct photoexcitation in Sec. 4.2 and the secondary NEEC process in a stationary and in an expanding plasma environment in Secs. 4.3 and 4.4, respectively. In the latter, we furthermore discuss the initial plasma conditions in dependence of the considered laser parameters and elaborate the influence of atomic processes on the plasma expansion. Sec. 4.5 concludes this Chapter with a comparison between the two excitation channels and a general set of qualitative criteria to identify the dominant nuclear excitation process.

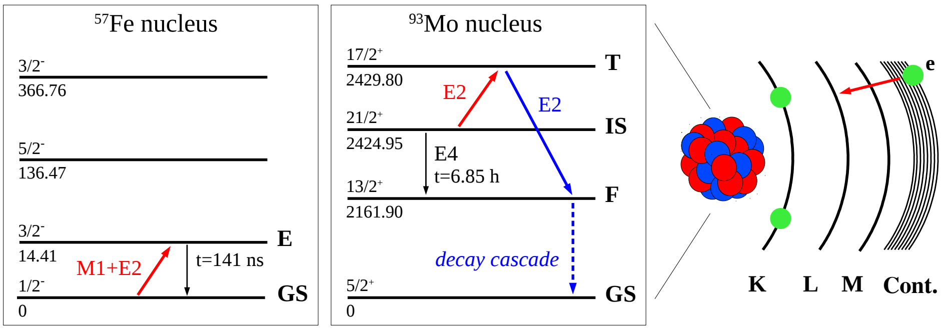

Figure 4.1: Nuclear excitation by electron capture for isomer triggering in ^{93}Mo and ground-state excitation in ^{57}Fe. A free electron (right-hand side) recombines into a highly charged ion with the simultaneous excitation of the nucleus (level schemes on the left-hand side). The ^{93}Mo nucleus is initially in a metastable excited state whereas ^{57}Fe is in the ground state. The nuclear excitation (red arrow) is induced by NEEC into the L shell (right-hand side) with subsequent decay to the nuclear ground state (long blue solid and dashed arrows in the ^{93}Mo level scheme, black arrow in the ^{57}Fe scheme). The nuclear levels are labeled with their total angular momentum, parity and energy (in keV) [194].

4.1 Theoretical treatment

The theoretical formalisms used to describe the direct photoexcitation and the microscopic NEEC process were introduced in Chaps. 2 and 3, respectively. Here, we address NEEC as secondary process in the XFEL-produced cold plasma and the plasma dynamics described by means of a hydrodynamical model. The effects of the latter on the secondary excitation channel are quantified then in Sec. 4.4. Finally, this Section ends with a short discussion about the considered nuclear samples and their manufacturing.

4.1.1 NEEC reaction rates in the plasma environment

In a plasma, free electrons with different kinetic energies are available. NEEC is a resonant process where a free electron is captured by an ion with the simultaneous excitation of its nucleus. The resonance bandwidth is determined by the Lorentz profile (3.23). Since the kinetic energy of free electrons in a plasma is distributed over a wide range, many resonant NEEC channels may exist. In the following we will shortly describe how such a situation can be handled theoretically in terms of reaction rates. Atomic units $\hbar = m_\mathrm{e} = e = 4\pi\varepsilon_0 = 1$ are used throughout this subsection.

As introduced in Sec. 3.1, the initial and intermediate states are given by Eq. (3.1) and Eq. (3.3), respectively. In order to restrict the number of possible initial configurations, for a lower-limit estimate, we consider in the following only NEEC into ions which are in their electronic ground states. In this case, the initial electronic configuration α_0 is uniquely identified by the charge state number q before electron capture. In the isolated resonance approximation, the total NEEC reaction rate in the plasma can be written as a summation over all charge states q and all capture channels α_{d},

$$\lambda_{\mathrm{neec}} = \sum_{q} \sum_{\alpha_{\mathrm{d}}} P_q \lambda_{\mathrm{neec}}^{q,\alpha_{\mathrm{d}}} \ , \tag{4.1}$$

where the partial NEEC rate into the capture level α_{d} of an ion in the charge state q is given by

$$\lambda_{\mathrm{neec}}^{q,\alpha_{\mathrm{d}}} = \int \mathrm{d}E \, \sigma_{\mathrm{neec}}^{\mathrm{i}\to\mathrm{d}}(E) \phi_{\mathrm{e}}(E) \ . \tag{4.2}$$

The single-resonance cross sections $\sigma_{\mathrm{neec}}^{\mathrm{i}\to\mathrm{d}}$ are defined in Eq. (3.22). The dependence on q is hidden here in the NEEC resonance energy E_{d} entering $\sigma_{\mathrm{neec}}^{\mathrm{i}\to\mathrm{d}}$ in the Lorentz profile. The factor P_q occurring in Eq. (4.1) denotes the probability that an ion of charge state q is present in the plasma. The electron flux ϕ_{e} in the plasma can be written as the product of the density of states $g(E)$, the Fermi-Dirac distribution $f_{\mathrm{FD}}(E, T_{\mathrm{e}})$ for a certain electron temperature T_{e} and the velocity $v(E)$,

$$\phi_{\mathrm{e}}(E) = g(E) f_{\mathrm{FD}}(E, T_{\mathrm{e}}) v(E) \ . \tag{4.3}$$

The temperature dependence of ϕ_{e} is only included in the Fermi-Dirac statistics f_{FD}. The density of states as well as the velocity are determined by taking the relativistic dispersion relation for the free electrons. The chemical potential μ_{e} of the electrons occurring in f_{FD} is fixed by adopting the normalization

$$\int \mathrm{d}E \, g(E) f_{\mathrm{FD}}(E, T_{\mathrm{e}}) = n_{\mathrm{e}} \ . \tag{4.4}$$

Thereby, n_{e} represents the number density of free electrons. By using the definition of the NEEC cross section and assuming that the free electron momentum and the NEEC interaction matrix elements are constant over the width of the Lorentz profile $L_{\mathrm{d}}(E - E_{\mathrm{d}})$, Eq. (4.2) can be simplified to

$$\lambda_{\mathrm{neec}}^{q,\alpha_{\mathrm{d}}} = \frac{2\pi^2}{p^2} Y_{\mathrm{neec}}^{\mathrm{i}\to\mathrm{d}} \Phi_{\mathrm{e}}^{\mathrm{res}}(E_{\mathrm{d}}) \ , \tag{4.5}$$

where the resonant electron flux is defined by

$$\Phi_{\mathrm{e}}^{\mathrm{res}}(E_{\mathrm{d}}) = \int \mathrm{d}E \, L_{\mathrm{d}}(E - E_{\mathrm{d}}) \phi_{\mathrm{e}}(E) \ . \tag{4.6}$$

The net NEEC rate λ_{neec} provided by Eq. (4.1) is strongly dependent on the available charge states and free electron energies which are both dictated by the plasma conditions. In turn, the latter will not be constant over time as the plasma undergoes expansion. We proceed to formulate a model that takes the spatial expansion of the plasma into account and provides the temporal dynamics of the plasma parameters required to calculate the net NEEC rates in the plasma environment.

4.1.2 Plasma expansion model

In the scenario under investigation, the plasma-formation occurs on the time scale of the XFEL pulse duration ($\sim$ 100 fs) while the plasma expansion time is in the range of ps. Accordingly, we neglect the plasma expansion during its formation in the laser-target interaction. In order to ascertain the effect of the plasma expansion on atomic processes after the interaction of the laser pulse with the target, we model the expansion of the target plasma by a quasi-neutral expansion of spherical clusters as studied in the context of the intense optical laser pulses interaction with spherical clusters [93, 94, 195–203]. We follow the analysis of Ref. [93] to describe the plasma expansion. The target plasma is assumed to maintain a uniform (but decreasing) density throughout the plasma sphere during the expansion while the electron temperature decreases with the adiabatic expansion of the plasma, described by

$$\frac{3}{2} n_{\mathrm{e}} V \, \mathrm{d}T_{\mathrm{e}} = -P_{\mathrm{e}} \, \mathrm{d}V \ , \tag{4.7}$$

where n_{e} is the number density of free electrons, and V is the volume of the plasma with the radius R, i.e., $V = 4\pi R^3/3$. Here and in the following, we use the Lorentz-Heaviside natural units $\hbar = c = k_{\mathrm{B}} = \epsilon_0 = \mu_0 = 1$ for the plasma modeling part. The pressure of free electrons P_{e} is given by the ideal gas law, $P_{\mathrm{e}} = n_{\mathrm{e}} T_{\mathrm{e}}$. Therefore, the time-dependent electron temperature $T_{\mathrm{e}}(t)$ and the plasma radius $R(t)$ satisfy the relation

$$T_{\mathrm{e}} = T_{\mathrm{e},0} \left(\frac{R_0}{R} \right)^2 \ , \tag{4.8}$$

where $T_{\mathrm{e},0}$ is the initial electron temperature and R_0 the initial plasma radius. During the plasma expansion, the electrons loose their thermal energy to the ions resulting into the electron and ion kinetic energies

$$\begin{aligned} n_{\mathrm{i}} V \frac{\mathrm{d}}{\mathrm{d}t} \left(\frac{3}{2} T_{\mathrm{i}} \right) &= -n_{\mathrm{e}} V \frac{\mathrm{d}}{\mathrm{d}t} \left(\frac{3}{2} T_{\mathrm{e}} \right) \ , \\ \frac{1}{2} m_{\mathrm{i}} \left(\frac{\mathrm{d}R}{\mathrm{d}t} \right)^2 &= \frac{3}{2} T_{\mathrm{i}} \ , \end{aligned} \tag{4.9}$$

with m_{i} being the ion mass. The equation of plasma expansion then reads [93]

$$m_{\mathrm{i}} \frac{\mathrm{d}^2 R}{\mathrm{d}t^2} = 3 \frac{n_{\mathrm{e}}}{n_{\mathrm{i}}} \frac{T_{\mathrm{e},0} \ R_0^2}{R^3} = 3 Z_{\mathrm{i}} \frac{T_{\mathrm{e},0} \ R_0^2}{R^3} \ , \tag{4.10}$$

where $Z_{\mathrm{i}} = n_{\mathrm{e}}/n_{\mathrm{i}}$ is the ratio of the electron density to the ion density. In the quasi-neutral limit, Z_{i} is therefore the average charge state of the ions. Integrating once for a fixed $Z_{\mathrm{i}} = Z_0$ yields

$$\left(\frac{\mathrm{d}R}{\mathrm{d}t} \right)^2 = v_{\mathrm{s}}^2 \left(1 - \frac{R_0^2}{R^2} \right) , \tag{4.11}$$

where $v_{\mathrm{s}} = (3 T_{\mathrm{e},0} Z_0 / m_{\mathrm{i}})^{1/2}$ is the ion sound velocity which, in the limit $R \to \infty$, is the characteristic speed for the plasma expansion [93, 94]. It may be noted that Peano *et* *al.* [204, 205] analyzed the expansion of spherical nanoplasmas with the Vlasov-Poisson equations, the particle-in-cell (PIC) method, and the ergodic model [204]. Comparisons between their results [204, 205] and those via the hydrodynamic expansion [Eq.(4.10)] (atomic processes not included) for plasmas with the dimensionless parameter $\tilde{T}_0 = 3\lambda_\mathrm{D}^2/R_0^2 = 7.2 \times 10^{-3}$ or $\tilde{T}_0 = 7.2 \times 10^{-2}$, where λ_D denotes the Debye length for the electrons, show that the hydrodynamic expansion model can adequately describe the expansion of spherical cluster targets heated by an intense optical laser pulse. In addition, 1D and 2D PIC simulations using the EPOCH code[1] for plasmas (atomic processes not included) with the parameters under consideration in this Chapter have also been performed. The expansion time obtained by the hydrodynamic expansion model is in good agreement with the PIC simulation results.

The quasi-neutral hydrodynamic plasma expansion described above requires the plasma density and the charge state as input parameters. One can exploit the different time scales involved in the plasma formation and subsequent plasma expansion, and as a first step calculate the average charge state by using the electron temperature from the plasma expansion model. One can then use this charge state to estimate the plasma expansion and consequently the electron temperature at a later time, thus establishing a feedback loop between the effective atomic processes (represented by the average charge state) and the plasma expansion. This is discussed in Sec. 4.4.2.

4.1.3 Nuclear targets

As already pointed out, we are going to investigate the nuclear photoexcitation with the XFEL at two nuclear species, the $^{93\mathrm{m}}$Mo isomer and the ^{57}Fe isotope. In the case of ^{57}Fe, the initial state is the stable ground state of the isotope, such that bulk iron samples enriched with the ^{57}Fe isotope (natural abundance 2.2%) can be fabricated. On the other hand, the ^{93}Mo solid-state sample should contain nuclei in the isomeric state with 2.5 MeV excitation energy. The isomers can be produced in $^{93}_{41}$Nb(p,n)$^{93\mathrm{m}}_{42}$Mo reactions [206], directly embedded into 1 μm thick solid–state niobium foils [207]. Considering the production reaction cross section values [206], we estimate that a $^{93\mathrm{m}}$Mo isomer density of 10^{16} cm^{-3} can be achieved in the solid–state 1 μm-thick Nb foils [207] using standard proton beams like the LINAC at GSI [208, 209] as shown in App. B. Correspondingly, the majority of atoms in the isomeric sample belongs to the niobium species ($Z = 41$) and their interaction with the XFEL photons will play the dominant role for the plasma parameters estimates. However, due to the very close atomic number values of molybdenum and niobium, the photoelectric response of the two atomic species is very similar. Here, we assume a thickness of 1 μm for both nuclear targets, which for the case of ^{57}Fe corresponds to a resonant thickness of $\xi = 3.9$.

4.2 Direct photoexcitation

The photoexcitation rates are calculated following the formalism introduced in Chap. 2 using reduced transition probability values from Ref. [194]. The limited laser coherence

---

[1] The EPOCH code was developed as part of the UK EPSRC funded projects EP/G054940/1.

	$^{93\mathrm{m}}$Mo			^{57}Fe		
	I_{eff} $\left(\frac{\mathrm{W}}{\mathrm{cm}^2}\right)$	$\rho_{\mathrm{ee}}^{\mathrm{laser}}$	$R_{\gamma}^{\mathrm{laser}}$ $\left(\frac{1}{\mathrm{s}}\right)$	I_{eff} $\left(\frac{\mathrm{W}}{\mathrm{cm}^2}\right)$	$\rho_{\mathrm{ee}}^{\mathrm{laser}}$	$R_{\gamma}^{\mathrm{laser}}$ $\left(\frac{1}{\mathrm{s}}\right)$
LCLS	5.2×10^{9}	1.9×10^{-20}	5.6×10^{-14}	3.1×10^{8}	9.1×10^{-16}	1.9×10^{-2}
SACLA	1.2×10^{9}	1.7×10^{-20}	1.7×10^{-14}	7.0×10^{7}	9.5×10^{-16}	6.6×10^{-3}
Eur. XFEL	6.5×10^{9}	2.4×10^{-21}	9.6×10^{-12}	3.9×10^{8}	1.2×10^{-16}	3.2
XFELO	6.7×10^{12}	4.5×10^{-14}	4.6×10^{-3}	4.0×10^{11}	2.2×10^{-9}	1.5×10^{9}

Table 4.1: Calculated excited state occupation number $\rho_{\mathrm{ee}}^{\mathrm{laser}}$ and signal photon rate $R_{\gamma}^{\mathrm{laser}}$ for ^{93}Mo and ^{57}Fe [210]. The laser parameters shown in Table 1.1 are employed here.

time is accounted for by introducing a corresponding decoherence rate in the Lindblad operator. The numerical solution of the master equation (2.1) for the density matrix is then carried out with the procedures implemented in *Mathematica*. We considered realistic parameters for the coherent high-frequency light sources shown in Table 1.1, corresponding to a laser focal spot of 10 μm^2 (i.e., focal radius of approx. 1.8 μm). Results for the total population of the excited level $\rho_{\mathrm{ee}}^{\mathrm{laser}}$ after a single laser pulse with effective intensity I_{eff} [see Eq. (1.1)] are presented in Table 4.1. These populations are obtained by summing the elements $\rho_{\mathrm{ee}}(M_{\mathrm{e}}) = \langle I_{\mathrm{e}} M_{\mathrm{e}} | \rho | I_{\mathrm{e}} M_{\mathrm{e}} \rangle$ evaluated at $t = T_{\mathrm{pulse}}$ over all possible projection quantum numbers M_{e} [156] where the populations $\rho_{\mathrm{ee}}(M_{\mathrm{e}})$ are determined by the set of differential equations (2.6). For both $^{93\mathrm{m}}$Mo and ^{57}Fe cases, the XFELO delivers the highest excitation rates per pulse among the considered laser facilities.

Comparing the effective laser intensities displayed in Table 4.1, it can be seen that the XFELO provides with 6.7×10^{12} W/cm^2 for $^{93\mathrm{m}}$Mo and 4.0×10^{11} W/cm^2 for ^{57}Fe the highest value of I_{eff}. The effective intensity of the LCLS, for instance, is 3 orders of magnitude smaller. Thus, due to its narrow bandwidth, the XFELO is able to provide in average 1000 times more resonant photons per pulse than the LCLS, SACLA or the Eur. XFEL.

Another and possibly less obvious reason for the outstanding excitation capabilities of the XFELO is its coherence properties. As already mentioned in the previous Section, all currently operating XFELs lack a good temporal coherence (indicated by T_{coh} in Table 1.1) because of the random fluctuations in the initial electron charge density. The poor temporal coherence is one of the main limiting factors for the nuclear excitation. For instance, the consideration of a totally coherent x-ray pulse ($T_{\mathrm{coh}} = \infty$) increases the nuclear excitation between 4 and 6 orders of magnitude.

Experimentally, the nuclear excitation is best accessible by measuring the number of photons of a specific transition emitted in the decay of the excited nuclear state E. In the case of isomer triggering, for instance, the triggering level T first decays to an intermediate state F followed by a decay cascade to the nuclear ground state G. In this cascade a characteristic photon of 1 MeV is emitted which can be used as signature for the isomer triggering. The rate of γ-ray signal photons at the detector is directly proportional to ρ_{ee},

$$R_\gamma^{\mathrm{laser}} = N_0 f_{\mathrm{rep}} B^{T\to F} \frac{1}{1+\alpha_{\mathrm{ic}}} \rho_{\mathrm{ee}} \ , \tag{4.12}$$

where $N_0 = n_0 A_{\mathrm{foc}} L$ represents the number of nuclei present in the focal spot A_{foc} and α_{ic} stands for the IC coefficient of the transition producing the 1 MeV signal photon. Furthermore, $B^{T\to F}$ denotes the branching ratio, i.e, the probability of a nucleus in T to not fall back to the state IS. For ^{93}Mo, this probability that the triggering level decays to the ground state via the emission of the 1 MeV signal photon can be approximated by one. In the case of ^{57}Fe, the resonantly scattered photons via the transition from the excited state E to the ground state G can be used as detection signal. In this case, a similar expression as Eq. (4.12) can be used, with a branching ratio value representing the probability that the excited nuclear state E decays radiatively. Taking the collective channel into account, this probability is approx. 82% for a sample thickness of 1 μm ($\xi = 3.9$).

Results for $R_\gamma^{\mathrm{laser}}$ are also shown in Table 4.1. Since the nuclear excitation per pulse is typically very small, the pulse repetition frequency f_{rep} of the laser plays a crucial role in order to have detectable signal rates. The Eur. XFEL, for instance, is expected to provide two orders of magnitude larger rates than the LCLS although the excited state population per pulse is smaller simply due to the high repetition frequency of 40,000 pulses per second. The XFELO may produce 4.6×10^{-3} and 1.5×10^{9} signal photons per second for $^{93\mathrm{m}}$Mo and ^{57}Fe, respectively. The large difference between $^{93\mathrm{m}}$Mo and ^{57}Fe comes mainly from the magnitude of the interaction matrix elements and the numbers of nuclei present in the samples, which are orders of magnitude apart. This difference also compensates that the effective intensity for the resonant photoexcitation of ^{57}Fe is about one order of magnitude smaller than for $^{93\mathrm{m}}$Mo.

4.3 Secondary NEEC in a stationary plasma

The net NEEC rate λ_{neec} provided by Eq. (4.1) is strongly dependent on the available charge states and free electron energies which are in turn both dictated by the plasma conditions. The charge state distribution (CSD) can be calculated by applying the collisional-radiative model implemented in FLYCHK [95]. In this model the CSD is completely determined by fixing the electron temperature T_{e} and the ion density n_{i} present in the plasma. In the following we investigate the role of the plasma conditions, considered to be stationary here, on λ_{neec} for the numerical case of $^{93\mathrm{m}}$Mo isomer triggering.

The microscopic transition rates Y_{neec} given in Eqs. (3.37) and (3.44) are computed numerically following the formalism introduced in Chap. 3. The electronic wave functions and binding energies are calculated by the relativistic multi-configurational Dirac Fock (MCDF) method implemented in the computer code GRASP92 [211]. The probabilities P_q are determined by the FLYCHK-CSD results and the electron flux ϕ_{e} is calculated following the expressions in Sec. 4.1.1. Finally, the convolution integral over the Lorentz profile and the electron flux appearing in Eq. (4.2) are solved by approximating the resonance profiles by Dirac delta distributions centered at E_{d}.

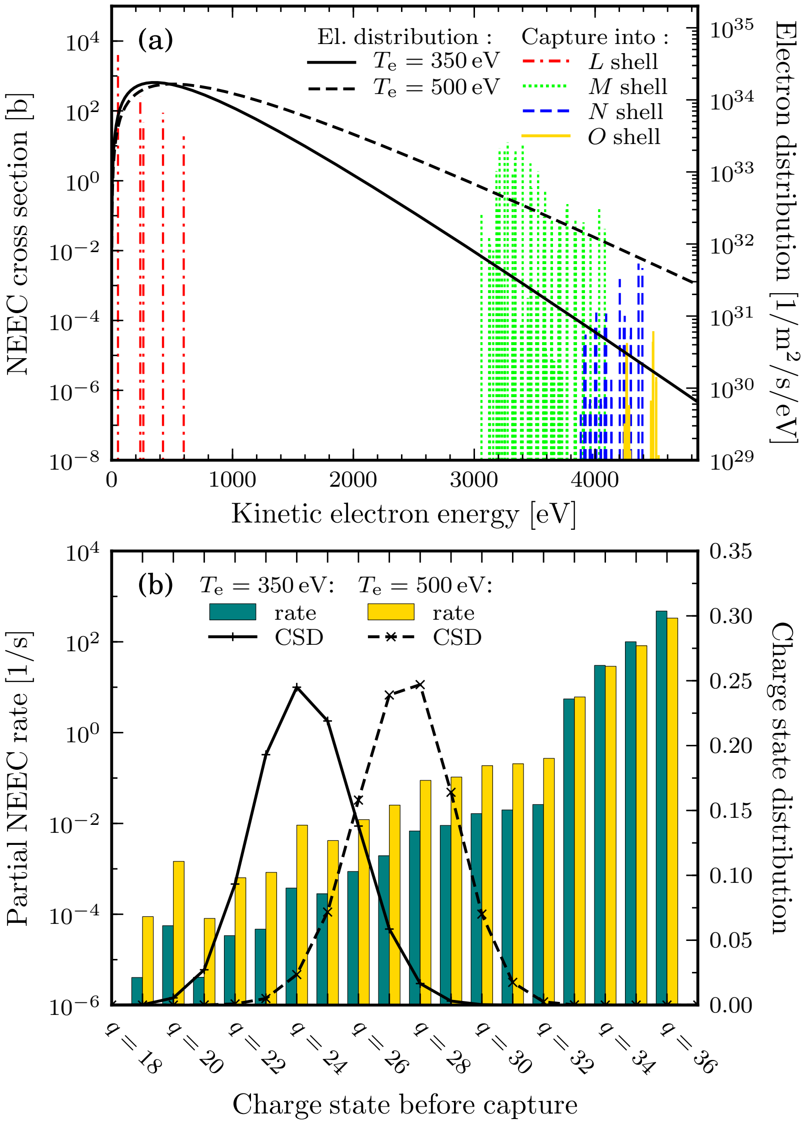

Figure 4.2: (a) NEEC resonance cross sections σ_{neec} for captures into the L, M, N and O shell (left axis) together with the electronic energy distribution (right axis). (b) Partial NEEC rate $\lambda^q_{\mathrm{neec}}$ (left axis) together with the corresponding CSD (right axis). Results are presented for two plasma temperatures, 350 eV and 500 eV [207].

capture orbital	$\Phi_{\mathrm{e}}^{\mathrm{res}}$ [1/m^2/s/eV]	$S_{\mathrm{neec}}^{IS\to F}$ [b eV]
$3d_{3/2}$	1.10×10^{31}	3.04×10^{-8}
$3d_{5/2}$	1.09×10^{31}	4.28×10^{-8}
$4d_{3/2}$	2.77×10^{30}	1.05×10^{-8}
$4d_{5/2}$	2.76×10^{30}	1.50×10^{-8}
$5d_{3/2}$	1.59×10^{30}	5.10×10^{-9}
$5d_{5/2}$	1.59×10^{30}	7.28×10^{-9}

Table 4.2: NEEC case study for a 350 eV plasma with ions initially in the charge state $q = 24$. Values for the resonant electron flux $\Phi_{\mathrm{e}}^{\mathrm{res}}$ and the NEEC resonance strength $S_{\mathrm{neec}}^{IS\to F}$ are presented for captures into $d_{3/2}$ and $d_{5/2}$ orbitals at an electron temperature $T_{\mathrm{e}} = 350$ eV.

In Fig. 4.2(a) NEEC cross sections are displayed for several capture levels together with the electron flux ϕ_{e}. For the latter we have exemplarily taken the temperatures $T_{\mathrm{e}} = 350$ eV and $T_{\mathrm{e}} = 500$ eV. The figure shows that the NEEC cross section decreases by going to more loosely bound capture levels. Due to the reduction of the binding energy, the kinetic energy of the initially free electron increases in order to still fulfill the NEEC resonance condition. Since $\sigma_{\mathrm{neec}}^{\mathrm{i}\to\mathrm{d}}$ is inversely proportional to the squared electron momentum, this leads to a decrease of the NEEC cross section.

Moreover, by comparing the cross section with the electron flux it can be seen that for $T_{\mathrm{e}} = 350$ eV and $T_{\mathrm{e}} = 500$ eV the resonance energies for M-, N- and O-shell recombinations are located at the tail of the electron distribution which diminishes exponentially. This behavior is once more explicitly shown in Table 4.2 where the resonant electron flux $\Phi_{\mathrm{e}}^{\mathrm{res}}$ for $T_{\mathrm{e}} = 350$ eV and the integrated cross section – the so-called resonance strength S_{neec} – are presented for increasingly less bound capture shells. We have considered the example of Mo ions with initially fully occupied K, L, M_1, M_2 and M_3 shells, corresponding to charge state $q = 24$. Moreover, NEEC into $d_{3/2}$ and $d_{5/2}$ orbitals has been considered. The results clearly show that both the NEEC resonance strength and the number of resonant electrons decrease by going to higher principal quantum numbers. This behavior can be recovered for all capture channels and initial charge states, as long as the NEEC resonance energy is much larger than the plasma temperature. Hence, a “cut-off” atomic level can be found for each charge state q starting from which the NEEC excitation can be neglected. Numerical results for λ_{neec} shown in the following always employ such cut-offs.

For the final NEEC reaction rate calculation, the three main ingredients are the electron energy distribution in the plasma, the availability of capture charge states and the magnitude of the NEEC cross sections σ_{neec}. In order to maximize the NEEC excitation rate one would prefer to have as many resonant free electrons as possible. As shown in Fig. 4.2(a) this is the case for the resonance energies of NEEC into the L shell which lie in the region around the maximum of ϕ_{e} in the case of $T_{\mathrm{e}} = 350$ eV and $T_{\mathrm{e}} = 500$ eV. However, as can be seen from the charge state distributions shown in Fig. 4.2(b), the number of available charge states in the plasma will be limited for a given electron temperature T_e. For instance, in the case of $T_\mathrm{e} = 350$ eV and $T_\mathrm{e} = 500$ eV only Mo charge states up to $q = 29$ and $q = 32$, respectively, are present in the plasma. Opening the NEEC resonance channels for the L shell requires the Mo ions to be at least in the charge state $q = 33$. Hence, we conclude that L-shell capture is not possible for the considered temperatures in Fig. 4.2.

In addition to the molybdenum CSD, Fig. 4.2(b) shows also the nuclear excitation probability in dependence of the charge state q obtained from Eq. (4.2) via a summation over all contributing α_d. Again, the temperatures $T_\mathrm{e} = 350$ eV and $T_\mathrm{e} = 500$ eV are considered. Our results show that the nuclear excitation probability growths with q because higher charge states open NEEC capture channels more deeply bound to the nucleus [207].

Finally, looking at the dependence of λ_neec on the electron temperature T_e we can conclude that increasing the temperature leads to a higher NEEC excitation rate for mainly two reasons: (i) higher temperatures involve higher available charge states which renders the capture into deeply bound electron shells possible; (ii) higher temperatures lead to an increase of the total number of available free electrons enhancing the resonant electron flux.

4.4 Secondary NEEC in an expanding plasma

4.4.1 Initial plasma conditions

In contrast to optical or infrared laser light, x-rays are able to produce directly inner-shell holes by photoionization and penetrate much further into the material leading to a very uniform irradiation of the solid. Moreover, the solid-state target is heated very rapidly by the laser pulse with duration of about 100 fs. On this time scale the ionic motion is negligible resulting in a plasma near to solid-state density. This rapid, isochoric heating of the plasma (the volume is nearly unaffected during the formation process) enables us to consider uniform temperature and density distributions at short times after the laser pulse.

The laser-induced creation of the plasma is mainly dominated by two processes: (i) photoionization, and, (ii) Auger decay. In the latter process an electron on a higher atomic shell decays to an inner-shell hole with the simultaneous emission of another electron into the continuum. The process of photoionization prefers the interaction with inner-shell electrons provided the photon energy exceeds the ionization potential of the electrons. In the case of niobium, for instance, the ionization edges of the K and L_1 shells lie at 19 keV and 2.7 keV [212], respectively. Hence, at most L-shell holes can be produced considering the resonant 4.85 keV x-rays. The laser-produced inner-shell holes are then subsequently refilled by either radiative or Auger decay.

In order to get a rough estimate of the initial plasma conditions directly after its creation, we follow the procedure used in Ref. [149]. We neglect the hydrodynamic expansion and the radiative losses for the first 100 fs when the laser pulse is present. (We note here that an extension of FLYCHK, the SCFLY code [213], was particularly designed to model the plasma generation phase. Unfortunately, SCFLY is not freely available.) Assuming an instantaneous equilibration time, equations of state (EOS) can be used to estimate the initial plasma conditions. Thereby, the deposited internal energy per pulse can be approximated by $e(J/g) = I_{\text{peak}}(W/cm^2)\kappa(cm^2/g)T_{\text{pulse}}(s)$ where κ represents the photoabsorption coefficient. Using the EOS tables $e(T_{\text{e}}, \rho_0)$ [214], the initial plasma temperature immediately after the creation process can be determined. Note that the ionic density is thereby assumed to remain initially at its solid-state density ρ_0 and at room temperature.

By using the LCLS laser parameters presented in Table 1.1, we obtain an initial temperature of $T_{\text{e},0} \approx 350$ eV for the Nb target. For the calculation we used a photoabsorption coefficient of 551.6 cm^2/g. Analogously, the initial stage of the Fe plasma can be estimated. Since due to the higher photon energy, the photoabsorption coefficient (63.0 cm^2/g) is much smaller in this case, we obtain a colder electron temperature from start on, namely $T_{\text{e},0} \approx 75$ eV.

4.4.2 Atomic effects in plasma expansion

In dense plasmas, atomic processes such as recombination and ionization are expected to play an important role on the plasma dynamics. In the following we sketch an approximate way to include the effects of the atomic processes on the hydrodynamic plasma expansion model described in Sec. 4.1.2 by using numerical results from the FLYCHK code [95].

FLYCHK was developed for describing plasma states like warm dense matter, highly transient states of matter or extremely hot and dense matter. It employs a schematic atomic structure in order to provide a fast and widely applicable plasma diagnosis tool. Each atomic level is represented only by its principal quantum number n. The atomic energy levels are computed from ionization potentials where the effect of the electronic continuum depression occurring in plasmas is taken into account by employing the model of Stewart and Pyatt [215]. The population kinetics model implemented in FLYCHK is based on rate equations including radiative and collisional transitions between bound states, photoionization, collisional ionization processes, Auger decay, electron capture, radiative recombination and three-body recombination. These rate equations are solved for a finite set of atomic levels which consists of ground states, single excited states ($n \leq 10$), autoionizing doubly excited states and inner shell excited states for all possible ionic stages.

With the model briefly described above, FLYCHK is able to determine ionization and level population distributions of a plasma (for some given conditions such as a given electron temperature and density). It can be applied for low-to-high Z ions under most conditions of laboratory plasmas, in either steady-state or time-dependent situations [95].

The plasma under consideration here is a cold dense plasma. Considering again the numerical example of isomer triggering of $^{93\text{m}}$Mo, the initial density of niobium ions is considered to be solid density and the initial electron temperature is several hundred eV. The result from FLYCHK shows that the time required to reach the steady state (with regard to the atomic processes) of such a plasma is on the order of several hundred fs. With the radius of the considered plasma of around 1.8 μm (according to the initial condition that the laser spot radius is around 1.8 μm), the characteristic time scale for the plasma expansion is on the order of 10 ps. Thus, the time scale for reaching the

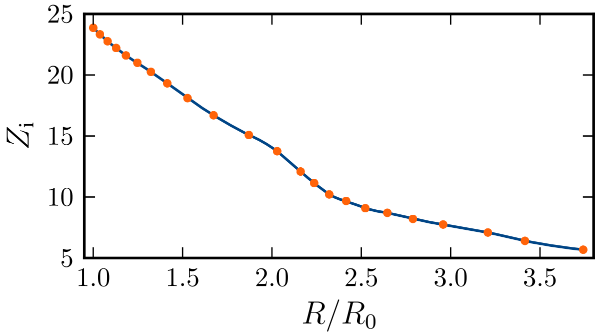

Figure 4.3: Steady-state average charge of niobium ions obtained from FLYCHK as a function of the plasma radius R (points) and its interpolation (solid line). We consider $n_{\mathrm{i},0} = 5.5 \times 10^{22}$ cm^{-3} and $T_{\mathrm{e},0} = 350$ eV.

steady state (with regard to the atomic processes) is much smaller than the time scale of expansion. Therefore, we can assume that the steady state with regard to the atomic processes establishes at each time instant during the expansion. As a first approximation, we can include the effects of atomic processes to the hydrodynamic expansion model by estimating the charge state of each time instant using FLYCHK.

According to Eq. (4.8) and to the ion density dynamics given by

$$n_{\mathrm{i}}(R) = n_{\mathrm{i},0} \left(\frac{R_0}{R} \right)^3 , \tag{4.13}$$

we may derive the dependence of the steady-state average charge $Z_{\mathrm{i}}(R)$ of the plasma on the plasma size R using FLYCHK. In the equation above, $n_{\mathrm{i},0}$ is the initial ion number density. Fig. 4.3 shows the average charge state of the ions for the case of $n_{\mathrm{i},0} = 5.5 \times 10^{22}$ cm^{-3} and $T_{\mathrm{e},0} = 350$ eV. The average charge state decreases with reducing temperature and ion density.

With the average charge state shown in Fig. 4.3 we can solve Eq. (4.10) in order to study the plasma expansion. The results are shown in Figs. 4.4, where the expansion velocity $v_{\mathrm{expn}} = \mathrm{d}R/\mathrm{d}t$ has been introduced. For comparison, the solution of Eq. (4.10) for the case where the charge state is fixed to $Z_{\mathrm{i}} \approx 23.86$ is also presented. We observe that the expansion velocity is smaller when the effects of atomic processes in plasmas are taken into account. This is because the average charge state, originally $Z_{\mathrm{i}} \approx 23.86$, decreases due to atomic processes with the plasma expansion. Thus, at larger times, the discrepancy between the two curves in Figs. 4.4 increases. We note however that the discrepancy remains small, on the level of 10%. Due to the plot scale, the discrepancy for T_{e} is less visible, although it is exactly following the relation (4.8) and it reaches the level of 10% at later times.

In order to ensure the self-consistency of our approximation (i.e., that the steady state with regard to the atomic processes establishes at each time instant during the expansion), a time-dependent FLYCHK calculation has also been performed, using the time-dependent T_{e} shown in Fig. 4.4(c), the time-dependent ion density given by Eq. (4.13)

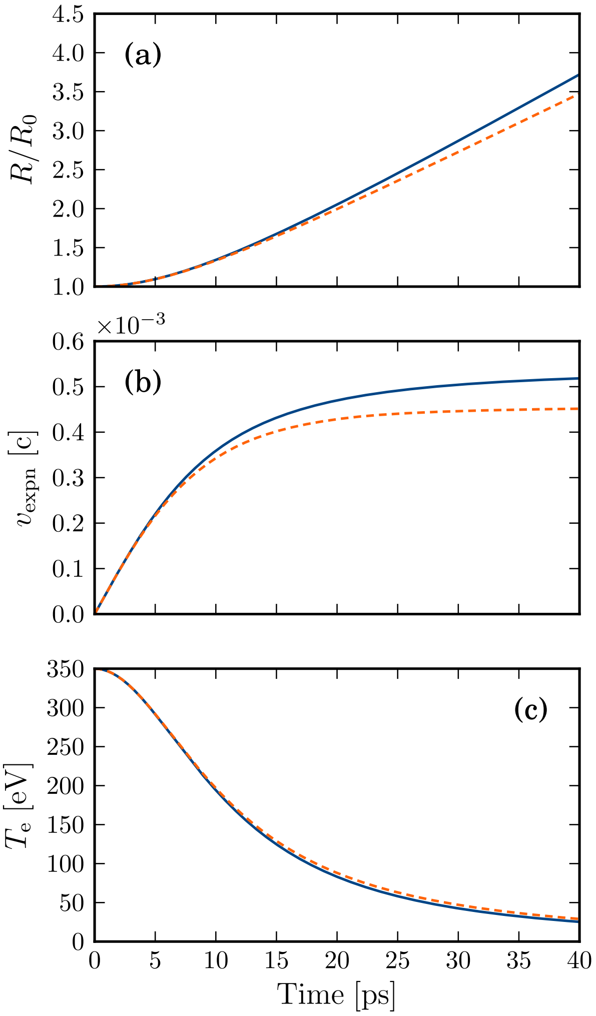

Figure 4.4: Plasma radius R (a), expansion velocity v_{expn} (b), and electron temperature T_{e} (c) as functions of the expansion time. We use the parameter set $n_{\mathrm{i},0} = 5.5 \times 10^{22}$ cm^{-3} (niobium ions) and $T_{\mathrm{e},0} = 350$ eV. Dashed orange curve denotes the result for the case where the steady-state average charge $Z_{\mathrm{i}}(R)$ provided by FLYCHK (and shown in Fig. 4.3) is employed in the calculations, i.e., the atomic processes effects are taken into account [210]. Solid green curve stands for the result for a fixed charge state $Z_{\mathrm{i}} \approx 23.86$.

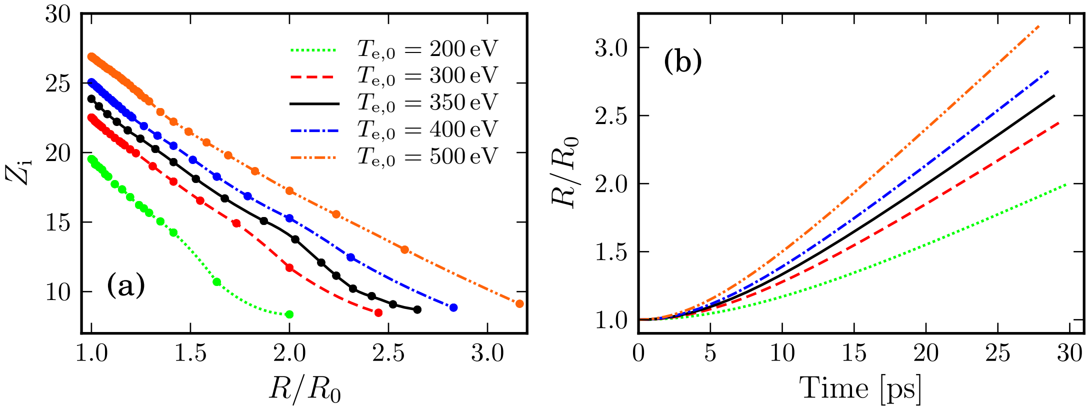

Figure 4.5: Steady-state average charge of niobium ions (points) obtained from FLYCHK (a), and plasma radius R as a function of the expansion time (b), for initial temperatures $T_{e,0}$ = 200 eV, $T_{e,0}$ = 300 eV, $T_{e,0}$ = 350 eV, $T_{e,0}$ = 400 eV, and $T_{e,0}$ = 500 eV [210]. Numerical interpolations are shown by the curves. We use $n_{i,0} = 5.5 \times 10^{22}$ cm^{-3}. The lowest charge state points correspond to cooling down the plasma to 50 eV electron temperature.

and $R(t)$ in Fig. 4.4(a) as input parameters. The results show that Z_i from the time-dependent FLYCHK calculation only slightly deviates ($\sim 5\%$) from the results in Fig. 4.3 for large R, while the results agree well for small R [210]. We conclude that on the degree of accuracy required for our calculations, the approximation used performs sufficiently well.

Further, we study the behavior of the average charge state and the plasma radius for several initial temperature values for both niobium (Figs. 4.5) and iron (Figs. 4.6) plasmas. Higher initial temperatures lead to higher charge states with a very similar qualitative behavior at later times in the expansion when the temperature decreases [210].

4.4.3 Total NEEC excitation

Due to the hydrodynamic expansion of the plasma, the electron temperature and density decrease with time during the plasma expansion leading to a time-dependent net NEEC rate. Fig. 4.7 presents the time dependence of λ_{neec} for several initial electron temperatures $T_{e,0}$. The ion density is always assumed to be at its solid-state value immediately after the plasma creation. As expected, λ_{neec} drops down to zero with time in all cases (i.e., with the plasma expansion) and takes larger values with increasing initial temperature.

The left column of Fig. 4.7 presents the NEEC reaction rates λ_{neec} for the case of ^{93m}Mo triggering. Comparing the orders of magnitude of λ_{neec} it can be seen that the NEEC excitation is strongly dependent on the initial plasma conditions dictated by the laser. Going from $T_{e,0}$ = 200 eV to $T_{e,0}$ = 500 eV enhances the NEEC excitation by approximately 7 orders of magnitude. The integration of λ_{neec} over time provides the

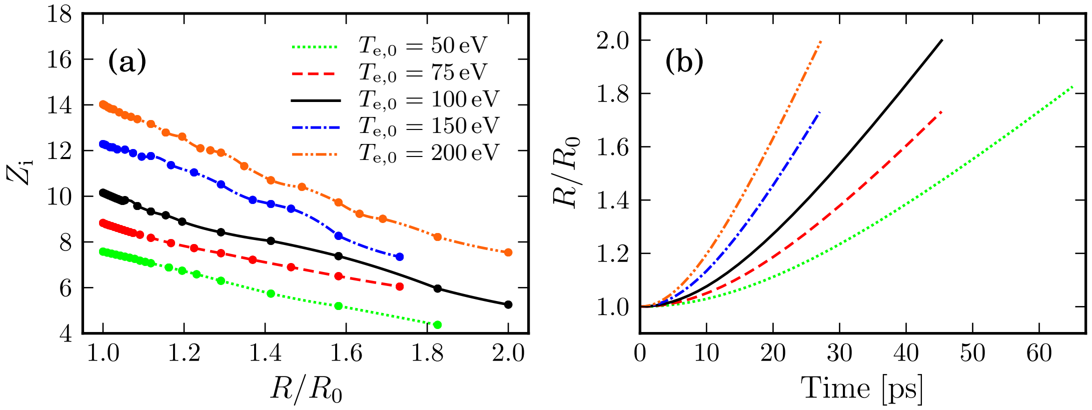

Figure 4.6: Steady-state average charge of iron ions (points) obtained from FLYCHK (a), and plasma radius R as a function of the expansion time (b), for initial temperatures $T_{e,0} = 50$ eV, $T_{e,0} = 75$ eV, $T_{e,0} = 100$ eV, $T_{e,0} = 150$ eV, and $T_{e,0} = 200$ eV [210]. Numerical interpolations are shown by the curves. The value $n_{i,0} = 8.5 \times 10^{22}$ cm^{-3} was used. The end points of the curves correspond to the electron temperature cooled down to 15 eV for $T_{e,0} = 50$ eV, 25 eV for $T_{e,0} = 75$ eV and $T_{e,0} = 100$ eV, and 50 eV for $T_{e,0} = 150$ eV and $T_{e,0} = 200$ eV, respectively.

excited state occupation number per nucleus (comparable to ρ_{ee}^{laser}),

$$\rho_{ee}^{\text{neec}} = \int_0^\infty dt\, \lambda_{\text{neec}} \, . \tag{4.14}$$

Performing the integration for the case of ^{93m}Mo results in $\rho_{ee}^{\text{neec}} \approx 1.8 \times 10^{-20}$ for $T_{e,0} = 200$ eV, $\rho_{ee}^{\text{neec}} \approx 1.4 \times 10^{-15}$ for $T_{e,0} = 350$ eV and $\rho_{ee}^{\text{neec}} \approx 1.6 \cdot 10^{-13}$ for $T_{e,0} = 500$ eV [210]. For all the three cases, the integration converged after approximately 6 ps. This value gives us the dominant NEEC interaction time during the hydrodynamic plasma expansion. We recall that in Ref. [207] the plasma conditions were considered constant for 100 ps. Our present results show that this is not the case and significant changes in the plasma affect the magnitude of the secondary nuclear excitation after already few ps.

We turn now to the NEEC reaction rates for ^{57}Fe presented in the right column of Fig. 4.7. While the relevant time scales are similar to the ones of ^{93m}Mo, on the order of 6 ps, the magnitude of the NEEC rates is in comparison tens of orders of magnitude below, and for all practical purposes negligible [210]. Let us investigate the reasons for such a dramatic difference. Iron has $Z = 26$ and correspondingly smaller binding energies than molybdenum ($Z = 43$), while at the same time the nuclear excitation energy is larger, 14.4 keV vs. 4.8 keV, respectively. The typical capture orbitals for both ions lie in the M atomic shell. Correspondingly, the continuum electron energies required for NEEC will be much larger for ^{57}Fe than for ^{93m}Mo. While the M-shell NEEC requires continuum electron energies between 3 and 4 keV, where the electron flux still has large values, in the case of ^{57}Fe the resonant continuum electrons should have more than 13 keV. For this energy value, the plasma at 75 eV temperature provides virtually no electrons at all, leading to the infinitesimal NEEC rate values in Fig. 4.7.

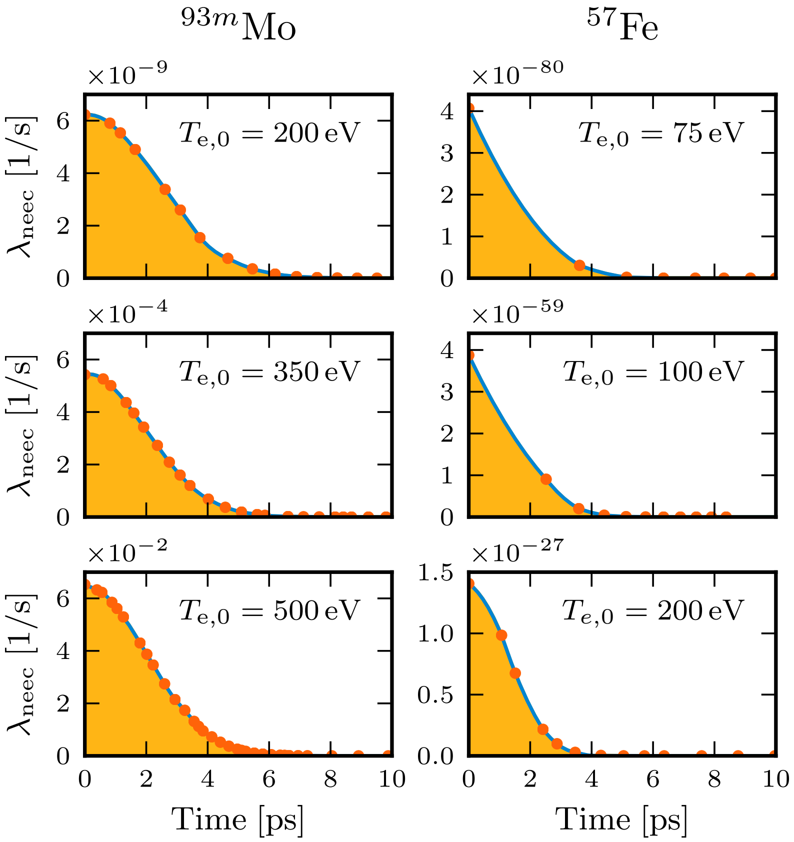

Figure 4.7: NEEC reaction rate as a function of time for $^{93\text{m}}$Mo (left graph column) and ^{57}Fe (right graph column). In the case of $^{93\text{m}}$Mo initial electron temperatures of 200 eV, 350 eV and 500 eV have been considered; for ^{57}Fe, the corresponding values are 75 eV, 100 eV and 200 eV, respectively [210].

4.5 Comparison between direct and secondary excitation

In order to obtain comparable results for $\rho_{\mathrm{ee}}^{\mathrm{laser}}$ and $\rho_{\mathrm{ee}}^{\mathrm{neec}}$ we fix the initial plasma conditions according to the chosen laser parameters. In particular, the laser intensity plays here an important role as outlined in Sec. 4.4.1. Restricting ourselves to the LCLS laser parameters, an initial electron temperature of $T_{\mathrm{e},0} = 350$ eV is estimated for the niobium target doped with $^{93\mathrm{m}}$Mo isomers. Comparing the corresponding excited state occupation numbers $\rho_{\mathrm{ee}}^{\mathrm{laser}}$ and $\rho_{\mathrm{ee}}^{\mathrm{neec}}$, we conclude that the indirect NEEC process is still about five orders of magnitude more efficient than the direct photoexcitation. One important aspect is here that the time of interaction is about 60 times longer for NEEC than for the direct photoexcitation. In contrast to $^{93\mathrm{m}}$Mo, the indirect NEEC process plays no role for the excitation of ^{57}Fe, since the NEEC reaction rate values are for all practical purposes negligible.

One important remark here is that the direct photoexcitation can be switched off by tuning the laser off resonance. In contrast, the secondary excitation remains present since the XFEL-produced plasma is not sensitive to small detunings. For instance, in the case of $^{93\mathrm{m}}$Mo the nuclear transition energy is only known up to an uncertainty of 80 eV. Since the XFEL bandwidths are several eV, this uncertainty can be a limiting factor for the experimental implementation of the direct photoexcitation channel. The secondary NEEC process occurs instead in the plasma environment with a rather broad electron distribution where many resonance channels can contribute. Hence, it is much more robust than photoexcitation against such uncertainties in the nuclear parameters. We also note that since the electron fluxes in the plasma are at the studied plasma temperatures several orders of magnitude larger than the corresponding photon fluxes, we neglect in our discussion the possible secondary nuclear photoexcitation process in the plasma. Other studies [82–86] on hot astrophysical plasmas show that this may change at higher, keV plasma temperatures. The study of NEEC in plasmas was so far restricted to astrophysical environments [82–85] or optical-laser-generated plasmas [87] where no equivalent of the direct photoexcitation channel under investigation here exists.

The values for $\rho_{\mathrm{ee}}^{\mathrm{neec}}$ are strongly dependent on the initial plasma conditions. Theoretically, the initial plasma conditions and in particular the electron temperature should be controllable by changing the laser intensity. Since $\rho_{\mathrm{ee}}^{\mathrm{neec}}$ grows exponentially with $T_{\mathrm{e},0}$ saturating for large $T_{\mathrm{e},0}$ in the considered temperature range and $T_{\mathrm{e},0}$ furthermore depends linearly on the laser intensity I between 10^{17} and 10^{18} W/cm^2, we expect for the considered parameter range an exponential dependence of the NEEC-induced excited state population $\rho_{\mathrm{ee}}^{\mathrm{neec}}$ on I. We note that for this estimate we consider the same initial size for the plasma, i.e., a constant laser focal spot. In contrast, the direct photoexcitation follows $\rho_{\mathrm{ee}}^{\mathrm{laser}} \propto I$. In addition, the XFEL intensity and consequently the plasma temperature can highly fluctuate from shot to shot. It is therefore reasonable to look at initial temperatures varying around the estimated value as it is realized in Fig. 4.7. For $^{93\mathrm{m}}$Mo, the indirect process is still on the same order of magnitude as the direct one for $T_{\mathrm{e},0} = 200$ eV. For an initial temperature of 500 eV the indirect NEEC process becomes even competitive with the photo-induced excitation via the coherent XFELO $\rho_{\mathrm{ee}}^{\mathrm{laser}} \approx 4.5 \times 10^{-14}$ although for the latter a 10 times longer pulse duration than for the LCLS has been considered. In the case of ^{57}Fe, the indirect excitation channel remains negligibly small in comparison to the direct process even by considering an initial electron temperature of 200 eV.

The reason why the nuclear excitation of $^{93\mathrm{m}}$Mo and ^{57}Fe behave inversely with respect to the direct and indirect excitations is two-fold. First, in the case of $^{93\mathrm{m}}$Mo triggering the microscopic NEEC cross section is much larger than the one for resonant photoexcitation, while the situation is reversed in the case of ^{57}Fe. The second and most important reason is related to the plasma conditions. In the case of resonant $^{93\mathrm{m}}$Mo triggering, the photoabsorption of the 4.85 keV photons by the niobium target ($\kappa = 551.6$ cm^2/g) is much stronger than the analog for 14.4 keV photons in iron ($\kappa = 63.0$ cm^2/g). Naturally, the more photons are absorbed, the more energy is initially deposited in the target leading to a higher initial electron temperature. Then for NEEC it is important that the available charge states in the plasma and the energy of the free electrons are not that far away from the resonance condition. While this is the case for $^{93\mathrm{m}}$Mo with a 4.85 keV nuclear transition energy, it is especially hard to realize in the limit of high nuclear transition energies like for ^{57}Fe.

Let us generalize our results based on the arguments presented above. A first insight into the relation between the resonant photoexcitation and microscopic NEEC cross sections can be gathered from the corresponding IC coefficients which are defined as the ratio between the IC and radiative decay rates. For high values of α_{ic} we expect NEEC to dominate over photoexcitation, which is typically the case for small nuclear transition energies in the keV region. Next, the prevailing initial free electron conditions are strongly dependent on the occurring x-ray atomic photoabsorption. The photoabsorption coefficient grows with increasing Z of the material and decreasing photon energy. Moreover, shell edges may lead to a stepwise enhancement of κ. However, a high electron temperature simultaneously leads to higher available charge states which again require smaller kinetic electron energies in order to fulfill the NEEC resonance condition. These opposite trends need to be balanced in order to match the available electron energies with the NEEC resonance condition for the open capture channels. Typically, in the temperature range of hundreds of eV the secondary excitation contributes significantly only for transition energies of few keV.

More concretely, in Table 4.3 we present the list of low-lying nuclear transitions first collected in Ref. [161] with the corresponding transition energy, multipolarity and IC coefficient α_{ic}. Also provided are the photoabsorption coefficient κ, the deepest ionization shell, an approximation of the initial plasma temperature $T_{\mathrm{e},0}$, the most probable charge state at this temperature Z_{i}, and finally the most NEEC-advantageous available capture shell in the plasma. The latter two quantities have been calculated with FLYCHK. For orientation, also the approximate ionization potential of the most advantageous available capture shell is presented. Since FLYCHK calculations are limited to the range $Z < 80$, the entries Z_{i} and the capture shell for $^{201}_{80}$Hg and $^{205}_{82}$Pb have been estimated by taking $Z = 79$. The initial temperatures in the table, with the exception of $^{93\mathrm{m}}$Mo and ^{57}Fe, discussed in detail in Sec. 4.4.1, have been obtained by accounting for the laser energy deposited into the sample with the help of mass photoabsorption coefficients [166]. Due to unavailable EOS tables, the averaged electron temperatures have been then roughly estimated by further considering energy conservation of the inner-shell photoionization and the first sequence of Auger decays.

Nuclide	E_n [keV]	$\mathcal{E}/\mathcal{M}L$	κ [cm^2/g]	ion. shell	$T_\mathrm{e,0}$ [eV]	Z_i	cap. shell	E_ion [keV]	α_ic
$^{201}_{80}$Hg	1.565	$\mathcal{M}1$	1975	N_1	670	43	N_4	0.378	3.5e+01
$^{193}_{78}$Pt	1.642	$\mathcal{M}1$	1628	N_1	510	40	N_3	0.519	1.2e+02
$^{205}_{82}$Pb	2.329	$\mathcal{E}2$	911	N_1	790	45	N_3	0.645	1.8e+07
$^{151}_{62}$Sm	4.821	$\mathcal{M}1$	362	M_1	740	42	M_3	1.420	6.2e+00
$^{93\mathrm{m}}_{42}$Mo	4.850	$\mathcal{E}2$	552	L_1	350	24	M_2	0.410	2.5e+04
$^{171}_{69}$Tm	5.036	$\mathcal{M}1$	442	M_1	850	46	M_4	1.515	1.6e+00
$^{83}_{37}$Rb	5.236	$\mathcal{M}1$	328	L_1	1080	32	L_1	2.065	7.5e+01
$^{181}_{73}$Ta	6.237	$\mathcal{E}1$	300	M_1	520	36	N_2	0.465	7.7e–01
$^{169}_{69}$Tm	8.410	$\mathcal{M}1$	118	M_1	630	43	M_5	1.468	1.7e–01
$^{187}_{76}$Os	9.756	$\mathcal{M}1$	107	M_1	510	37	N_3	0.468	4.8e–01
$^{167}_{69}$Tm	10.400	$\mathcal{M}1$	291	L_1	220	25	N_4	0.180	3.1e–02
$^{137}_{57}$La	10.590	$\mathcal{M}1$	166	L_1	580	37	M_3	1.123	3.7e–01
$^{134}_{55}$Cs	11.244	$\mathcal{M}1$	129	L_1	1420	43	L_3	5.012	1.2e+00
$^{73}_{32}$Ge	13.285	$\mathcal{E}2$	124	K	220	18	L_3	1.217	4.1e+02
$^{57}_{26}$Fe	14.413	$\mathcal{M}1$	63	K	75	12	M_1	0.093	1.0e–01
$^{149}_{62}$Sm	22.507	$\mathcal{M}1$	28	L_1	350	28	M_5	1.080	3.1e–03
$^{119}_{50}$Sn	23.871	$\mathcal{M}1$	12	L_1	120	14	N_2	0.089	1.1e–02

Table 4.3: Low-lying nuclear transitions suitable for resonant photoexcitation via XFELs. Transition energies E_n and multipolarities $\mathcal{E}/\mathcal{M}L$, photoabsorption coefficients κ, deepest ionization subshells, estimates of the initial plasma temperature $T_\mathrm{e,0}$, the most probable charge states Z_i in the plasma, the most advantageous capture orbitals for NEEC available in the plasma together with the corresponding ionization energies E_ion and IC coefficients α_ic are presented in the columns. The list is sorted by increasing nuclear transition energies E_n.

Based on the present analysis, we conclude that isotopes with high nuclear transition energies like ${}^{57}_{26}$Fe, ${}^{149}_{62}$Sm and ${}^{119}_{50}$Sn, which in addition only allow for NEEC into the M or even higher shells, will not present significant secondary nuclear excitation in the XFEL-produced plasma [210]. Nuclei with small transition energies as it is the case for the first table entries down to ${}^{83}_{37}$Rb are very likely to present significant secondary nuclear excitation in the plasma, due to the abundant electron flux at the required energies and the encouraging IC coefficient. As for the intermediate region with 6 keV$< E_{\mathrm{n}} <$13 keV, here a more careful analysis is required. The capture into L-shell orbitals in the case of ${}^{134}_{55}$Cs and ${}^{73}_{32}$Ge speaks for more available free electrons in the plasma at the resonance energy. However, due to the low Z of germanium, it is likely that only in the case of ${}^{134}_{55}$Cs secondary NEEC plays a role in the net nuclear excitation. In the cases of ${}^{169}_{69}$Tm, ${}^{187}_{76}$Os, ${}^{167}_{69}$Tm and ${}^{137}_{57}$La, the rather large transition energies, together with high capture orbitals into the M- or N-shell and the small IC coefficients indicate unlikely strong NEEC influence. Finally, the small IC coefficient in the case of ${}^{181}_{73}$Ta also rather speaks against strong secondary NEEC. However, since the arguments above do not relate to the time scale difference between NEEC and photoexcitation and the unavoidable detuning for the photoexcitation channel, we conclude that dedicated simulations are required to draw solid conclusions for the nuclei in the intermediate energy region.

Part II

Single x-rays controlled by nuclear transitions

Chapter 5

Nuclear forward scattering

In 1958, Rudolf Mössbauer discovered that nuclear transitions inside solids can occur by recoilless absorption and reemission [101,102,216]. This became known as the Mössbauer effect. The detection of recoil-free nuclear fluorescence opened the possibility to measure nuclear energy spectra with a very high precision, a technique soon known as Mössbauer spectroscopy. Since γ-rays have typically very narrow line widths in comparison to their energies, the resonant scattering is very sensitive to tiny energy changes which may reveal information about the environment surrounding the nuclei. In this manner Mössbauer spectroscopy has for instance been applied to measure isomeric shifts, quadrupole and hyperfine splittings, and is widely used in nuclear physics, solid-state physics, chemistry and biophysics.

In the beginning, Mössbauer spectroscopy was limited to γ-ray sources composed of the radioactive parent nuclei corresponding to the species under investigation. The decay of the parent nuclei produced resonant photons applicable to nuclear resonance spectroscopy, but with a very low photon emission rate. This limitation could however be overcome by the development of synchrotron light sources in the 1970s. The idea to employ the brilliant and frequency-tunable synchrotron radiation (SR) for Mössbauer spectroscopy [217–219] advanced enormously the investigation of the light-nucleus interaction which eventually led to the development of nuclear forward scattering (NFS) [103,157,220–222].

The usage of broadband synchrotron pulses in NFS experiments, first demonstrated in 1985 [223], opens the possibility to detect the pure nuclear fluorescence not only in dependence of frequency but also in dependence of time [224]. This idea relies on two key features: (i) in contrast to conventional Mössbauer γ-ray sources, SR pulses have a very short pulse duration ($\sim$ ps) which can be considered to behave δ-like in time in comparison to the nuclear response ($\sim$ ns); (ii) the lifetime τ of a nuclear excited state is typically much longer than the time scale of any other process contributing to the scattered radiation field like for instance the electronic background. Combining these two properties it is possible to measure the time spectrum of the pure nuclear response of the target simply by time gating.

A typical NFS setup is shown in Fig. 5.1(a) where the SR pulse impinges in normal incidence on a nuclear solid-state sample and the scattered intensity is recorded in the forward direction. Like the name "nuclear forward scattering" promises, the forward direction plays a special role in the scattering process. Since the time scales of the nuclear excitation by the SR pulse and the subsequent decay are so much different, the scattering can be described as two independent processes, the formation of the excited state and

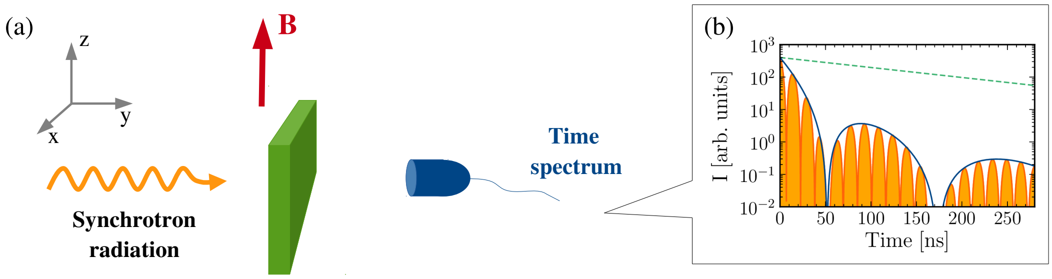

Figure 5.1: NFS setup (a) and characteristic NFS time spectrum (b). Synchrotron radiation impinges perpendicular on a nuclear target resonantly interacting with some nuclear Mössbauer species. The scattered field is detected in the forward direction (a). The magnetic field splits the nuclear states in the corresponding Zeeman sublevels, resulting in the characteristic NFS time spectrum (b) with the quantum beat pattern (orange curve) modulated by a so-called dynamical beat (blue curve). The nuclear decay is collectively enhanced in comparison to the exponential behavior of a single nucleus (green dashed curve).

the subsequent γ-ray emission [103]. Due to the typically narrow nuclear line width and the low degeneracy of the SR, it can be safely assumed that each pulse contains maximally one resonant photon such that at most one nucleus can be excited. If the photon is absorbed recoillessly by a nuclear Mössbauer transition, it will be impossible to distinguish which nucleus has been excited. In this way a collective, delocalized excitation is created, called nuclear exciton [103, 221]. It can be written as a superposition of single excited states $|g, e_j\rangle$, where the j^{th} nucleus is excited and all others remain in the ground state [104, 225, 226]:

$$|E\rangle = \frac{1}{\sqrt{N}} \sum_{j=1}^{N} \mathrm{e}^{\mathrm{i}\boldsymbol{k}\boldsymbol{r}_j} |g, e_j\rangle \ . \tag{5.1}$$

Here, the wave vector of the incident radiation is denoted by $\boldsymbol{k}$, $\boldsymbol{r}_j$ is the position of the j^{th} nucleus and N the number of contributing nuclei.

Applying the Weisskopf-Wigner theory of spontaneous decay [4] it can be shown that the nuclear exciton preferably decays by the emission of a photon into the forward direction along $\boldsymbol{k}$ [225–227], provided the final state remains indistinguishable from the initial one. This requires that the photon is absorbed and re-emitted recoillessly and that neither a nuclear spin flip nor internal conversion occur. Furthermore, the collective excitation defined in Eq. (5.1) is spatially coherent leading to an increased radiative transition width [103]. For instance, the ratio between internal conversion (IC) and radiative decay of the first excited state of an isolated ^{57}Fe nucleus is $\Gamma_{\text{IC}}/\Gamma_{\text{rad}} \approx 8$, implying that IC is 8 times more probable than spontaneous emission. The formation of a spatially coherent, delocalized excitation in a nuclear ensemble may change this ratio drastically such that radiative decay dominates IC in the forward direction. Accordingly, in comparison to the exponential decay of an isolated nucleus, we expect to see a speed-up of the spontaneous decay in NFS.

In Fig. 5.1(b) a typical time spectrum of NFS is shown. It is completely different from a simple exponential decay like it is expected for an isolated, resonant absorber [green dashed curve in Fig. 5.1(b)]. Actually, this kind of time spectrum is characteristic for NFS and therefore, it is important to understand the peculiar features imprinted by the nuclear ensemble: the so-called dynamical and quantum beats [103]. The dynamical beat is illustrated by the blue curve in Fig. 5.1(b). It is caused by multiple scattering events where the resonant photon is absorbed and re-emitted several times inside the target by a single nuclear transition. Therefore, it is essential that the decay into the forward direction preserves the photon energy. The temporal behavior of the dynamical beat can be represented by the product of a Bessel function of first kind J_1 and an exponential decay [174, 228]

$$\left(\frac{\xi}{\sqrt{\xi\Gamma_0 t}} J_1\left(2\sqrt{\xi\Gamma_0 t}\right)\right)^2 \mathrm{e}^{-\Gamma_0 t} , \tag{5.2}$$

where Γ_0 represents the natural width of the nuclear excited state and ξ is the effective resonant thickness of the nuclear sample. The derivation of Eq. (5.2) will be given in the next Section. The effective thickness is proportional to the number of nuclei contributing to the resonant nuclear scattering ($\xi \propto N_0$). For small times ($\xi\Gamma_0 t < 1$) Eq. (5.2) can be approximated by

$$\mathrm{e}^{-(\xi+1)\Gamma_0 t} \tag{5.3}$$

which represents an exponential decay with enhanced decay constant $(\xi + 1)\Gamma_0$. The enhancement of the decay is proportional to ξ and hence proportional to the number of participating nuclear scatterers which shows that the already mentioned speed-up of the spontaneous decay is a collective effect. In Chap. 2, this speed-up of the spontaneous decay has already been introduced as the collective nuclear decay rate.

The second characteristic pattern of the time spectrum, the quantum beat, is caused by a magnetic field (either external or internal) at the nuclear target. This B-field produces hyperfine interactions which lead to a splitting of the nuclear states into their Zeeman sublevels. Due to the broadband nature of the SR it is possible to drive more than one hyperfine transition simultaneously. The interference of these transitions with different frequencies subsequently leads to a beating pattern in the time spectrum, e.g., the quantum beat. The full spectrum with dynamical and quantum beats is illustrated by the orange curve in Fig. 5.1(b).

This Chapter is devoted to the theoretical treatment of NFS. Therefore, we are going to leave the simple picture of the nuclear exciton formation with subsequent decay and rather describe NFS as a real scattering problem. There are a number of theoretical approaches to treat the pulse propagation through a resonant medium. Solutions founded on Maxwell's equations use a complex space- and time-dependent polarizability to describe the nuclear medium. Based on such a model, Kagan and Afanas'ev derived the first time-dependent theory of NFS with synchrotron light [229]. At the same time, Hannon and Trammel developed a description of NFS based on Green's function techniques of quantum electrodynamics as it is applied in the quantum theory of crystal optics [230, 231]. Comprehensive reviews can be found in Refs. [221] and [103], respectively. Since then, both models have been extensively used to analyze experimental data on NFS where insights into advanced geometries with complicated interactions could be gained. Meanwhile, there is furthermore an approach applying Heitler's quantum theory of radiation to NFS setups with SR [232, 233].

The approach we are using follows Refs. [174, 228, 234] where Maxwell's equations are directly solved in time and space. This kind of treatment allows us to easily incorporate time-dependent interactions like timed rotations of the magnetic field. Actually, Ref. [174] provides a general way of solving the problem of NFS in terms of a semiclassical description, applicable to arbitrary time-dependent interactions. Here, we rather present a reduced version of the model introduced in Ref. [174], adapted to our purposes. In Sec. 5.1, first the wave equation for the coherent propagation of the x-ray pulse through the resonant medium is derived. Its solution requires the light-induced macroscopic current density to be expressed in terms of transition amplitudes between single-particle states which is the topic of Sec. 5.2. Sec. 5.3 is then devoted to the general solution of the wave equation. Afterwards in Secs. 5.4, 5.5 and 5.6, explicit time-dependent hyperfine interactions are discussed. Atomic units $\hbar = m_\mathrm{e} = e = 4\pi\varepsilon_0 = 1$ are used throughout this Chapter.

5.1 Wave equation

In order to set up a wave equation to describe NFS, let us again consider the typical setup shown in Fig. 5.1(a). The target surface lies in the x-z plane perpendicular to the y-direction, an external magnetic field points along the z-direction and determines the quantization axis of the system. The incident radiation propagates along the y-axis, hits the nuclear sample at $y = 0$ and can be described as a plane wave modulated in time,

$$\boldsymbol{\mathcal{E}}_\mathrm{in}(\boldsymbol{r}, t) = \boldsymbol{E}_\mathrm{in}(t)\mathrm{e}^{\mathrm{i}(\boldsymbol{kr}-\omega t)} , \tag{5.4}$$

where $\boldsymbol{k}$ is the wave vector and ω the carrier frequency of the incoming field. We are interested in the scattered intensity behind the target in the forward direction.

We describe the coherent nuclear scattering process with a semiclassical approach where the electromagnetic field is considered to behave classically whereas the nuclear system is treated quantum mechanically. In order to facilitate the treatment of time-dependent hyperfine interactions later, it is natural to solve the scattering problem directly in space and time based on Refs. [174, 228, 234]. Accordingly, the coherent propagation of the electromagnetic field through the resonant medium is thereby described by Maxwell's equation

$$\left(\nabla^2 - \frac{1}{c^2}\frac{\partial^2}{\partial t^2}\right)\boldsymbol{\mathcal{E}}(\boldsymbol{r}, t) = \frac{4\pi}{c^2}\frac{\partial}{\partial t}\boldsymbol{\mathcal{J}}(\boldsymbol{r}, t) , \tag{5.5}$$

where $\boldsymbol{\mathcal{J}}(\boldsymbol{r}, t)$ denotes the macroscopic current density induced by the incident radiation.

The electromagnetic field $\boldsymbol{\mathcal{E}}(\boldsymbol{r}, t)$ inside the nuclear target and the macroscopic current density $\boldsymbol{\mathcal{J}}(\boldsymbol{r}, t)$ can be written in the same form as the incident radiation $\boldsymbol{\mathcal{E}}_\mathrm{in}(\boldsymbol{r}, t)$, namely

$$\boldsymbol{\mathcal{E}}(\boldsymbol{r}, t) = \boldsymbol{E}(y, t)\mathrm{e}^{\mathrm{i}(\boldsymbol{kr}-\omega t)} , \tag{5.6}$$

$$\boldsymbol{\mathcal{J}}(\boldsymbol{r}, t) = \boldsymbol{J}(y, t)\mathrm{e}^{\mathrm{i}(\boldsymbol{kr}-\omega t)} . \tag{5.7}$$

The amplitudes $\boldsymbol{E}(y,t)$ and $\boldsymbol{J}(y,t)$ only depend on the spatial coordinate y because absorption as well as refraction occur along the propagation direction. Since $\boldsymbol{E}(y,t)$ and $\boldsymbol{J}(y,t)$ furthermore change only slowly in time in comparison to the exponent, the so-called slowly-varying amplitude approximation can be applied, reducing Maxwell's equation to

$$\frac{\partial}{\partial y}\boldsymbol{E}(y,t) = -\frac{2\pi}{c}\boldsymbol{J}(y,t) \tag{5.8}$$

with boundary condition

$$\boldsymbol{E}(0,t) = \boldsymbol{E}_{\mathrm{in}}(t) \ . \tag{5.9}$$

Once we have solved Eq. (5.8), the forward scattered intensity spectrum behind the target is given by

$$I(t) = |\boldsymbol{E}(L,t)|^2 \ , \tag{5.10}$$

where L denotes the thickness of the nuclear sample. In order to find a solution for Eq. (5.8), it is first necessary to derive an explicit expression for the macroscopic nuclear current density $\boldsymbol{J}(y,t)$.

5.2 Nuclear current density

The macroscopic nuclear current density $\boldsymbol{\mathcal{J}}(\boldsymbol{r},t)$ can be written as a sum over all individual nuclear current densities which are usually written down in momentum space,

$$\boldsymbol{\mathcal{J}}(\boldsymbol{r},t) = \int \frac{\mathrm{d}^3\boldsymbol{k}'}{(2\pi)^3}\,\mathrm{e}^{\mathrm{i}\boldsymbol{k}'\boldsymbol{r}}\sum_\alpha \langle\psi_\alpha(t)|\boldsymbol{j}(\boldsymbol{k}')|\psi_\alpha(t)\rangle \mathrm{e}^{-\mathrm{i}\boldsymbol{k}'\boldsymbol{r}_\alpha} \ , \tag{5.11}$$

where $\boldsymbol{r}_\alpha$ represents the position of nucleus α, $|\psi_\alpha(t)\rangle$ stands for the time dependent nuclear wave function and $\boldsymbol{j}(\boldsymbol{k}')$ is the momentum representation of the operator for the current density of a single nucleus in the Schrödinger picture.

In order to evaluate the matrix element of the nuclear current density operator, we first need to define the Hamiltonian for an individual nucleus. Since we consider resonant light-nucleus interactions of energetically well separated nuclear transitions, each nucleus can be represented as a two level system with transition energy $\omega_0 = E_{\mathrm{e}} - E_{\mathrm{g}}$ and a natural line width Γ_0. In addition, the ground and excited states are characterized by their total spin quantum number $\boldsymbol{I}_\lambda$ with projections M_λ and magnetic moments $\boldsymbol{\mu}_\lambda$ ($\lambda \in \{g,e\}$). The general Hamiltonian is given by

$$H = H_0 + H_{\mathrm{hf}}(t) + H_\gamma(t) \ . \tag{5.12}$$

Here, H_0 represents the unperturbed nuclear Hamiltonian determined by

$$H_0 = \Big(E_\lambda - \mathrm{i}\frac{\Gamma_0}{2}\delta_{\lambda,e}\Big)|I_\lambda M_\lambda\rangle\langle I_\lambda M_\lambda| \ , \tag{5.13}$$

where $\delta_{\lambda,e}$ represents the Kronecker delta which is one only for $\lambda = e$ and otherwise zero. The hyperfine interactions $H_{\mathrm{hf}}(t)$ can be time dependent. An explicit form of $H_{\mathrm{hf}}(t)$ is given later in Secs. 5.4, 5.5 and 5.6 when the special cases of the considered hyperfine interactions are discussed. Here, we first discuss the problem for a general $H_{\mathrm{hf}}(t)$.

The Hamiltonian $H_\gamma(t)$ describes the light-nucleus interaction and is given in Eq. (2.2). Here, it is important that Eq. (2.2) can be rewritten such that we obtain [235, 236]

$$H_\gamma(t) = \frac{\mathrm{i}}{\omega}\boldsymbol{j}^\dagger(\boldsymbol{k})\boldsymbol{E}(y_\alpha, t)\mathrm{e}^{\mathrm{i}(\boldsymbol{k}\boldsymbol{r}_\alpha - \omega t)} \ . \tag{5.14}$$

In the derivation of this expression the Coulomb gauge, the special form of the electromagnetic field given in Eq. (5.6) and the slowly varying amplitude approximation were employed.

The time-dependent matrix element $\langle\psi_\alpha(t)|\boldsymbol{j}(\boldsymbol{k})|\psi_\alpha(t)\rangle$ occurring in Eq. (5.11) can be written as

$$\langle\psi_\alpha(t)|\boldsymbol{j}(\boldsymbol{k}')|\psi_\alpha(t)\rangle = \langle I_\mathrm{g}M_\mathrm{g}|U^\dagger(t,-\infty)\boldsymbol{j}(\boldsymbol{k}')U(t,-\infty)|I_\mathrm{g}M_\mathrm{g}\rangle \ , \tag{5.15}$$

where the system was assumed to be in the ground state with specific spin I_g and spin projection quantum number M_g at time $t = -\infty$. The time evolution operator $U(t, t')$ is defined by

$$U(t, t') = T\exp\left(-\mathrm{i}\int_{t'}^{t}\mathrm{d}t'\,(H_0 + H_\mathrm{hf}(t'))\right) \ , \tag{5.16}$$

with T being the so-called time ordering operator. Since the light-nucleus interaction can be assumed to be weak ($H_\gamma \ll H_0 + H_\mathrm{hf}$), it is possible to apply perturbation theory for calculating $\langle\psi_\alpha(t)|\boldsymbol{j}(\boldsymbol{k})|\psi_\alpha(t)\rangle$. The detailed derivation is presented in App. C. An important remark is that resonant scattering is always a second order process because the resonant photon absorption is followed by a reemission process.

In the calculation of the macroscopic nuclear current density $\boldsymbol{\mathcal{J}}(\boldsymbol{r}, t)$ (see App. C) an important step is the assumption of a macroscopic nuclear ensemble. This assumption allows us to exploit the following relation

$$\sum_\alpha \mathrm{e}^{\mathrm{i}(\boldsymbol{k}-\boldsymbol{k}')\boldsymbol{r}_\alpha} = (2\pi)^3 n_0 \delta(\boldsymbol{k} - \boldsymbol{k}') \ , \tag{5.17}$$

where n_0 is the number of resonant nuclei per unit volume. Accordingly, the interplay of all individual nuclei contributing to the scattering process determines the directionality of NFS. If the number of contributing nuclear scatterers is macroscopic, the angular dependence of the scattering is proportional to the delta function $\delta(\boldsymbol{k} - \boldsymbol{k}')$, leading to nuclear forward scattering.

Using the derived expression for the macroscopic current density $\boldsymbol{\mathcal{J}}(\boldsymbol{r}, t)$ it is possible to express the wave equation of NFS in terms of individual nuclear current densities (see App. C), namely

$$\frac{\partial}{\partial y}\boldsymbol{E}(y, t) = -\sum_\ell K_\ell \boldsymbol{J}_\ell(\boldsymbol{k}, t)\int_{-\infty}^{t}\mathrm{d}t'\,\boldsymbol{J}_\ell^*(\boldsymbol{k}, t')\cdot\boldsymbol{E}(y, t') \ . \tag{5.18}$$

The occurring matrix elements $\boldsymbol{J}_\ell^*$ and $\boldsymbol{J}_\ell$ describe the nuclear excitation and de-excitation, respectively. They are defined by

$$\begin{aligned} \boldsymbol{J}_\ell^*(\boldsymbol{k}, t) &= \langle\psi_{I_\mathrm{e}M_\mathrm{e}}(t)|\boldsymbol{j}^\dagger(\boldsymbol{k})|\psi_{I_\mathrm{g}M_\mathrm{g}}(t)\rangle\mathrm{e}^{-\mathrm{i}\omega_0 t} \ , \\ \boldsymbol{J}_\ell(\boldsymbol{k}, t) &= \langle\psi_{I_\mathrm{g}M_\mathrm{g}}(t)|\boldsymbol{j}(\boldsymbol{k})|\psi_{I_\mathrm{e}M_\mathrm{e}}(t)\rangle\mathrm{e}^{\mathrm{i}\omega_0 t} \ , \end{aligned} \tag{5.19}$$

where $|\psi_{I_\lambda M_\lambda}(t)\rangle$ $(\lambda = g, e)$ are the time dependent eigenstates of the nuclear spin operators $\boldsymbol{I}_\lambda$. Note that ℓ is a multi-index standing for the projection quantum numbers M_g and M_e.

Now, let us have a closer look on Eq. (5.18). Under the integral sign on the RHS the scalar product $\boldsymbol{J}_\ell^*(\boldsymbol{k}, t') \cdot \boldsymbol{E}(y, t')$ appears. It describes a nuclear excitation at time t' induced by the electromagnetic field $\boldsymbol{E}$. This nuclear excitation subsequently decays via the emission of a photon at time t which is represented by $\boldsymbol{J}_\ell(\boldsymbol{k}, t)$ in front of the integral. Moreover, since it is a priori not known when the nuclear activation takes place, the excitation process needs to be integrated over all possible excitation times, hence, from $-\infty$ to t. The summation over ℓ comes from the fact that all allowed transitions need to be taken into account for the wave propagation. For instance, when several transitions with different frequencies are driven at once, the summation over ℓ results in the already mentioned quantum beat pattern. Furthermore, the weight coefficients K_ℓ appearing in Eq. (5.18) are given by

$$K_\ell = \frac{2\pi n_0}{kc^2(2I_\mathrm{g} + 1)} f_\mathrm{LM}(\boldsymbol{k}) \ , \tag{5.20}$$

where f_LM is the Lamb-Mössbauer factor describing the probability of a recoilless absorption and k denotes the absolute value of the wave vector $\boldsymbol{k}$.

The wave equation (5.18) describes the coherent propagation of an electromagnetic field due to NFS under time-dependent hyperfine interactions. Because of the collective interplay between many nuclear scatterers, the nuclear scattering process exhibits a high directionality into the forward direction. Eq. (5.18) predicts the forward scattered response. The appearance of the characteristic NFS beat pattern, the dynamical and quantum beats, is treated in more detail in the next Sections. There, we first present a general solution of Eq. (5.18). This solution is then afterwards applied to the special cases of static hyperfine interactions, instantaneous B-field rotations and prompt deactivation and activation of the magnetic field, which represent the basic tools for our control schemes of hard x-rays discussed in Chaps. 6, 7 and 8.

5.3 General solution

In order to solve Eq. (5.18) it is helpful to introduce dimensionless space and time variables ξ and τ, respectively. They are defined by

$$\begin{aligned} \xi &= \frac{1}{4}\sigma_\mathrm{R} n_0 y \ , \\ \tau &= \Gamma_0 t \ , \end{aligned} \tag{5.21}$$

where σ_R is the total nuclear cross section of resonant absorption and Γ_0 the full natural transition width. For the special case of $y = L$, the spatial variable ξ is also known as effective thickness of the resonant scattering as it was introduced in the beginning of this Chapter. Using these definitions and after rescaling the nuclear transition currents $\boldsymbol{J}_\ell^*$

and $\boldsymbol{J}_\ell$ according to

$$\begin{aligned}\boldsymbol{J}_\ell^* &\mapsto \left[\frac{f_{\mathrm{LM}}(\boldsymbol{k})(1+\alpha_{\mathrm{ic}})4\omega}{(2I_{\mathrm{e}}+1)c^3\Gamma_0}\right]^{1/2} \boldsymbol{J}_\ell^* \ , \\ \boldsymbol{J}_\ell &\mapsto \left[\frac{f_{\mathrm{LM}}(\boldsymbol{k})(1+\alpha_{\mathrm{ic}})4\omega}{(2I_{\mathrm{e}}+1)c^3\Gamma_0}\right]^{1/2} \boldsymbol{J}_\ell \ ,\end{aligned} \tag{5.22}$$

the wave equation reduces to

$$\frac{\partial}{\partial\xi}\boldsymbol{E}(\xi,\tau) = -\sum_\ell \boldsymbol{J}_\ell(\boldsymbol{k},\tau)\int_{-\infty}^{\tau} \mathrm{d}\tau'\, \boldsymbol{J}_\ell^*(\boldsymbol{k},\tau')\cdot\boldsymbol{E}(\xi,\tau') \ . \tag{5.23}$$

This equation is similar to a Schrödinger equation where time is replaced by the effective thickness ξ. Analogously to perturbation theory it is possible to represent the solution of Eq. (5.23) as a power series in ξ,

$$\boldsymbol{E}(\xi,\tau) = \sum_{p=0}^{\infty}\boldsymbol{E}^{(p)}(\xi,\tau) = \sum_{p=0}^{\infty}\frac{(-\xi)^p}{p!}\boldsymbol{E}^{(p)}(\tau) \ . \tag{5.24}$$

The term $p=0$ represents the boundary condition given in Eq. (5.9) and reads

$$\boldsymbol{E}^{(0)}(\xi,\tau) = \boldsymbol{E}_{\mathrm{in}}(\tau) \ . \tag{5.25}$$

Accordingly, the 0^{th} order scattering experiences no resonant interaction because it leaves the nuclear target unperturbed. For this reason, $\boldsymbol{E}^{(0)}$ must be independent of the effective thickness ξ.

All higher order terms are obtained from power matching in ξ by inserting Eq. (5.24) into the wave equation. It turns out (see App. C) that the p^{th} order scattering fulfills Eq. (5.23), where $\boldsymbol{E}$ on the RHS is replaced by the $(p-1)^{\mathrm{th}}$ order term $\boldsymbol{E}^{(p-1)}$,

$$\frac{\partial}{\partial\xi}\boldsymbol{E}^{(p)}(\xi,\tau) = -\sum_\ell \boldsymbol{J}_\ell(\boldsymbol{k},\tau)\int_{-\infty}^{\tau} \mathrm{d}\tau'\, \boldsymbol{J}_\ell^*(\boldsymbol{k},\tau')\cdot\boldsymbol{E}^{(p-1)}(\xi,\tau') \ . \tag{5.26}$$

By using the explicit ξ-dependence of $\boldsymbol{E}^{(p)}(\xi,\tau)$ given in Eq. (5.24), the following recursion relation is obtained

$$\boldsymbol{E}^{(p)}(\tau) = \sum_\ell \boldsymbol{J}_\ell(\boldsymbol{k},\tau)\int_{-\infty}^{\tau} \mathrm{d}\tau'\, \boldsymbol{J}_\ell^*(\boldsymbol{k},\tau')\cdot\boldsymbol{E}^{(p-1)}(\tau') \ . \tag{5.27}$$

This equation shows that the order p indicates the number of scattering events which occur inside the nuclear sample. For instance, $\boldsymbol{E}^{(1)}$ represents the single scattering solution with only one resonant absorption and reemission. Due to this interpretation the terms $\boldsymbol{E}^{(p)}$ are often referred as multiple scattering amplitudes.

Since the first order is in most cases the dominating scattering contribution (in particular for thin samples or in general for small interaction times), it is useful to write down the explicit form of $\boldsymbol{E}^{(1)}$:

$$\begin{aligned}\boldsymbol{E}^{(1)}(\tau) &= \sum_\ell \boldsymbol{J}_\ell(\boldsymbol{k},\tau)\int_{-\infty}^{\tau} \mathrm{d}\tau'\, \boldsymbol{J}_\ell^*(\boldsymbol{k},\tau')\cdot\boldsymbol{E}^{(0)}(\tau') \\ &= \sum_\ell \boldsymbol{J}_\ell(\boldsymbol{k},\tau)\left(\boldsymbol{J}_\ell^*(\boldsymbol{k},0)\cdot\boldsymbol{e}_{\mathrm{p}}\right) \ .\end{aligned} \tag{5.28}$$

In the second line the incident radiation was assumed to be a SR pulse with polarization $\boldsymbol{e}_\mathrm{p}$ which can be represented as δ-distribution in time,

$$\boldsymbol{E}_\mathrm{in}(\tau) = \boldsymbol{e}_\mathrm{p}\delta(\tau) \ . \tag{5.29}$$

This δ-like pulse eliminates the integration over τ' in Eq. (5.28) and fixes the time of the initial nuclear excitation to $\tau' = 0$.

In general the integrals occurring in the recursion relation (5.27) cannot be solved analytically and require a numerical treatment. Note that for most situations the number of scattering orders taken into account can be limited by some p_max. However, if there is only a single resonance seen by the incident pulse (e.g. no hyperfine splitting), it will be possible to obtain an analytic solution as shown in the next Section.

5.4 Static hyperfine interactions

In the case of static hyperfine interactions the Hamiltonian H_hf can be written as

$$H_\mathrm{hf} = -\frac{\mu_\lambda}{I_\lambda}\boldsymbol{I}_\lambda \cdot \boldsymbol{B} \ , \tag{5.30}$$

where $\boldsymbol{I}_\lambda$ is the nuclear spin operator, I_λ its eigenvalue and $\boldsymbol{B}$ denotes the magnetic field at the nucleus. In the following it is assumed that the magnetic field points along the z-direction, $\boldsymbol{B} = B_0\boldsymbol{e}_z$. Moreover, we introduce the factor $\epsilon_\lambda = \mu_\lambda B_0/I_\lambda$ standing for the energy splitting caused by the hyperfine interactions.

In the case of a static magnetic field it is possible to express the time-dependent nuclear transition currents $\boldsymbol{J}^*_\ell$ and $\boldsymbol{J}_\ell$ in terms of the time-independent matrix elements of the current density operator $\langle I_\mathrm{e}M_\mathrm{e}|\boldsymbol{j}^\dagger|I_\mathrm{g}M_\mathrm{g}\rangle$ and $\langle I_\mathrm{g}M_\mathrm{g}|\boldsymbol{j}|I_\mathrm{e}M_\mathrm{e}\rangle$, respectively. Therefore, the nuclear spin eigenstates must be evolved in time [see Eqs. (5.12) and (5.16)],

$$|\psi_{I_\lambda M_\lambda}(t)\rangle = U(t,0)|I_\lambda M_\lambda\rangle = \mathrm{e}^{-\mathrm{i}(E_\lambda - \mathrm{i}\frac{\Gamma_0}{2}\delta_{\lambda,e} - \epsilon_\lambda M_\lambda)t}|I_\lambda M_\lambda\rangle \ , \tag{5.31}$$

where it was assumed that $|\psi_{I_\lambda M_\lambda}(t)\rangle$ coincides with $|I_\lambda M_\lambda\rangle$ at $t = 0$. Inserting Eq. (5.31) into the definition of the nuclear transition currents given by Eqs. (5.19) leads to the following time dependence

$$\begin{aligned} \boldsymbol{J}^*_\ell(\boldsymbol{k},\tau) &= \mathrm{e}^{\mathrm{i}\Omega_\ell\tau - \tau/2}\boldsymbol{j}^*_\ell(\boldsymbol{k}) \ , \\ \boldsymbol{J}_\ell(\boldsymbol{k},\tau) &= \mathrm{e}^{-\mathrm{i}\Omega_\ell\tau - \tau/2}\boldsymbol{j}_\ell(\boldsymbol{k}) \ , \end{aligned} \tag{5.32}$$

with

$$\Omega_\ell = \left(M_\mathrm{g}\epsilon_\mathrm{g} - M_\mathrm{e}\epsilon_\mathrm{e}\right)/\Gamma_0 \tag{5.33}$$

describing the frequency correction due to magnetic hyperfine splitting in units of Γ_0. The amplitudes $\boldsymbol{j}^*_\ell$ and $\boldsymbol{j}_\ell$ appearing in Eqs. (5.32) denote the time-independent transition elements of the current density operators $\boldsymbol{j}^\dagger$ and $\boldsymbol{j}$, respectively,

$$\begin{aligned} \boldsymbol{j}^*_\ell(\boldsymbol{k}) &= \left[\frac{f_\mathrm{LM}(\boldsymbol{k})(1+\alpha_\mathrm{ic})4\omega}{(2I_\mathrm{e}+1)c^3\Gamma_0}\right]^{1/2} \langle I_\mathrm{e}M_\mathrm{e}|\boldsymbol{j}^\dagger|I_\mathrm{g}M_\mathrm{g}\rangle \ , \\ \boldsymbol{j}_\ell(\boldsymbol{k}) &= \left[\frac{f_\mathrm{LM}(\boldsymbol{k})(1+\alpha_\mathrm{ic})4\omega}{(2I_\mathrm{e}+1)c^3\Gamma_0}\right]^{1/2} \langle I_\mathrm{g}M_\mathrm{g}|\boldsymbol{j}|I_\mathrm{e}M_\mathrm{e}\rangle \ . \end{aligned} \tag{5.34}$$

The explicit forms of $\boldsymbol{j}_\ell^*$ and $\boldsymbol{j}_\ell$ depend on the type of transition to which the electromagnetic field couples. In the case of $\mathcal{M}1$ transitions (e.g., the 14.4 keV transition in ^{57}Fe) the amplitudes are given by

$$\boldsymbol{j}_\ell^*(\boldsymbol{k}) = \sqrt{3 f_{\mathrm{LM}}(\boldsymbol{k})} \sum_{q=0,\pm1} \begin{pmatrix} I_{\mathrm{g}} & 1 & I_{\mathrm{e}} \\ -M_{\mathrm{g}} & q & M_{\mathrm{e}} \end{pmatrix} (-1)^{q+I_{\mathrm{g}}-M_{\mathrm{g}}} \left(\hat{\boldsymbol{k}} \times \boldsymbol{\varepsilon}_{-q}^*\right) ,$$

$$\boldsymbol{j}_\ell(\boldsymbol{k}) = \sqrt{3 f_{\mathrm{LM}}(\boldsymbol{k})} \sum_{q=0,\pm1} \begin{pmatrix} I_{\mathrm{g}} & 1 & I_{\mathrm{e}} \\ -M_{\mathrm{g}} & q & M_{\mathrm{e}} \end{pmatrix} (-1)^{q+I_{\mathrm{g}}-M_{\mathrm{g}}} \left(\hat{\boldsymbol{k}} \times \boldsymbol{\varepsilon}_{-q}\right) , \tag{5.35}$$

where $\hat{\boldsymbol{k}} = \boldsymbol{k}/k$ and $\begin{pmatrix} I_{\mathrm{g}} & 1 & I_{\mathrm{e}} \\ -M_{\mathrm{g}} & q & M_{\mathrm{e}} \end{pmatrix}$ stands for the Wigner 3j-symbol [170] which dictates the selection rules of the driven transition and ensures angular momentum conservation. For instance, $\mathcal{M}1$ transitions only allow for a change in the magnetic projection quantum number of either $q = 0$ or $q = \pm 1$. Moreover, the cross products $\hat{\boldsymbol{k}} \times \boldsymbol{\varepsilon}_{-q}^*$ and $\hat{\boldsymbol{k}} \times \boldsymbol{\varepsilon}_{-q}$ determine the directions of the nuclear currents. Here, $\boldsymbol{\varepsilon}_q$ stands for the spherical unit vectors which can be expressed in terms of the Cartesian unit vectors $\boldsymbol{e}_x$, $\boldsymbol{e}_y$ and $\boldsymbol{e}_z$ [see Eq. (2.11)]. It is important that the spherical unit vectors are always chosen such that $\boldsymbol{\varepsilon}_0$ points along the quantization axis of the system. So far it was explicitly assumed that the magnetic field $\boldsymbol{B}$ and hence the quantization axis is parallel to $\boldsymbol{e}_z$. In order to generalize to arbitrary B-field directions only the spherical unit vectors need to be changed properly, meaning $\boldsymbol{\varepsilon}_0$ must coincide with the quantization axis. The vectors $\boldsymbol{\varepsilon}_{\pm1}$ can then be chosen arbitrarily under the condition that they are mutually orthogonal and perpendicular to $\boldsymbol{\varepsilon}_0$.

By inserting the explicit forms of the nuclear transition currents $\boldsymbol{J}_\ell^*$ and $\boldsymbol{J}_\ell$ given in Eqs. (5.32) into Eq. (5.27) one obtains the recursive solution for static hyperfine interactions

$$\boldsymbol{E}^{(p)}(\tau) = \sum_\ell \mathrm{e}^{-\mathrm{i}\Omega_\ell \tau - \tau/2} \boldsymbol{j}_\ell(\boldsymbol{k}) \int_{-\infty}^{\tau} \mathrm{d}\tau' \, \mathrm{e}^{\mathrm{i}\Omega_\ell \tau' - \tau'/2} \boldsymbol{j}_\ell^*(\boldsymbol{k}) \cdot \boldsymbol{E}^{(p-1)}(\tau') . \tag{5.36}$$

In general, the integrals appearing in this equation need to be solved numerically. However, for the case of an absent magnetic field an analytic solution of the wave equation can be derived. The absence of the magnetic field implies that there is no Zeeman splitting of the nuclear states. Correspondingly, the frequency terms Ω_ℓ which describe the correction to the nuclear resonance frequency ω_0 in dependence of the magnetic projection quantum numbers vanish and the nuclear system reduces to a single resonance. According to Eq. (5.36) the p^{th} scattering amplitude can be written as

$$\boldsymbol{E}^{(p)}(\tau) = \sum_\ell \mathrm{e}^{-\tau/2} \boldsymbol{j}_\ell(\boldsymbol{k}) \int_{-\infty}^{\tau} \mathrm{d}\tau' \, \mathrm{e}^{-\tau'/2} \boldsymbol{j}_\ell^*(\boldsymbol{k}) \cdot \boldsymbol{E}^{(p-1)}(\tau') . \tag{5.37}$$

In the following the incident radiation is assumed to be δ-like in time with polarization $\boldsymbol{e}_{\mathrm{p}}$. Moreover, we particularize to $\mathcal{M}1$ transitions in order to exploit the expression for $\boldsymbol{j}_\ell^*$ and $\boldsymbol{j}_\ell$ given in Eqs. (5.35). Using the orthogonality property of the 3j-symbols one obtains

$$\boldsymbol{E}(\xi, \tau) = \boldsymbol{e}_{\mathrm{p}} \mathrm{e}^{-\tau/2} \left(\delta(\tau) - \xi \sum_{p=0}^{\infty} \frac{(-\xi\tau)^p}{(p+1)!p!} \right) = \boldsymbol{e}_{\mathrm{p}} \mathrm{e}^{-\tau/2} \left(\delta(\tau) - \xi \frac{J_1(2\sqrt{\xi\tau})}{\sqrt{\xi\tau}} \right) . \tag{5.38}$$

The second term in Eq. (5.38) exactly describes the dynamical beat already provided in Eq. (5.2). After the introduction of the scattering orders $\boldsymbol{E}^{(p)}$ it is now clear that multiple scattering effects are responsible for the dynamical beat pattern in the time spectrum.

Note that for a single resonance the quantum beat pattern totally disappears because the nuclear system can be defined by a single frequency namely the resonance ω_0. However, if the magnetic field is not equal to zero two or even more transitions may be driven simultaneously, e.g., ℓ_1 and ℓ_2 with $\Omega_{\ell_1} \neq \Omega_{\ell_2}$. Since the final scattering amplitude contains a summation over all contributing hyperfine transitions ℓ, an interference between ℓ_1 and ℓ_2 may be imprinted in the measured time spectrum. This interference pattern will strongly depend on the frequency difference $(\Omega_{\ell_1} - \Omega_{\ell_2})$ and is called quantum beating.

5.5 Instantaneous rotations of the magnetic field

In this Section nuclear forward scattering is studied in the presence of instantaneous magnetic field rotations. The corresponding Hamiltonian for the occurring hyperfine interactions can be written as

$$H_{\mathrm{hf}}(t) = -\mu_\lambda \frac{\boldsymbol{I}_\lambda}{I_\lambda} \cdot \left[\boldsymbol{B}_{\mathrm{I}}\Theta(t_0 - t) + \boldsymbol{B}_{\mathrm{II}}\Theta(t - t_0)\right] = \begin{cases} -\epsilon_\lambda (I_\lambda)_{z_{\mathrm{I}}} & \text{for} \quad t < t_0 \ , \\ -\epsilon_\lambda (I_\lambda)_{z_{\mathrm{II}}} & \text{for} \quad t > t_0 \ , \end{cases} \tag{5.39}$$

where the magnetic fields are defined by $\boldsymbol{B}_{\mathrm{I}} = B_0 \boldsymbol{e}_{z_{\mathrm{I}}}$ and $\boldsymbol{B}_{\mathrm{II}} = B_0 \boldsymbol{e}_{z_{\mathrm{II}}}$. The operators $(I_\lambda)_{z_{\mathrm{I}}}$ and $(I_\lambda)_{z_{\mathrm{II}}}$ represent the z_{I}- and z_{II}-components of the nuclear spin operator $\boldsymbol{I}_\lambda$. The time of rotation is represented by t_0.

Analogously to the previous Section the main task is to express the time-dependent transition currents in terms of the amplitudes $\boldsymbol{j}_\ell^*$ and $\boldsymbol{j}_\ell$. This again requires to calculate the general time evolution of $|\psi_{I_\lambda M_\lambda}(t)\rangle$ for $t > t_0$, but now under hyperfine interactions given by Eq. (5.39). Since H_{hf} can be divided in two parts, $t < t_0$ and $t > t_0$ (each individual part describes a static B-field), the result of the previous Section can be used.

The idea is first to propagate in time from 0 to t_0 and afterwards from t_0 to t,

$$|\psi_{I_\lambda M_\lambda}(t)\rangle = U(t,0)|I_\lambda M_\lambda\rangle = U_{\mathrm{II}}(t,t_0)U_{\mathrm{I}}(t_0,0)|I_\lambda M_\lambda\rangle \ , \tag{5.40}$$

where the indices I and II indicate the splitting into two time sectors each with static hyperfine interactions. In order to apply the first evolution $U_{\mathrm{I}}(t_0,0)$, the system is assumed to be initially at time $t = 0$ in an eigenstate of $\boldsymbol{I}_\lambda$ and $(I_\lambda)_{z_{\mathrm{I}}}$ which is henceforth denoted by $|I_\lambda M_\lambda\rangle_{z_{\mathrm{I}}}$. Note that the index z_{I} is usually omitted if it is not important to explicitly name the quantization axis.

The time evolution from 0 to t_0 results in [see Eq. (5.16)]

$$U_{\mathrm{I}}(t_0,0)|I_\lambda M_\lambda\rangle_{z_{\mathrm{I}}} = \mathrm{e}^{-\mathrm{i}\int_0^{t_0}\mathrm{d}t'\left(H_0 - \epsilon_\lambda (I_\lambda)_{z_{\mathrm{I}}}\right)}|I_\lambda M_\lambda\rangle_{z_{\mathrm{I}}} = \mathrm{e}^{-\mathrm{i}(E_\lambda - \mathrm{i}\frac{\Gamma_0}{2}\delta_{\lambda,e} - \epsilon_\lambda M_\lambda)t_0}|I_\lambda M_\lambda\rangle_{z_{\mathrm{I}}} \ . \tag{5.41}$$

In order to apply U_{II} onto Eq. (5.41) the eigenstates $|I_\lambda M_\lambda\rangle_{z_{\mathrm{I}}}$ need to be expressed in terms of $|I_\lambda M_\lambda\rangle_{z_{\mathrm{II}}}$ which represent the eigenstates $\boldsymbol{I}_\lambda$ and $(I_\lambda)_{z_{\mathrm{II}}}$. This can be achieved by using the so-called Wigner rotation matrices $\mathcal{D}^{I_\lambda}_{M'_\lambda M_\lambda}(\alpha,\beta,\gamma)$ [170] according to

$$|I_\lambda M_\lambda\rangle_{z_{\mathrm{I}}} = \sum_{M'_\lambda} \mathcal{D}^{I}_{M'_\lambda M_\lambda}(\alpha,\beta,\gamma)|I_\lambda M'_\lambda\rangle_{z_{\mathrm{II}}} \ , \tag{5.42}$$

where the Euler angles α, β and γ define the rotation of the quantization axis from z_{I} to z_{II}. Using this relation yields

$$\begin{aligned} U_{\mathrm{II}}(t,t_0)|I_\lambda M_\lambda\rangle_{z_{\mathrm{I}}} &= \sum_{M'_\lambda} \mathcal{D}^{I}_{M'_\lambda M_\lambda}(\alpha,\beta,\gamma) U_{\mathrm{II}}(t,t_0)|I_\lambda M'_\lambda\rangle_{z_{\mathrm{II}}} \\ &= \sum_{M'_\lambda} \mathcal{D}^{I}_{M'_\lambda M_\lambda}(\alpha,\beta,\gamma) \mathrm{e}^{-\mathrm{i}\int_{t_0}^{t}\mathrm{d}t'\left(H_0-\epsilon_\lambda(I_\lambda)_{z_{\mathrm{II}}}\right)}|I_\lambda M'_\lambda\rangle_{z_{\mathrm{II}}} \\ &= \sum_{M'_\lambda} \mathcal{D}^{I}_{M'_\lambda M_\lambda}(\alpha,\beta,\gamma) \mathrm{e}^{-\mathrm{i}(E_\lambda - \mathrm{i}\frac{\Gamma_0}{2}\delta_{\lambda,e} - \epsilon_\lambda M'_\lambda)(t-t_0)}|I_\lambda M'_\lambda\rangle_{z_{\mathrm{II}}} \ . \end{aligned} \tag{5.43}$$

Finally, inserting Eq. (5.41) and Eq. (5.43) into Eq. (5.40) leads to

$$|\psi_{I_\lambda M_\lambda}(t)\rangle = \mathrm{e}^{-\mathrm{i}(E_\lambda - \mathrm{i}\frac{\Gamma_0}{2}\delta_{\lambda,e})t}\mathrm{e}^{\mathrm{i}\epsilon_\lambda M_\lambda t_0} \sum_{M'_\lambda} \mathcal{D}^{I_\lambda}_{M'_\lambda M_\lambda}(\alpha,\beta,\gamma)\mathrm{e}^{\mathrm{i}\epsilon_\lambda M'_\lambda (t-t_0)}|I_\lambda M'_\lambda\rangle_{z_{\mathrm{II}}} \ . \tag{5.44}$$

Now, we have everything at hand in order to express $\boldsymbol{J}^*_\ell$ and $\boldsymbol{J}_\ell$ in terms of $\boldsymbol{j}^*_\ell$ and $\boldsymbol{j}_\ell$. The procedure is analogue to the calculation for the case of static hyperfine interactions. We obtain for $\tau > \tau_0$

$$\begin{aligned} \boldsymbol{J}^*_{\ell,\mathrm{II}}(\boldsymbol{k},\tau) &= \mathrm{e}^{\mathrm{i}\Omega_\ell\tau_0 - \tau/2} \sum_{\ell'} \mathcal{D}^{I_{\mathrm{g}}\,*}_{M'_{\mathrm{g}} M_{\mathrm{g}}}(\alpha,\beta,\gamma)\mathcal{D}^{I_{\mathrm{e}}}_{M'_{\mathrm{e}} M_{\mathrm{e}}}(\alpha,\beta,\gamma)\mathrm{e}^{\mathrm{i}\Omega_{\ell'}(\tau-\tau_0)}\boldsymbol{j}^*_{\ell',\mathrm{II}}(\boldsymbol{k}) \ , \\ \boldsymbol{J}_{\ell,\mathrm{II}}(\boldsymbol{k},\tau) &= \mathrm{e}^{-\mathrm{i}\Omega_\ell\tau_0 - \tau/2} \sum_{\ell'} \mathcal{D}^{I_{\mathrm{g}}}_{M'_{\mathrm{g}} M_{\mathrm{g}}}(\alpha,\beta,\gamma)\mathcal{D}^{I_{\mathrm{e}}\,*}_{M'_{\mathrm{e}} M_{\mathrm{e}}}(\alpha,\beta,\gamma)\mathrm{e}^{-\mathrm{i}\Omega_{\ell'}(\tau-\tau_0)}\boldsymbol{j}_{\ell',\mathrm{II}}(\boldsymbol{k}) \ . \end{aligned} \tag{5.45}$$

The index II indicates that for $\tau > \tau_0$ the quantization axis points along $\boldsymbol{e}_{z_{\mathrm{II}}}$ determining the spherical unit vectors included in $\boldsymbol{j}^*_{\ell',\mathrm{II}}$ and $\boldsymbol{j}_{\ell',\mathrm{II}}$. As can be seen from Eqs. (5.45) a rotation of the magnetic field leads to a redistribution of the nuclear currents. For $\tau > \tau_0$ the rotated currents are determined by a coherent superposition of the time-independent transition amplitudes. Thereby, the summation is performed over the whole spectrum of hyperfine transitions ℓ' with weight coefficients given by the product of the Wigner $\mathcal{D}$-matrices and phase factors $\mathrm{e}^{\pm\mathrm{i}\Omega_{\ell'}\tau}$ shifted backwards in time by τ_0. In Chap. 6 it is shown how this transformation can be used for the control of the polarization properties of the scattered x-rays. For times $\tau < \tau_0$ the nuclear currents $\boldsymbol{J}^*_{\ell,\mathrm{I}}$ and $\boldsymbol{J}_{\ell,\mathrm{I}}$ are given by Eqs. (5.32), respectively. Note that whenever we are discussing explicit rotation setups in the following Chapters, τ_0 will be given in *nanoseconds* instead of using units of $1/\Gamma_0$ for the sake of convenience.

5.6 Fast switchings of the magnetic field

In this Section the hyperfine interactions investigated so far are generalized to the case where it is not only allowed to rotate but also to switch the magnetic field off and on.

Consider therefore an initially applied B-field to be switched off at time $t = t_0$ and on again at $t = t_1$. Thereby, the magnetic field after t_1 does not necessarily need to point in the same direction than the initial one, only their amplitudes are supposed to remain unchanged. For this situation the hyperfine interactions are determined by

$$H_{\mathrm{hf}}(t) = -\mu_\lambda \frac{\boldsymbol{I}_\lambda}{I_\lambda} \cdot \left[\boldsymbol{B}_{\mathrm{I}}\Theta(t_0 - t) + \boldsymbol{B}_{\mathrm{III}}\Theta(t - t_1)\right] = \begin{cases} -\epsilon_\lambda (I_\lambda)_{z_{\mathrm{I}}} & \text{for} \quad t < t_0 \ , \\ 0 & \text{for} \quad t_0 < t < t_1 \ , \\ -\epsilon_\lambda (I_\lambda)_{z_{\mathrm{III}}} & \text{for} \quad t > t_1 \ . \end{cases} \tag{5.46}$$

Here, the notations of the previous Section are adopted.

Analogously to the previous Section, it is intended to express the nuclear currents $\boldsymbol{J}_\ell^*$ and $\boldsymbol{J}_\ell$ in terms of the time-independent transition amplitudes $\boldsymbol{j}_\ell^*$ and $\boldsymbol{j}_\ell$. In comparison to the case of instantaneous B-field rotations the only difference in the calculation is that the time evolution of $|\psi_{I_\lambda M_\lambda}(t)\rangle$ splits up into three time sectors instead of two, but conceptually nothing changes. Hence, following the same steps as before, we obtain for $\tau_0 < \tau < \tau_1$

$$\begin{aligned} \boldsymbol{J}_{\ell,\mathrm{II}}^*(\boldsymbol{k},\tau) &= \mathrm{e}^{\mathrm{i}\Omega_\ell \tau_0 - \tau/2} \boldsymbol{j}_{\ell',\mathrm{II}}^*(\boldsymbol{k}) \ , \\ \boldsymbol{J}_{\ell,\mathrm{II}}(\boldsymbol{k},\tau) &= \mathrm{e}^{-\mathrm{i}\Omega_\ell \tau_0 - \tau/2} \boldsymbol{j}_{\ell',\mathrm{II}}(\boldsymbol{k}) \ , \end{aligned} \tag{5.47}$$

and for $\tau > \tau_1$

$$\begin{aligned} \boldsymbol{J}_{\ell,\mathrm{III}}^*(\boldsymbol{k},\tau) &= \mathrm{e}^{\mathrm{i}\Omega_\ell \tau_0 - \tau/2} \sum_{\ell'} \mathcal{D}^{I_{\mathrm{g}}\,*}_{M_{\mathrm{g}}' M_{\mathrm{g}}}(\alpha,\beta,\gamma) \mathcal{D}^{I_{\mathrm{e}}}_{M_{\mathrm{e}}' M_{\mathrm{e}}}(\alpha,\beta,\gamma) \mathrm{e}^{\mathrm{i}\Omega_{\ell'}(\tau-\tau_1)} \boldsymbol{j}_{\ell',\mathrm{III}}^*(\boldsymbol{k}) \ , \\ \boldsymbol{J}_{\ell,\mathrm{III}}(\boldsymbol{k},\tau) &= \mathrm{e}^{-\mathrm{i}\Omega_\ell \tau_0 - \tau/2} \sum_{\ell'} \mathcal{D}^{I_{\mathrm{g}}}_{M_{\mathrm{g}}' M_{\mathrm{g}}}(\alpha,\beta,\gamma) \mathcal{D}^{I_{\mathrm{e}}\,*}_{M_{\mathrm{e}}' M_{\mathrm{e}}}(\alpha,\beta,\gamma) \mathrm{e}^{-\mathrm{i}\Omega_{\ell'}(\tau-\tau_1)} \boldsymbol{j}_{\ell',\mathrm{III}}(\boldsymbol{k}) \ . \end{aligned} \tag{5.48}$$

For $\tau < \tau_0$ the currents are again determined by Eqs. (5.32).

From Eqs. (5.47) it can be seen that by switching off the magnetic field the nuclear currents are frozen in time and only depend on the switching instant τ_0. After the application of $\boldsymbol{B}_{\mathrm{III}}$ the currents are again given by a coherent summation of the transition amplitudes. However, the occurring phase factors $\mathrm{e}^{\pm\mathrm{i}\Omega_{\ell'}\tau}$ are now shifted backwards in time by τ_1 instead of τ_0 compared to the previous Section.

Chapter 6

Polarization control of hard x-rays

The controlled manipulation of nuclear forward scattering (NFS) has been investigated in a number of setups over the last decades including phase shifts [97, 98], vibrating targets [100, 235], sequences of multiple targets [237, 238], magnetic fields rotations [96, 110,236,239], external field control [111,158,164], or radio-frequency fields [240,241]. The idea to actively manipulate the nuclear response in the course of NFS with SR by abrupt changes of the magnetic field goes back to Shvyd'ko [239]. In a subsequent work [96] it was experimentally and theoretically shown that a single x-ray photon can be stored inside an ^{57}Fe target by dynamically controlling the nuclear response via timed rotations of the magnetic field. Depending on the moment of field switching, the collective nuclear decay could be suppressed.

In order to be able to apply a B-field rotation timely synchronized with the nuclear excitation, it is mandatory to have a sharp excitation pulse in time space. It is therefore natural to consider SR facilities as x-ray sources because the pulse duration behaves δ-like in time in comparison with the time scale of the nuclear response. Furthermore, the low degeneracy of synchrotron light with regard to the nuclear transition width ensures the weak excitation regime and hence the single-photon character of the control procedure described in this Chapter. A typical NFS setup at SR facilities is depicted in Fig. 5.1 along with the characteristic time spectrum for a static magnetic field.

This Chapter is devoted to the polarization control of hard x-rays during NFS based on dynamical manipulation via magnetic field rotations. In Sec. 6.1, the polarization response of NFS is first discussed for static hyperfine interactions. Afterwards in Sec. 6.2, the single scattering approximation is used to derive a control procedure of the polarization response. This section is based on results presented in Refs. [96,239] and extends the concepts to the domain of polarization control with applications in information science. How to obtain control of the output field beyond the first scattering order is the topic of Sec. 6.3. There, the formalism of Ref. [96] is extended beyond the single scattering approximation.

6.1 Polarization effects in static NFS

Before we explain how the polarization of hard x-rays can be dynamically manipulated in the course of nuclear forward scattering, let us discuss the polarization properties of NFS for a static hyperfine field. The case of static hyperfine interactions has been treated in Sec. 5.4. The corresponding interaction Hamiltonian is given by Eq. (5.30). Following the notation of the previous Chapter, the polarization of the incident SR pulse is denoted by $\boldsymbol{e}_\mathrm{p}$ [compare Eq. (5.29)]. The linear polarization basis vectors $\boldsymbol{e}_s$ ($s = \sigma, \pi$) are defined by convention in the following way

$$\begin{aligned} \boldsymbol{e}_\sigma &= \boldsymbol{e}_x \ , \\ \boldsymbol{e}_\pi &= \boldsymbol{e}_z \ . \end{aligned} \tag{6.1}$$

The definition of σ- and π-polarization thereby follows the conventions settled in the description of SR pulses [242]. If the electric field vector is in the horizontal plane, it is referred to as σ-polarized. The π-polarization vector is then subsequently determined by $\boldsymbol{e}_\sigma \times \boldsymbol{k}/k$ where $\boldsymbol{k}$ is the wave vector of the incident field, here $\boldsymbol{k} \parallel \boldsymbol{e}_y$.

Analogously to the linear polarization vectors, circular polarization basis vectors can be defined by

$$\begin{aligned} \boldsymbol{e}_+ &= \frac{1}{\sqrt{2}} \left(\boldsymbol{e}_x + \mathrm{i} \boldsymbol{e}_z \right) \ , \\ \boldsymbol{e}_- &= \frac{1}{\sqrt{2}} \left(\boldsymbol{e}_x - \mathrm{i} \boldsymbol{e}_z \right) \ , \end{aligned} \tag{6.2}$$

where the right- and left-circular polarizations $\boldsymbol{e}_+$ and $\boldsymbol{e}_-$ have positive and negative helicities, respectively.

Since it turns out that the polarization state of the scattered light is strongly dependent on the magnetic field orientation determining the quantization axis of the system, it is helpful to distinguish particular B-field geometries:

- In the **Voigt geometry** the magnetic field vector lies in the plane perpendicular to the propagation direction of the incident electromagnetic field. Especially interesting are the cases where $\boldsymbol{B} \parallel \boldsymbol{e}_\sigma$ and $\boldsymbol{B} \parallel \boldsymbol{e}_\pi$ which are henceforth denoted by 0°- and 90°-Voigt geometries, respectively.
- The **Faraday geometry** is defined by a magnetic field parallel or anti-parallel to the wave vector of the incident radiation: $\boldsymbol{B} \parallel \boldsymbol{k}$ or $\boldsymbol{B} \parallel -\boldsymbol{k}$.

In order to simplify the discussion of the polarization properties of the electric field after NFS only electric and magnetic dipole transitions ($\mathcal{E}1$ and $\mathcal{M}1$) are considered. From the recursive solution for static hyperfine fields given by Eq. (5.37) it can be verified that the s-component of the scattered radiation is proportional to $(\boldsymbol{j}_\ell(\boldsymbol{k}) \cdot \boldsymbol{e}_s)(\boldsymbol{j}^*_\ell(\boldsymbol{k}) \cdot \boldsymbol{e}_{s'})$ where s' denotes the incident polarization. For the case of a 0°- or 90°-Voigt geometry the following relation can be shown to hold [235, 236],

$$\Big(\boldsymbol{j}_\ell(\boldsymbol{k}) \cdot \boldsymbol{e}_s\Big)\Big(\boldsymbol{j}^*_\ell(\boldsymbol{k}) \cdot \boldsymbol{e}_{s'}\Big) \propto \delta_{s,s'} \qquad \text{with} \quad s, s' \in \{\sigma, \pi\} \ . \tag{6.3}$$

This means for incident linearly polarized light the 0°- and 90°-Voigt geometry prohibits the mixing of σ- and π-polarization. In other words, if the SR pulse is either σ- or π-polarized, the radiation is scattered into its initial polarization state.

A way to understand the polarization dependence of NFS is to consider the indistinguishability required for the formation of the nuclear exciton. As already explained in Chap. 5, the directionality of NFS goes back to the formation of a delocalized nuclear excitation inside the target for which the indistinguishability of the scattering process is mandatory. For this reason, the photons emitted preferably in the forward direction occur in scattering processes for which the nucleus decays back to the same magnetic sublevel from where it was excited. For instance, in the case of a σ-polarized SR pulse which drives a nuclear target inside a magnetic field pointing along the z-direction, only transitions with $\Delta M = 0$ can be driven. The second scalar product in Eq. (6.3) determining the selection rules of the excitation vanishes for all other transitions. Since in the case of $\boldsymbol{B} \parallel \boldsymbol{e}_\pi$ the transition amplitudes of the $\Delta M = 0$ transitions are additionally perpendicular to the π-component $\boldsymbol{e}_\pi$, the indistinguishability of the process ensures the conservation of the incoming polarization.

For arbitrary B-field orientations Eq. (6.3) does not hold anymore such that σ-polarized x-rays can be scattered into π-polarized states, and the other way around [242]. However, in the case of a Voigt geometry it is always possible to find two orthogonal polarization vectors (namely the vectors parallel and perpendicular to $\boldsymbol{B}$) for which the relation (6.3) is fulfilled.

In the case of a magnetic field pointing along the propagation direction of the incident wave, polarization mixing between the linear polarizations $\boldsymbol{e}_\sigma$ and $\boldsymbol{e}_\pi$ always occurs. However, in the Faraday geometry circular polarization states are conserved [242]. Hence, Eq. (6.3) holds for the Faraday geometry if s and s' are replaced by circular polarizations.

Accordingly, nuclear forward scattering does not conserve in general the polarization state of the scattered x-rays [242]. However, there are particular geometries determined by the orientation of the magnetic field where polarization mixing is forbidden. In the following section it is shown that the scattered light polarization can be dynamically controlled by switchings between these geometries.

6.2 Dynamical control of nuclear polarization response

The general concept for the polarization control is to instantaneously jump between polarization eigengeometries of NFS potentially leading to transformations between orthogonal polarization states. The description of such abrupt changes of the magnetic field direction in terms of the hyperfine interaction Hamiltonian H_{hf} has been the topic of Sec. 5.5. For the specific form of H_{hf} given in Eq. (5.39), the resulting nuclear transition currents $\boldsymbol{J}_\ell^*$ and $\boldsymbol{J}_\ell$ are summarized in Eqs. (5.45). Here, we apply these results to explicitly derive the scattered radiation field. It turns out that the polarization response of the nuclear target is not only affected by the angle and axis of rotation, but also strongly depends on the moment of magnetic field rotation.

The first order scattering amplitude for a δ-like excitation pulse with polarization $\boldsymbol{e}_{\mathrm{p}}$ is given by Eq. (5.28). Plugging the explicit time dependence of the nuclear currents (5.32) into Eq. (5.28), the first order solution can be written for $0 < \tau < \tau_0$ as

$$\begin{aligned} \boldsymbol{E}^{(1)}(\xi,\tau) &= -\xi \sum_\ell \boldsymbol{J}_{\ell,\mathrm{I}}(\boldsymbol{k},\tau) \left(\boldsymbol{J}^*_{\ell,\mathrm{I}}(\boldsymbol{k},0) \cdot \boldsymbol{e}_{\mathrm{p}} \right) \\ &= -\xi \sum_\ell \boldsymbol{\mathcal{A}}^{(1)}_{\ell,\mathrm{I}}(\boldsymbol{k})\, \mathrm{e}^{-\mathrm{i}\Omega_\ell \tau - \tau/2} \,. \end{aligned} \tag{6.4}$$

Accordingly, the single scattering events can be expressed as a coherent summation over all contributing nuclear transitions ℓ where the summands factorize into a time-dependent phase factor $\mathrm{e}^{-\mathrm{i}\Omega_\ell \tau - \tau/2}$ and a time-independent amplitude $\boldsymbol{\mathcal{A}}_{\ell,\mathrm{I}}^{(1)}$ which is determined by

$$\boldsymbol{\mathcal{A}}_{\ell,\mathrm{I}}^{(1)}(\boldsymbol{k}) = \boldsymbol{j}_{\ell,\mathrm{I}}(\boldsymbol{k}) \left(\boldsymbol{j}_{\ell,\mathrm{I}}^{*}(\boldsymbol{k}) \cdot \boldsymbol{e}_{\mathrm{p}} \right) \ . \tag{6.5}$$

In order to describe the scattered radiation field after an instantaneous B-field rotation at $\tau = \tau_0$, the transformation of the nuclear transition currents described in Eqs. (5.45) is considered. The first order solution for $\tau > \tau_0$ reads

$$\begin{aligned} \boldsymbol{E}^{(1)}(\xi, \tau) &= -\xi \sum_{\ell} \boldsymbol{J}_{\ell,\mathrm{II}}(\boldsymbol{k}, \tau) \left(\boldsymbol{J}_{\ell,\mathrm{I}}^{*}(\boldsymbol{k}, 0) \cdot \boldsymbol{e}_{\mathrm{p}} \right) \\ &= -\xi \sum_{\ell} \boldsymbol{\mathcal{A}}_{\ell,\mathrm{II}}^{(1)}(\boldsymbol{k})\, \mathrm{e}^{-\mathrm{i}\Omega_\ell (\tau - \tau_0) - \tau/2} \ , \end{aligned} \tag{6.6}$$

where the time-independent amplitude is defined by

$$\boldsymbol{\mathcal{A}}_{\ell,\mathrm{II}}^{(1)}(\boldsymbol{k}) = \boldsymbol{j}_{\ell,\mathrm{II}}(\boldsymbol{k}) \sum_{\ell'} \mathrm{e}^{-\mathrm{i}\Omega_{\ell'} \tau_0} \mathcal{D}_{M_\mathrm{g} M_\mathrm{g}'}^{I_\mathrm{g}}(\alpha, \beta, \gamma) \mathcal{D}_{M_\mathrm{e} M_\mathrm{e}'}^{I_\mathrm{e}\,*}(\alpha, \beta, \gamma) \left(\boldsymbol{j}_{\ell',\mathrm{I}}^{*}(\boldsymbol{k}) \cdot \boldsymbol{e}_{\mathrm{p}} \right) \ . \tag{6.7}$$

As seen from Eq. (6.6), the single scattering solution for $\tau > \tau_0$ has still the same form as Eq. (6.4) with the replacements $\tau \mapsto \tau - \tau_0$ (except in the decay factor $\mathrm{e}^{-\tau/2}$) and $\boldsymbol{\mathcal{A}}_{\ell,\mathrm{I}}^{(1)} \mapsto \boldsymbol{\mathcal{A}}_{\ell,\mathrm{II}}^{(1)}$. The time-independent amplitude $\boldsymbol{\mathcal{A}}_{\ell,\mathrm{II}}^{(1)}$ looks however completely different from $\boldsymbol{\mathcal{A}}_{\ell,\mathrm{I}}^{(1)}$. The most essential feature is that $\boldsymbol{\mathcal{A}}_{\ell,\mathrm{II}}^{(1)}$ depends first on the geometry of magnetic field rotation determined by the Euler angles α, β and γ, and second on the moment of switching τ_0. Since both dependencies are adjustable from outside they can be used as control parameters for the amplitude $\boldsymbol{\mathcal{A}}_{\ell,\mathrm{II}}^{(1)}$ which renders possible to actively manipulate the magnitude and direction of the scattered radiation field for $\tau > \tau_0$.

Physically, Eq. (6.7) describes a redistribution of the nuclear excitation among the Zeeman levels due to a change of the quantization axis produced by the instantaneous rotation of the magnetic hyperfine field. The initial excitation process is described by the scalar product $\boldsymbol{j}_{\ell',\mathrm{I}}^{*} \cdot \boldsymbol{e}_{\mathrm{p}}$ which is still evaluated in the time section where the magnetic field is given by $\boldsymbol{B}_{\mathrm{I}}$. The abrupt B-field rotation transforms these initially excited currents into a multiplet of currents determined by the new quantization axis. The dependence of this transformation on the rotation geometry and the moment of switching is determined by the product of Wigner rotation matrices $\mathcal{D}_{M_\mathrm{g} M_\mathrm{g}'}^{I_\mathrm{g}} \mathcal{D}_{M_\mathrm{e} M_\mathrm{e}'}^{I_\mathrm{e}\,*}$ and the phase factor $\mathrm{e}^{-\mathrm{i}\Omega_{\ell'} \tau_0}$, respectively, which act as weighting coefficients for the nuclear redistribution. The de-excitation process proceeds via the transition amplitudes $\boldsymbol{j}_{\ell,\mathrm{II}}$ which are determined by the new magnetic field direction $\boldsymbol{B}_{\mathrm{II}}$. By adjusting the rotation parameters it is possible to actively manipulate the interplay between the decay transition amplitudes $\boldsymbol{j}_{\ell,\mathrm{II}}$ such that the polarization response of the nuclear target can be controlled by tuning either on constructive or destructive interference [96].

For the case of ^{57}Fe nuclei, this control procedure is illustrated in Fig. 6.1. Thereby, it is assumed that initially only the two $\Delta M = 0$ transitions are driven, for instance by choosing σ-polarized SR and $\boldsymbol{B}_{\mathrm{I}}$ parallel to the z-direction. The abrupt rotation of the magnetic field transforms each of these currents into a sextet of new currents

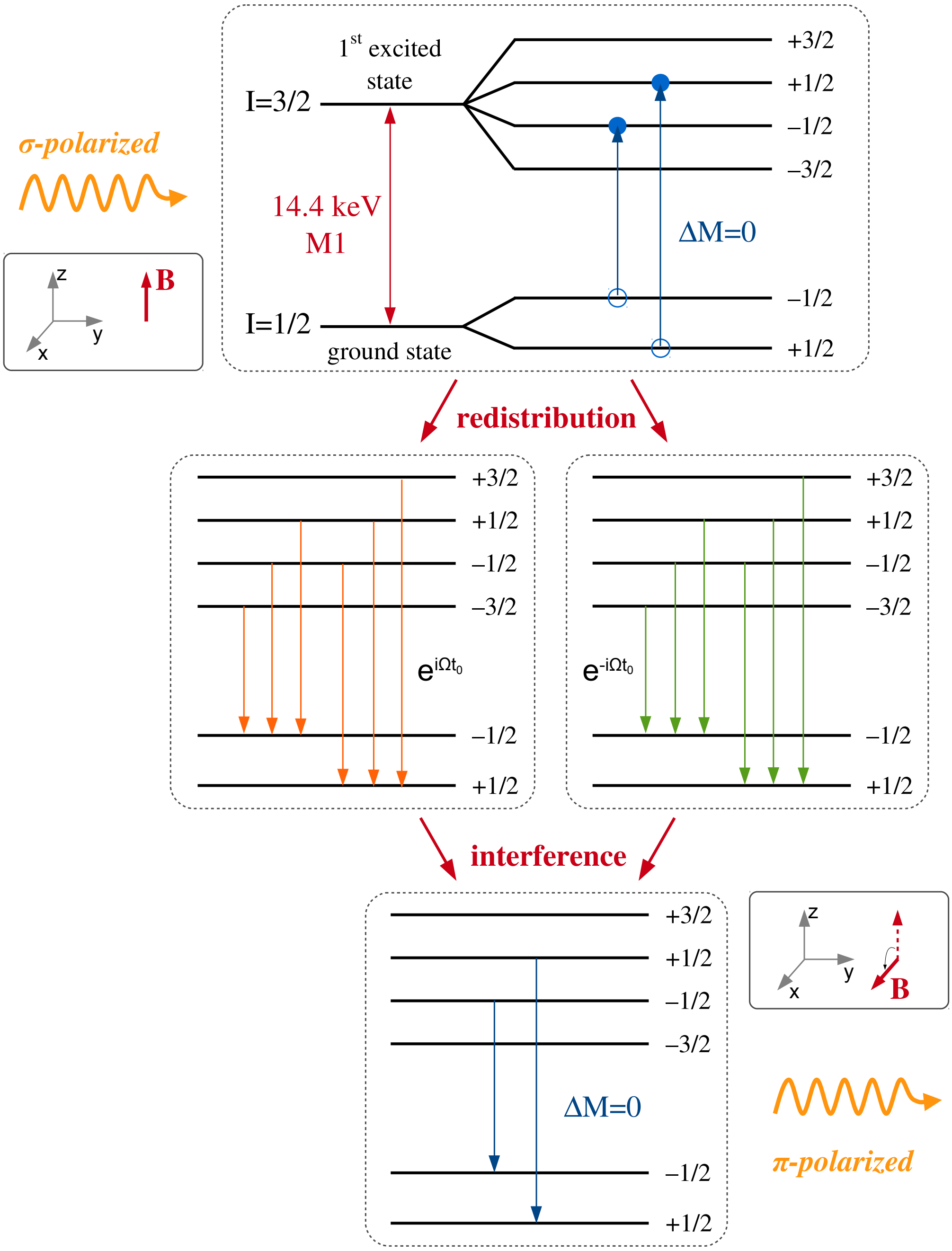

Figure 6.1: Initially σ-polarized x-rays are converted into π-polarization states by a timed rotation of the B-field from z to x. Within the initial geometry only the two $\Delta M = 0$ transitions are driven by the incident σ-polarized light. The instantaneous magnetic field rotation corresponds to an abrupt change of the quantization axis redistributing the excited nuclear currents. The moment of switching τ_0 is chosen such that the "new" $\Delta M = \pm 1$ hyperfine transitions interfere destructively resulting in the emission of π-polarized x-rays after τ_0.

defined by the new magnetic field direction. The relative strengths and phases of the transformed currents are determined by the angle and axis of rotation and the moment of switching [96]. Considering for instance a rotation from the z to the x direction, the switching time can be chosen such that the $\Delta M = \pm 1$ transitions interfere destructively. In this case only the currents with $\Delta M = 0$ survive as shown in Fig. 6.1. Since the de-excitation occurs in the presence of $\boldsymbol{B}_{\mathrm{II}}$ this scheme converts initially σ-polarized into π-polarized light.

In order to find the right switching time for σ to π conversion the amplitudes $\boldsymbol{\mathcal{A}}^{(1)}_{\ell,\mathrm{II}}$ need to be analyzed in detail. In the following, we consider ^{57}Fe targets and restrict ourselves to 90° magnetic field rotations from z to x in order to elaborate the behavior of the NFS spectrum caused by the nuclear redistribution. Both the case of initially σ- and of π-polarized radiation are discussed. Subsequently, the effects caused by multiple scattering contributions are evaluated.

6.2.1 90°-Voigt rotation: from z to x

In this subsection, we consider a rotation of the magnetic field initially pointing along the z-direction by 90° counterclockwise around the y-axis (propagation direction) as shown in Fig. 6.1. In terms of the Euler angles this rotation is characterized by [170]

$$\alpha = 0, \quad \beta = \frac{\pi}{2} \quad \text{and} \quad \gamma = 0 \; . \tag{6.8}$$

Since both α and γ identically vanish the Wigner $\mathcal{D}$-matrices occurring in Eq. (6.7) reduce to

$$\mathcal{D}^{I}_{M'M}(\alpha,\beta,\gamma) = \mathrm{e}^{-\mathrm{i}M'\alpha} d^{I}_{M'M}(\beta) \mathrm{e}^{-\mathrm{i}M\gamma} = d^{I}_{M'M}(\beta) \; , \tag{6.9}$$

where the d-matrices describe a rotation about the y-axis [170]. Inserting Eq. (6.9) into Eq. (6.7) and setting $\beta = \pi/2$ one obtains

$$\boldsymbol{\mathcal{A}}^{(1)}_{\ell,\mathrm{II}}(\boldsymbol{k}) = \boldsymbol{j}_{\ell,\mathrm{II}}(\boldsymbol{k}) \sum_{\ell'} \mathrm{e}^{-\mathrm{i}\Omega_{\ell'}\tau_0} d^{I_{\mathrm{g}}}_{M_{\mathrm{g}}M'_{\mathrm{g}}}\left(\frac{\pi}{2}\right) d^{I_{\mathrm{e}}}_{M_{\mathrm{e}}M'_{\mathrm{e}}}\left(\frac{\pi}{2}\right) \left(\boldsymbol{j}^{*}_{\ell',\mathrm{I}}(\boldsymbol{k}) \cdot \boldsymbol{e}_{\mathrm{p}}\right) \; . \tag{6.10}$$

Thereby we have taken into account that the d-matrices are chosen to be real. The explicit values of $d^{I_{\mathrm{e}}}_{M_{\mathrm{e}}M'_{\mathrm{e}}}(\frac{\pi}{2})$ and $d^{I_{\mathrm{g}}}_{M_{\mathrm{g}}M'_{\mathrm{g}}}(\frac{\pi}{2})$ for I_{g}=1/2 and I_{e}=3/2 can be found in App. D. In order to further evaluate Eq. (6.10) the initial polarization $\boldsymbol{e}_{\mathrm{p}}$ of the incoming radiation need to be fixed.

Before doing so, a shorter notation is introduced where the transitions $M_{\mathrm{g}} \leftrightarrow M_{\mathrm{e}}$ are labeled by

$$\begin{aligned}
\ell &= 3 && - && 1/2 \leftrightarrow 3/2 \; , \\
\ell &= 2 && - && 1/2 \leftrightarrow 1/2 \; , \\
\ell &= 1 && - && 1/2 \leftrightarrow -1/2 \; , \\
\ell &= -1 && - && -1/2 \leftrightarrow 1/2 \; , \\
\ell &= -2 && - && -1/2 \leftrightarrow -1/2 \; , \\
\ell &= -3 && - && -1/2 \leftrightarrow -3/2 \; .
\end{aligned} \tag{6.11}$$

Within this notation, $\Delta M = 0$ and $\Delta M = \pm 1$ correspond to the even and odd ℓ, respectively, where the relationship $\Omega_\ell = -\Omega_{-\ell}$ is fulfilled [compare Eq. (5.33)].

Initially σ-polarized x-rays

In the case of initially σ-polarized x-rays, only the $\Delta M = 0$ transitions are driven initially due to $\mathcal{M}1$ selection rules (see Fig. 6.1). Mathematically, the selection rules are enforced by the scalar product $\boldsymbol{j}^*_{\ell',\mathrm{I}} \cdot \boldsymbol{e}_\mathrm{p}$ which in the considered geometry ($\boldsymbol{B}_\mathrm{I} \parallel \boldsymbol{e}_\mathrm{z}$ and $\boldsymbol{e}_\mathrm{p} = \boldsymbol{e}_\sigma$) is only non-vanishing for even ℓ'. Therefore, the summation over ℓ' occurring in Eq. (6.10) reduces to $\ell' = \pm 2$. Moreover, using Eqs. (5.35) it can be shown that the transition amplitude $\boldsymbol{j}_{\ell,\mathrm{II}}$ points along $\boldsymbol{e}_\pi$ ($\boldsymbol{e}_\sigma$) for transitions of even (odd) ℓ (see App. D) which determines the directionality of $\boldsymbol{\mathcal{A}}^{(1)}_{\ell,\mathrm{II}}$. Explicitly performing the summation over ℓ' leads to the following relation (see App. D)

$$\boldsymbol{\mathcal{A}}^{(1)}_{\ell,\mathrm{II}}(\boldsymbol{k}) \propto \begin{cases} \sin(\Omega_2 \tau_0)\, \boldsymbol{e}_\pi & \text{for even } \ell \;, \\ \cos(\Omega_2 \tau_0)\, \boldsymbol{e}_\sigma & \text{for odd } \ell \;. \end{cases} \tag{6.12}$$

In Fig. 6.2 the magnitudes of $\boldsymbol{\mathcal{A}}^{(1)}_{\ell,\mathrm{II}}$ are plotted for even and odd transitions in dependence of τ_0 along with the unperturbed, first order NFS intensity spectrum $|\boldsymbol{E}^{(1)}(\xi,\tau)|^2$. In the graphs showing the amplitudes, the proportionality predicted in Eq. (6.12) can be clearly identified. Moreover, by comparing for instance the upper plot with the unperturbed intensity spectrum it can be seen that the time instants where the amplitudes for even ℓ vanish, coincide with the maxima of $|\boldsymbol{E}^{(1)}(\xi,\tau)|^2$, whereas in the case of odd ℓ, the roots of $\boldsymbol{\mathcal{A}}^{(1)}_{\ell,\mathrm{II}}$ exactly agree with the minima of the intensity spectrum.

By inserting the amplitudes of Eq. (6.12) into Eq. (6.6) the first order solution of the scattered radiation field after magnetic field switching is obtained,

$$\begin{aligned} \boldsymbol{E}^{(1)}(\xi,\tau) \propto -\xi \Big\{ & \sin(\Omega_2\tau_0)\sin(\Omega_2(\tau-\tau_0))\boldsymbol{e}_\pi \\ & + \frac{1}{2}\cos(\Omega_2\tau_0)\left[\cos(\Omega_1(\tau-\tau_0)) + 3\cos(\Omega_3(\tau-\tau_0))\right]\boldsymbol{e}_\sigma \Big\} \;. \end{aligned} \tag{6.13}$$

It can be seen that after rotation of the B-field the emission via an even transition ($\ell = \pm 2$) results in π-polarized light whereas the odd transitions ($\ell = \pm 1, \pm 3$) determine the σ-polarized component.

Accordingly, switching at $\tau_0 = (2n+1)\,\frac{\pi}{2}/\Omega_2$ ($n = 0,1,2,\dots$) corresponding to the roots of $\cos(\Omega_2\tau_0)$ or the minima of the unperturbed NFS spectrum results in a amplitude $\boldsymbol{\mathcal{A}}^{(1)}_{\ell,\mathrm{II}}$ which is only non-vanishing for even ℓ. In this case, the odd transitions interfere destructively due to the timed rotation of the magnetic field and hence, the initially σ-polarized radiation is emitted as π-polarized after the magnetic field rotation as graphically illustrated in Fig. 6.1. This kind of switching scheme which converts linearly orthogonal polarizations into each other has already been experimentally verified in Ref. [96].

In contrast, a rotation of the magnetic field at the maxima $\tau_0 = n\,2\pi/\Omega_2$ ($n = 0,1,2,\dots$) corresponding to the roots of $\sin(\Omega_2\tau_0)$ leads to destructive interference among the even transitions (see Fig. 6.2). In this case the reemission of the initially driven $\Delta M = 0$ currents is transferred to the $\Delta M = \pm 1$ hyperfine transitions due to the timed redistribution of the nuclear excitation. Subsequently, the scattered radiation field after

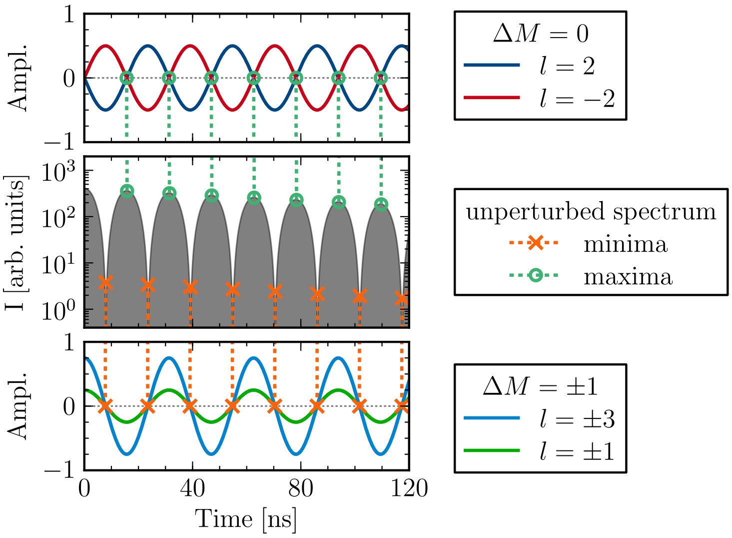

Figure 6.2: The magnitudes of $\boldsymbol{\mathcal{A}}^{(1)}_{\ell,\mathrm{II}}$ are shown in dependence of τ_0 for even and odd ℓ along with the first order NFS intensity spectrum $|\boldsymbol{E}^{(1)}(\xi,\tau)|^2$ (middle graph). Initially σ-polarized x-rays and an effective target thickness of $\xi = 10$ are considered. In the case of even ℓ, the zero crossings of $\boldsymbol{\mathcal{A}}^{(1)}_{\ell,\mathrm{II}}$ correspond to maxima of the spectrum, whereas in the case of odd ℓ, the amplitudes $\boldsymbol{\mathcal{A}}^{(1)}_{\ell,\mathrm{II}}$ identically vanish at time instants corresponding to minima of $|\boldsymbol{E}^{(1)}(\xi,\tau)|^2$.

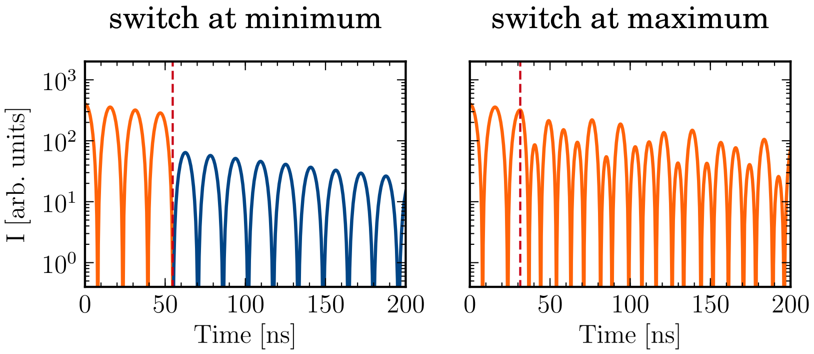

Figure 6.3: Effect of instantaneous B-field rotation on NFS intensity spectra. Two moments of switching (red dashed lines) have been considered, $\tau_0 = 54.7$ ns corresponding to a minimum (left graph) and $\tau_0 = 31.6$ ns corresponding to a maximum of the first order spectrum (right graph). The first order solution $|\boldsymbol{E}^{(1)}(\xi,\tau)|^2$ is shown for $\xi = 10$ and initially σ-polarized light. σ and π polarization components are presented in orange and blue, respectively.

B-field switching remains σ-polarized but is processed via the odd transitions in the new basis due to the destructive interference of terms with even ℓ.

Fig. 6.3 exemplarily demonstrates the effect of the magnetic field rotation on the scattered radiation field. In the left graph the NFS intensity spectrum is plotted in first order for a B-field switching at $\tau_0 = 54.7$ ns (red dashed line) which corresponds to a minimum of the unperturbed spectrum. It can be seen that the initially σ-polarized light is converted to π-polarized light for times larger than τ_0 with a reduction factor of 1/2 in comparison to the unperturbed spectrum before switching. Moreover, the quantum beat period before and after switching remains unchanged since $\boldsymbol{E}^{(1)}$ given in Eq. (6.13) is completely determined by the initially driven $\Delta M = 0$ currents. For a switching at a maximum of the unperturbed spectrum (e.g. $\tau_0 = 31.6$ ns in the right graph of Fig. 6.3) the polarization before and after the magnetic field rotation is conserved whereas the quantum beat period changes because the absorption via $\Delta M = 0$ at $\tau = 0$ is re-emitted via the $\Delta M = \pm 1$ transitions for $\tau > \tau_0$.

In the following the most important aspects of NFS under a 90° magnetic field rotation from z to x for initially σ-polarized x-rays are summarized:

- switching at zero crossings of odd $\boldsymbol{\mathcal{A}}^{(1)}_{\ell,\mathrm{II}}$: $\tau_0 = (2n+1)\,\frac{\pi}{2}/\Omega_2$
  - correspond to **minima** of unperturbed spectrum
  - σ-polarized x-rays are converted to π-polarized for $\tau > \tau_0$
  - $\Delta M = \pm 1$ interfere destructively for $\tau > \tau_0$
  - NFS spectrum (before and after switching) determined by $\Delta M = 0$ transitions
  - absorption from even ℓ, reemission via even ℓ
- switching at zero crossings of even $\boldsymbol{\mathcal{A}}^{(1)}_{\ell,\mathrm{II}}$: $\tau_0 = n\,2\pi/\Omega_2$
  - correspond to **maxima** of unperturbed spectrum
  - σ-polarization is conserved due to the B-field rotation
  - $\Delta M = 0$ interfere destructively for $\tau > \tau_0$
  - NFS spectrum (after switching) determined by $\Delta M = \pm 1$ transitions
  - absorption from even ℓ, reemission via odd ℓ

Initially π-polarized x-rays

Following the same lines as for initially σ-polarized x-rays, the time independent amplitudes for incident π-polarization evaluate to (see App. D)

$$\boldsymbol{\mathcal{A}}^{(1)}_{\ell,\mathrm{II}}(\boldsymbol{k}) \propto \begin{cases} [\sin(\Omega_1\tau_0) + 3\sin(\Omega_3\tau_0)]\ \boldsymbol{e}_\sigma & \text{for} \quad \ell = \pm 1\ , \\ [\cos(\Omega_1\tau_0) + 3\cos(\Omega_3\tau_0)]\ \boldsymbol{e}_\pi & \text{for} \quad \ell = \pm 2\ , \\ [\sin(\Omega_1\tau_0) - \sin(\Omega_3\tau_0)]\ \boldsymbol{e}_\sigma & \text{for} \quad \ell = \pm 3\ . \end{cases} \tag{6.14}$$

Here, the amplitudes are given by a superposition of sine and cosine functions with frequencies Ω_1 and Ω_3 (belonging to the initially driven $\Delta M = \pm 1$ transitions). In

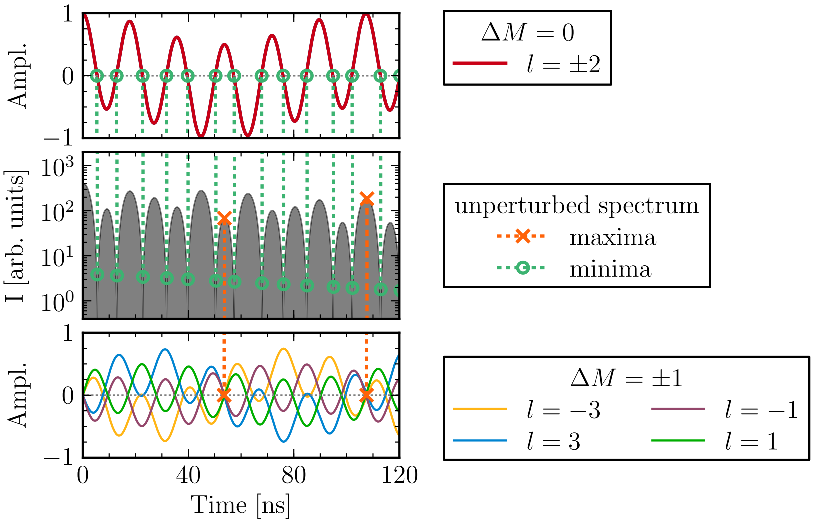

Figure 6.4: The same composition as in Fig. 6.2 for initially π-polarized x-rays. Here, the zero crossings of the amplitudes $\boldsymbol{\mathcal{A}}^{(1)}_{\ell,\mathrm{II}}$ with even ℓ coincide with minima of $|\boldsymbol{E}^{(1)}(\xi,\tau)|^2$, whereas the simultaneous zero crossings for all odd amplitudes fall on time instants corresponding to maxima of $|\boldsymbol{E}^{(1)}(\xi,\tau)|^2$.

Fig. 6.4 the amplitudes for even and odd ℓ are plotted together with the unperturbed NFS intensity spectrum $|\boldsymbol{E}^{(1)}(\xi,\tau)|^2$ analogously as in the case of initial σ-polarization. As seen from the figure, the roots of $\boldsymbol{\mathcal{A}}^{(1)}_{\ell=\pm 2,\mathrm{II}}$ coincide with the minima of the unperturbed spectrum. For the odd transitions it is much more difficult to find time instants where all amplitudes vanish at once. Nevertheless, the simultaneous roots of $\boldsymbol{\mathcal{A}}^{(1)}_{\ell=\pm 1,\mathrm{II}}$ and $\boldsymbol{\mathcal{A}}^{(1)}_{\ell=\pm 3,\mathrm{II}}$ exactly correspond to local maxima of the unperturbed, first order spectrum. However, in the case of initially π-polarized radiation the maxima of the spectrum need not to be zero points of the amplitudes.

Analogously to the case of initially σ-polarized x-rays, the amplitudes defined in Eq. (6.14) can be inserted into Eq. (6.6) in order to obtain an expression for the scattered radiation field in first order after magnetic switching. Since it is exactly the same procedure we restrict ourselves to presenting only the most important features:

- switching at zero crossings of even $\boldsymbol{\mathcal{A}}^{(1)}_{\ell,\mathrm{II}}$:
  - correspond to **minima** of unperturbed spectrum
  - π-polarized x-rays are converted to σ-polarized for $\tau > \tau_0$
  - $\Delta M = 0$ interfere destructively for $\tau > \tau_0$
  - NFS spectrum (before and after switching) determined by $\Delta M = \pm 1$ transitions
  - absorption from odd ℓ, reemission via odd ℓ
- switching at zero crossings of odd $\boldsymbol{\mathcal{A}}^{(1)}_{\ell,\mathrm{II}}$:

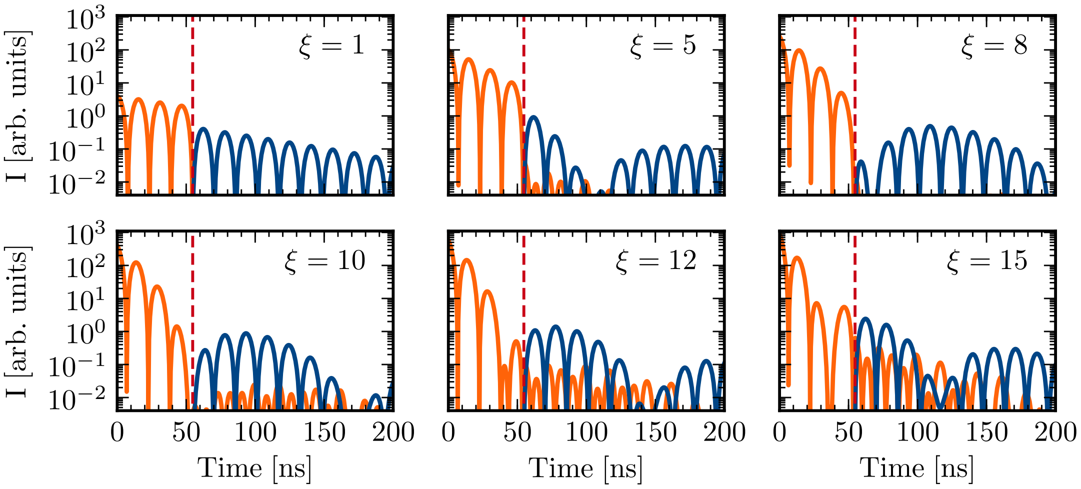

Figure 6.5: Effect of multiple scattering events. NFS intensity spectra $|\boldsymbol{E}(\xi,\tau)|^2$ with $p_{\max} = 14$ are shown for $\xi = 1$, $\xi = 5$, $\xi = 8$, $\xi = 10$, $\xi = 12$ and $\xi = 15$. A fixed switching moment of $\tau_0 = 54.7$ ns has been chosen corresponding to a minimum of unperturbed, first order spectrum. The incident radiation has been assumed to be σ-polarized. The color coding follows Fig. 6.3.

- correspond to **maxima** of unperturbed spectrum, but not all maxima are valid switching times
- π-polarization is conserved due to the B-field rotation
- $\Delta M = \pm 1$ interfere destructively for $\tau > \tau_0$
- NFS spectrum (after switching) determined by $\Delta M = 0$ transitions
- absorption from odd ℓ, reemission via even ℓ

6.2.2 Effect of multiple scattering

The moments of switching determined via Eq. (6.7) give full control over the first order scattering solution $\boldsymbol{E}^{(1)}$ involving only single scattering events. In particular for thin samples and small interaction times where the probability of multiple absorption and reemission events is strongly suppressed, $\boldsymbol{E}^{(1)}$ represents the dominant contribution to the NFS intensity spectrum. Hence, using $\boldsymbol{\mathcal{A}}^{(1)}_{\ell,\mathrm{II}}$ for the determination of τ_0 is sufficient to control the collective nuclear polarization response in the limit of thin targets and small times. The effect of multiple scattering contributions in dependence of the effective target thickness ξ is shown in Fig. 6.5. We have exemplarily chosen a fixed moment of switching $\tau_0 = 54.7$ ns which according to Eq. (6.6) converts initially σ-polarized x-ray photons into π-polarized states. In the cases of $\xi = 1$, $\xi = 5$ and $\xi = 8$ this behavior is clearly confirmed in Fig. 6.5. Increasing the target thickness further, leads to higher and higher distortions from the “wrong” polarization component due to multiple scattering effects not accounted for in Eq. (6.6). For instance, the relative contribution of the σ-polarized component after magnetic field rotation is more than doubled (3.4% to 7.2%) by going from from $\xi = 10$ to $\xi = 12$. At the latest starting with $\xi = 15$ (total distortion of around 14% after τ_0), the sole dominance of the first order $\boldsymbol{E}^{(1)}$ seems to break down and multiple scattering events start to play a distinct role, giving rise to scattered radiation of the "wrong" polarization, in particular immediately after the magnetic field rotation.

Note that the parameter regime of ξ where the first order polarization control is applicable, is also slightly dependent on the moment of switching τ_0. For instance, in the case of $\tau_0 = 54.7$ ns the polarization conversion works better for $\xi = 8$ in comparison to the smaller thickness of $\xi = 5$ (see Fig. 6.5). The reason is that $\tau_0 = 54.7$ ns is close to a minimum of the dynamical beat modulation for $\xi = 8$. Moving τ_0 to an earlier time, e.g. $\tau_0 = 39.1$ ns, clearly re-establishes the general trend of higher distortions in the case of thicker targets.

6.3 Control beyond the single scattering approximation

Eq. (6.6) describes the scattered radiation field in first order where only single scattering events are taken into account. As we have seen in the previous Section, the first order is the dominant order in the limit of thin targets and small interaction times. Consequently, the choice of τ_0 based on Eq. (6.7) is sufficient to dynamically control the polarization response of nuclear targets with small ξ. However, when applying timed rotations of the magnetic field for thicker targets, multiple scattering effects lead to distortions of the polarization purity already at effective target thicknesses larger than $\xi = 10$. This raises the question whether it is possible to have polarization control beyond the first scattering order, corresponding to a more accurate choice of τ_0.

To accomplish that, the total electric field given in Eq. (5.24) has to be rewritten as a sum of multiple scattering amplitudes

$$\boldsymbol{E}(\xi,\tau) = \boldsymbol{E}_0(\xi,\tau) + \boldsymbol{E}_1(\xi,\tau) + \boldsymbol{E}_2(\xi,\tau) + \cdots = \sum_{n=0}^{\infty} \boldsymbol{E}_n(\xi,\tau) \ , \tag{6.15}$$

where $\boldsymbol{E}_n$ describes the contribution to the scattered radiation field with exactly n absorption events for times $\tau > \tau_0$. This kind of decomposition is illustratively sketched in Fig. 6.6 for $\boldsymbol{E}_0$ and $\boldsymbol{E}_1$. We will show in the following that each term $\boldsymbol{E}_n$ can be written as a product of a time-independent amplitude controllable via τ_0 and some time-dependent factor, similar to Eq. (6.6). In particular $\boldsymbol{E}_0$ shows exactly the same behavior given in Eq. (6.6) except that the time-independent amplitudes become regulated by the effective target thickness.

In the remaining part of this Chapter we assume $\tau > \tau_0$, since we are mainly concerned about the scattered field after the moment of switching. For $\tau < \tau_0$ the solution is again determined by Eq. (6.4). The first step to decompose $\boldsymbol{E}$ into the form of Eq. (6.15) is to insert the recursion relation given by Eq. (5.27) into the perturbation expansion (5.24) leading to

$$\boldsymbol{E}(\xi,\tau) = \sum_{p=1}^{\infty} \frac{(-\xi)^p}{p!} \sum_{\ell} \boldsymbol{J}_\ell(\boldsymbol{k},\tau) \int_0^\tau \mathrm{d}\tau' \, \boldsymbol{J}_\ell^*(\boldsymbol{k},\tau') \cdot \boldsymbol{E}^{(p-1)}(\tau') \ . \tag{6.16}$$

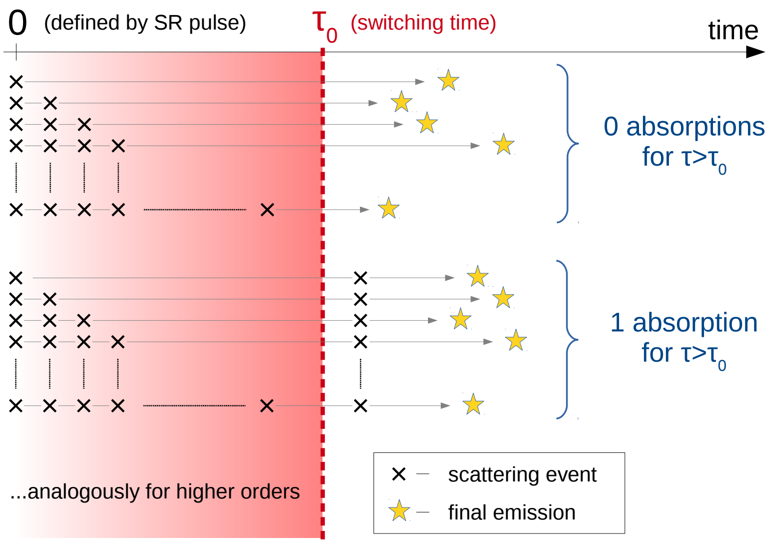

Figure 6.6: Decomposition of the scattered radiation field into contributions determined by the number of absorption events at times after the moment of magnetic field switching. The cases $\boldsymbol{E}_0$ and $\boldsymbol{E}_1$ are exemplarily shown corresponding to exactly 0 and 1 absorption events for $\tau > \tau_0$, respectively.

In order to further evaluate Eq. (6.16), the integration over τ' is split into two parts, an integral from 0 to τ_0 and one from τ_0 to τ. This splitting allows us to make use of the explicit time dependence of $\boldsymbol{J}^*_\ell$ and $\boldsymbol{J}_\ell$ given by Eqs. (5.32) and (5.45) for the time sectors I ($\tau < \tau_0$) and II ($\tau > \tau_0$), respectively. We obtain

$$\begin{aligned}\boldsymbol{E}(\xi,\tau) = &\sum_{p=1}^{\infty} \frac{(-\xi)^p}{p!} \sum_\ell \boldsymbol{J}_{\ell,\mathrm{II}}(\boldsymbol{k},\tau) \\ &\times \left(\int_0^{\tau_0} \mathrm{d}\tau'\, \boldsymbol{J}^*_{\ell,\mathrm{I}}(\boldsymbol{k},\tau') \cdot \boldsymbol{E}^{(p-1)}(\tau') + \int_{\tau_0}^{\tau} \mathrm{d}\tau'\, \boldsymbol{J}^*_{\ell,\mathrm{II}}(\boldsymbol{k},\tau') \cdot \boldsymbol{E}^{(p-1)}(\tau') \right) .\end{aligned} \tag{6.17}$$

Let us have a closer look at the $(p-1)^{\mathrm{th}}$ scattering amplitude $\boldsymbol{E}^{(p-1)}$ occurring in Eq. (6.17). In general, $\boldsymbol{E}^{(p-1)}$ can have multiple scattering contributions in both time regions, for times $\tau < \tau_0$ and for times $\tau > \tau_0$. For the further evaluation of the second integral it is helpful to divide $\boldsymbol{E}^{(p-1)}$ into a part where all the absorption events happen before the moment of switching, and a part with at least one absorption after τ_0. For this kind of splitting we make again use of the recursive solution in Eq. (5.27). Successively expressing $\boldsymbol{E}^{(p-1)}$ in terms of $\boldsymbol{E}^{(p-2)}$, $\boldsymbol{E}^{(p-2)}$ in terms of $\boldsymbol{E}^{(p-3)}$, etc., and by dividing the occurring time integrations into the regions $\tau < \tau_0$ and $\tau > \tau_0$, we obtain

$$\begin{aligned}
\boldsymbol{E}(\xi,\tau) &= \sum_{p=1}^{\infty} \frac{(-\xi)^p}{p!} \sum_{\ell} \boldsymbol{J}_{\ell,\mathrm{II}}(\boldsymbol{k},\tau) \Bigg(\int_0^{\tau_0} \mathrm{d}\tau'\, \boldsymbol{J}^*_{\ell,\mathrm{I}}(\boldsymbol{k},\tau') \cdot \boldsymbol{E}^{(p-1)}(\tau') \\
&\quad + \int_{\tau_0}^{\tau} \mathrm{d}\tau'\, \boldsymbol{J}^*_{\ell,\mathrm{II}}(\boldsymbol{k},\tau') \cdot \sum_{\ell'} \boldsymbol{J}_{\ell'}(\boldsymbol{k},\tau') \int_0^{\tau'} \mathrm{d}\tau''\, \boldsymbol{J}^*_{\ell'}(\boldsymbol{k},\tau'') \cdot \boldsymbol{E}^{(p-2)}(\tau'') \Bigg) \\
&= \sum_{p=1}^{\infty} \frac{(-\xi)^p}{p!} \sum_{\ell} \boldsymbol{J}_{\ell,\mathrm{II}}(\boldsymbol{k},\tau) \Bigg(\int_0^{\tau_0} \mathrm{d}\tau'\, \boldsymbol{J}^*_{\ell,\mathrm{I}}(\boldsymbol{k},\tau') \cdot \boldsymbol{E}^{(p-1)}(\tau') \\
&\quad + \int_{\tau_0}^{\tau} \mathrm{d}\tau'\, \boldsymbol{J}^*_{\ell,\mathrm{II}}(\boldsymbol{k},\tau') \cdot \sum_{\ell'} \boldsymbol{J}_{\ell',\mathrm{II}}(\boldsymbol{k},\tau') \int_0^{\tau_0} \mathrm{d}\tau''\, \boldsymbol{J}^*_{\ell',\mathrm{I}}(\boldsymbol{k},\tau'') \cdot \boldsymbol{E}^{(p-2)}(\tau'') \\
&\quad + \int_{\tau_0}^{\tau} \mathrm{d}\tau'\, \boldsymbol{J}^*_{\ell,\mathrm{II}}(\boldsymbol{k},\tau') \cdot \sum_{\ell'} \boldsymbol{J}_{\ell',\mathrm{II}}(\boldsymbol{k},\tau') \int_{\tau_0}^{\tau'} \mathrm{d}\tau''\, \boldsymbol{J}^*_{\ell',\mathrm{II}}(\boldsymbol{k},\tau'') \cdot \boldsymbol{E}^{(p-2)}(\tau'') \Bigg) \\
&= \sum_{p=1}^{\infty} \frac{(-\xi)^p}{p!} \sum_{\ell} \boldsymbol{J}_{\ell,\mathrm{II}}(\boldsymbol{k},\tau) \Bigg(\int_0^{\tau_0} \mathrm{d}\tau'\, \boldsymbol{J}^*_{\ell,\mathrm{I}}(\boldsymbol{k},\tau') \cdot \boldsymbol{E}^{(p-1)}(\tau') \\
&\quad + \int_{\tau_0}^{\tau} \mathrm{d}\tau'\, \boldsymbol{J}^*_{\ell,\mathrm{II}}(\boldsymbol{k},\tau') \cdot \sum_{\ell'} \boldsymbol{J}_{\ell',\mathrm{II}}(\boldsymbol{k},\tau') \int_0^{\tau_0} \mathrm{d}\tau''\, \boldsymbol{J}^*_{\ell',\mathrm{I}}(\boldsymbol{k},\tau'') \cdot \boldsymbol{E}^{(p-2)}(\tau'') \\
&\quad + \int_{\tau_0}^{\tau} \mathrm{d}\tau'\, \boldsymbol{J}^*_{\ell,\mathrm{II}}(\boldsymbol{k},\tau') \cdot \sum_{\ell'} \boldsymbol{J}_{\ell',\mathrm{II}}(\boldsymbol{k},\tau') \int_{\tau_0}^{\tau'} \mathrm{d}\tau''\, \boldsymbol{J}^*_{\ell',\mathrm{II}}(\boldsymbol{k},\tau'') \cdot \sum_{\ell''} \boldsymbol{J}_{\ell'',\mathrm{II}}(\boldsymbol{k},\tau'') \\
&\qquad \times \int_0^{\tau_0} \mathrm{d}\tau'''\, \boldsymbol{J}^*_{\ell'',\mathrm{I}}(\boldsymbol{k},\tau''') \cdot \boldsymbol{E}^{(p-3)}(\tau''') \\
&\quad + \ldots \Bigg) \,.
\end{aligned} \tag{6.18}$$

The part $\boldsymbol{E}_0$ with no absorption events after τ_0 can be easily extracted from Eq. (6.18). It evaluates to

$$\begin{aligned}
\boldsymbol{E}_0(\xi,\tau) &= \sum_{p=1}^{\infty} \frac{(-\xi)^p}{p!} \sum_{\ell} \boldsymbol{J}_{\ell,\mathrm{II}}(\boldsymbol{k},\tau) \int_0^{\tau_0} \mathrm{d}\tau'\, \boldsymbol{J}^*_{\ell,\mathrm{I}}(\boldsymbol{k},\tau') \cdot \boldsymbol{E}^{(p-1)}(\tau') \\
&= \sum_{\ell} \boldsymbol{J}_{\ell,\mathrm{II}}(\boldsymbol{k},\tau) \int_0^{\tau_0} \mathrm{d}\tau'\, \boldsymbol{J}^*_{\ell,\mathrm{I}}(\boldsymbol{k},\tau') \cdot \sum_{p=1}^{\infty} \frac{(-\xi)^p}{p!} \boldsymbol{E}^{(p-1)}(\tau') \\
&= \sum_{\ell} \boldsymbol{J}_{\ell,\mathrm{II}}(\boldsymbol{k},\tau) \int_0^{\tau_0} \mathrm{d}\tau'\, \boldsymbol{J}^*_{\ell,\mathrm{I}}(\boldsymbol{k},\tau') \cdot \sum_{p=0}^{\infty} \frac{(-\xi)^{p+1}}{(p+1)!} \boldsymbol{E}^{(p)}(\tau') \,,
\end{aligned} \tag{6.19}$$

where we first changed the order of summations and afterwards renamed the summation index p to $p+1$. Employing furthermore the explicit time dependence of $\boldsymbol{J}_{\ell,\mathrm{II}}$ given in Eqs. (5.45), we obtain the following form

$$\boldsymbol{E}_0(\xi,\tau) = \sum_{\ell} \boldsymbol{\mathcal{A}}_{\ell,\mathrm{II}}(\boldsymbol{k},\xi)\, \mathrm{e}^{-\mathrm{i}\Omega_\ell(\tau-\tau_0)-\tau/2} \,, \tag{6.20}$$

with the time-independent amplitude $\boldsymbol{\mathcal{A}}_{\ell,\mathrm{II}}$ given by

$$\boldsymbol{\mathcal{A}}_{\ell,\mathrm{II}}(\boldsymbol{k},\xi) = \boldsymbol{j}_{\ell,\mathrm{II}}(\boldsymbol{k}) \sum_{\ell'} \mathrm{e}^{-\mathrm{i}\Omega_\ell \tau_0} \mathcal{D}^{I_\mathrm{g}}_{M_\mathrm{g} M'_\mathrm{g}}(\alpha,\beta,\gamma) \\ \times \mathcal{D}^{I_\mathrm{e}\,*}_{M_\mathrm{e} M'_\mathrm{e}}(\alpha,\beta,\gamma) \left(\int_0^{\tau_0} \mathrm{d}\tau' \, \boldsymbol{J}^*_{\ell',\mathrm{I}}(\boldsymbol{k},\tau') \cdot \sum_{p=0}^{\infty} \frac{(-\xi)^{p+1}}{(p+1)!} \boldsymbol{E}^{(p)}(\tau') \right) . \quad (6.21)$$

In contrast to the first order amplitude $\boldsymbol{\mathcal{A}}^{(1)}_{\ell,\mathrm{II}}$ defined in Eq. (6.7), $\boldsymbol{\mathcal{A}}_{\ell,\mathrm{II}}$ depends on the effective target thickness ξ. However, it is possible to express $\boldsymbol{\mathcal{A}}_{\ell,\mathrm{II}}$ in terms of ξ-independent amplitudes $\boldsymbol{\mathcal{A}}^{(p)}_{\ell,\mathrm{II}}$ by explicitly writing the summation over the scattering orders p,

$$\boldsymbol{\mathcal{A}}_{\ell,\mathrm{II}}(\boldsymbol{k},\xi) = -\frac{\xi}{1!}\boldsymbol{\mathcal{A}}^{(1)}_{\ell,\mathrm{II}}(\boldsymbol{k}) + \frac{\xi^2}{2!}\boldsymbol{\mathcal{A}}^{(2)}_{\ell,\mathrm{II}}(\boldsymbol{k}) - \frac{\xi^3}{3!}\boldsymbol{\mathcal{A}}^{(3)}_{\ell,\mathrm{II}}(\boldsymbol{k}) \pm \cdots = \sum_{p=1}^{\infty} \frac{(-\xi)^p}{p!}\boldsymbol{\mathcal{A}}^{(p)}_{\ell,\mathrm{II}}(\boldsymbol{k}) , \quad (6.22)$$

with

$$\boldsymbol{\mathcal{A}}^{(p)}_{\ell,\mathrm{II}}(\boldsymbol{k}) = \boldsymbol{j}_{\ell,\mathrm{II}}(\boldsymbol{k}) \sum_{\ell'} \mathrm{e}^{-\mathrm{i}\Omega_\ell \tau_0} \mathcal{D}^{I_\mathrm{g}}_{M_\mathrm{g} M'_\mathrm{g}}(\alpha,\beta,\gamma) \\ \times \mathcal{D}^{I_\mathrm{e}\,*}_{M_\mathrm{e} M'_\mathrm{e}}(\alpha,\beta,\gamma) \left(\int_0^{\tau_0} \mathrm{d}\tau' \, \boldsymbol{J}^*_{\ell',\mathrm{I}}(\boldsymbol{k},\tau') \cdot \boldsymbol{E}^{(p-1)}(\tau') \right) . \quad (6.23)$$

This decomposition clearly proves that Eq. (6.20) describes the scattered field beyond first order. In the limit of small ξ, single scattering events dominate the nuclear scattering process such that $\boldsymbol{\mathcal{A}}_{\ell,\mathrm{II}}$ reduces essentially to the first order amplitude $\boldsymbol{\mathcal{A}}^{(1)}_{\ell,\mathrm{II}}$. In this case, the higher orders $p > 1$ can be treated as small corrections.

For large ξ, also higher orders in $\boldsymbol{E}_n$ gain in importance. These higher orders can be evaluated in the same manner like $\boldsymbol{E}_0$. For instance, in the case of exactly one absorption event after τ_0, we obtain

$$\boldsymbol{E}_1(\xi,\tau) = \sum_{\ell} \boldsymbol{J}_{\ell,\mathrm{II}}(\boldsymbol{k},\tau) \int_{\tau_0}^{\tau} \mathrm{d}\tau' \, \boldsymbol{J}^*_{\ell,\mathrm{II}}(\boldsymbol{k},\tau') \cdot \left(\sum_{\ell'} \boldsymbol{\mathcal{B}}_{\ell',\mathrm{II}}(\boldsymbol{k},\xi) \, \mathrm{e}^{-\mathrm{i}\Omega_{\ell'}(\tau'-\tau_0)-\tau'/2} \right) , \quad (6.24)$$

where the amplitudes $\boldsymbol{\mathcal{B}}_{\ell,\mathrm{II}}$ can be written as

$$\boldsymbol{\mathcal{B}}_{\ell,\mathrm{II}}(\boldsymbol{k},\xi) = \frac{\xi^2}{2!}\boldsymbol{\mathcal{A}}^{(1)}_{\ell,\mathrm{II}}(\boldsymbol{k}) - \frac{\xi^3}{3!}\boldsymbol{\mathcal{A}}^{(2)}_{\ell,\mathrm{II}}(\boldsymbol{k}) + \frac{\xi^4}{4!}\boldsymbol{\mathcal{A}}^{(3)}_{\ell,\mathrm{II}}(\boldsymbol{k}) \mp \cdots = \sum_{p=1}^{\infty} \frac{(-\xi)^{p+1}}{(p+1)!}\boldsymbol{\mathcal{A}}^{(p)}_{\ell,\mathrm{II}}(\boldsymbol{k}) . \quad (6.25)$$

As seen from Eqs. (6.24) and (6.25), the magnetic field rotation at τ_0 can only influence the nuclear response of excitations created earlier, in agreement with the principle of causality. Note that based on Eqs. (6.20) and (6.24), it is straightforward to generalize these results to the n^{th} order $\boldsymbol{E}_n$.

In Fig. 6.7, numerical evaluated NFS intensity spectra $|\boldsymbol{E}(\xi,\tau)|^2$ including all scattering orders up to $p_{\mathrm{max}} = 14$ are presented for effective target thicknesses $\xi = 1$, $\xi = 5$, $\xi = 8$, $\xi = 10$, $\xi = 12$ and $\xi = 15$. Analogously to Fig. 6.5, a magnetic field switching is applied

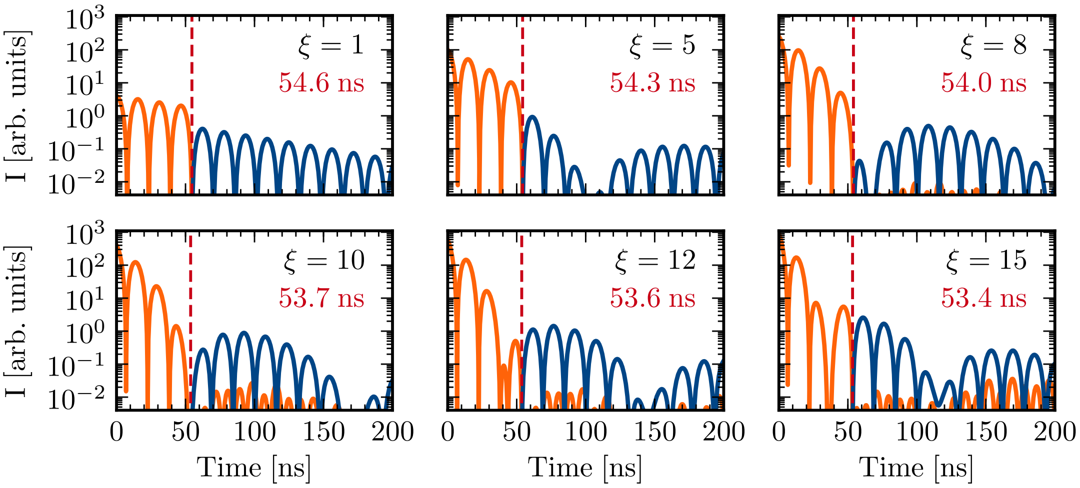

Figure 6.7: Polarization control beyond first order. Intensity spectra are shown analogously to Fig. 6.5. The difference is that the switching moments (red dashed lines) are calculated beyond first order by numerically evaluating $\boldsymbol{\mathcal{A}}_{\ell,\mathrm{II}}$. The times τ_0 (written in red) depend on the effective target thickness ξ.

such that the incident σ-polarization is expected to be scattered into π-polarization states. In contrast to Fig. 6.5, the moments of switching in Fig. 6.7 are chosen in dependence of the target thickness ξ by numerically evaluating the amplitudes $\boldsymbol{\mathcal{A}}_{\ell,\mathrm{II}}$ given in Eq. (6.21). Comparing the polarization control beyond first order (Fig. 6.7) with the first order results (Fig. 6.5), it can be verified that the polarization purity after τ_0 is strongly increased especially for large ξ. Regarding the integrated intensity for times larger than τ_0, the distortions from the "wrong" polarization state could be optimized for all considered ξ values to a relative contribution below 3.2%. In particular for $\xi = 15$, this corresponds to an improvement in the polarization purity by a factor of approximatively 4.5. In the limit of thin samples, the moments of switching deviate only weakly from τ_0 calculated via the first order approximation (6.7). Increasing the target thickness leads to a larger and larger deviation, for instance, from $\xi = 1$ to $\xi = 15$ the discrepancy increases from 0.1 ns to 1.3 ns. Having a closer look at the case $\xi = 15$ reveals that in particular immediately after the B-field rotation the purity of the polarization response is strongly enhanced in comparison to the first order result. At times much larger than τ_0 distortions from higher orders $\boldsymbol{E}_n$ (absorption and reemission events after τ_0) start to play a role not influenceable via the magnetic field rotation. Nevertheless, a switching moment determined by the amplitudes $\boldsymbol{\mathcal{A}}_{\ell,\mathrm{II}}$ (including all scattering events before τ_0) is able to control the nuclear polarization response for targets up to $\xi = 12$. For samples with $\xi \geq 15$, distortions from the "wrong" polarization are expected to become stronger due to stronger contributions from higher orders $\boldsymbol{E}_n$ with $n \neq 0$. In the limit of thin targets ($\xi \leq 8$), the first order polarization control seems to be sufficient.

Chapter 7

Logical gates with polarization-encoded single x-rays

Due to the exponentially increasing computation complexity over the years, the number of transistors per chip grows continuously, becoming technically more and more demanding. It is therefore a crucial objective of information technology to build computing devices (classical as well as quantum mechanical) in a more and more compact form. Photons, for instance, can be used as flying information carriers which enable fast and efficient information processing schemes sustainable over long distances. However, applying Moore's law [243] to photonic circuits, it turns out that the size of future devices will be quickly limited by the diffraction limit of the used photons ($\sim \mu$m for optical wavelengths). The usage of x-ray photons would drastically reduce the fundamental limitation on nanoscale photonic circuits because of the remarkable focusing abilities in the keV photonic energy range. Currently, x-ray beams have been focused down to the nm range [10–12], and today's x-ray waveguides typically employ a spatial confinement between ten up to tens of nm [124]. The potential sub-Å spatial resolution of x-rays [126] promotes the vision of future information storage and processing schemes in their most compact form, namely on the scale of single atoms.

While atomic transitions are naturally used to resonantly manipulate optical photons, nuclear transitions may be the elementary counterparts for x-rays. For quantum optics applications, nuclear transitions present a clean, well isolated system with very long coherence times, while x-rays attract with their good detection efficiency, penetration power and spatial resolution. Admittedly, experimental challenges at the large coherent x-ray source facilities today will require a different paradigm compared to tabletop optical experiments. However, control at the single-photon level has been recently demonstrated also in a laboratory-scale Mössbauer setup, where the coherent manipulation of waveforms of individual x-rays has been achieved [100]. Such control procedures operated at single-photon nuclear interfaces along with the recent development in x-ray optics [26, 27, 115–119] open the perspective to extend fields like quantum information and quantum communication to photon energies in the keV-range.

The extension of information science to x-ray wavelengths requires precise control tools not only for the waveforms, but also for polarization, frequency and phase of single-photon wave packets. In this Chapter, we concentrate on the polarization properties of x-ray photons. We investigate theoretically how polarization-encoded single x-rays can be coherently processed by means of resonant nuclear interactions via the procedure introduced in Chap. 6. The main result of this Chapter is the design of logical gates for single x-ray photons. The platform where it is possible to integrate unary logical

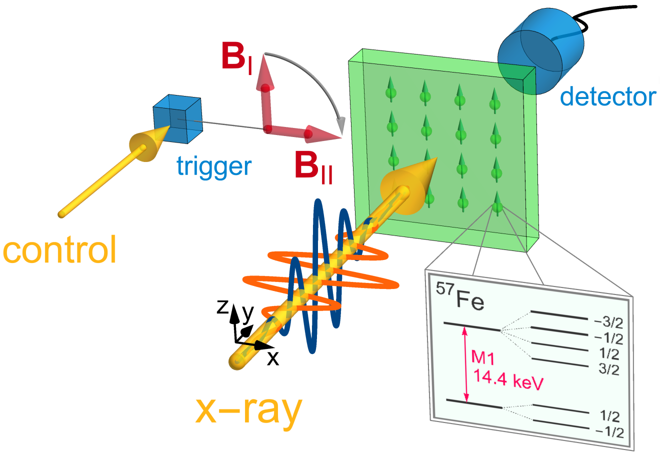

Figure 7.1: Nuclear forward scattering setup. σ- (orange) or π-polarized (blue) x-rays scatter off a nuclear target in the forward direction. A spatially separated control photon triggers a magnetic field rotation from the z- to the x-axis. The hyperfine-split nuclear level scheme of ^{57}Fe is illustrated in the inset.

operations for x-rays within a single setup is introduced right at the beginning in Sec. 7.1. Afterwards, in Sec. 7.2 it is explicitly shown how the single-input logical gates can be implemented on this platform by polarization control schemes employing magnetic field rotations. Sec. 7.3 is finally devoted to binary logical operations. Introducing a second, temporally synchronized control photon opens the possibility to put forward Boolean operations with x-rays.

7.1 The universal platform for single x-ray manipulations

Analogously to Chaps. 5 and 6, the setup of nuclear resonant scattering is considered (see Fig. 7.1). A broadband x-ray pulse resonant to the 14.4 keV Mössbauer transition in ^{57}Fe impinges on an iron target. In the presence of a nuclear hyperfine magnetic field, the ground and excited nuclear states of ^{57}Fe undergo Zeeman splitting according to their spin values as illustrated in the inset of Fig. 7.1. Due to the Fourier limit of the temporally narrow incident x-ray pulses, several polarization-selected hyperfine transitions labeled with ℓ can be simultaneously driven leading to well-known quantum beats in the NFS intensity spectrum [103]. For instance, initially σ-(π-)polarized x-rays couple to all $\Delta M = 0$ ($\Delta M = \pm 1$) transitions provided the magnetic field $\boldsymbol{B}_{\mathrm{I}}$ points along the z-direction. Since only those photons are coherently scattered into the forward direction for which the nucleus returns to its original ground state Zeeman level, the σ-(π-)polarization is conserved in the course of NFS with constant hyperfine field $\boldsymbol{B}_{\mathrm{I}}$ as explained in Sec. 6.1.

Abrupt rotations of the nuclear hyperfine magnetic field offer means of polarization control of the nuclear signal as shown in Secs. 6.2 and 6.3. The magnetic field at the nuclear target $\boldsymbol{B}_{\mathrm{I}}$ is initially assumed to be constant and to point along the z-axis. A fast rotation of the magnetic field following nuclear excitation (for instance, to $\boldsymbol{B}_{\mathrm{II}}$

parallel to the x-axis by a 90° counterclockwise rotation around the y-direction) leads to an almost instantaneous change of the quantization axis and a redistribution of the collective excitation among the Zeeman levels. Each initially excited nuclear current [159, 174] is transferred into a sextet of new currents which can interfere constructively or destructively depending on the switching geometry and exact rotation moment τ_0 [96].

We consider ^{57}Fe-enriched FeBO$_3$ as target which is a canted antiferromagnet. The FeBO$_3$ crystal attracts with a very pure nuclear signal [244] and excellent switching properties of the magnetic field. Practically, a constant, weak magnetic field first induces a magnetization of the nuclear spins. Applying a second, pulsed magnetic field (stronger than the constant B-field) leads to a fast realignment of the hyperfine fields while keeping the nuclear magnetic moment unchanged. Experimentally the timescale of such abrupt rotations has been reported to be faster than 4 ns [245] due to the special magnetization properties of FeBO$_3$. In the following, we will consider an effective target thickness of $\xi = 10$.

At present, typically in x-ray-nuclear-transition interfaces only one excitation, i.e., one resonant x-ray photon, exists in the system at any given time [104]. The photon is in a coherent state rather than a Fock state, allowing for a semi-classical treatment of the light-nucleus interaction [4] as introduced in Chaps. 5 and 6. Entanglement occurs in the system only in its single-photon version [112, 246], by having the x-ray photon entangle two spatially or temporally separated field modes. Furthermore, in contrast to nuclear magnetic resonance techniques [125] that employ nuclear ground state spins as information carriers and process them with microwave fields, here we envisage magnetic fields to modify the properties of an x-ray transition to an excited nuclear state. These are rather unusual factors for the implementation of logical operations as known from the optical [247–251] or microwave regimes [252–255], that call for a new approach.

7.2 Unary logical operations

Classically, there are four single-input, i.e, unary, logic gates: the Identity leaves the target bit unchanged; the True and False operations give “T” and “F”, respectively, independent of the input; and the Negation flips the operated bit from either “F” to “T” or from “T” to “F” [see truth tables in Fig. 7.2(b)]. The photonic information carriers can be encoded as x-ray orthogonal polarization states, for instance “F” as π- and “T” as σ-polarization. The unary gates for polarization-encoded x-rays can be implemented in resonant NFS by making use of the polarization control scheme introduced in Chap. 6. There it has been shown that linear polarizations states can be converted into their orthogonal counterparts by applying a timed 90°-rotation (from z to x) of the magnetic field as schematically illustrated in Fig. 6.1. In order to realize logical operations within this setup, switching instances τ_0 have to be found where σ- and π-polarizations are simultaneously converted into (pure) opposite polarization states.

Let us discuss the finding of these switching instants τ_0 at the example of the Negation. In this case, the moment of switching has to be chosen such that initially σ- and initially π-polarized x-rays are scattered into π- and σ-polarization states, respectively. This requirement translates to finding an instance τ_0 where the amplitudes $\boldsymbol{\mathcal{A}}_{\ell=\pm1,\pm3,\mathrm{II}}$

(a) Unary logical gates in the course of NFS

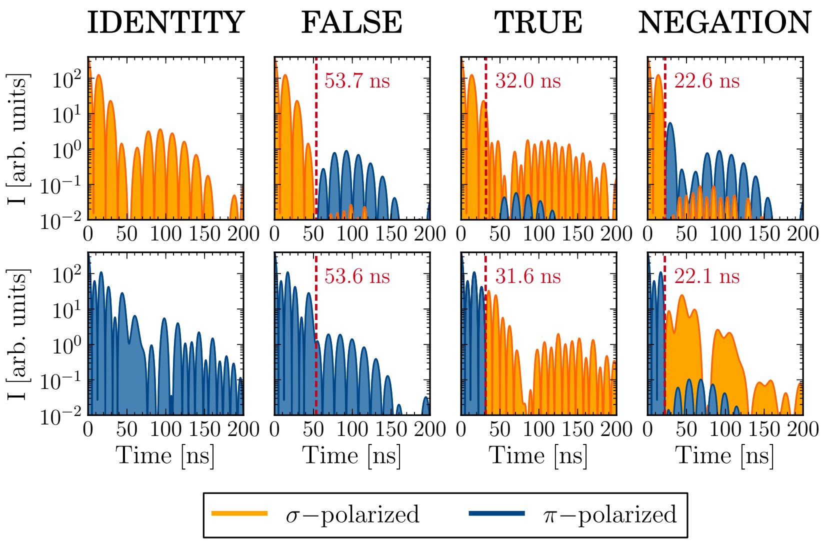

(b) Truth tables for Identity, False, True and Negation.

In	Out
F	F
T	T

In	Out
F	F
T	F

In	Out
F	T
T	T

In	Out
F	T
T	F

Figure 7.2: (a) NFS intensity spectra with an optical depth of ξ=10 are shown for initially σ- (top row) and $\pi-$polarized (bottom row) x-rays. The switching times τ_0 (red dashed lines) determine the implemented logical operation. (b) Truth tables for the logical Identity, False, True and Negation are presented.

for $\boldsymbol{e}_\mathrm{p} = \boldsymbol{e}_\sigma$ and $\boldsymbol{\mathcal{A}}_{\ell=\pm 2,\mathrm{II}}$ for $\boldsymbol{e}_\mathrm{p} = \boldsymbol{e}_\pi$ identically vanish at the same time. Numerically evaluating Eq. (6.21), we can prove that such almost simultaneous switching times exist leading to the desired behavior for $\boldsymbol{E}_0$ for times $\tau > \tau_0$ [see Eq. (6.20)]. Following this procedure for the Identity, True and False operations, the unary x-ray gates can be implemented within the same setup by choosing the proper τ_0 [256].

Our results are presented in Fig. 7.2. In the top row the incident radiation is σ-polarized (orange line and filling) whereas the bottom row shows the scattered photon yield for initially π-polarized x-rays (blue line and filling). The numerical results for the scattered field shown in Fig. 7.2(a) include all scattering orders up to $p_\mathrm{max} = 14$ which is sufficient for an effective target thickness of $\xi = 10$. Fig. 7.2 shows that depending on the moments of magnetic field rotation, it is possible to convert orthogonal polarizations into each other in the course of NFS. For instance, a magnetic field rotation of 90° at $\tau \approx 22.3$ ns simultaneously converts σ into π and vice versa as shown in the last column of Fig. 7.2(a), successfully implementing the logical Negation for all times $\tau > \tau_0$. In the same manner, it is also possible to realize the True, False and Identity operations. The latter does not need any switching of the magnetic field since the chosen geometry conserves σ- and π-polarization in the case of static hyperfine fields.

	Identity	False	True	Negation
ϵ^{σ} (%)	0	95.2	93.5 (92.9)	87.4
ϵ^{π} (%)	0	92.5	82.9	73.6
η^{σ} (%)	100	97.0	98.3 (99.2)	95.9
η^{π} (%)	100	99.4	99.9	99.3

Table 7.1: Loss rate ε and probability of realization η are presented for the case of optimized switching moments as used in Fig. 7.2. Superscripts σ and π refer to initial polarization state of the incoming radiation.

In order to quantify the success rate of the implemented x-ray gates, the measures ε and η are introduced via

$$\varepsilon = \frac{\int_0^{\tau_0} \mathrm{d}\tau \left|\boldsymbol{E}(\xi,\tau)\right|^2}{\int_0^{\infty} \mathrm{d}\tau \left|\boldsymbol{E}(\xi,\tau)\right|^2} = \frac{I_{\tau<\tau_0}}{I_{\mathrm{tot}}} \ , \tag{7.1}$$

and

$$\eta = \frac{\int_{\tau_0}^{\infty} \mathrm{d}\tau \left|\boldsymbol{E}_{\mathrm{gate}}(\xi,\tau)\right|^2}{\int_{\tau_0}^{\infty} \mathrm{d}\tau \left|\boldsymbol{E}(\xi,\tau)\right|^2} = \frac{I_{\mathrm{gate}}}{I_{\tau>\tau_0}} \ . \tag{7.2}$$

The quantity ε is defined as the integrated intensity for times smaller than the moment of switching $I_{\tau<\tau_0}$ divided by the total integrated intensity I_{tot}. Since the gate operation can be only realized for $\tau > \tau_0$, ε gives a measure of the intensity loss at times $\tau < \tau_0$. Due to multiple scattering events, the scattered radiation field after τ_0 also contains distortions from the "wrong" polarization output. The quantity η describes the probability of realization for the x-ray gates for times $\tau > \tau_0$. In Eq. (7.2), $\boldsymbol{E}_{\mathrm{gate}}$ corresponds to the polarization component of a successful gate operation, e.g., in the case of the True: $\boldsymbol{E}_{\mathrm{gate}} = \boldsymbol{E} \cdot \boldsymbol{e}_{\sigma}$.

In Table 7.1, numerical values ε and η are presented for the realizations shown in Fig. 7.2 in dependence of the initial polarization state. Since the Identity operation is accomplished without any switching, it shows no loss and a success rate of 100%. The non-trivial cases, the False, True and Negation, in particular suffer from high loss rates, larger than 70%. The probabilities of realization η for $\tau > \tau_0$ approach values close to unity. Even in the case of the Negation for initially σ-polarized x-rays which represents the worst scenario in terms of η, a success rate of 95.9% is reached.

In general, the polarization purity of the scattered radiation after the magnetic field switching is limited by three factors. First, in our choice of τ_0 we rely on Eq. (6.21) in which we have disregarded the possibility of further multiple scattering after the magnetic field switching at τ_0. This approximation leads to small polarization mixing in the case of $\xi = 10$ as shown by the complete numerical calculation, see Fig. 7.2(a). Thereby, the unwanted polarization component contributes less than 5% to the total intensity after τ_0, see Table 7.1. Second, theoretically the switching times for an individual unary gate may differ by up to 0.5 ns depending on whether the incident radiation is σ- or π polarized. For instance, in the case of the Negation unary gate, $\tau_0^{\sigma} = 22.6$ ns and $\tau_0^{\pi} = 22.1$ ns

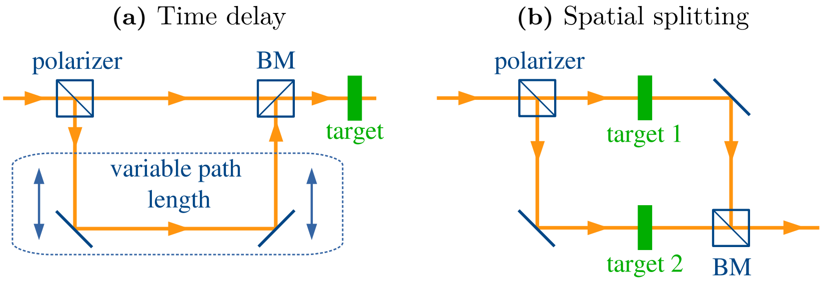
(a) Time delay

(b) Spatial splitting

Figure 7.3: The initial x-ray pulse can be temporally (a) or spatially (b) split depending on its polarization.

[these are the values used in Fig. 7.2(a)]. Even if we choose an averaged switching time in between, the calculated probability of realization η is still better than 95% for all four unary gates. Third, so far experimentally the switching time is known only to be less than 4 ns [245] for a setup employing ^{57}Fe-enriched FeBO$_3$ [257, 258]. However, the good performance of switching experiments [96, 239] indicates that the magnetic field rotation occurs on a shorter time than 4 ns. Already a rotation duration of 1 ns, leading to 1 ns uncertainty of τ_0 corresponds to $\eta = 90\%$ for the most affected case of the Negation gate, motivating thus improvements in the experimental determination and control of the fast switching instant τ_0.

Beside perturbations from the "wrong" polarization component, the condition $\tau > \tau_0$ strongly reduces the total probabilities of realization, since photons released before the time τ_0 defined by the vertical dashed line in Fig. 7.2(a) are lost. Rotations at late times therefore lead inevitably to significant losses ε, in the case of the logical Negation, for instance, in average more than 80% of the scattered photons. In the following we introduce two approaches that circumvent some of the depicted limitations.

A first approach is to introduce a polarization-sensitive time delay line by using a polarizer as shown in Fig. 7.3(a). The instant of nuclear excitation becomes then dependent on the polarization of the incident SR pulse. Since the polarization is assumed to be either σ or π initially, the time delay can be chosen such that the two switching times exactly match and losses are minimized. For instance, in order to implement the logical Negation via a switching time of 6.9 ns, the π-polarization needs to be delayed by 1.9 ns which reduces the losses from approx. 80% to approx. 38% in the case of initially π-polarized light. Practically, such a time delay line [259, 260] can be realized with modern x-ray optics like channel-cut silicon crystals as polarizers [133, 134, 261] and almost 100% reflecting x-ray mirrors [118]. In Refs. [262, 263], for instance, 8 keV photons have been temporally delayed up to 3 ns.

Similarly, in a second approach the polarizer can be used to spatially split the SR pulse in order to use two separated nuclear targets (see Fig. 7.3(b)). The magnetic field rotations can be then chosen independently of each other. Analogously to the first approach, the switching times can then be optimized individually for each input polarization state potentially leading to theoretical probabilities of realization larger than 95%. The two spatially separated paths are later on recombined via a beam mixer

BM [262].

So far we have restricted ourselves to the case where the incoming photon has been either σ- or π-polarized. What about single-photon states being initially in a quantum mechanical superposition of σ and π? Are the logical gates still working for such superposition states? In order to answer these questions, let us consider the superposition

$$|\Psi\rangle = \alpha|\sigma\rangle + \beta|\pi\rangle \ , \tag{7.3}$$

where $|\sigma\rangle$ and $|\pi\rangle$ denote σ- and π-polarization states, respectively, and α and β are some arbitrary complex amplitudes. Following the notation of Chaps. 5 and 6, $|\Psi\rangle$ represents the incoming radiation and can be written as

$$\boldsymbol{E}_{\mathrm{in}}(\tau) = (\alpha\boldsymbol{e}_\sigma + \beta\boldsymbol{e}_\pi)\delta(\tau) \ . \tag{7.4}$$

In the following, we will evaluate how the scattered radiation field looks like for an input state given in Eq. (7.4). In order to do so, we first have a look at the single scattering amplitude $\boldsymbol{E}^{(1)}$ which is completely determined by $\boldsymbol{\mathcal{A}}^{(1)}_{\ell,\mathrm{I}}$ for $\tau < \tau_0$ and $\boldsymbol{\mathcal{A}}^{(1)}_{\ell,\mathrm{II}}$ for $\tau > \tau_0$. Inserting Eq. (7.4) into Eq. (6.5) and Eq. (6.7), respectively, leads to

$$\begin{aligned}\boldsymbol{\mathcal{A}}^{(1)}_{\ell,\mathrm{I}}(\boldsymbol{k}) &= \boldsymbol{j}_{\ell,\mathrm{I}}(\boldsymbol{k})\left(\boldsymbol{j}^*_{\ell,\mathrm{I}}(\boldsymbol{k})\cdot\left(\alpha\boldsymbol{e}_\sigma + \beta\boldsymbol{e}_\pi\right)\right)\\ &= \alpha{\boldsymbol{\mathcal{A}}^{(1)}_{\ell,\mathrm{I}}}^{\sigma}(\boldsymbol{k}) + \beta{\boldsymbol{\mathcal{A}}^{(1)}_{\ell,\mathrm{I}}}^{\pi}(\boldsymbol{k})\end{aligned} \tag{7.5}$$

and

$$\begin{aligned}\boldsymbol{\mathcal{A}}^{(1)}_{\ell,\mathrm{II}}(\boldsymbol{k}) &= \boldsymbol{j}_{\ell,\mathrm{II}}(\boldsymbol{k})\sum_{\ell'}\mathrm{e}^{-\mathrm{i}\Omega_\ell\tau_0}\mathcal{D}^{I_{\mathrm{g}}}_{M_{\mathrm{g}}M'_{\mathrm{g}}}(\alpha,\beta,\gamma)\mathcal{D}^{I_{\mathrm{e}}\,*}_{M_{\mathrm{e}}M'_{\mathrm{e}}}(\alpha,\beta,\gamma)\\ &\quad\times\int_0^{\tau_0}\mathrm{d}\tau'\,\boldsymbol{J}^*_{\ell',\mathrm{I}}(\boldsymbol{k},\tau')\cdot(\alpha\boldsymbol{e}_\sigma + \beta\boldsymbol{e}_\pi)\delta(\tau')\\ &= \alpha{\boldsymbol{\mathcal{A}}^{(1)}_{\ell,\mathrm{II}}}^{\sigma}(\boldsymbol{k}) + \beta{\boldsymbol{\mathcal{A}}^{(1)}_{\ell,\mathrm{II}}}^{\pi}(\boldsymbol{k}) \ .\end{aligned} \tag{7.6}$$

In both cases, the amplitudes split up into a part determined by the σ-component of the incoming x-ray pulse $\boldsymbol{E}_{\mathrm{in}}$ and a part originating from the π-component of $\boldsymbol{E}_{\mathrm{in}}$. In order to obtain a similar decomposition of the second order amplitudes $\boldsymbol{\mathcal{A}}^{(2)}_{\ell,\mathrm{II}}(\boldsymbol{k})$, Eq. (6.4) is used to express $\boldsymbol{E}^{(1)}$ in terms of the amplitudes $\boldsymbol{\mathcal{A}}^{(1)}_{\ell,\mathrm{I}}$ for $\tau < \tau_0$. Inserting subsequently Eq. (7.5) into Eq. (6.4) and then into Eq. (6.23) leads directly to

$$\begin{aligned}\boldsymbol{\mathcal{A}}^{(2)}_{\ell,\mathrm{II}}(\boldsymbol{k}) &= \boldsymbol{j}_{\ell,\mathrm{II}}(\boldsymbol{k})\sum_{\ell'}\mathrm{e}^{-\mathrm{i}\Omega_\ell\tau_0}\mathcal{D}^{I_{\mathrm{g}}}_{M_{\mathrm{g}}M'_{\mathrm{g}}}(\alpha,\beta,\gamma)\mathcal{D}^{I_{\mathrm{e}}\,*}_{M_{\mathrm{e}}M'_{\mathrm{e}}}(\alpha,\beta,\gamma)\\ &\quad\times\int_0^{\tau_0}\mathrm{d}\tau'\,\boldsymbol{J}^*_{\ell',\mathrm{I}}(\boldsymbol{k},\tau')\cdot\sum_{\ell''}\left(\alpha{\boldsymbol{\mathcal{A}}^{(1)}_{\ell'',\mathrm{I}}}^{\sigma}(\boldsymbol{k}) + \beta{\boldsymbol{\mathcal{A}}^{(1)}_{\ell'',\mathrm{I}}}^{\pi}(\boldsymbol{k})\right)\mathrm{e}^{-\mathrm{i}\Omega_{\ell''}\tau'-\tau'/2}\\ &= \alpha{\boldsymbol{\mathcal{A}}^{(2)}_{\ell,\mathrm{II}}}^{\sigma}(\boldsymbol{k}) + \beta{\boldsymbol{\mathcal{A}}^{(2)}_{\ell,\mathrm{II}}}^{\pi}(\boldsymbol{k}) \ .\end{aligned} \tag{7.7}$$

It can be analogously shown that higher orders decompose in the same way finally resulting in

$$\boldsymbol{\mathcal{A}}_{\ell,\mathrm{II}}(\boldsymbol{k},\xi) = \alpha\boldsymbol{\mathcal{A}}^{\sigma}_{\ell,\mathrm{II}}(\boldsymbol{k},\xi) + \beta\boldsymbol{\mathcal{A}}^{\pi}_{\ell,\mathrm{II}}(\boldsymbol{k},\xi) \ . \tag{7.8}$$

Since moreover the amplitudes $\boldsymbol{\mathcal{B}}_{\ell,\mathrm{II}}$, $\boldsymbol{\mathcal{C}}_{\ell,\mathrm{II}}$, etc., can be written in this form, the total scattered field amplitude splits up in the same manner. For instance, the contribution $\boldsymbol{E}_0$ without nuclear scattering events after τ_0 can be explicitly written as

$$\boldsymbol{E}_0(\xi,\tau) = \alpha\boldsymbol{E}_0^{\sigma}(\xi,\tau) + \beta\boldsymbol{E}_0^{\pi}(\xi,\tau) \ , \tag{7.9}$$

where the superscript σ (π) indicates that this contribution originates solely from the initially σ-(π-)polarized component. Note that $\boldsymbol{E}_0^{\sigma}$ and $\boldsymbol{E}_0^{\pi}$ in general have arbitrary polarization depending on the scattering events prior to τ_0.

What does this mean for the initial superposition state $|\Psi\rangle$? Since the total scattered field amplitude splits up into a part coming from $|\sigma\rangle$ and a part coming from $|\pi\rangle$, the proposed processing schemes for single x-rays can be applied to arbitrary superposition states. The gate transformations can be explicitly generalized to

$$\begin{aligned}
\textsc{Identity:}\quad & |\Psi\rangle \to \alpha\,\psi^{\sigma}_{\mathrm{id}}(t)|\sigma\rangle + \beta\,\psi^{\pi}_{\mathrm{id}}(t)|\pi\rangle \ , \\
\textsc{False:}\quad & |\Psi\rangle \to \alpha\,\psi^{\sigma}_{\mathrm{false}}(t)|\pi\rangle + \beta\,\psi^{\pi}_{\mathrm{false}}(t)|\pi\rangle \ , \\
\textsc{True:}\quad & |\Psi\rangle \to \alpha\,\psi^{\sigma}_{\mathrm{true}}(t)|\sigma\rangle + \beta\,\psi^{\pi}_{\mathrm{true}}(t)|\sigma\rangle \ , \\
\textsc{Negation:}\quad & |\Psi\rangle \to \alpha\,\psi^{\sigma}_{\mathrm{neg}}(t)|\pi\rangle + \beta\,\psi^{\pi}_{\mathrm{neg}}(t)|\sigma\rangle \ .
\end{aligned} \tag{7.10}$$

Here, the time-dependent scattering amplitudes ψ describe the resonant scattering process after the magnetic field rotation ($\tau > \tau_0$). Small perturbations from the "wrong" polarization state due to scattering events after τ_0 involve higher orders $\boldsymbol{E}_n$ and have been neglected in Eqs. (7.10). The amplitudes ψ are determined via Eq. (7.9) where only the 0^{th} order $\boldsymbol{E}_0$ (after τ_0) is taken into account.

7.3 Boolean algebra with x-rays

We now turn to the implementation of Boolean operations with x-rays by means of binary logical gates. Since the x-ray-nuclear interface hosts a single photon only, a second, temporally synchronized photon is required as control. A simple but elegant idea to induce an effective nonlinearity between control and target photons is to have the magnetic field rotation triggered by the detection of the second control photon [256]. The latter can be spatially separated from the x-ray line as shown in Fig. 7.1 in order to distinguish between control and target mode. Since the nature of the implemented logical operation is completely determined by τ_0, the trigger photon responsible for the magnetic field switching acts as control for the polarization-encoded x-ray.

The magnetic field rotation could be applied at a predetermined switching time τ_0 (counted from the incidence of the x-ray target pulse at $\tau = 0$), in case a control photon is detected at the trigger. Alternatively, the detection event of the control photon may trigger a prompt rotation of the magnetic field. In this case the switching instant τ_0 is no longer predetermined but rather set during operation, and coincides with the incidence of the control photon at the trigger. In the following, we consider the latter, more general procedure where the moment τ_0 is determined during operation.

The control photon is considered to be temporally synchronized with the target pulse exhibiting a time delay $\Delta\tau$ (see Fig. 7.4). In order to render the triggering process

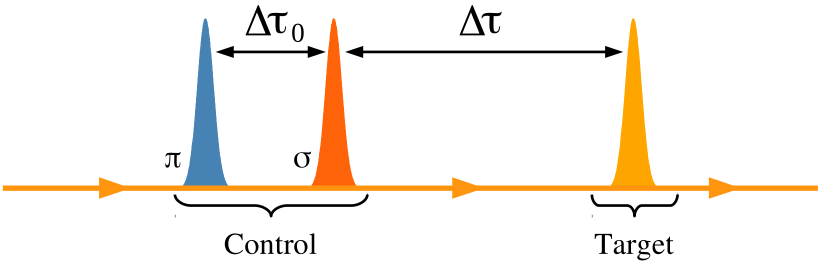

Figure 7.4: Time sequence of target and control pulse. A time delay $\Delta\tau$ between target and control pulse is introduced. The π-polarized component of the control pulse (blue) is furthermore delayed by $\Delta\tau_0$ with respect to the σ-polarized component (orange).

dependent on the polarization of the control path, a polarization-sensitive element such as a polarizer can be used. We consider two kind of procedures: (i) the polarizer is placed in front of the trigger such that only photons of a certain polarization reach the detector which activates the magnetic field rotation; (ii) the polarizer is embedded into a time delay line as illustrated in Fig. 7.3(a) in order to obtain an arrival time of the control pulse at the trigger sensitive to its polarization. In the latter case, either the σ- or π-component is delayed in comparison to its orthogonal counterpart by a time period $\Delta\tau_0$. The resulting pulse sequence with the corresponding time delays $\Delta\tau$ and $\Delta\tau_0$ is sketched in Fig. 7.4 for the case where the π-component experiences a time shift with respect to the σ-polarized part. Note that whenever procedure (i) is applicable or $\Delta\tau_0 = 0$, the switching scheme can be reduced such that the practical implementation is feasible by the simplified triggering procedure with a predetermined switching instant τ_0.

In the following, we discuss on the canonical example of the exclusive OR (XOR) how Boolean operations can be physically implemented with x-ray photons. The truth table of the XOR operation is given in Table 7.2, the output is “T” if and only if control and target photons are in opposite states. In general, the control photon may encode information for instance in polarization, time bin [264–266], or path. We employ the same information encoding as for the target x-ray photon where “F” and “T” are encoded as π- and σ-polarized states, respectively. In the case of the XOR, the NFS setup is required to operate as Identity if the control photon is σ-polarized $C = \pi$ and as Negation if $C = \sigma$. This can be explicitly implemented by a time delay of the control pulse $\Delta\tau = 22.3$ ns (see Table 7.2) and by a polarizer allowing only σ-polarized photons to reach the trigger (illustrated as “×” in Table 7.2). The timed magnetic field rotation then results in a flip of the polarization of the target photon if $C = \sigma$. If $C = \pi$, no magnetic field rotation is applied leaving the polarization untouched.

In Table 7.2 possible implementations for the commutative Boolean operations with two inputs are summarized by means of a pulse sequence determined by $\Delta\tau$ and $\Delta\tau_0$. For $\Delta\tau_0$ we distinguish if either the π- or σ-polarization component is delayed. Moreover, the “×” indicates that the corresponding polarization component is removed by a polarizer such that it does not reach the trigger. Each time a “×” appears or $\Delta\tau_0 = 0$, the operation can be practically realized with a predetermined switching instant. For instance, in the case of the XOR operation, a predetermined switching moment of 22.3 ns can be used if

Operation	Implementation	Time delay $\Delta\tau$	Time delay $\Delta\tau_0$		Truth table
			π	σ	
FALSE	False *if* $C = \pi$ False *if* $C = \sigma$	53.7 ns			F T F F F T F F
AND	False *if* $C = \pi$ Identity *if* $C = \sigma$	53.7 ns		×	F T F F F T F T
NAND	True *if* $C = \pi$ Negation *if* $C = \sigma$	22.3 ns		9.3 ns	F T F T T T T F
OR	Identity *if* $C = \pi$ True *if* $C = \sigma$	31.6 ns	×		F T F F T T T T
NOR	Negation *if* $C = \pi$ False *if* $C = \sigma$	22.3 ns	31.4 ns		F T F T F T F F
XOR	Identity *if* $C = \pi$ Negation *if* $C = \sigma$	22.3 ns	×		F T F F T T T F
XNOR	Negation *if* $C = \pi$ Identity *if* $C = \sigma$	22.3 ns		×	F T F T F T F T
TRUE	True *if* $C = \pi$ True *if* $C = \sigma$	31.6 ns			F T F T T T T T

Table 7.2: Boolean operations with two inputs. The implementation of the commutative, binary logical operations is shown including the corresponding control pulse delay τ, polarization delay τ_0 and condensed truth tables. The following optimized moments of switching have been considered for the unary gates: $\tau_0 = 53.7$ ns for False, $\tau_0 = 31.6$ ns for True and $\tau_0 = 22.3$ ns for Negation.

it is ensured that only σ-polarized control photons reach the trigger.

The XOR operation is the classical counterpart to a controlled NOT (CNOT) gate. The CNOT gate flips the state of a target qubit conditional on a control (C) qubit being in the logical state "T" [125]. Since the information associated with the control photon is destroyed during operation in our setup, and the polarization control relies on resonant scattering, the presented setup corresponds to a nondeterministic version of a destructive CNOT gate [267,268], which cannot be used directly for reversible computing [269]. Two-photon interference phenomena like the Hong-Ou-Mandel effect [270] may be employed to build real non-destructive quantum gates in the x-ray domain.

A proof-of-principle experiment for the operation of Boolean algebra with x-rays can be carried out already today at SR facilities which have access to the keV photon energy regime and short pulses ($\sim$ ps) compared to the time-scale of the nuclear response ($\sim$ ns). Moreover, the high pulse repetition rate renders it possible to record the presented intensity spectra in a reasonable time. The magnetic field rotation can be triggered by the detection of the control photon temporally synchronized with the synchrotron pulse clock. A fast triggering process is guaranteed by todays photodiodes which have response times shorter than 1 ns [271,272]. A tilt of the polarization plane of the scattered x-rays can be measured with a precision down to a few arcsec by using a special polarizer-analyzer setup [261]. Experiments at novel x-ray free electron sources (with their high brightness) [151,152] will facilitate the implementation of binary x-ray gates where both target and control photons are resonant to the nuclear transitions and originate from the same x-ray pulse.

In conclusion, we have shown that the light-nucleus interaction in NFS can be used to perform logical operations on single x-ray photons by applying nuclear hyperfine magnetic field rotations. X-ray single-input gates can be compiled within a single setup where solely the variation of the magnetic field switching moment τ_0 determines the nature of the logical operation. The introduction of a temporally synchronized control photon allows to design a triggering procedure along which Boolean operations with two input states can be performed. The realization of these basic logical operations may extend information science to photon energies in the x-ray domain in the near future involving potential spatial resolutions on the scale of single atoms.

Chapter 8

Quantum eraser with x-ray quanta

Quantum interference, the key concept in complementarity (gedanken)experiments, occurs whenever a quantum system can choose between several paths from a common initial state $|i\rangle$ to the same final state $|f\rangle$. The most famous interference experiment is Young's double-slit setup. As long as the path chosen by the particle through the double-slit remains unrevealed, one can observe interference fringes in a position measurement somewhere behind the slits. According to the complementarity principle, a detector capable of determining the path taken by the particle through the double-slit (and supply *which-way* information) will destroy the interference pattern. The physical mechanism via which the interference is lost typically relies on random classical momentum kicks which are introduced by the detector revealing *which-way* information in the system [273]. This is however not always the case. In more recent quantum optics experiments, the path chosen by the particle, this time an atom or ion, can be marked by employing further degrees of freedom related to their internal, quantum structure. In this case, even if the acquisition of *which-way* information involves a momentum kick, this is a coherent quantum process rather than a classical random one. While the interference disappears due to this marking, one can later choose to "erase" the *which-way* information and restore the interference behavior, in a process first proposed in Ref. [136] and illustratively called *quantum eraser.* If the instant of erasure is chosen such that it occurs only after detection of the particle (allowing determination of its earlier behavior as wave or particle) one speaks of a delayed-choice quantum eraser [274, 275].

Complementarity is closely related to Heisenberg's uncertainty relations [276] that describe the limitations on the possible accuracy of classical measurements of a quantum system. Over the years, the dilemmas of complementarity gedankenexperiments such as Einstein's recoiling-slit experiment [273] or Feynman's electron-light scattering scheme [277] were solved invoking the position-momentum uncertainty relation [276], prompting the question whether complementarity is always enforced by the uncertainty relations. A vivid theoretical debate [278–282] as well as several experiments [283–285] showed that complementarity is more fundamental than the uncertainty relation, i.e., one can find cases in which the effect of Heisenberg's uncertainty relations is not sufficient to justify the occurring complementarity.

Analogously to position and momentum, the time-energy complementarity relation has as counterpart the time-energy uncertainty relation, $\Delta E \Delta t \geq \hbar/2$. We recall that the latter, although generally accepted as valid, does not rely on the same mathematical basis as other uncertainty relations, i.e., it is not a direct mathematical consequence of the replacement of classical numbers by operators. Time is not an operator in quantum mechanics, it is just a parameter. Although from the theoretical and philosophical side the debates on the concept of time in quantum mechanics are ongoing [286–289], there are only few experiments with quantum particles which do not involve time-related measurements. A number of double-slit-type setups recording interference between paths differing in time rather than spatially have been investigated both theoretically and experimentally. These include a double-slit experiment in the time-energy domain where the slits are related to different time windows of attosecond duration [290–292], a streaking temporal double-slit in an orthogonal two-color laser field [293], vacuum-mediated interference in atomic resonant fluorescence [294] or oscillations of Mössbauer neutrinos [295].

In this Chapter, we investigate theoretically a quantum eraser setup exploiting the complementarity between time and energy in a so-far unexplored parameter regime. The novelty arises from the use of hard x-ray quanta instead of optical or infrared photons. We envisage interference occurring in driving the 14.4 keV Mössbauer transition in ^{57}Fe by x-rays from a synchrotron radiation (SR) source. Under the presence of a hyperfine magnetic field, the splitting of the ground and first excited states will lead to the indistinguishable excitation of two transitions as shown in Fig. 8.1(d) and to the detection of an interference pattern, the so-called quantum beat [see Fig. 8.1(b)]. Subsequent manipulations of the x-ray photon polarization in a marking procedure leads to the disappearance of the interference. By appropriate quantum erasure of the which-way information, the interference pattern can be restored in a very similar manner as explained in the original quantum eraser proposal [278]. Due to their long coherence times, the use of nuclear transitions leads to very small relative values for the energy transfer occurring in the marking procedure compared to the actual photon energy, $\Delta E/E \sim 10^{-13}$.

The Chapter is structured as follows. Sec. 8.1 introduces the interference mechanisms in the course of nuclear forward scattering (NFS) leading to the interference spectra in the collective decay. Sec. 8.2 continues with the description of the path marking techniques and describes two versions of quantum erasure. Numerical results are presented here for both discussed setups.

8.1 Interference mechanisms in NFS

In order to obtain quantum interference we exploit the collective effects rising in NFS of SR on Mössbauer solid-state samples (see Fig. 8.1). Due to the recoilless excitation and decay of the nuclear excited state, as long as the initial and the final states are the same for all nuclei in the sample, it is impossible to pin-point which nucleus or nuclei were involved in the excitation. In this respect, we have here the generalized, N-scatterer version of Young's interference experiment with (optical) light scattered from two atoms [283]. The collective excitation leads to directional scattering in the forward direction allowing a spatial separation of the coherent (collective) and incoherent (without interference) decays [103]. The collective coherent decay and consequently the interference effects occur in the forward direction as already explained in Chap. 5.

A typical NFS setup is shown in Fig. 8.1(a). The x-rays, typically from a SR source monochromatized to the nuclear transition energy, propagate along the y-direction and

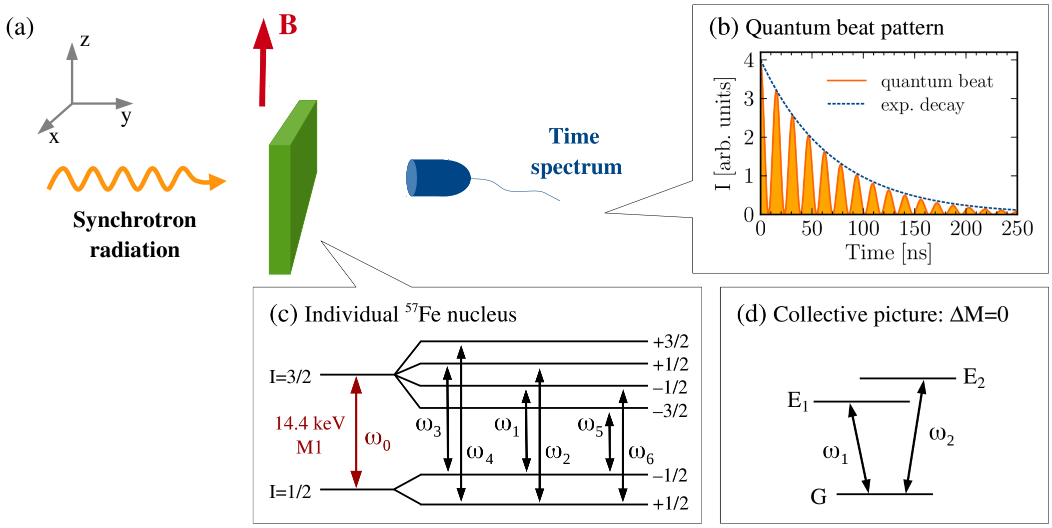

Figure 8.1: (a) Typical NFS setup with magnetic field $\boldsymbol{B}$. (b) NFS time spectrum for a thin target with quantum beat pattern (orange curve). (c) Nuclear level scheme of an individual ^{57}Fe nucleus under hyperfine splitting. (d) Collective picture with a common ground state G and excited levels E_1 and E_2 driven via the $\Delta M = 0$ transitions.

impinge on the nuclear sample with an incident angle of 90°. The radiation is linearly polarized with x-(z-)polarized light denoted as σ-(π-)polarization by convention [242]. The time spectrum of the resonantly scattered radiation is detected in the forward direction. The nuclear response occurs on a much longer time scale than the x-ray pulse duration and the non-resonant, electronic response, allowing for time gating of the signal [104]. Due to the typically narrow nuclear resonances and the low brilliance of x-ray sources, at most one nucleus can be excited in the sample per pulse (see also Chap. 5).

The most used nuclear transition in NFS is the one connecting the stable ground state of ^{57}Fe (nuclear spin $I_g = 1/2$) with the the first excited state (nuclear spin $I_e = 3/2$, mean lifetime τ=141 ns) at 14.413 keV. The recoilless nature of this transition in solid-state nuclear targets leads to the formation of a delocalized, collective excitation which decays coherently into the forward direction leading to a relative speed-up and enhancement of the NFS yield (see Chap. 5). The formation of the exciton can be interpreted as an interference effect for the scattering of the resonant photon or photons off a collection of N nuclei. As long as the identity of the interacting nucleus is not revealed, for instance via spin flip, recoil or an internal conversion electron, the collective excitation occurs.

In the presence of a nuclear hyperfine magnetic field, the ground and excited nuclear states undergo Zeeman splitting according to their spin values as illustrated in the inset of Fig. 8.1(c). Due to the Fourier limit of the temporally narrow incident x-ray pulses, several polarization-selected hyperfine transitions can be simultaneously driven leading to well-known quantum beats in the NFS intensity spectrum [103]. For instance, initially σ-(π-)polarized x-rays couple to all $\Delta M = 0$ ($\Delta M = \pm 1$) transitions provided the magnetic field $\boldsymbol{B}$ points along the z-direction. Since only those photons are coherently scattered into the forward direction for which the nucleus returns to its original ground state Zeeman level, the σ-(π-)polarization is conserved in the course of NFS with constant hyperfine field $\boldsymbol{B}_\mathrm{I}$ (see Sec. 6.1). In such a setup, the quantum mechanical state of a single nucleus can in general be expressed as the following superposition

$$|\Psi\rangle = \sum_{i=1}^{2} \Big(c_{e_i} |e_i, 0\rangle + c_{g_i} |g_i, 0\rangle \Big) + c_1 |g_1, 1_{\omega_1}\rangle + c_2 |g_2, 1_{\omega_2}\rangle \ , \tag{8.1}$$

where $|g_i, 0\rangle$ and $|e_i, 0\rangle$ $(i \in \{1,2\})$ represent the states with a ground or excited nuclear sublevel, respectively, and the radiation field in vacuum, $|g_i, 1_{\omega_i}\rangle$ $(i \in \{1,2\})$ denote the states after the reemission process in the course of NFS involving one photon with either frequency ω_1 or ω_2, and c_{g_i}, c_{e_i} and c_i $(i \in \{1,2\})$ are the corresponding probability coefficients. According to the full quantum mechanical description, the two $\Delta M = 0$ transitions do not interfere for a single nucleus due to the different initial and final states involved. The beat pattern between ω_1 and ω_2 evaluates in this case to

$$\begin{aligned} \langle \Psi | E_1^{(-)} E_2^{(+)} | \Psi \rangle &\propto \langle g_1, 1_{\omega_1} | a_1^\dagger a_2 \mathrm{e}^{\mathrm{i}(\omega_1 - \omega_2)t} | g_2, 1_{\omega_2} \rangle \\ &\propto \langle 1_{\omega_1} | a_1^\dagger a_2 | 1_{\omega_2} \rangle \mathrm{e}^{\mathrm{i}(\omega_1 - \omega_2)t} \langle g_1 | g_2 \rangle \\ &\propto \mathrm{e}^{\mathrm{i}(\omega_1 - \omega_2)t} \underbrace{\langle g_1 | g_2 \rangle}_{=0} \ , \end{aligned} \tag{8.2}$$

where the field operators $E_i^{(\pm)}$ are proportional to $a_i \mathrm{e}^{-\mathrm{i}\omega_i t}$ and $a_i^\dagger \mathrm{e}^{\mathrm{i}\omega_i t}$, respectively, with a_i and $a_i^\dagger$ being the photon creation and annihilation operators belonging to frequency ω_i $(i \in \{1,2\})$. The beat pattern disappears for a single nucleus because the Zeeman levels g_1 and g_2 are orthogonal to each other, $\langle g_1 | g_2 \rangle = 0$.

In an ensemble of many nuclei collective effects come into play. In this case, the two $\Delta M = 0$ transitions are connected by the collective ground state which contains nuclei on both hyperfine levels,

$$|G\rangle = \underbrace{|g_1^{(1)}\rangle \dots |g_1^{(N_1)}\rangle}_{N_1} \underbrace{|g_2^{(N_1+1)}\rangle \dots |g_2^{(N)}\rangle}_{N_2} \ , \tag{8.3}$$

where $|g_1\rangle$ and $|g_2\rangle$ denote the two ground magnetic sublevels and N_i is the number of nuclei in the ground state $|g_i\rangle$ $(i \in \{1,2\})$ with $N_1 + N_2 = N$. At room temperature, typically $N_1 \approx N_2$. The excited state on the other hand can be described as a timed Dicke state [296]

$$|E_\mu\rangle = \frac{1}{\sqrt{N_\mu}} \sum_{n}^{N_\mu} \mathrm{e}^{\mathrm{i}\boldsymbol{k}\cdot\boldsymbol{r}_n} |g_1^{(1)}\rangle \dots |e_\mu^{(n)}\rangle \dots |g_2^{(N)}\rangle \ , \tag{8.4}$$

in which the n^{th} nucleus has been excited via the transition μ, with the notation $\mu = 1$ for the transition $M_\mathrm{g} = 1/2 \rightarrow M_\mathrm{e} = 1/2$ and $\mu = 2$ for $M_\mathrm{g} = -1/2 \rightarrow M_\mathrm{e} = -1/2$, depending on the initial ground state spin projection M_g. The position of the excited nucleus is given by $\boldsymbol{r}_n$ and $\boldsymbol{k}$ represents the wave vector of the resonant incident x-ray field. The scattering channels with $\Delta M = 0$ are equivalent in this system to the transitions $|G\rangle \to |E_1\rangle$ and $|G\rangle \to |E_2\rangle$, as illustrated in the level scheme in Fig. 8.1(d).

We show in the following that interference effects can occur in this setup (see Ref. [4]). Having at most one excitation inside the nuclear ensemble, the general state of the system can be written as

$$|\Psi_{\text{coll}}\rangle = \sum_{i=1}^{2} C_{E_i}|E_i, 0\rangle + C_G|G, 0\rangle + C_1|G, 1_{\omega_1}\rangle + C_2|G, 1_{\omega_2}\rangle \tag{8.5}$$

with C_{E_i}, C_G and C_i representing the probability amplitudes for being in $|E_i, 0\rangle$, $|G, 0\rangle$ and $|G_i, 1_{\omega_i}\rangle$ ($i \in \{1, 2\}$), respectively. Following the same steps as in the case of a single nucleus, we obtain

$$\begin{aligned}\langle\Psi_{\text{coll}}|E_1^{(-)}E_2^{(+)}|\Psi_{\text{coll}}\rangle &\propto \langle G, 1_{\omega_1}|a_1^\dagger a_2 \mathrm{e}^{\mathrm{i}(\omega_1-\omega_2)t}|G, 1_{\omega_2}\rangle \\ &\propto \mathrm{e}^{\mathrm{i}(\omega_1-\omega_2)t} \underbrace{\langle G|G\rangle}_{=1} \; .\end{aligned} \tag{8.6}$$

Here, we observe a beat pattern since the two $\Delta M = 0$ transitions are connected via the common ground state $|G\rangle$. This is equivalent with the coherent addition of classical fields, that we introduced in Chap. 5 and that we will use in the following.

8.2 Which-way information and quantum eraser

The occurrence of the quantum beat pattern in the course of NFS can be explained in analogy to a double-slit setup. Instead of the interference of two spatial path ways like in a conventional double-slit experiment, the quantum beat pattern in the course of NFS is caused by the interplay between the frequency paths contributing to the scattering process, e.g., $\omega_{1,\ldots,6}$ in the case of ^{57}Fe [see Fig. 8.1(b)]. In the following we will restrict ourselves to the interference of the two $\Delta M = 0$ transitions, ω_1 and ω_2. We put forward two versions of a quantum eraser setup. The general idea of both is to first mark the originally interfering paths via orthogonal polarization states, leading to a wash-out of the interference fringes. By applying a projection to a different polarization basis which acts as a quantum eraser, the which-way information is lost and the interference fringes reappear.

8.2.1 Scheme 1: Two-target scenario

The setup of scheme 1 consists of two ^{57}Fe targets with magnetic fields $\boldsymbol{B}_1$ and $\boldsymbol{B}_2$, respectively, a high-speed shutter [297] behind the first target and a polarizer directly in front of the detectors, as illustrated in Fig. 8.2. In the following, we will describe the propagation of the SR pulse through this setup step by step. The essential building blocks of a quantum eraser will be identified and the required conditions evaluated.

The incident SR pulse is considered to be σ-polarized initially and the magnetic field at target 1 is chosen to point along the z-direction such that only the two $\Delta M = 0$

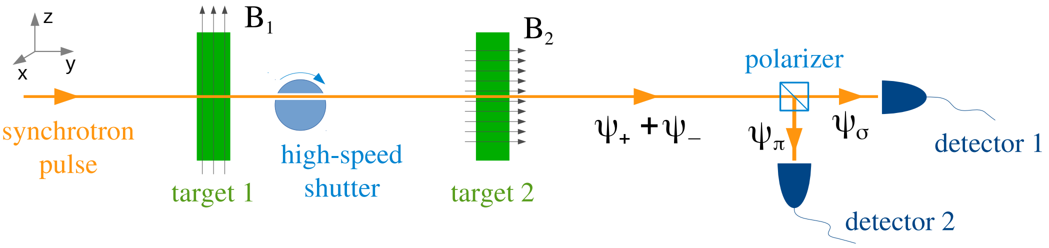

Figure 8.2: Quantum-eraser scheme 1. The σ-polarized synchrotron pulse is resonantly scattered off target 1 ($\boldsymbol{B}_1 \parallel \boldsymbol{e}_z$) via the two $\Delta M = 0$ transitions. The high-speed shutter cuts the SR pulse such that the incoming radiation field at target 2 is solely the nuclear response of target 1. Following the nuclear scattering off target 2 ($\boldsymbol{B}_2 \parallel \boldsymbol{e}_y$) a polarizer splits the σ- and π-polarization components.

transitions are driven. For the considered B-field geometry the σ-polarization is conserved in the course of the nuclear resonance scattering as explained in Sec. 6.1. Under the action of the applied hyperfine field, target 1 adopts essentially the role of the double slit in the original quantum eraser proposal [278], imprinting the quantum beat pattern on the scattered field.

Fig. 8.3(a) shows the time spectrum of the forward scattered intensity directly behind target 1. Due to the two scattering paths in frequency space, $\ell = -2$ and $\ell = 2$ (following the notation of Chap. 6), the quantum beat interference pattern appears in the time spectrum. Apart of the interference between the $\Delta M = 0$ channels, the dynamical beat modulation caused by multiple scattering events inside the sample is also visible in the intensity spectrum. In the calculation presented in Fig. 8.3(a), an effective target thickness for sample 1 of $\xi_1 = 7$ has been considered.

The effect of the shutter behind target 1 is to select a certain time window of the scattered field. This time window can be controlled by the shutter properties like the diameter, the width or the position of the slit, and by the applied rotation frequency [297]. In Fig. 8.3(b) for instance, we assumed that only photons emitted from $t_0 = 7$ ns until $t_1 = 74$ ns are able to pass the shutter and to reach the second target. The choice of $t_0 > 0$ also removes the broadband SR pulse which behaves essentially δ-like in time in comparison to the nuclear response. In frequency space, the high-speed shutter creates two spectrally narrow x-ray pulses at frequencies $\omega_1 = \omega_0 - \Omega_2$ and $\omega_2 = \omega_0 + \Omega_2$, respectively, by inverting the two $\Delta M = 0$ absorption dips. Note that due to the broadband nature of SR light and the narrow nuclear transition widths, typically at most a single resonant x-ray photon is involved in the scattering process, either with freuqency ω_1 or ω_2.

The magnetic field at the second iron target points along the y-axis which is the direction of propagation. This is known as the Faraday geometry and in this case only $\Delta M = \pm 1$ transitions are allowed according to angular momentum conservation. Photons emitted via the $\Delta M = +1$ and $\Delta M = -1$ are right and left circularly polarized, respectively. The idea on how to delete the interference pattern imprinted at target 1 is

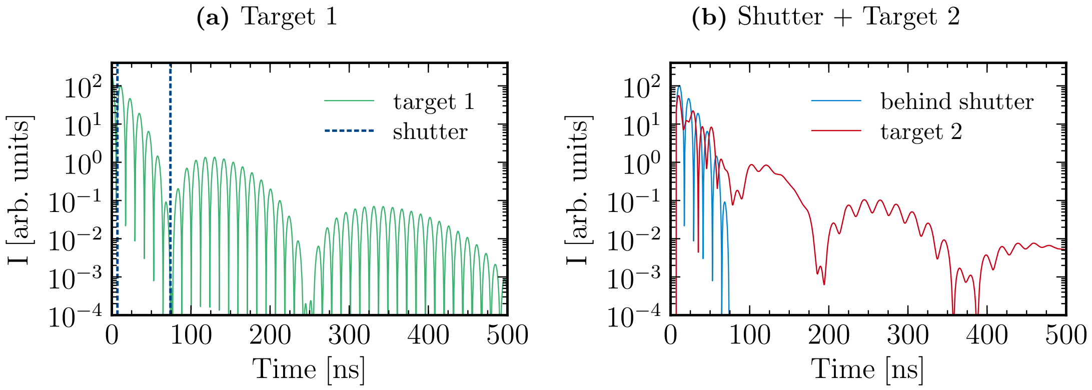

Figure 8.3: (a) NFS intensity spectrum $|\boldsymbol{E}(\xi,\tau)|^2$ directly behind target 1. The scattering via the two $\Delta M = 0$ transitions results in the characteristic quantum beat pattern. Due to the shutter only photons emitted in the time window from 7 ns until 74 ns [region between blue dashed lines in (a), blue curve in (b)] reach target 2. (b) The magnetic field $\boldsymbol{B}_2$ is chosen such that the interference between the $\Delta M = 0$ frequency components is destroyed in the intensity spectrum $|\boldsymbol{E}(\xi,\tau)|^2$ (red curve) directly behind target 2. Effective thicknesses of $\xi_1 = \xi_2 = 7$ and a maximal scattering order of $p_{\max} = 19$ have been considered in the calculations.

to tune the strengths of the magnetic fields B_1 and B_2 such that the spectrally narrow peaks impinging on target 2 are marked with orthogonal circular polarizations. One choice is to set the conditions $\omega_1^{(1)} = \omega_3^{(2)}$ and $\omega_2^{(1)} = \omega_6^{(2)}$. By using Eqs. (5.30) and (5.33) we obtain

$$\frac{B_1}{B_2} = \frac{\mu_g/I_g + \mu_e/I_e}{\mu_g/I_g - \mu_e/I_e} \,, \tag{8.7}$$

where μ_g and μ_e denote the magnetic moments of the ground and the excited states, respectively. In terms of the nuclear magneton μ_n, the magnetic moments of ^{57}Fe are given by $\mu_g = 0.09044\,\mu_n$ and $\mu_e = -0.1549\,\mu_n$ [194]. In the same manner, one can impose $\omega_1^{(1)} = \omega_5^{(2)}$ and $\omega_2^{(1)} = \omega_4^{(2)}$ which can be realized by

$$\frac{B_1}{B_2} = \frac{\mu_g/I_g - 3\mu_e/I_e}{\mu_g/I_g - \mu_e/I_e} \,. \tag{8.8}$$

The intensity spectrum behind target 2 shown in Fig. 8.3(b) is calculated with Zeeman splittings of $\epsilon_g^{(1)} \approx 48\,\Gamma_0$ and $\epsilon_e^{(1)} \approx -27\,\Gamma_0$ at target 1, and $\epsilon_g^{(2)} \approx 28\,\Gamma_0$ and $\epsilon_e^{(2)} \approx -16\,\Gamma_0$ at target 2, corresponding to the case where $\omega_1^{(1)} = \omega_5^{(2)}$ and $\omega_2^{(1)} = \omega_4^{(2)}$ [see Eqs. (5.30) and (5.33)]. Moreover, an effective thickness of $\xi_2 = 7$ has been considered. As can be seen from Fig. 8.3(b), for photons interacting with both targets the *which-way* information is successfully obtained, destroying the interference pattern. The condition of double interaction is certainly fulfilled at times larger than t_1 such that the quantum beat completely disappears in this region. Only the dynamical beat signature remains in the intensity spectrum with small oscillations coming from interactions with off-resonant transitions.

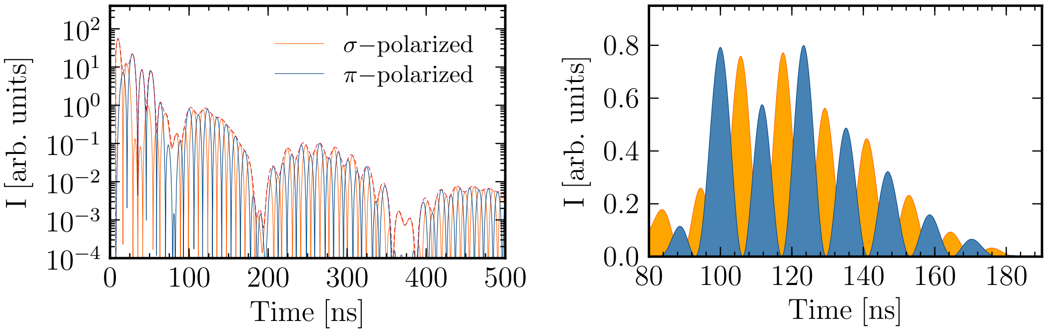

Figure 8.4: The σ- (orange curve) and π-components (blue curve) of the intensity spectrum $|\boldsymbol{E}(\xi,\tau)|^2$ are shown. While the left graph covers the region from 0 to 500 ns, the right graph zooms into the time window between 80 and 190 ns. In the calculations scattering orders up to $p_{\mathrm{max}} = 19$ have been taken into account.

After the successful marking of the scattering paths with orthogonal polarizations the question arises, how to erase again the *which-way* information obtained by the resonant scattering off the second target? Since the two scattering paths are marked with circular polarizations, a polarizer projecting on the linear polarization basis $\boldsymbol{e}_\sigma$ and $\boldsymbol{e}_\pi$ destroys the orthogonality and restores the interference pattern as shown in Fig. 8.4. The left graph of Fig. 8.4 presents the intensity spectrum at detector 1 (orange curve) and detector 2 (blue curve) over the whole time range employed in Fig. 8.3, whereas the right graph of Fig. 8.4 zooms into the time region between 80 ns and 190 ns. In the latter, the relative shift between the σ- and the π-components of a quarter of a beating period can be clearly seen. The σ- and π-polarized parts take the role of the fringes and anti-fringes introduced in Ref. [278].

As seen by the small oscillations in Fig. 8.3(b), the marking via orthogonal polarizations is slightly distorted due to off-resonant interactions. In order to minimize the latter, the incoming spectrally narrow peaks as well as the absorption lines need to be well separated in frequency space, involving high magnetic fields. In the calculations presented in Figs. 8.3 and 8.4, for instance, magnetic field strengths of $B_1 \approx 39$ T and $B_2 \approx 23$ T have been considered in order to obtain the intended hyperfine splittings. Since such high magnetic field strengths are difficult to realize in laboratory, it is worth to explore if a quantum eraser scenario is also feasible in a setup where a strong internal hyperfine field can be employed, e.g. by using antiferromagnetic $\mathrm{FeBO_3}$ crystals.

8.2.2 Scheme 2: Interferometer-like setup

Instead of using two targets in a sequence, it is also possible to realize a quantum eraser scheme by employing an x-ray interferometer setup involving two spatially separated targets, one in each interferometer arm. The general idea is to apply a time delay in one of the arms such the a relative phase is imprinted. Considering for instance a geometry where only the two $\Delta M = 0$ transitions, ω_1 and ω_2, are driven, it turns out that a time delay in one of the arms produces a phase shift for each frequency component exactly

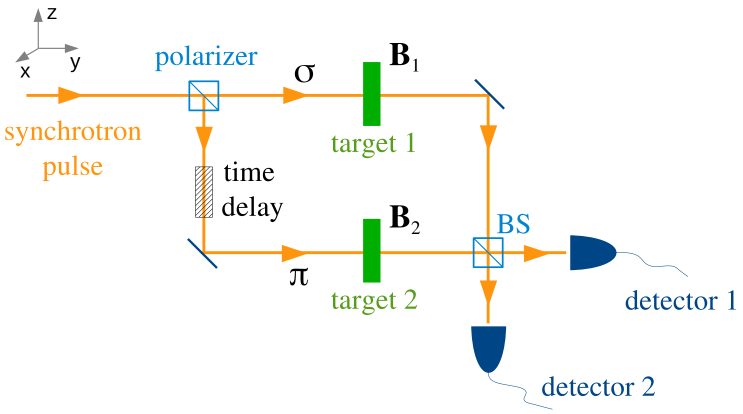

Figure 8.5: Quantum-eraser scheme 2. The incoming x-ray photon is split into its σ- and π-polarized components by a polarizer. The split beams are later on mixed with the help of two mirrors and a beam splitter (BS). In each arm a nuclear ^{57}Fe target is inserted. The two targets experience the magnetic fields $\boldsymbol{B}_1$ and $\boldsymbol{B}_2$, respectively. A relative time delay between arm 1 and 2 is introduced.

opposite in sign. How this phase shift can be employed to destroy and recover the quantum beat pattern of NFS is explained in the following.

The x-ray interferometer we are considering is schematically presented in Fig. 8.5. In comparison to a conventional Mach-Zehnder-interferometer, a peculiarity here is the initial polarizer which splits the σ-polarized component from the π-polarized part. After the polarizer, the split beam interacts with two nuclear samples, one in each interferometer arm, in the presence of the magnetic fields $\boldsymbol{B}_1$ and $\boldsymbol{B}_2$, respectively. The π-polarized pulse furthermore experiences a time delay $\Delta\tau$ in comparison to the σ-polarized counterpart, before reaching target 2. Finally, both spatially separated arms come together at a beam splitter (BS) [119] where they are recombined.

The interferometer system composed of a polarizer, two mirrors, two spatially separated nuclear targets and finally a beam splitter (BS) as shown in Fig. 8.5 can be theoretically described in the following way [5]

$$\begin{pmatrix} \boldsymbol{E}^{(1)}_{\text{out}-1} \\ \boldsymbol{E}^{(1)}_{\text{out}-2} \end{pmatrix} = \frac{1}{2} \underbrace{\begin{pmatrix} 1 & \mathrm{i} \\ \mathrm{i} & 1 \end{pmatrix}}_{\text{“BS”}} \underbrace{\begin{pmatrix} -1 & 0 \\ 0 & -1 \end{pmatrix}}_{\text{“mirrors”}} \underbrace{\begin{pmatrix} \psi_1 & 0 \\ 0 & \psi_2 \end{pmatrix}}_{\text{“targets”}} \underbrace{\begin{pmatrix} |\sigma\rangle\langle\sigma| & 0 \\ 0 & |\pi\rangle\langle\pi| \end{pmatrix} \begin{pmatrix} 1 & \mathrm{i} \\ \mathrm{i} & 1 \end{pmatrix}}_{\text{“polarizer”}} \begin{pmatrix} \boldsymbol{E}_{\text{in}} \\ 0 \end{pmatrix} . \tag{8.9}$$

Here, $\boldsymbol{E}_{\text{in}}$ represents the incoming synchrotron pulse and $\boldsymbol{E}^{(1)}_{\text{out}-1}$ and $\boldsymbol{E}^{(1)}_{\text{out}-2}$ the output at detector 1 and 2, respectively, in the single scattering approximation. Considering the synchrotron pulse initially in an arbitrary linear polarization state, as given by the superposition in Eq. (7.4) with $\alpha, \beta \in \mathbb{R}$ and normalization $\alpha^2 + \beta^2 = 1$, and performing the matrix multiplications occurring in Eq. (8.9), we obtain

$$\begin{pmatrix} \boldsymbol{E}^{(1)}_{\text{out}-1} \\ \boldsymbol{E}^{(1)}_{\text{out}-2} \end{pmatrix} = \frac{1}{2} \begin{pmatrix} -\alpha \boldsymbol{E}^{(1)^\sigma}(\xi,\tau) + \beta \boldsymbol{E}^{(1)^\pi}(\xi,\tau) \\ -\mathrm{i}\alpha \boldsymbol{E}^{(1)^\sigma}(\xi,\tau) - \mathrm{i}\beta \boldsymbol{E}^{(1)^\pi}(\xi,\tau) \end{pmatrix} . \tag{8.10}$$

Following the notation of Chap. 7, $\boldsymbol{E}^{(1)^\sigma}$ and $\boldsymbol{E}^{(1)^\pi}$ denote the first order contributions originating from the initially σ- and π-polarized component, respectively. Important to remark is that we only consider thin targets in this section such that the single scattering approximation is always the dominating contribution of the forward scattered field. Moreover, the time delay $\Delta\tau$ was not yet accounted for in Eqs. (8.9) and (8.10). It is later on incorporated into the nuclear response $\boldsymbol{E}^{(1)^\pi}$ coming from target 2.

So far, the description in Eq. (8.10) is rather general, as neither the incident radiation pulse nor the B-field geometry have been fixed. Since we consider two spatially separated nuclear targets, the magnetic fields at each individual sample can be chosen independently of each other. In the following, we now first choose the magnetic fields $\boldsymbol{B}_1$ and $\boldsymbol{B}_2$ such that only the $\Delta M = 0$ transitions are driven in both targets. Explicitly, this can be achieved by a magnetic field $\boldsymbol{B}_1$ at target 1 parallel to the z-axis and $\boldsymbol{B}_2$ at target 2 parallel to the x-axis. The magnitudes of both are assumed to coincide. In order to evaluate the terms $\boldsymbol{E}^{(1)^\sigma}$ and $\boldsymbol{E}^{(1)^\pi}$ corresponding to the scattered field from each individual target, we employ the description of NFS introduced in Chaps. 5 and 6 where a semi-classical wave equation is used. According to Eq. (6.4), the first order solutions for the considered geometry can be written as

$$\begin{aligned}\boldsymbol{E}^{(1)^\sigma}(\xi,\tau) &= -\xi\Big\{\boldsymbol{\mathcal{A}}^{(1)^\sigma}_{\ell=-2,\mathrm{I}}(\boldsymbol{k})\mathrm{e}^{\mathrm{i}\Omega_2\tau} + \boldsymbol{\mathcal{A}}^{(1)^\sigma}_{\ell=2,\mathrm{I}}(\boldsymbol{k})\mathrm{e}^{-\mathrm{i}\Omega_2\tau}\Big\}\mathrm{e}^{-\tau/2} \\ &= -\xi\frac{f_{\mathrm{LM}}}{2}\Big\{\mathrm{e}^{\mathrm{i}\Omega_2\tau} + \mathrm{e}^{-\mathrm{i}\Omega_2\tau}\Big\}\mathrm{e}^{-\tau/2}\boldsymbol{e}_\sigma \end{aligned} \tag{8.11}$$

and

$$\begin{aligned}\boldsymbol{E}^{(1)^\pi}(\xi,\tau) &= -\xi\Big\{\boldsymbol{\mathcal{A}}^{(1)^\pi}_{\ell=-2,\mathrm{I}}(\boldsymbol{k})\mathrm{e}^{\mathrm{i}\Omega_2(\tau-\Delta\tau)} + \boldsymbol{\mathcal{A}}^{(1)^\pi}_{\ell=2,\mathrm{I}}(\boldsymbol{k})\mathrm{e}^{-\mathrm{i}\Omega_2(\tau-\Delta\tau)}\Big\}\mathrm{e}^{-(\tau-\Delta\tau)/2} \\ &= -\xi\frac{f_{\mathrm{LM}}}{2}\Big\{\mathrm{e}^{\mathrm{i}\Omega_2(\tau-\Delta\tau)} + \mathrm{e}^{-\mathrm{i}\Omega_2(\tau-\Delta\tau)}\Big\}\mathrm{e}^{-(\tau-\Delta\tau)/2}\boldsymbol{e}_\pi\ , \end{aligned} \tag{8.12}$$

where the amplitudes $\boldsymbol{\mathcal{A}}^{(1)^\sigma}_{\ell,\mathrm{I}}$ and $\boldsymbol{\mathcal{A}}^{(1)^\pi}_{\ell=,\mathrm{I}}$ are defined in Eq. (6.5) following the notation of Eq. (7.5). Using the expressions for the nuclear hyperfine currents $\boldsymbol{j}^*_\ell$ and $\boldsymbol{j}_\ell$ provided in Eqs. (5.35), the amplitudes are explicitly evaluated in the step from the first to the second line in Eqs. (8.11) and (8.12). Furthermore, the time delay $\Delta\tau$ is incorporated into the scattered field $\boldsymbol{E}^{(1)^\pi}$ originating from target 2 [see Eq. (8.12)].

Inserting the NFS solutions of the individual targets [Eqs. (8.11) and (8.12)] into Eq. (8.10), leads to

$$\begin{aligned}\boldsymbol{E}^{(1)}_{\mathrm{out}-1}(\xi,\tau) &= -\xi\frac{f_{\mathrm{LM}}}{4}\Big\{\mathrm{e}^{\mathrm{i}\Omega_2\tau}(-\alpha\boldsymbol{e}_\sigma + \beta'\mathrm{e}^{\mathrm{i}\Phi}\boldsymbol{e}_\pi) + \mathrm{e}^{-\mathrm{i}\Omega_2\tau}(-\alpha\boldsymbol{e}_\sigma + \beta'\mathrm{e}^{-\mathrm{i}\Phi}\boldsymbol{e}_\pi)\Big\}\mathrm{e}^{-\tau/2}\ , \\ \boldsymbol{E}^{(1)}_{\mathrm{out}-2}(\xi,\tau) &= \mathrm{i}\xi\frac{f_{\mathrm{LM}}}{4}\Big\{\mathrm{e}^{\mathrm{i}\Omega_2\tau}(\alpha\boldsymbol{e}_\sigma + \beta'\mathrm{e}^{\mathrm{i}\Phi}\boldsymbol{e}_\pi) + \mathrm{e}^{-\mathrm{i}\Omega_2\tau}(\alpha\boldsymbol{e}_\sigma + \beta'\mathrm{e}^{-\mathrm{i}\Phi}\boldsymbol{e}_\pi)\Big\}\mathrm{e}^{-\tau/2}\ , \end{aligned} \tag{8.13}$$

where we have introduced the phase $\Phi = \Omega_2\Delta\tau$ and the coefficient $\beta' = \beta\mathrm{e}^{\Delta\tau/2}$. As seen from Eqs. (8.13), the π component experiences a relative phase shift of Φ in comparison to the σ-polarized part in the case of $\ell = -2$, while the phase shift is of opposite sign for $\ell = 2$ (the notation of ℓ was introduced in Chap. 6).

Let us first discuss the simplest scenario with zero time delay, $\Delta\tau = 0$. In this case β' reduces to β and the phase Φ is identically zero such that the factor $\mathrm{e}^{\mathrm{i}\Phi}$ evaluates to one. The polarization response of each frequency component follows the superposition state of the incident radiation $\boldsymbol{E}_{\mathrm{in}}$. Taking the modulus squared of $\boldsymbol{E}^{(1)}_{\mathrm{out}-1}$ and $\boldsymbol{E}^{(1)}_{\mathrm{out}-2}$, respectively, the intensity spectra at each detector have the same form given by,

$$I^{(1)}_{\mathrm{out}}(\xi,\tau) = \xi^2 \frac{f^2_{\mathrm{LM}}}{8}\Big\{1 + \cos(2\Omega_2 t)\Big\}\mathrm{e}^{-\tau} \; . \tag{8.14}$$

As can be seen from Eqs. (8.14), in the case of $\Delta\tau = 0$ the quantum beat pattern represented by the cosine term is preserved in the intensity output. Since the interferometer arms are characterized by orthogonal polarizations in the considered scenario, there is no interference term between arm 1 and arm 2 occurring in the intensity spectra. For this reason, the signals at detectors 1 and 2 coincide and it is sufficient to discuss only one of the outputs whenever talking about intensities in the following.

In order to switch off the quantum interference between the two hyperfine transitions $\ell = -2$ and $\ell = 2$, a nonzero time delay $\Delta\tau$ can be employed. The idea is to choose $\Delta\tau$ such that the two scattering channels in frequency space, $\ell = -2$ and $\ell = 2$, are marked by orthogonal polarization states, e.g., left and right circularly polarized. Therefore, the condition $\frac{\beta'}{\alpha}\mathrm{e}^{\mathrm{i}\Phi} = \pm\mathrm{i}$ needs to be fulfilled. Since α and β are chosen to be real, the only possible solution is to set $\Phi = (2n+1)\pi/2$ $(n = 0, 1, 2, \dots)$ and $\beta' = \alpha$. Choosing for instance $n = 0$, the phase requirement $\Phi = \pi/2$ can be achieved by a time delay of $\Delta\tau = \pi/(2\Omega_2)$ corresponding to a quarter of the beating period. In order to get completely rid of the quantum beat, the initial polarization has to be slightly rotated away from 45° $(\beta = \alpha)$ in order to compensate for the exponential decay term $\mathrm{e}^{-\Delta\tau/2}$ $(\beta' = \alpha)$. Taking the normalization $\alpha^2 + \beta^2 = 1$ and the condition $\beta' = \alpha$ into account, it is possible to fix the incident polarization in dependence of the time delay $\Delta\tau$,

$$\begin{aligned} \alpha(\Delta\tau) &= \sqrt{\frac{1}{\mathrm{e}^{-\Delta\tau}+1}} \; , \\ \beta(\Delta\tau) &= \sqrt{\frac{1}{\mathrm{e}^{\Delta\tau}+1}} \; . \end{aligned} \tag{8.15}$$

Evaluating Eqs. (8.13) for $\Phi = \pi/2$ and $\beta' = \alpha$, leads to the following field amplitudes at detector 1 and 2, respectively,

$$\begin{aligned} \boldsymbol{E}^{(1)}_{\mathrm{out}-1}(\xi,\tau) &= \xi\alpha\frac{f_{\mathrm{LM}}}{4}\Big\{\mathrm{e}^{\mathrm{i}\Omega_2\tau}(\boldsymbol{e}_\sigma - \mathrm{i}\boldsymbol{e}_\pi) + \mathrm{e}^{-\mathrm{i}\Omega_2\tau}(\boldsymbol{e}_\sigma + \mathrm{i}\boldsymbol{e}_\pi)\Big\}\mathrm{e}^{-\tau/2} \; , \\ \boldsymbol{E}^{(1)}_{\mathrm{out}-2}(\xi,\tau) &= \mathrm{i}\alpha\xi\frac{f_{\mathrm{LM}}}{4}\Big\{\mathrm{e}^{\mathrm{i}\Omega_2\tau}(\boldsymbol{e}_\sigma + \mathrm{i}\boldsymbol{e}_\pi) + \mathrm{e}^{-\mathrm{i}\Omega_2\tau}(\boldsymbol{e}_\sigma - \mathrm{i}\boldsymbol{e}_\pi)\Big\}\mathrm{e}^{-\tau/2} \; . \end{aligned} \tag{8.16}$$

Since the phase shift Φ is of opposite sign for the two frequency slits $\ell = -2$ and $\ell = 2$, each slit is marked by orthogonal polarization states, in Eqs. (8.16) for instance, $\boldsymbol{e}_-$ for $\ell = -2$ and $\boldsymbol{e}_+$ for $\ell = 2$ in the case of $\boldsymbol{E}_{\mathrm{out}-1}$, and vice versa in the case of $\boldsymbol{E}_{\mathrm{out}-2}$. As the orthogonal polarizations store the *which-way* information of the scattering process, the interference between the $\Delta M = 0$ hyperfine transitions should vanish in the intensity

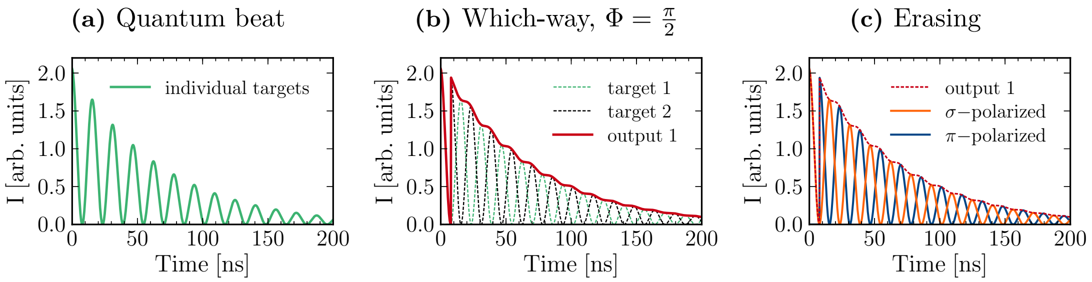
(a) Quantum beat **(b)** Which-way, $\Phi = \frac{\pi}{2}$ **(c)** Erasing

Figure 8.6: Quantum eraser via a relative time delay. (a) The individual targets exhibit the quantum beat pattern due to interference between the two $\Delta M = 0$ transitions. (b) Employing a time delay corresponding to $\Phi = \pi/2$ marks the scattering paths with orthogonal polarizations, destroying the interference. (c) The *which-way* information is erased and the interference is recovered by projecting onto the linear polarization basis, $\boldsymbol{e}_\sigma$ and $\boldsymbol{e}_\pi$.

spectra at the detectors. In order to prove this, we calculate $I^{(1)}_{\text{out}-1}$ and $I^{(1)}_{\text{out}-2}$ in the same manner as for zero time delay, resulting in

$$I^{(1)}_{\text{out}}(\xi, \tau) = \xi^2 \frac{f^2_{\text{LM}}}{8} \mathrm{e}^{-\tau} \ . \tag{8.17}$$

In comparison to Eqs. (8.14), the quantum beat represented by the cosine function disappeared as expected.

In Fig. 8.6, we show numerical results of the intensity spectra at detector 1 for the cases $\Phi = 0$ [Fig. 8.6(a)] and $\Phi = \pi/2$ [Fig. 8.6(b)]. Scattering orders up to $p_{\max} = 14$ have been included in the calculations. A detuning of $\Omega_2 \approx 28\,[\Gamma_0]$ due to Zeeman splitting has been considered, resulting in a time delay of $\Delta\tau/\Gamma_0 = 7.8$ ns for the special case of $\Phi = \pi/2$. Furthermore, the numerical results correspond to an effective target thickness $\xi = 1$ and an incident polarization characterized by $\alpha = 0.717$ and $\beta = 0.697$ determined via the condition $\beta' = \alpha$ for the case of $\Phi = \pi/2$. Fig. 8.6(a) shows that the quantum interference between the frequency slits $\ell = -2$ and $\ell = 2$ is preserved for $\Delta\tau = 0$ as already pointed out in Eq. (8.14).

In the case of $\Phi = \pi/2$, the frequency paths $\ell = -2$ and $\ell = 2$ should not interfere anymore, because the marking via the orthogonal polarizations $\boldsymbol{e}_-$ and $\boldsymbol{e}_+$ contains the *which-way* information (in frequency space) of the scattering process [see Eqs. (8.16)]. This behavior is clearly confirmed in Fig. 8.6(b) where the intensity spectrum displays a simple exponential decay (red curve) instead of the quantum beat interference pattern.

In order to restore the quantum interference by erasing the *which-way* information, a projection on the linear polarization basis (for instance with a polarizer) can be employed behind the beam splitter. Projecting on the σ- and π-polarization basis erases the *which-way* information stored in the orthogonal polarizations $\boldsymbol{e}_-$ and $\boldsymbol{e}_+$, reproducing the quantum beat pattern. The resulting intensity spectra are presented in Fig. 8.6(c). Following the lines of the quantum eraser concept [278], the relatively shifted intensity spectra for the σ and π components can be interpreted as fringes and anti-fringes.

So far, we consider the time delay $\Delta\tau$ would be introduced by an external element, e.g., a time-delay line [259,260,262,263]. Instead of using an external element, fast switchings

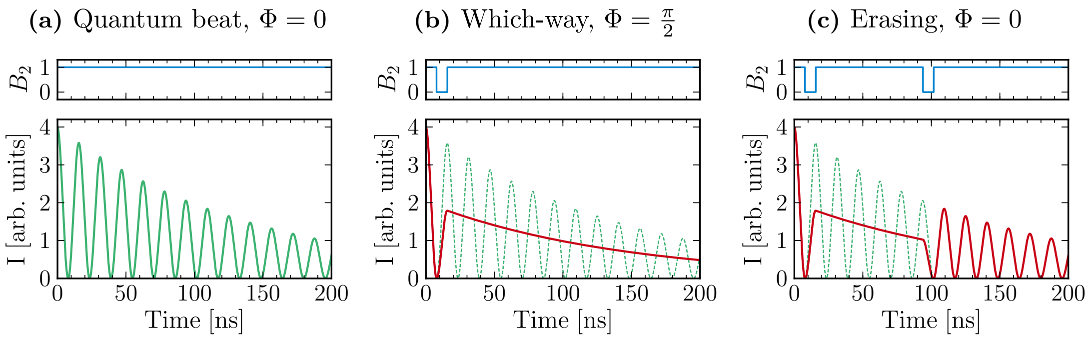

(a) Quantum beat, $\Phi = 0$ **(b)** Which-way, $\Phi = \frac{\pi}{2}$ **(c)** Erasing, $\Phi = 0$

Figure 8.7: Quantum eraser via an intrinsic storage scheme. The first-order intensity spectrum $|\boldsymbol{E}^{(1)}_{\text{out}-1}|^2$ is shown along with the time sequence of magnetic field switchings. The initial quantum beats (a) are first annihilated via a relative phase shift $\Phi = \pi/2$ (b) and subsequently restored by erasing the *which-way* information via a second storage sequence, introducing an additional $\pi/2$ phase shift (c).

of the magnetic field at target 2 can be employed to coherently store the incident field for a while [110]. The hyperfine interaction for the case of a magnetic field instantaneously turned off and on again is described by the Hamiltonian given in Eq. (5.46). Instead of using the general scheme considered in Eq. (5.46) where the magnetic field can have arbitrary directions before and after switching, we restrict ourselves to a switching sequence with $\boldsymbol{B}_2$ pointing along the x-axis, for both $\tau < \tau_0$ as well as $\tau > \tau_1$. Simplifying Eqs. (5.47) and (5.48) to this special case and following the procedure as it has been employed for a prompt rotation of the hyperfine field in Chap. 6, we finally obtain the following scattering output (in first order) coming from target 2,

$$\boldsymbol{E}^{(1)^\pi}(\xi,\tau) = \begin{cases} -\xi\frac{f_{\text{LM}}}{2}\left\{\mathrm{e}^{\mathrm{i}\Omega_2\tau} + \mathrm{e}^{-\mathrm{i}\Omega_2\tau}\right\}\mathrm{e}^{-\tau/2}\boldsymbol{e}_\pi & \text{for} \quad \tau < \tau_0 \ , \\ -\xi\frac{f_{\text{LM}}}{2}\left\{\mathrm{e}^{\mathrm{i}\Omega_2\tau_0} + \mathrm{e}^{-\mathrm{i}\Omega_2\tau_0}\right\}\mathrm{e}^{-\tau/2}\boldsymbol{e}_\pi & \text{for} \quad \tau_0 < \tau < \tau_1 \ , \\ -\xi\frac{f_{\text{LM}}}{2}\left\{\mathrm{e}^{\mathrm{i}\Omega_2(\tau-\tau_1+\tau_0)} + \mathrm{e}^{-\mathrm{i}\Omega_2(\tau-\tau_1+\tau_0)}\right\}\mathrm{e}^{-\tau/2}\boldsymbol{e}_\pi & \text{for} \quad \tau > \tau_1 \ . \end{cases} \tag{8.18}$$

Turning the magnetic field instantaneously off at a time instant $\tau_0 = (2n+1)\pi/(2\Omega_2)$ ($n = 0, 1, 2, \dots$) which corresponds to a minimum of the quantum beat, results in a strongly suppressed emission at times $\tau_0 < \tau < \tau_1$ where $\boldsymbol{B}_2 = 0$. After switching the magnetic field on again at τ_1, the initial emission spectrum is recovered with an amplitude decreased by the exponential decay factor $\mathrm{e}^{-(\tau_1-\tau_0)/2}$. By using this storage scheme, a time delay $\Delta\tau = \tau_1 - \tau_0$ (corresponding to the storage time) can be induced in comparison to the scattered field from target 1. Plugging Eq. (8.11) and Eq. (8.18) into Eqs. (8.10), leads for times $\tau > \tau_1$ qualitatively to the same behavior as an external time delay line as given in Eqs. (8.13) with the replacement $\beta' \mapsto \beta$. Choosing a setup with $\Delta\tau = \pi/(2\Omega_2)$ and an incident linear polarization of 45° ($\alpha = \beta = 1/\sqrt{2}$) marks the two frequency slits ($\ell = -2$ and $\ell = 2$) by orthogonal polarization states, accomplishing the destruction of the interference pattern as shown in Fig. 8.7(b). In order to restore the interference ability between the two scattering path ways, it is possible to either make use of a polarizer to project on the σ- and π-polarization basis as done in Fig. 8.6(c) or to apply a second magnetic field switching introducing another relative time delay of $\pi/(2\Omega_2)$. The latter scenario is illustrated in Fig. 8.7(c) where the cancellation of the interference pattern and its subsequent recovery can be followed in dependence on the sequence of magnetic field switchings.

In contrast to an external time delay line, the intrinsic photon storage requires no adjustment of the incident polarization away from 45° [see Eq. (8.15)] to accomplish the erasing scheme. Moreover, time delays longer than a few ns seem to be easier feasible and additional degrees of control abilities like B-field rotations are accessible, in comparison to external time delay lines. However, in order to apply switchings of the magnetic field in the first place, special iron samples without intrinsic Zeeman splitting like stainless steel are necessary. Turning magnetic fields of a few Tesla rapidly off and on may be realized according to Ref. [227] by two methods: (i) high-voltage snapper capacitors can be employed to regulate the pulse currents in magnetic coils; (ii) with the help of the lighthouse effect [104] the nuclear sample can be quickly moved out of the region where the magnetic field is applied. The scenario with an external time delay element on the other hand does not require any switching schemes, opening the possibility to make use of the high intrinsic hyperfine field occuring in magnetized $FeBO_3$ targets.

Summary & Outlook

In this Thesis, light-nucleus interaction has been investigated following two directions. First, the qualitative and quantitative changes which can be expected for nuclear quantum optics experiments performed at high-intensity XFEL sources in the near future have been studied in terms of secondary nuclear excitation in potentially occurring plasma environments. Second, we have proposed control schemes for hard x-rays operated in the opposite limit, namely single-photon nuclear interfaces, which offer new prospects for quantum information studies and time-energy complementarity tests.

In Chapter 4, the role of secondary nuclear excitation channels in photoexcitation scenarios with the XFEL has been investigated. The resonant driving of nuclear transitions with the XFEL is most likely to employ high-density, solid-state targets in order to improve the excitation rates. Secondary nuclear excitation might occur in the produced cold, dense plasma. We have quantified the magnitude of the possible secondary excitation via NEEC taking into account the plasma dynamics after the laser pulse via a hydrodynamic model. Our results show that the NEEC excitation process lasts for several ps until the plasma expansion completely diminishes the excitation rate. In contrast, the direct photoexcitation can only occur during the presence of the laser pulse, on the order of 100 fs. Due to the unique interaction between x-rays and matter, the XFEL-induced plasma is typically determined by a uniform state of well-characterized temperature and density in the beginning. The plasma conditions such as initial temperature, ion charge state distribution or electron flux play a crucial role for the magnitude of the occurring secondary excitation.

Our results show that for small nuclear transition energies and advantageous free electron energy distributions, as it is the case for isomer triggering of $^{93\mathrm{m}}$Mo, secondary NEEC may exceed by as much as five orders of magnitude. For larger nuclear transition energies, in the case of the 14.4 keV Mössbauer transition in ^{57}Fe, secondary NEEC can be safely neglected. Therefore, we may conclude that nuclear quantum optics experiments with bulk iron samples in normal incidence will not suffer from strong decoherence rates due to plasma-related processes. Based on our present results for $^{93\mathrm{m}}$Mo and ^{57}Fe, a general set of criteria for identifying the parameter regime for which secondary effects in the plasma are important has furthermore been worked out. Our findings will be of relevance for the layout of first nuclear excitation experiments at XFEL facilities in the near future.

In Chapter 7, the manipulation of hard x-rays at single-photon nuclear interfaces has been studied. Our findings prove that nuclear transitions can act as logical gates for polarization-encoded x-rays by controlling the collective nuclear response via timed rotations of the magnetic field. An x-ray photonic realization of single-input gates can be compiled by the mere variation of the magnetic field switching moment. Since the unary operations can be realized using a single setup, an additional control photon which triggers the magnetic field rotation can be exploited to design destructive operations with two input states, like a destructive x-ray C-NOT gate. The implementation of such basic logical operations with x-rays by using nuclear transitions may potentially advance quantum information in the future towards new and promising parameter regimes characterized by long coherence times and sub-Å spatial resolution, opening the perspective for more compact photonic devices.

In Chapter 8, we have proposed two quantum eraser schemes potentially shifting time-energy complementarity tests towards so-far unexplored parameter regimes in the hard x-ray domain. The essential idea of both schemes is to cancel the quantum interference between two hyperfine transitions by marking the scattering paths with orthogonal polarizations. The knowledge of the *which-way* information leads to the cancellation of the quantum beat pattern in the NFS time spectrum. By using a polarizer projecting on the linear polarization basis, the *which-way* information can be erased and the beat pattern is restored.

In the following, a short outlook is given for possible future investigations based on our present results.

Secondary nuclear processes in grazing incidence setups

The competition between the direct photoexcitation and the secondary NEEC process in XFEL-induced plasmas has been studied in normal-incidence setups with solid-state targets. Caution is however advised for extending these conclusions for experiments with x-ray thin film cavities containing ^{57}Fe layers, which operate in grazing incidence. These cavities have turned out to be an ideal playground for the mutual control of x-rays and nuclear transitions with synchrotron sources over the last years and are expected to play a crucial role in the further development of nuclear quantum optics in the nonlinear excitation domain. However, the usage of the XFEL in this case may lead to plasma formation which strongly influences the proper functionality of the x-ray cavities, potentially destroying envisaged enhancement or coherence effects. Extending our ideas to this cavity geometry could help to reveal and predict the role of plasma-mediated processes in this case which is of importance for future nuclear quantum optics experiments at the XFEL employing x-ray thin film cavities.

Effect of nuclear processes for the plasma dynamics

In our current approach the nuclear excitation processes and the plasma expansion are treated separately. In order to reveal potential nuclear effects on the dynamics of the XFEL-induced plasma, a self-consistent treatment is required. One approach could be to incorporate the nuclear processes into the hydrodynamic expansion in terms of a rate equation model. Since NEEC is highly dependent on the prevailing electron energy and ion charge state distributions, measured excitation rates may even contain information usable for plasma analysis.

XFEL-induced plasmas with optimized conditions for NEEC

Our investigation of secondary NEEC has so far been restricted to setups and parameter regimes initially designed for the direct nuclear photoexcitation. The frequency of the XFEL radiation, for instance, has been so far chosen resonant to the nuclear transition under investigation, in order to allow for direct photoexcitation. The theoretical framework derived in this Thesis can however be used to extract a parameter set optimized for very efficient secondary processes. Disregarding the direct excitation channel, the photon frequency can be determined such that a plasma state is created, optimized for secondary NEEC. Since NEEC is anyway expected to give a valuable contribution to the plasma-mediated nuclear excitation in cold, high-density plasmas for certain nuclear transitions, such studies towards an optimized XFEL scenario may bring us a step closer to the first experimental NEEC signature.

Extensions for the coherent manipulation of single hard x-rays

The control schemes presented in Part II of this Thesis employed NFS setups with temporally short, broadband x-ray pulses applied on ^{57}Fe targets. Three possible directions how to extend these methods are specified in the following. First, since in the optical domain quantum optical control schemes are mostly operated with spectrally narrow photons, it is natural to ask whether similar procedures can be designed for polarization-encoded x-ray pulses, spectrally on the order of the nuclear transition width. Second, it may be helpful to consider other nuclear species than ^{57}Fe, having nuclear spins different from $I_{\mathrm{g}} = 1/2$ and $I_{\mathrm{e}} = 3/2$. Utilizing the particular level structures could further improve and extend the proposed setups. Finally, one could also investigate quantum interference phenomena like the Houng-Ou-Mandel effect [5]. Such photon-photon correlations have the potential to advance the presented binary logical operations to real non-destructive two-qubit gates.

Fully quantum mechanical approach to NFS

The description of the light-nucleus interaction used in this Thesis follows a semiclassical approach where the radiation field is considered to behave classically. This treatment is valid for photons in a coherent state as it is the case, for instance, for SR pulses. The XFEL in contrast is a very powerful light source approaching the coherence properties of lasers in the conventional sense. This progress will help to leave the linear excitation regime, going from one to multiple nuclear excitations per pulse. In this regime, the study of photon-photon correlations becomes accessible where the quantum properties of the radiation field gain in importance. Therefore, the development of a fully quantum mechanical treatment of NFS becomes necessary in order to reveal quantum features of nuclear excitation and of x-ray pulse propagation. Such a theory would also allow to explore the preservation of the quantum characteristics of single x-ray quanta in recently proposed storage and release schemes employing NFS.

Appendix A

Supplement for NEEC theory

NEEC matrix element: electric transitions

In order to calculate the electric NEEC matric element [Eq. (3.36)] for a fixed multipolarity L, we first make use of the expansion given in Eq. (3.33),

$$\begin{aligned}\langle\Psi_{\mathrm{d}}|\hbar_{\mathrm{en}}|\Psi_{\mathrm{i}}\rangle = \frac{1}{R_0^{L+2}}\sum_M \frac{4\pi}{2L+1}\langle I_{\mathrm{d}}M_{\mathrm{d}}|\mathbb{Q}_{LM}|I_{\mathrm{i}}M_{\mathrm{i}}\rangle \sum_{\kappa m}\mathrm{i}^l \mathrm{e}^{\mathrm{i}\Delta_\kappa}\sum_{m_l} C(l\ \frac{1}{2}\ j; m_l\ m_{\mathrm{s}}\ m) \\ \times Y^*_{lm_l}(\theta_{\boldsymbol{p}},\varphi_{\boldsymbol{p}})\,\langle n_{\mathrm{d}}\kappa_{\mathrm{d}}m_{\mathrm{d}}|Y^*_{LM}(\theta_{\mathrm{e}},\varphi_{\mathrm{e}})\int_0^\infty dr_{\mathrm{n}} r_{\mathrm{n}}^2\frac{r_<^L}{r_>^{L+1}}\delta(R_0-r_{\mathrm{n}})|\varepsilon\kappa m\rangle\ .\end{aligned} \tag{A.1}$$

How to express the nuclear part $\langle I_{\mathrm{d}}M_{\mathrm{d}}|\mathbb{Q}_{LM}|I_{\mathrm{i}}M_{\mathrm{i}}\rangle$ in terms of reduced transition probablilities has already been discussed in Eqs. (2.21) and (2.22). In order to further evaluate Eq. (A.1), the main task is to calculate the electronic contribution which can be written as

$$\begin{aligned}&\langle n_{\mathrm{d}}\kappa_{\mathrm{d}}m_{\mathrm{d}}|Y^*_{LM}(\theta_{\mathrm{e}},\varphi_{\mathrm{e}})\int_0^\infty \mathrm{d}r_{\mathrm{n}}\, r_{\mathrm{n}}^2\frac{r_<^L}{r_>^{L+1}}\delta(R_0-r_{\mathrm{n}})|\varepsilon\kappa m\rangle \\ &\quad= \int_0^\infty \mathrm{d}r_{\mathrm{e}}\, r_{\mathrm{e}}^2\int_0^\infty \mathrm{d}r_{\mathrm{n}}\, r_{\mathrm{n}}^2\frac{r_<^L}{r_>^{L+1}}\delta(R_0-r_{\mathrm{n}})\Big\{g_{n_{\mathrm{d}}\kappa_{\mathrm{d}}}(r_{\mathrm{e}})g_{\varepsilon\kappa}(r_{\mathrm{e}})\langle\kappa_{\mathrm{d}}m_{\mathrm{d}}|Y^*_{LM}(\theta_{\mathrm{e}},\varphi_{\mathrm{e}})|\kappa m\rangle \\ &\qquad + f_{n_{\mathrm{d}}\kappa_{\mathrm{d}}}(r_{\mathrm{e}})f_{\varepsilon\kappa}(r_{\mathrm{e}})\langle-\kappa_{\mathrm{d}}m_{\mathrm{d}}|Y^*_{LM}(\theta_{\mathrm{e}},\varphi_{\mathrm{e}})|-\kappa m\rangle\Big\} \\ &\quad= I^{(1)}_{L,\kappa_{\mathrm{d}},\kappa}\langle\kappa_{\mathrm{d}}m_{\mathrm{d}}|Y^*_{LM}(\theta_{\mathrm{e}},\varphi_{\mathrm{e}})|\kappa m\rangle + I^{(2)}_{L,\kappa_{\mathrm{d}},\kappa}\langle-\kappa_{\mathrm{d}}m_{\mathrm{d}}|Y^*_{LM}(\theta_{\mathrm{e}},\varphi_{\mathrm{e}})|-\kappa m\rangle\ .\end{aligned} \tag{A.2}$$

Here, we applied the representations of $|\varepsilon\kappa m\rangle$ and $|n_{\mathrm{d}}\kappa_{\mathrm{d}}m_{\mathrm{d}}\rangle$ given in Eqs. (3.39) and (3.40), respectively, and introduced the notations $|\kappa m\rangle$ and $|\kappa_{\mathrm{d}}m_{\mathrm{d}}\rangle$ which denote the spin-angular functions Ω_κ^m and $\Omega_{\kappa_{\mathrm{d}}}^{m_{\mathrm{d}}}$, respectively. Furthermore, the occurring integrals have been abbreviated by $I^{(1)}_{L,\kappa_{\mathrm{d}},\kappa}$ and $I^{(2)}_{L,\kappa_{\mathrm{d}},\kappa}$. Making use of the Wigner-Eckart theorem and the relation $Y^*_{LM}=(-1)^M Y_{L-M}$, the matrix elements $\langle\kappa_{\mathrm{d}}m_{\mathrm{d}}|Y^*_{LM}|\kappa m\rangle$ and $\langle-\kappa_{\mathrm{d}}m_{\mathrm{d}}|Y^*_{LM}|-\kappa m\rangle$ can be written in the following form

$$\langle\kappa_1 m_1|Y^*_{LM}|\kappa_2 m_2\rangle = \frac{(-1)^{j_2-m_2+M}}{\sqrt{2L+1}}C(j_1\ j_2\ L; m_1\ -m_2\ -M)\langle\kappa_1\|Y_L\|\kappa_2\rangle\ . \tag{A.3}$$

Following Ref. [298], the reduced matrix element occurring in Eq. (A.3) is given by

$$\begin{aligned}\langle\kappa_1\|Y_L\|\kappa_2\rangle &= (-1)^{j_2-1/2+L}\left[\frac{(2j_1+1)(2j_2+1)(2L+1)}{4\pi}\right]^{1/2}\begin{pmatrix} j_1 & j_2 & L \\ \frac{1}{2} & -\frac{1}{2} & 0\end{pmatrix} \\ &= (-1)^{L+2j_1}\left[\frac{(2j_1+1)(2L+1)}{4\pi}\right]^{1/2} C(j_1\ L\ j_2; \frac{1}{2}\ 0\ \frac{1}{2})\ . \end{aligned} \tag{A.4}$$

Here, we employed the connection between the Wigner $3j$-symbols and the Clebsch-Gordan coefficients given in Eq. (3.43). Note that we use a slightly different definition of the reduced matrix elements than the one used in Ref. [298]. Inserting Eq. (A.4) into Eq. (A.3) and setting $\kappa_1 = \kappa_\mathrm{d}$, $m_1 = m_\mathrm{d}$, $\kappa_2 = \kappa$ and $m_2 = m$, we obtain

$$\begin{aligned}\langle\kappa_\mathrm{d} m_\mathrm{d}|Y^*_{LM}|\kappa m\rangle &= (-1)^{j-m+M+L+2j_\mathrm{d}} \\ &\times\left(\frac{2j_\mathrm{d}+1}{4\pi}\right)^{1/2} C(j_\mathrm{d}\ j\ L; m_\mathrm{d}\ -m\ -M)C(j_\mathrm{d}\ L\ j;\frac{1}{2}\ 0\ \frac{1}{2})\ . \end{aligned} \tag{A.5}$$

It can be easily shown that the same relation holds for $\langle-\kappa_\mathrm{d} m_\mathrm{d}|Y^*_{LM}|-\kappa m\rangle$ such that Eq. (A.2) simplifies to

$$\begin{aligned}&\langle n_\mathrm{d}\kappa_\mathrm{d} m_\mathrm{d}|Y^*_{LM}(\theta_\mathrm{e},\varphi_\mathrm{e})\int_0^\infty \mathrm{d}r_\mathrm{n}\, r_\mathrm{n}^2\frac{r_<^L}{r_>^{L+1}}\delta(R_0-r_\mathrm{n})|\varepsilon\kappa m\rangle \\ &= (-1)^{j-m+M+L+2j_\mathrm{d}}\left(\frac{2j_\mathrm{d}+1}{4\pi}\right)^{1/2} C(j_\mathrm{d}\ j\ L; m_\mathrm{d}\ -m\ -M)C(j_\mathrm{d}\ L\ j;\frac{1}{2}\ 0\ \frac{1}{2}) \\ &\quad\times\underbrace{\left(I^{(1)}_{L,\kappa_\mathrm{d},\kappa}+I^{(2)}_{L,\kappa_\mathrm{d},\kappa}\right)}_{=R^{(\mathcal{E})}_{L,\kappa_\mathrm{d},\kappa}}\ . \end{aligned} \tag{A.6}$$

Plugging Eq. (A.6) into Eq. (A.1) and expressing the nuclear part in terms of the reduced matrix elements [Eq. (2.21)], we obtain the following solution for the NEEC matrix element in the case of electric transitions,

$$\begin{aligned}&\langle I_\mathrm{d} M_\mathrm{d}, n_\mathrm{d}\kappa_\mathrm{d} m_\mathrm{d}, 0|\hbar_\mathrm{en}|I_\mathrm{i} M_\mathrm{i}, \varepsilon\kappa m, 0\rangle \\ &= \frac{1}{R_0^{L+2}}\sum_M (-1)^{I_\mathrm{d}+M_\mathrm{i}+L+M+m+3j_\mathrm{d}}\left[\frac{4\pi(2j_\mathrm{d}+1)}{(2L+1)^3}\right]^{1/2}\langle I_\mathrm{d}\|\mathbb{Q}_L\|I_\mathrm{i}\rangle \\ &\quad\times C(I_\mathrm{i}\ I_\mathrm{d}\ L; -M_\mathrm{i}\ M_\mathrm{d}\ M)C(j\ j_\mathrm{d}\ L; -m\ m_\mathrm{d}\ -M)C(j_\mathrm{d}\ L\ j;\frac{1}{2}\ 0\ \frac{1}{2})\, R^{(\mathcal{E})}_{L,\kappa_\mathrm{d},\kappa}\ . \end{aligned} \tag{A.7}$$

This solution can be used to derive the NEEC rate $Y^{(\mathcal{E}L)}_\mathrm{neec}$ given in Eq. (3.37). Starting from Eq. (3.34) and employing the normalization condition of the spherical harmonics, Y_neec can be expressed directly in terms of the matrix elements provided in Eq. (A.7).

Using further the orthogonality properties of the Clebsch-Gordan coefficients leads to

$$
\begin{aligned}
Y^{(\mathcal{E}L)}_{\mathrm{neec}} &= \frac{2\pi(2J_{\mathrm{d}}+1)}{2(2I_{\mathrm{i}}+1)(2J_{\mathrm{i}}+1)(2j_{\mathrm{d}}+1)} \\
&\quad\times \sum_{M_{\mathrm{i}} m_{\mathrm{s}}} \sum_{M_{\mathrm{d}} m_{\mathrm{d}}} \int d\Omega_{\boldsymbol{p}} \left|\langle I_{\mathrm{d}} M_{\mathrm{d}}, n_{\mathrm{d}}\kappa_{\mathrm{d}} m_{\mathrm{d}}, 0|\mathcal{H}_{\mathrm{en}}|I_{\mathrm{i}} M_{\mathrm{i}}, \boldsymbol{p} m_{\mathrm{s}}, 0\rangle\right|^2 \rho_{\mathrm{i}} \\
&= \frac{2\pi(2J_{\mathrm{d}}+1)}{2(2I_{\mathrm{i}}+1)(2J_{\mathrm{i}}+1)(2j_{\mathrm{d}}+1)} \\
&\quad\times \sum_{M_{\mathrm{i}}} \sum_{M_{\mathrm{d}} m_{\mathrm{d}}} \sum_{\kappa m} \left|\langle I_{\mathrm{d}} M_{\mathrm{d}}, n_{\mathrm{d}}\kappa_{\mathrm{d}} m_{\mathrm{d}}, 0|\mathcal{H}_{\mathrm{en}}|I_{\mathrm{i}} M_{\mathrm{i}}, \varepsilon\kappa m, 0\rangle\right|^2 \rho_{\mathrm{i}} \\
&= \frac{4\pi^2\rho_{\mathrm{i}}}{(2L+1)^2} R_0^{-2(L+2)} \mathcal{B}(\mathcal{E}L, I_{\mathrm{i}} \to I_{\mathrm{d}}) \frac{2J_{\mathrm{d}}+1}{2J_{\mathrm{i}}+1} \sum_{\kappa} C(j_{\mathrm{d}}\ L\ j; \frac{1}{2}\ 0\ \frac{1}{2})^2 |R^{(\mathcal{E})}_{L,\kappa_{\mathrm{d}},\kappa}|^2 \ .
\end{aligned}
\tag{A.8}
$$

NEEC matrix element: magnetic transitions

In the case of magnetic transitions of fixed multipolarity L, the NEEC matrix element [Eq. (3.41)] can be written as

$$
\begin{aligned}
\langle \Psi_{\mathrm{d}}|\mathcal{H}_{\mathrm{magn}}|\Psi_{\mathrm{i}}\rangle = 4\pi\mathrm{i} \sum_{LM} (-1)^M \sqrt{\frac{L+1}{L}} \frac{1}{2L+1} \langle I_{\mathrm{d}} M_{\mathrm{d}}|\mathcal{M}_{LM}|I_{\mathrm{i}} M_{\mathrm{i}}\rangle \sum_{\kappa m} \mathrm{i}^l \mathrm{e}^{\mathrm{i}\Delta_\kappa} \sum_{m_l} Y^*_{l m_l}(\theta_{\boldsymbol{p}}, \varphi_{\boldsymbol{p}}) \\
\times C(l\ \frac{1}{2}\ j; m_l\ m_{\mathrm{s}}\ m) \langle n_{\mathrm{d}}\kappa_{\mathrm{d}} m_{\mathrm{d}}| r_{\mathrm{e}}^{-(L+1)} \boldsymbol{\alpha}\cdot \boldsymbol{Y}^{-M}_{LL}(\theta_{\mathrm{e}}, \varphi_{\mathrm{e}})|\varepsilon\kappa m\rangle \ ,
\end{aligned}
\tag{A.9}
$$

where $\boldsymbol{\alpha}$ can be expressed in terms of the Pauli matrices $\boldsymbol{\sigma} = (\sigma_x, \sigma_y, \sigma_z)$,

$$
\boldsymbol{\alpha} = \begin{pmatrix} 0 & \boldsymbol{\sigma} \\ \boldsymbol{\sigma} & 0 \end{pmatrix} \ . \tag{A.10}
$$

Analogously to the case of electric transitions, the main task in the calculation of Eq. (A.9) is to compute the electronic part. Making use of Eqs. (3.39) and (3.40), we obtain

$$
\begin{aligned}
&\langle n_{\mathrm{d}}\kappa_{\mathrm{d}} m_{\mathrm{d}}| r_{\mathrm{e}}^{-(L+1)} \boldsymbol{\alpha}\cdot \boldsymbol{Y}^{-M}_{LL}(\theta_{\mathrm{e}}, \varphi_{\mathrm{e}})|\varepsilon\kappa m\rangle \\
&\quad = \mathrm{i}\int_0^\infty \mathrm{d}r_{\mathrm{e}}\, r_{\mathrm{e}}^2 r_{\mathrm{e}}^{-(L+1)} \Big\{ g_{n_{\mathrm{d}}\kappa_{\mathrm{d}}}(r_{\mathrm{e}}) f_{\varepsilon\kappa}(r_{\mathrm{e}}) \langle \kappa_{\mathrm{d}} m_{\mathrm{d}}|\boldsymbol{\sigma}\cdot \boldsymbol{Y}^{-M}_{LL}(\theta_{\mathrm{e}}, \varphi_{\mathrm{e}})|-\kappa m\rangle \\
&\qquad - f_{n_{\mathrm{d}}\kappa_{\mathrm{d}}}(r_{\mathrm{e}}) g_{\varepsilon\kappa}(r_{\mathrm{e}}) \langle -\kappa_{\mathrm{d}} m_{\mathrm{d}}|\boldsymbol{\sigma}\cdot \boldsymbol{Y}^{-M}_{LL}(\theta_{\mathrm{e}}, \varphi_{\mathrm{e}})|\kappa m\rangle \Big\} \\
&\quad = \mathrm{i}J^{(1)}_{L,\kappa_{\mathrm{d}},\kappa} \langle \kappa_{\mathrm{d}} m_{\mathrm{d}}|\boldsymbol{\sigma}\cdot \boldsymbol{Y}^{-M}_{LL}(\theta_{\mathrm{e}}, \varphi_{\mathrm{e}})|-\kappa m\rangle - \mathrm{i}J^{(2)}_{L,\kappa_{\mathrm{d}},\kappa} \langle -\kappa_{\mathrm{d}} m_{\mathrm{d}}|\boldsymbol{\sigma}\cdot \boldsymbol{Y}^{-M}_{LL}(\theta_{\mathrm{e}}, \varphi_{\mathrm{e}})|\kappa m\rangle \ ,
\end{aligned}
\tag{A.11}
$$

where the integrals $J^{(1)}_{L,\kappa_{\mathrm{d}},\kappa}$ and $J^{(2)}_{L,\kappa_{\mathrm{d}},\kappa}$ have been introduced. In order to evaluate the occurring matrix elements of the scalar product $\boldsymbol{\sigma}\cdot \boldsymbol{Y}^{-M}_{LL}$, the spherical composite tensor

$T_{JM}(Y_L, \boldsymbol{\sigma})$ is introduced,

$$T_{JM}(Y_L, \boldsymbol{\sigma}) = \boldsymbol{\sigma} \cdot \boldsymbol{Y}^M_{JL}(\theta, \varphi) = \sum_\nu \sum_q C(L\ 1\ J; \nu\ q\ M) Y_{L\nu}(\theta, \varphi)\, (\boldsymbol{\sigma} \cdot \boldsymbol{\varepsilon}_q)\ . \tag{A.12}$$

Applying the Wigner-Eckart theorem, we obtain

$$\langle \kappa_1 m_1 | T_{JM}(Y_L, \boldsymbol{\sigma}) | \kappa_2 m_2 \rangle = \frac{(-1)^{j_2 - m_2}}{\sqrt{2J+1}} C(j_1\ j_2\ J; m_1\ \ -m_2\ M) \langle \kappa_1 \| T_J(Y_L, \boldsymbol{\sigma}) \| \kappa_2 \rangle\ , \tag{A.13}$$

where the reduced matrix element is determined by [298]

$$\begin{aligned} \langle \kappa_1 \| T_J(Y_L, \boldsymbol{\sigma}) \| \kappa_2 \rangle &= (-1)^{2J} \left[(2j_1+1)(2j_2+1)(2J+1) \right]^{1/2} \\ &\times \begin{Bmatrix} j_1 & j_2 & J \\ l_1 & l_2 & L \\ 1/2 & 1/2 & 1 \end{Bmatrix} \langle l_1 \| Y_L \| l_2 \rangle \langle \frac{1}{2} \| \boldsymbol{\sigma} \| \frac{1}{2} \rangle\ . \end{aligned} \tag{A.14}$$

Here, l_1 and l_2 denote the orbital angular momentum corresponding to κ_1 and κ_2, respectively. Furthermore, the Wigner $9j$-symbol [298] has been used in Eq. (A.14). The reduced matrix elements $\langle l_1 \| Y_L \| l_2 \rangle$ and $\langle \frac{1}{2} \| \boldsymbol{\sigma} \| \frac{1}{2} \rangle$ are given by [298]

$$\langle l_1 \| Y_L \| l_2 \rangle = (-1)^{L - l_2} \left[\frac{(2l_1+1)(2l_2+1)(2L+1)}{4\pi} \right]^{1/2} \begin{pmatrix} L & l_2 & l_1 \\ 0 & 0 & 0 \end{pmatrix} \tag{A.15}$$

and

$$\langle \frac{1}{2} \| \boldsymbol{\sigma} \| \frac{1}{2} \rangle = \sqrt{6}\ , \tag{A.16}$$

respectively. Plugging Eqs. (A.15) and (A.16) into Eq. (A.14) and setting $J = L$, the following form of $\langle \kappa_1 \| T_L(Y_L, \boldsymbol{\sigma}) \| \kappa_2 \rangle$ can be obtained,

$$\begin{aligned} \langle \kappa_1 \| T_L(Y_L, \boldsymbol{\sigma}) \| \kappa_2 \rangle &= (-1)^{j_2 - L + 1/2} \left[\frac{(2j_1+1)(2j_2+1)(2L+1)}{4\pi L(L+1)} \right]^{1/2} \\ &\times (\kappa_2 - \kappa_1) \begin{pmatrix} j_1 & j_2 & L \\ \frac{1}{2} & -\frac{1}{2} & 0 \end{pmatrix}\ . \end{aligned} \tag{A.17}$$

Here, the condition $l_1 + l_2 + L =$ "even" has been employed which translates to the parity conservation law of magnetic transitions if used in Eq. (A.11): $(-1)^l (-1)^{l_\mathrm{d}} = (-1)^{L+1}$. Applying Eq. (A.17) onto the electronic matrix element given in Eq. (A.11) results in

$$\begin{aligned} &\langle n_\mathrm{d} \kappa_\mathrm{d} m_\mathrm{d} | r_\mathrm{e}^{-(L+1)} \boldsymbol{\alpha} \cdot \boldsymbol{Y}^{-M}_{LL}(\theta_\mathrm{e}, \varphi_\mathrm{e}) | \varepsilon \kappa m \rangle \\ &= \mathrm{i}(-1)^{j - L + 1/2} \left[\frac{(2j+1)(2L+1)}{4\pi L(L+1)} \right]^{1/2} C(j\ L\ j_\mathrm{d}; m\ \ -M\ m_\mathrm{d}) \begin{pmatrix} j_\mathrm{d} & j & L \\ \frac{1}{2} & -\frac{1}{2} & 0 \end{pmatrix} \\ &\times (\kappa + \kappa_\mathrm{d}) \underbrace{\left(J^{(1)}_{L,\kappa_\mathrm{d},\kappa} + J^{(2)}_{L,\kappa_\mathrm{d},\kappa} \right)}_{= R^{(\mathcal{M})}_{L,\kappa_\mathrm{d},\kappa}}\ . \end{aligned} \tag{A.18}$$

Inserting this equation into Eq. (A.9) and using Eq. (2.15), we finally obtain

$$
\begin{aligned}
&\langle I_{\mathrm{d}} M_{\mathrm{d}}, n_{\mathrm{d}} \kappa_{\mathrm{d}} m_{\mathrm{d}}, 0 | \hbar_{\mathrm{magn}} | I_{\mathrm{i}} M_{\mathrm{i}}, \varepsilon \kappa m, 0 \rangle \\
&\quad = \sum_{M} (-1)^{I_{\mathrm{i}} - M_{\mathrm{i}} + M + j - L - 1/2} \left[\frac{4\pi(2j+1)}{L^2(2L+1)^2} \right]^{1/2} \langle I_{\mathrm{d}} \| \mathscr{M}_L \| I_{\mathrm{i}} \rangle \, (\kappa + \kappa_{\mathrm{d}}) \\
&\qquad \times C(j\ L\ j_{\mathrm{d}}; m\ \ {-M}\ m_{\mathrm{d}}) C(I_{\mathrm{d}}\ I_{\mathrm{i}}\ L; M_{\mathrm{d}}\ \ {-M_{\mathrm{i}}}\ M) \begin{pmatrix} j_{\mathrm{d}} & j & L \\ \frac{1}{2} & -\frac{1}{2} & 0 \end{pmatrix} R^{(\mathcal{M})}_{L, \kappa_{\mathrm{d}}, \kappa}
\end{aligned}
\tag{A.19}
$$

The NEEC transition rate $Y^{(\mathcal{M}L)}_{\mathrm{neec}}$ can be calculated analogously to the case of electric transitions, which leads to

$$
\begin{aligned}
Y^{(\mathcal{M}L)}_{\mathrm{neec}} &= \frac{2\pi(2J_{\mathrm{d}}+1)}{2(2I_{\mathrm{i}}+1)(2J_{\mathrm{i}}+1)(2j_{\mathrm{d}}+1)} \\
&\qquad \times \sum_{M_{\mathrm{i}}} \sum_{M_{\mathrm{d}} m_{\mathrm{d}}} \sum_{\kappa m} \left| \langle I_{\mathrm{d}} M_{\mathrm{d}}, n_{\mathrm{d}} \kappa_{\mathrm{d}} m_{\mathrm{d}}, 0 | \hbar_{\mathrm{magn}} | I_{\mathrm{i}} M_{\mathrm{i}}, \epsilon \kappa m, 0 \rangle \right|^2 \rho_{\mathrm{i}} \\
&= \frac{4\pi^2 \rho_{\mathrm{i}}}{L^2(2L+1)^2} \mathcal{B}(\mathcal{M}L, I_{\mathrm{i}} \to I_{\mathrm{d}}) \frac{2J_{\mathrm{d}}+1}{2J_{\mathrm{i}}+1} \sum_{\kappa} (2j+1)(\kappa_{\mathrm{d}} + \kappa)^2 \begin{pmatrix} j_{\mathrm{d}} & j & L \\ \frac{1}{2} & -\frac{1}{2} & 0 \end{pmatrix}^2 \\
&\qquad \times \left| R^{(\mathcal{M})}_{L, \kappa_{\mathrm{d}}, \kappa} \right|^2 .
\end{aligned}
\tag{A.20}
$$

Appendix B

^{93}Mo isomer production

The long–lived nuclear excited state $^{93\mathrm{m}}$Mo can be produced in $^{93}_{41}$Nb(p,n)$^{93\mathrm{m}}_{42}$Mo reactions. In this way it is possible to create the isomers directly implanted into solid–state niobium foils used as target in the considered XFEL scenario. Cross sections for the isomer production have already been measured experimentally in several works [299–305] and are presented in Fig. B.1 as a function of the impinging proton energy.

We estimate the $^{93\mathrm{m}}$Mo production rate according to

$$I[^{93\mathrm{m}}\mathrm{Mo}] = \frac{N_{\mathrm{A}}\rho L}{A}\sigma\Phi\epsilon, \tag{B.1}$$

where σ represents the reaction cross section, Φ the proton flux and ϵ the transmission efficiency. The factor $N_{\mathrm{A}}\rho L/A$ denotes the area density and is solely determined by the Nb target properties. Therein, $N_{\mathrm{A}} = 6.022 \times 10^{23}$ mol^{-1} is the Avogadro constant, $\rho = 8.57$ g/cm^3 stands for the mass density and $A = 93$ g/mol for the atomic mass of niobium, and $L = 1$ μm represents the target thickness. Numerically this evaluates to 5.5×10^{18} Nb atoms/cm^2.

The cross section σ of the isomer production strongly depends on the energy of the incoming protons as seen from Fig. B.1. According to [301–303, 305] σ is maximized in the energy region from 10 to 15 MeV, with values between 10 and 30 mb. In the following we consider for exemplification a proton beam of 12 MeV energy. Since the energy loss of 12 MeV protons is only about 18 keV per 1 μm Nb foil, several target foils could be manufactured at once. By taking a stack of 100 foils the 12 MeV protons slow down by merely 2 MeV[1]. Thus, essentially the whole energy range where the isomer production is most efficient would be covered by such a proton beam, guaranteeing cross section values between 10 and 30 mb. Additionally, at 12 MeV proton energy a minimal beam flux of 10^{13} protons/s can be assumed[2] which leads together with a transmission efficiency $\epsilon = 1$ and a cross section $\sigma = 30$ mb to an isomer production rate of $I[^{93\mathrm{m}}\mathrm{Mo}] = 1.7 \times 10^6$ s^{-1}. As a technical remark we note that in this procedure the Nb foils need to be cooled, since the total energy deposition of the proton beam is relatively high during the whole irradiation time. Moreover, manufacturing and handling of more than 100 foils is practically unrealistic.

By taking the exponential decay of the isomeric state into account, the number of

---

[1] The energy loss in the Nb foils was calculated using the ATIMA code [306].

[2] Cyclotron-based facilities with proton beam intensities higher than 100 μA are commercially available, see e.g. [307].

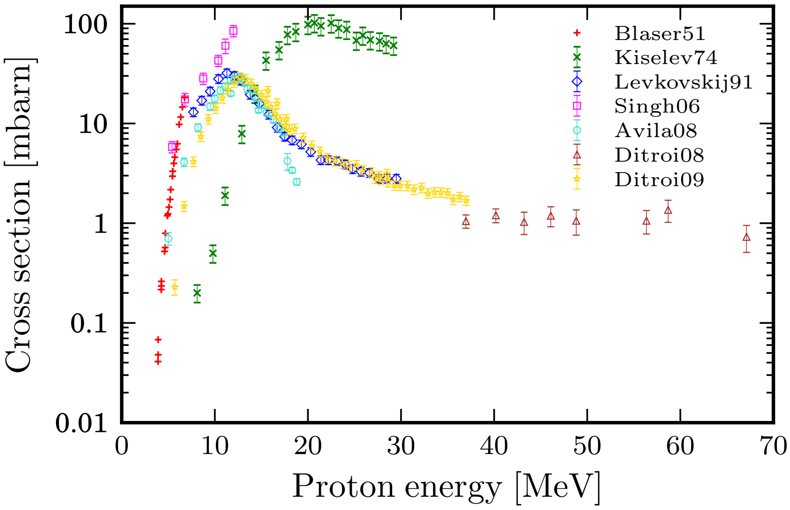

Figure B.1: Experimental cross sections for $^{93}_{41}$Nb(p,n)$^{93m}_{42}$Mo reaction as a function of the proton energy. The data is taken from [206]. The experimental data sets indicated in the legend as *Blaser51, Kiselev74, Levkovskij91, Singh06, Avila08, Ditroi08*, and *Ditroi09* can be found in Refs. [299–305], respectively.

produced isomers per foil after an irradiation time t can be expressed as

$$N[^{93\mathrm{m}}\mathrm{Mo}]\,(t) = \frac{I[^{93\mathrm{m}}\mathrm{Mo}]}{\lambda}\left(1 - e^{-\lambda t}\right), \tag{B.2}$$

where $\lambda = \ln 2/T_{1/2}$ denotes the exponential decay constant. The $^{93\mathrm{m}}$Mo half life is given by $T_{1/2} = 6.85$ h [194]. For instance, after an irradiation time of $t = 5 \times T_{1/2}$ the number of isomers in the sample foil adds up to 5.6×10^{10} for $\sigma = 30$ mb. In Table B.1 values for $N[^{93\mathrm{m}}\mathrm{Mo}]$ for different times t can be found considering reaction cross sections of either 10 or 30 mb.

The number of produced isomers given by Eq. (B.2) is spatially distributed over the spot size of the impinging proton beam which is typically in the order of 1 mm^2 for the considered beam intensity. Since the XFEL can be focused much better, for instance on a spot of 10 μm^2 as it was assumed in the present work, the isomer density can safely be assumed to be homogeneous in this area. Considering the foil thickness of 1 μm, one obtains after an irradtion time of $t = 5 \times T_{1/2}$ an isomer density of

$$n[^{93\mathrm{m}}\mathrm{Mo}] = \frac{5.5 \times 10^{10}}{10^{-2}\ \mathrm{cm}^2 \cdot 10^{-4}\ \mathrm{cm}} = 5.5 \times 10^{16}\ \mathrm{cm}^{-3}. \tag{B.3}$$

In our calculations we use the more conservative value of 1×10^{16} cm^{-3} produced isomers.

t (s)	$N[^{93\mathrm{m}}\mathrm{Mo}]$	
	$\sigma = 10$ mb	$\sigma = 30$ mb
1	5.55×10^5	1.67×10^6
$1 \times T_{1/2}$	1.90×10^9	5.70×10^9
$2 \times T_{1/2}$	9.87×10^9	2.96×10^{10}
$3 \times T_{1/2}$	1.48×10^{10}	4.44×10^{10}
$4 \times T_{1/2}$	1.73×10^{10}	5.18×10^{10}
$5 \times T_{1/2}$	1.91×10^{10}	5.55×10^{10}
$6 \times T_{1/2}$	1.94×10^{10}	5.74×10^{10}
$7 \times T_{1/2}$	1.96×10^{10}	5.83×10^{10}
$8 \times T_{1/2}$	1.97×10^{10}	5.88×10^{10}
$9 \times T_{1/2}$	1.97×10^{10}	5.90×10^{10}
$10 \times T_{1/2}$	1.97×10^{10}	5.91×10^{10}

Table B.1: Number of isomers $N[^{93\mathrm{m}}\mathrm{Mo}]$ in each μm Nb foil for different irradiation times t for two production cross section values.

Appendix C

Supplement for NFS theory

The macroscopic nuclear current density $\boldsymbol{\mathcal{J}}$

In order to obtain the form of the wave equation given in Eq. (5.18), the macroscopic nuclear current density [Eq. (5.11)]

$$\boldsymbol{\mathcal{J}}(\boldsymbol{r},t) = \int \frac{\mathrm{d}^3\boldsymbol{k}'}{(2\pi)^3} \mathrm{e}^{\mathrm{i}\boldsymbol{k}'\boldsymbol{r}} \sum_\alpha \langle\psi_\alpha(t)|\boldsymbol{j}(\boldsymbol{k}')|\psi_\alpha(t)\rangle \mathrm{e}^{-\mathrm{i}\boldsymbol{k}'\boldsymbol{r}_\alpha} \tag{C.1}$$

needs to be expressed in terms of the nuclear transition currents $\boldsymbol{J}_\ell^*$ and $\boldsymbol{J}_\ell$ [Eqs. (5.19)]. The first step is to calculate the matrix element of an individual nucleus given in Eq. (5.15), which can be rewritten in the following form

$$\begin{aligned}
&\langle\psi_\alpha(t)|\boldsymbol{j}(\boldsymbol{k})|\psi_\alpha(t)\rangle \\
&\quad = \langle I_\mathrm{g}M_\mathrm{g}|U^\dagger(t,-\infty)\boldsymbol{j}(\boldsymbol{k})U(t,-\infty)|I_\mathrm{g}M_\mathrm{g}\rangle \\
&\quad = \sum_{M_\mathrm{g}',M_\mathrm{e}} \langle I_\mathrm{g}M_\mathrm{g}|U^\dagger(t,-\infty)|I_\mathrm{g}M_\mathrm{g}'\rangle\langle I_\mathrm{g}M_\mathrm{g}'|\boldsymbol{j}(\boldsymbol{k})|I_\mathrm{e}M_\mathrm{e}\rangle\langle I_\mathrm{e}M_\mathrm{e}|U(t,-\infty)|I_\mathrm{g}M_\mathrm{g}\rangle\ .
\end{aligned} \tag{C.2}$$

Here, it was assumed that the system is in $|I_\mathrm{g}M_\mathrm{g}\rangle$ at $t=-\infty$. Applying perturbation theory the matrix element $\langle I_\mathrm{e}M_\mathrm{e}|U(t,-\infty)|I_\mathrm{g}M_\mathrm{g}\rangle$ involving a transition from the ground to the excited state can be calculated. Taking into account only the first non-vanishing order leads to

$$\begin{aligned}
&\langle I_\mathrm{e}M_\mathrm{e}|U(t,-\infty)|I_\mathrm{g}M_\mathrm{g}\rangle \\
&\quad = -\mathrm{i}\int_{-\infty}^{t}\mathrm{d}t' \sum_{M_\mathrm{g}'',M_\mathrm{e}'} \langle I_\mathrm{e}M_\mathrm{e}|U(t,t')|I_\mathrm{e}M_\mathrm{e}'\rangle\langle I_\mathrm{e}M_\mathrm{e}'|H_\gamma(t')|I_\mathrm{g}M_\mathrm{g}''\rangle \\
&\qquad\quad \times \langle I_\mathrm{g}M_\mathrm{g}''|U(t',-\infty)|I_\mathrm{g}M_\mathrm{g}\rangle \\
&\quad = -\mathrm{i}\int_{-\infty}^{t}\mathrm{d}t' \sum_{M_\mathrm{g}'',M_\mathrm{e}'} \langle I_\mathrm{e}M_\mathrm{e}|U(t,t')|I_\mathrm{e}M_\mathrm{e}'\rangle\langle I_\mathrm{e}M_\mathrm{e}'|\frac{\mathrm{i}}{\omega}\boldsymbol{j}^\dagger(\boldsymbol{k})\boldsymbol{E}(y_\alpha,t')\mathrm{e}^{\mathrm{i}(\boldsymbol{k}\boldsymbol{r}_\alpha-\omega t')}|I_\mathrm{g}M_\mathrm{g}''\rangle \\
&\qquad\quad \times \langle I_\mathrm{g}M_\mathrm{g}''|U(t',-\infty)|I_\mathrm{g}M_\mathrm{g}\rangle \\
&\quad = \frac{1}{\omega}\int_{-\infty}^{t}\mathrm{d}t' \sum_{M_\mathrm{g}'',M_\mathrm{e}'} \langle I_\mathrm{e}M_\mathrm{e}|U(t,t')|I_\mathrm{e}M_\mathrm{e}'\rangle\langle I_\mathrm{e}M_\mathrm{e}'|\boldsymbol{j}^\dagger(\boldsymbol{k})|I_\mathrm{g}M_\mathrm{g}''\rangle\boldsymbol{E}(y_\alpha,t')\mathrm{e}^{\mathrm{i}(\boldsymbol{k}\boldsymbol{r}_\alpha-\omega t')} \\
&\qquad\quad \times \langle I_\mathrm{g}M_\mathrm{g}''|U(t',-\infty)|I_\mathrm{g}M_\mathrm{g}\rangle\ .
\end{aligned} \tag{C.3}$$

In the step from the first to the second equal sign, the explicit form of H_γ given in Eq. (5.14) has been inserted. Plugging Eq. (C.3) into Eq. (C.2), we obtain

$$\begin{aligned}
&\langle\psi_\alpha(t)|\boldsymbol{j}(\boldsymbol{k})|\psi_\alpha(t)\rangle \\
&\quad= \langle I_\mathrm{g}M_\mathrm{g}|U^\dagger(t,-\infty)|I_\mathrm{g}M'_\mathrm{g}\rangle\langle I_\mathrm{g}M'_\mathrm{g}|\boldsymbol{j}(\boldsymbol{k})|I_\mathrm{e}M'_\mathrm{e}\rangle \int_{-\infty}^{t} \mathrm{d}t'\langle I_\mathrm{e}M'_\mathrm{e}|U(t,t')|I_\mathrm{e}M_\mathrm{e}\rangle \\
&\qquad\times \langle I_\mathrm{e}M_\mathrm{e}|H_\gamma(t')|I_\mathrm{g}M''_\mathrm{g}\rangle\langle I_\mathrm{g}M''_\mathrm{g}|U(t',-\infty)|I_\mathrm{g}M_\mathrm{g}\rangle \\
&\quad= \frac{1}{\omega}\sum_{M'_\mathrm{g},M_\mathrm{e}}\sum_{M''_\mathrm{g},M'_\mathrm{e}} \langle I_\mathrm{g}M_\mathrm{g}|U^\dagger(t,-\infty)|I_\mathrm{g}M'_\mathrm{g}\rangle\langle I_\mathrm{g}M'_\mathrm{g}|\boldsymbol{j}(\boldsymbol{k})|I_\mathrm{e}M_\mathrm{e}\rangle \int_{-\infty}^{t}\mathrm{d}t' \\
&\qquad\times \langle I_\mathrm{e}M_\mathrm{e}|U(t,t')|I_\mathrm{e}M'_\mathrm{e}\rangle\langle I_\mathrm{e}M'_\mathrm{e}|\boldsymbol{j}^\dagger(\boldsymbol{k})|I_\mathrm{g}M''_\mathrm{g}\rangle\langle I_\mathrm{g}M''_\mathrm{g}|U(t',-\infty)|I_\mathrm{g}M_\mathrm{g}\rangle \\
&\qquad\times \boldsymbol{E}(y_\alpha,t')\mathrm{e}^{\mathrm{i}(\boldsymbol{k}\boldsymbol{r}_\alpha-\omega t')} \\
&\quad= \frac{1}{\omega}\sum_{M_\mathrm{e}}\langle I_\mathrm{g}M_\mathrm{g}|U^\dagger(t,-\infty)\boldsymbol{j}(\boldsymbol{k})U(t,-\infty)|I_\mathrm{e}M_\mathrm{e}\rangle \int_{-\infty}^{t}\mathrm{d}t'\,\boldsymbol{E}(y_\alpha,t')\mathrm{e}^{\mathrm{i}(\boldsymbol{k}\boldsymbol{r}_\alpha-\omega t')} \\
&\qquad\times \langle I_\mathrm{e}M_\mathrm{e}|U^\dagger(t',-\infty)\boldsymbol{j}^\dagger(\boldsymbol{k})U(t',-\infty)|I_\mathrm{g}M_\mathrm{g}\rangle\ ,
\end{aligned} \tag{C.4}$$

where in the last step the following property of the time evolution operator has been employed

$$U(t,t') = U(t,-\infty)U^\dagger(t',-\infty)\ . \tag{C.5}$$

Using the final result of Eq. (C.4), the macroscopic nuclear current density [Eq. (5.11)] evaluates to

$$\begin{aligned}
\boldsymbol{\mathcal{J}}(\boldsymbol{r},t) &= \int\frac{\mathrm{d}^3\boldsymbol{k}'}{(2\pi)^3}\mathrm{e}^{\mathrm{i}\boldsymbol{k}'\boldsymbol{r}}\sum_\alpha\frac{\mathrm{e}^{\mathrm{i}(\boldsymbol{k}-\boldsymbol{k}')\boldsymbol{r}_\alpha}}{(2I_\mathrm{g}+1)\omega}\sum_{M_\mathrm{g},M_\mathrm{e}}\langle I_\mathrm{g}M_\mathrm{g}|U^\dagger(t,-\infty)\boldsymbol{j}(\boldsymbol{k})U(t,-\infty)|I_\mathrm{e}M_\mathrm{e}\rangle \\
&\qquad\times\int_{-\infty}^{t}\mathrm{d}t'\,\boldsymbol{E}(y_\alpha,t')\mathrm{e}^{-\mathrm{i}\omega t'}\langle I_\mathrm{e}M_\mathrm{e}|U^\dagger(t',-\infty)\boldsymbol{j}^\dagger(\boldsymbol{k})U(t',-\infty)|I_\mathrm{g}M_\mathrm{g}\rangle \\
&= \int\frac{\mathrm{d}^3\boldsymbol{k}'}{(2\pi)^3}\mathrm{e}^{\mathrm{i}\boldsymbol{k}'\boldsymbol{r}}\frac{(2\pi)^3 n_0\delta(\boldsymbol{k}-\boldsymbol{k}')}{(2I_\mathrm{g}+1)\omega}\sum_{M_\mathrm{g},M_\mathrm{e}}\langle I_\mathrm{g}M_\mathrm{g}|U^\dagger(t,-\infty)\boldsymbol{j}(\boldsymbol{k})U(t,-\infty)|I_\mathrm{e}M_\mathrm{e}\rangle \\
&\qquad\times\int_{-\infty}^{t}\mathrm{d}t'\,\boldsymbol{E}(y,t')\mathrm{e}^{-\mathrm{i}\omega t'}\langle I_\mathrm{e}M_\mathrm{e}|U^\dagger(t',-\infty)\boldsymbol{j}^\dagger(\boldsymbol{k})U(t',-\infty)|I_\mathrm{g}M_\mathrm{g}\rangle \\
&= \frac{n_0}{(2I_\mathrm{g}+1)\omega}\mathrm{e}^{\mathrm{i}\boldsymbol{k}\boldsymbol{r}}\sum_{M_\mathrm{g},M_\mathrm{e}}\langle\psi_{I_\mathrm{g}M_\mathrm{g}}(t)|\boldsymbol{j}(\boldsymbol{k})|\psi_{I_\mathrm{e}M_\mathrm{e}}(t)\rangle\int_{-\infty}^{t}\mathrm{d}t'\,\boldsymbol{E}(y,t')\mathrm{e}^{-\mathrm{i}\omega t'} \\
&\qquad\times\langle\psi_{I_\mathrm{e}M_\mathrm{e}}(t')|\boldsymbol{j}^\dagger(\boldsymbol{k})|\psi_{I_\mathrm{g}M_\mathrm{g}}(t')\rangle \\
&= \frac{n_0}{(2I_\mathrm{g}+1)\omega}\,\mathrm{e}^{\mathrm{i}(\boldsymbol{k}\boldsymbol{r}-\omega t)}\sum_\ell\boldsymbol{J}_\ell(\boldsymbol{k},t)\int_{-\infty}^{t}\mathrm{d}t'\,\boldsymbol{J}^*_\ell(\boldsymbol{k},t')\boldsymbol{E}(y,t')\ .
\end{aligned} \tag{C.6}$$

In the last step of this calculation, the definitions of the nuclear transition currents $\boldsymbol{J}^*_\ell$ and $\boldsymbol{J}_\ell$ given in Eqs. (5.19) have been used. Moreover, we averaged over the projection quantum number M_g of the initial state $|I_\mathrm{g}M_\mathrm{g}\rangle$. Inserting the final result of Eq. (C.6) into the original wave equation (5.8) of the slowly-varying amplitudes, we obtain

$$\begin{aligned}\frac{\partial}{\partial y}\boldsymbol{E}(y,t) &= -\frac{2\pi}{c}\,\frac{n_0}{(2I_\mathrm{g}+1)\omega}\,\sum_\ell \boldsymbol{J}_\ell(\boldsymbol{k},t)\int_{-\infty}^{t}\mathrm{d}t'\,\boldsymbol{J}_\ell^*(\boldsymbol{k},t')\boldsymbol{E}(y,t')\\ &= -\sum_\ell \underbrace{\frac{2\pi n_0}{(2I_\mathrm{g}+1)kc^2}}_{=K_\ell}\,\boldsymbol{J}_\ell(\boldsymbol{k},t)\int_{-\infty}^{t}\mathrm{d}t'\,\boldsymbol{J}_\ell^*(\boldsymbol{k},t')\boldsymbol{E}(y,t') \qquad \text{(C.7)}\end{aligned}$$

where the last line coincides with Eq. (5.18). Since we neglected thermal vibrations of the nuclei, the Lamb-Mössbauer factor f_LM has been assumed to be one in our derivation. It can be simply taken into account by scaling K_ℓ with f_LM, as it was done in the definition given in Eq. (5.20).

Wave equation for $\boldsymbol{E}^{(p)}(\xi,\tau)$ [Eq. (5.26)]

In order to derive the wave equation for the individual scattering orders p, the power series given by Eq. (5.24) is inserted into Eq. (5.23),

$$\frac{\partial}{\partial\xi}\sum_{p=0}^{\infty}\boldsymbol{E}^{(p)}(\xi,\tau) = -\sum_\ell \boldsymbol{J}_\ell(\boldsymbol{k},\tau)\int_{-\infty}^{\tau}\mathrm{d}\tau'\boldsymbol{J}_\ell^*(\boldsymbol{k},\tau')\cdot\sum_{p=0}^{\infty}\boldsymbol{E}^{(p)}(\xi,\tau)\ . \qquad \text{(C.8)}$$

For the left-hand side of this equation, the derivative of $\boldsymbol{E}^{(p)}(\xi,\tau)$ with respect to ξ evaluates to

$$\frac{\partial}{\partial\xi}\boldsymbol{E}^{(p)}(\xi,\tau) = \frac{\partial}{\partial\xi}\frac{(-\xi)^p}{p!}\boldsymbol{E}^{(p)}(\tau) = -\sum_{p=0}^{\infty}\frac{(-\xi)^{p-1}}{(p-1)!}\boldsymbol{E}^{(p)}(\tau) \propto \mathcal{O}(\xi^{p-1})\ , \qquad \text{(C.9)}$$

which is of the order $\mathcal{O}(\xi^{p-1})$. On the other hand, the p^th scattering order occuring on the right-hand side in Eq. (C.8) is proportional to ξ^p,

$$\boldsymbol{E}^{(p)}(\xi,\tau) = \sum_{p=0}^{\infty}\frac{(-\xi)^p}{p!}\boldsymbol{E}^{(p)}(\tau) \propto \mathcal{O}(\xi^p)\ . \qquad \text{(C.10)}$$

Performing a power matching in ξ one can recognize that $\frac{\partial}{\partial\xi}\boldsymbol{E}^{(p)}(\xi,\tau)$ is determined by $\boldsymbol{E}^{(p-1)}(\xi,\tau)$, finally leading to Eq. (5.26),

$$\frac{\partial}{\partial\xi}\boldsymbol{E}^{(p)}(\xi,\tau) = -\sum_\ell \boldsymbol{J}_\ell(\boldsymbol{k},\tau)\int_{-\infty}^{\tau}\mathrm{d}\tau'\boldsymbol{J}_\ell^*(\boldsymbol{k},\tau')\cdot\boldsymbol{E}^{(p-1)}(\xi,\tau')\ . \qquad \text{(C.11)}$$

Appendix D

NFS off ^{57}Fe targets under 90°-Voigt rotations

Nuclear transition currents $\boldsymbol{j}_\ell$ for $\mathcal{M}1$ transitions

Here, we calculate the nuclear transition currents [Eq. (5.35)]

$$\boldsymbol{j}_\ell(\boldsymbol{k}) = \sqrt{3 f_{\mathrm{LM}}(\boldsymbol{k})} \sum_{q=0,\pm1} \begin{pmatrix} I_{\mathrm{g}} & 1 & I_{\mathrm{e}} \\ -M_{\mathrm{g}} & q & M_{\mathrm{e}} \end{pmatrix} (-1)^{q+I_{\mathrm{g}}-M_{\mathrm{g}}} \left(\hat{\boldsymbol{k}} \times \boldsymbol{\varepsilon}_{-q}\right) \tag{D.1}$$

for an explicit B-field geometry. We consider two scenarios: (I) $\boldsymbol{B} \parallel \boldsymbol{e}_z$, (II) $\boldsymbol{B} \parallel \boldsymbol{e}_x$. In both cases, the pulse propagation axis is fixed according to $\hat{\boldsymbol{k}} = \boldsymbol{e}_y$.

In the case of $\boldsymbol{B} \parallel \boldsymbol{e}_z$, the following spherical unit vectors are involved:

$$\begin{aligned} \boldsymbol{\varepsilon}_0 &= \boldsymbol{e}_z \ , \\ \boldsymbol{\varepsilon}_{\pm1} &= \mp \frac{1}{\sqrt{2}} \left(\boldsymbol{e}_x \pm \mathrm{i} \boldsymbol{e}_y\right) \ . \end{aligned} \tag{D.2}$$

The cross product $\hat{\boldsymbol{k}} \times \boldsymbol{\varepsilon}_{-q}$ appearing in Eq. (D.1) can take one of the following values

$$\begin{aligned} \hat{\boldsymbol{k}} \times \boldsymbol{\varepsilon}_0 &= \boldsymbol{e}_y \times \boldsymbol{e}_z = \boldsymbol{e}_x \ , \\ \hat{\boldsymbol{k}} \times \boldsymbol{\varepsilon}_{\pm1} &= \mp \frac{1}{\sqrt{2}} \boldsymbol{e}_y \times \left(\boldsymbol{e}_x \pm \mathrm{i} \boldsymbol{e}_y\right) = \pm \frac{1}{\sqrt{2}} \boldsymbol{e}_z \ , \end{aligned} \tag{D.3}$$

where we made use of the orthogonality properties of the Cartesian unit vectors. The further calculation of the transition currents $\boldsymbol{j}_{\ell,\mathrm{I}}$ is separately treated for the cases $q = 0$ and $q = \pm1$.

Case $q = 0$: According to the Wigner $3j$-symbol occurring in Eq. (D.1), we have the following selection rule for the magnetic projection quantum numbers: $q - M_{\mathrm{g}} + M_{\mathrm{e}} = 0$. Hence, $q = 0$ exactly corresponds to even ℓ transitions with $\Delta M = 0$. Applying Eq. (D.3) and explicitly calculating the Clebsch-Gordan coefficients leads to

$$\boldsymbol{j}_{\ell=\pm2,\mathrm{I}}(\boldsymbol{k}) = -\sqrt{\frac{f_{\mathrm{LM}}(\boldsymbol{k})}{2}} \boldsymbol{e}_\sigma \ . \tag{D.4}$$

Case $q = \pm1$: Analogously to the previous case, the Wigner $3j$-symbol restricts the change in the magnetic projection quantum number to $\Delta M = \pm1$, corresponding to transitions of odd ℓ. The transition currents $\boldsymbol{j}_{\ell,\mathrm{I}}$ evaluate to

$$\begin{aligned}
\boldsymbol{j}_{\ell=\pm1,\mathrm{I}}(\boldsymbol{k}) &= \pm\sqrt{\frac{f_{\mathrm{LM}}(\boldsymbol{k})}{8}}\boldsymbol{e}_{\pi} \ , \\
\boldsymbol{j}_{\ell=\pm3,\mathrm{I}}(\boldsymbol{k}) &= \mp\sqrt{\frac{3f_{\mathrm{LM}}(\boldsymbol{k})}{8}}\boldsymbol{e}_{\pi} \ .
\end{aligned} \tag{D.5}$$

Scenario (II) with $\boldsymbol{B} \parallel \boldsymbol{e}_x$ can be treated analogously. Redefining the spherical unit vectors according to

$$\begin{aligned}
\boldsymbol{\varepsilon}_0 &= \boldsymbol{e}_x \ , \\
\boldsymbol{\varepsilon}_{\pm1} &= \mp\frac{1}{\sqrt{2}}\left(-\boldsymbol{e}_z \pm \mathrm{i}\boldsymbol{e}_y\right) \ ,
\end{aligned} \tag{D.6}$$

and following the same steps as before, leads to the following expressions for the transition currents $\boldsymbol{j}_{\ell,\mathrm{II}}$,

$$\begin{aligned}
\boldsymbol{j}_{\ell=\pm1,\mathrm{II}}(\boldsymbol{k}) &= \pm\sqrt{\frac{f_{\mathrm{LM}}(\boldsymbol{k})}{8}}\boldsymbol{e}_{\sigma} \ , \\
\boldsymbol{j}_{\ell=\pm2,\mathrm{II}}(\boldsymbol{k}) &= \sqrt{\frac{f_{\mathrm{LM}}(\boldsymbol{k})}{2}}\boldsymbol{e}_{\pi} \ , \\
\boldsymbol{j}_{\ell=\pm3,\mathrm{II}}(\boldsymbol{k}) &= \mp\sqrt{\frac{3f_{\mathrm{LM}}(\boldsymbol{k})}{8}}\boldsymbol{e}_{\sigma} \ .
\end{aligned} \tag{D.7}$$

Amplitude $\boldsymbol{\mathcal{A}}^{(1)}_{\ell,\mathrm{I}}$ & first order solution

The amplitude $\boldsymbol{\mathcal{A}}^{(1)}_{\ell,\mathrm{I}}$ is defined in Eq. (6.5). Using the results in Eqs. (D.4) and (D.5), we obtain

$$\begin{aligned}
\boldsymbol{\mathcal{A}}^{(1)}_{\ell=\pm1,\mathrm{I}}(\boldsymbol{k}) &= \frac{f_{\mathrm{LM}}(\boldsymbol{k})}{8}\,\boldsymbol{e}_{\pi}\left(\boldsymbol{e}_{\pi}\cdot\boldsymbol{e}_{\mathrm{p}}\right) \ , \\
\boldsymbol{\mathcal{A}}^{(1)}_{\ell=\pm2,\mathrm{I}}(\boldsymbol{k}) &= \frac{f_{\mathrm{LM}}(\boldsymbol{k})}{2}\,\boldsymbol{e}_{\sigma}\left(\boldsymbol{e}_{\sigma}\cdot\boldsymbol{e}_{\mathrm{p}}\right) \ , \\
\boldsymbol{\mathcal{A}}^{(1)}_{\ell=\pm3,\mathrm{I}}(\boldsymbol{k}) &= \frac{3f_{\mathrm{LM}}(\boldsymbol{k})}{8}\,\boldsymbol{e}_{\pi}\left(\boldsymbol{e}_{\pi}\cdot\boldsymbol{e}_{\mathrm{p}}\right) \ ,
\end{aligned} \tag{D.8}$$

where $\boldsymbol{e}_{\mathrm{p}}$ denotes the polarization of the incident SR pulse. In order to obtain the first order solution $\boldsymbol{E}^{(1)}$ [Eq. (6.4)], the occurring summation over ℓ needs to be performed explicitly. With the help of Eqs. (D.8), we obtain for $\boldsymbol{e}_{\mathrm{p}} = \boldsymbol{e}_{\sigma}$ the following expression

$$\begin{aligned}
\boldsymbol{E}^{(1)}(\xi,\tau) &= -\xi\sum_{\ell=\pm2}\boldsymbol{\mathcal{A}}^{(1)}_{\ell,\mathrm{I}}(\boldsymbol{k})\,\mathrm{e}^{-\mathrm{i}\Omega_{\ell}\tau-\tau/2} \\
&= -\xi\left\{\boldsymbol{\mathcal{A}}^{(1)}_{\ell=-2,\mathrm{I}}(\boldsymbol{k})\,\mathrm{e}^{\mathrm{i}\Omega_2\tau-\tau/2} + \boldsymbol{\mathcal{A}}^{(1)}_{\ell=2,\mathrm{I}}(\boldsymbol{k})\,\mathrm{e}^{-\mathrm{i}\Omega_2\tau-\tau/2}\right\} \\
&= -\xi\,\frac{f_{\mathrm{LM}}(\boldsymbol{k})}{2}\left\{\mathrm{e}^{\mathrm{i}\Omega_2\tau} + \mathrm{e}^{-\mathrm{i}\Omega_2\tau}\right\}\mathrm{e}^{-\tau/2}\boldsymbol{e}_{\sigma} \\
&= -\xi\,f_{\mathrm{LM}}(\boldsymbol{k})\cos(\Omega_2\tau)\mathrm{e}^{-\tau/2}\boldsymbol{e}_{\sigma} \ .
\end{aligned} \tag{D.9}$$

The case of $\boldsymbol{e}_\mathrm{p} = \boldsymbol{e}_\pi$ can be treated analogously, leading to

$$\begin{aligned}\boldsymbol{E}^{(1)}(\xi,\tau) &= -\xi \sum_{\ell=\pm1,\pm3} \boldsymbol{\mathcal{A}}^{(1)}_{\ell,\mathrm{I}}(\boldsymbol{k})\,\mathrm{e}^{-\mathrm{i}\Omega_\ell\tau-\tau/2} \\ &= -\xi\,\frac{f_\mathrm{LM}(\boldsymbol{k})}{8}\left\{\mathrm{e}^{\mathrm{i}\Omega_1\tau}+\mathrm{e}^{-\mathrm{i}\Omega_1\tau}+3\mathrm{e}^{\mathrm{i}\Omega_3\tau}+3\mathrm{e}^{-\mathrm{i}\Omega_3\tau}\right\}\mathrm{e}^{-\tau/2}\boldsymbol{e}_\pi \\ &= -\xi\,\frac{f_\mathrm{LM}(\boldsymbol{k})}{4}\left\{\cos(\Omega_1\tau)+3\cos(\Omega_3\tau)\right\}\mathrm{e}^{-\tau/2}\boldsymbol{e}_\pi\ . \end{aligned} \tag{D.10}$$

Wigner's d-matrices for a 90°-Voigt rotation

$d^{1/2}_{MM'}(\pi/2)$	$M'=1/2$	$M'=-1/2$
$M=1/2$	$1/\sqrt{2}$	$1/\sqrt{2}$
$M=-1/2$	$-1/\sqrt{2}$	$1/\sqrt{2}$

$d^{3/2}_{MM'}(\pi/2)$	$M'=3/2$	$M'=1/2$	$M'=-1/2$	$M'=-3/2$
$M=3/2$	$1/\sqrt{8}$	$\sqrt{3/8}$	$\sqrt{3/8}$	$\sqrt{1/8}$
$M=1/2$	$-\sqrt{3/8}$	$-1/\sqrt{8}$	$1/\sqrt{8}$	$\sqrt{3/8}$
$M=-1/2$	$\sqrt{3/8}$	$-1/\sqrt{8}$	$-1/\sqrt{8}$	$\sqrt{3/8}$
$M=-3/2$	$-1/\sqrt{8}$	$\sqrt{3/8}$	$-\sqrt{3/8}$	$1/\sqrt{8}$

Table D.1: Wigner's d-matrix $d^I_{MM'}(\pi/2)$ for $I=1/2$ and $I=3/2$ [170].

Amplitude $\boldsymbol{\mathcal{A}}^{(1)}_{\ell,\mathrm{II}}$ for incident σ-polarized x-rays

The time-independent amplitude $\boldsymbol{\mathcal{A}}^{(1)}_{\ell,\mathrm{II}}$ for $\boldsymbol{e}_\mathrm{p} = \boldsymbol{e}_\sigma$ is given by [compare Eq. (6.10)]

$$\boldsymbol{\mathcal{A}}^{(1)}_{\ell,\mathrm{II}}(\boldsymbol{k}) = \boldsymbol{j}_{\ell,\mathrm{II}}(\boldsymbol{k})\sum_{\ell'}\mathrm{e}^{-\mathrm{i}\Omega_{\ell'}\tau_0} d^{I_\mathrm{g}}_{M_\mathrm{g}M'_\mathrm{g}}\left(\frac{\pi}{2}\right) d^{I_\mathrm{e}}_{M_\mathrm{e}M'_\mathrm{e}}\left(\frac{\pi}{2}\right)\left(\boldsymbol{j}^*_{\ell',\mathrm{I}}(\boldsymbol{k})\cdot\boldsymbol{e}_\sigma\right)\ . \tag{D.11}$$

In the following, we will explicitly calculate these amplitudes by using Table D.1 for the d-matrices and Eqs. (D.4), (D.5) and (D.7) for the nuclear transition currents $\boldsymbol{j}_{\ell,\mathrm{II}}$ and $\boldsymbol{j}^*_{\ell',\mathrm{I}}$.

Case $\ell = \pm 1$:

$$\begin{aligned}
\boldsymbol{\mathcal{A}}^{(1)}_{\ell=\pm1,\mathrm{II}}(\boldsymbol{k}) &= \mp \boldsymbol{j}_{\ell=\pm1,\mathrm{II}}(\boldsymbol{k}) \left\{ \frac{1}{4} \mathrm{e}^{\mathrm{i}\Omega_2\tau_0} \left(\boldsymbol{j}^*_{\ell'=-2,\mathrm{I}}(\boldsymbol{k}) \cdot \boldsymbol{e}_\sigma \right) + \frac{1}{4} \mathrm{e}^{-\mathrm{i}\Omega_2\tau_0} \left(\boldsymbol{j}^*_{\ell'=2,\mathrm{I}}(\boldsymbol{k}) \cdot \boldsymbol{e}_\sigma \right) \right\} \\
&= \pm \boldsymbol{j}_{\ell=\pm1,\mathrm{II}}(\boldsymbol{k}) \, \frac{1}{4} \sqrt{\frac{f_{\mathrm{LM}}(\boldsymbol{k})}{2}} \left\{ \mathrm{e}^{\mathrm{i}\Omega_2\tau_0} + \mathrm{e}^{-\mathrm{i}\Omega_2\tau_0} \right\} \\
&= \pm \boldsymbol{j}_{\ell=\pm1,\mathrm{II}}(\boldsymbol{k}) \, \frac{1}{2} \sqrt{\frac{f_{\mathrm{LM}}(\boldsymbol{k})}{2}} \, \cos(\Omega_2\tau_0) \\
&= \frac{f_{\mathrm{LM}}(\boldsymbol{k})}{8} \cos(\Omega_2\tau_0) \boldsymbol{e}_\sigma \ .
\end{aligned} \tag{D.12}$$

Case $\ell = \pm 2$:

$$\begin{aligned}
\boldsymbol{\mathcal{A}}^{(1)}_{\ell=\pm2,\mathrm{II}}(\boldsymbol{k}) &= \boldsymbol{j}_{\ell=\pm2,\mathrm{II}}(\boldsymbol{k}) \left\{ \pm \frac{1}{4} \mathrm{e}^{\mathrm{i}\Omega_2\tau_0} \left(\boldsymbol{j}^*_{\ell'=-2,\mathrm{I}}(\boldsymbol{k}) \cdot \boldsymbol{e}_\sigma \right) \mp \frac{1}{4} \mathrm{e}^{-\mathrm{i}\Omega_2\tau_0} \left(\boldsymbol{j}^*_{\ell'=2,\mathrm{I}}(\boldsymbol{k}) \cdot \boldsymbol{e}_\sigma \right) \right\} \\
&= \boldsymbol{j}_{\ell=\pm2,\mathrm{II}}(\boldsymbol{k}) \, \frac{1}{4} \sqrt{\frac{f_{\mathrm{LM}}(\boldsymbol{k})}{2}} \left\{ \mp \mathrm{e}^{\mathrm{i}\Omega_2\tau_0} \pm \mathrm{e}^{-\mathrm{i}\Omega_2\tau_0} \right\} \\
&= \mp \mathrm{i} \, \boldsymbol{j}_{\ell=\pm2,\mathrm{II}}(\boldsymbol{k}) \, \frac{1}{2} \sqrt{\frac{f_{\mathrm{LM}}(\boldsymbol{k})}{2}} \, \sin(\Omega_2\tau_0) \\
&= \mp \mathrm{i} \, \frac{f_{\mathrm{LM}}(\boldsymbol{k})}{4} \sin(\Omega_2\tau_0) \boldsymbol{e}_\pi \ .
\end{aligned} \tag{D.13}$$

Case $\ell = \pm 3$:

$$\begin{aligned}
\boldsymbol{\mathcal{A}}^{(1)}_{\ell=\pm3,\mathrm{II}}(\boldsymbol{k}) &= \pm \boldsymbol{j}_{\ell=\pm3,\mathrm{II}}(\boldsymbol{k}) \left\{ \frac{\sqrt{3}}{4} \mathrm{e}^{\mathrm{i}\Omega_2\tau_0} \left(\boldsymbol{j}^*_{\ell'=-2,\mathrm{I}}(\boldsymbol{k}) \cdot \boldsymbol{e}_\sigma \right) + \frac{\sqrt{3}}{4} \mathrm{e}^{-\mathrm{i}\Omega_2\tau_0} \left(\boldsymbol{j}^*_{\ell'=2,\mathrm{I}}(\boldsymbol{k}) \cdot \boldsymbol{e}_\sigma \right) \right\} \\
&= \mp \boldsymbol{j}_{\ell=\pm3,\mathrm{II}}(\boldsymbol{k}) \, \frac{\sqrt{3}}{4} \sqrt{\frac{f_{\mathrm{LM}}(\boldsymbol{k})}{2}} \left\{ \mathrm{e}^{\mathrm{i}\Omega_2\tau_0} + \mathrm{e}^{-\mathrm{i}\Omega_2\tau_0} \right\} \\
&= \mp \boldsymbol{j}_{\ell=\pm3,\mathrm{II}}(\boldsymbol{k}) \, \frac{\sqrt{3}}{4} \sqrt{\frac{f_{\mathrm{LM}}(\boldsymbol{k})}{2}} \, \cos(\Omega_2\tau_0) \\
&= \frac{3 f_{\mathrm{LM}}(\boldsymbol{k})}{8} \cos(\Omega_2\tau_0) \boldsymbol{e}_\sigma \ .
\end{aligned} \tag{D.14}$$

Amplitude $\boldsymbol{\mathcal{A}}^{(1)}_{\ell,\mathrm{II}}$ for incident π-polarized x-rays

The case of incident π-polarized x-rays can be solved analogously to the previous case. Taking $\boldsymbol{e}_{\mathrm{p}} = \boldsymbol{e}_{\pi}$ and following the same lines as before, we obtain

$$\begin{aligned}
\boldsymbol{\mathcal{A}}^{(1)}_{\ell=\pm 1,\mathrm{II}}(\boldsymbol{k}) &= \pm\mathrm{i}\,\frac{f_{\mathrm{LM}}(\boldsymbol{k})}{16}\Big\{\sin(\Omega_1\tau_0) + 3\sin(\Omega_3\tau_0)\Big\}\,\boldsymbol{e}_{\sigma}\ , \\
\boldsymbol{\mathcal{A}}^{(1)}_{\ell=\pm 2,\mathrm{II}}(\boldsymbol{k}) &= \frac{f_{\mathrm{LM}}(\boldsymbol{k})}{8}\Big\{\cos(\Omega_1\tau_0) + 3\cos(\Omega_3\tau_0)\Big\}\,\boldsymbol{e}_{\pi}\ , \\
\boldsymbol{\mathcal{A}}^{(1)}_{\ell=\pm 3,\mathrm{II}}(\boldsymbol{k}) &= \pm\mathrm{i}\,\frac{3f_{\mathrm{LM}}(\boldsymbol{k})}{16}\Big\{\sin(\Omega_1\tau_0) - \sin(\Omega_3\tau_0)\Big\}\,\boldsymbol{e}_{\sigma}\ . \qquad \text{(D.15)}
\end{aligned}$$

Bibliography

[1] J. M. Washington, ed., *A Testament of Hope: The essential writings and speeches of Martin Luther King, Jr* (HarperOne, New York, 1986).

[2] T. H. Maiman, "Stimulated Optical Radiation in Ruby," Nature **187**, 493 (1960).

[3] A. L. Schawlow and C. H. Townes, "Infrared and Optical Masers," Phys. Rev. **112**, 1940 (1958).

[4] M. O. Scully and M. S. Zubairy, *Quantum Optics* (Cambridge University Press, New York, 1997).

[5] G. S. Agarwal, *Quantum Optics* (Cambridge University Press, New York, 2013).

[6] P. Meystre and M. S. III, *Elements of Quantum Optics* (Springer Verlag, Berlin, 1999), 3rd ed.

[7] B. W. Adams, C. Buth, S. M. Cavaletto, J. Evers, Z. Harman, C. H. Keitel, A. Pálffy, A. Picón, R. Röhlsberger, Y. Rostovtsev, and K. Tamasaku, "X-ray quantum optics," J. Mod. Opt. **60**, 2 (2013).

[8] D. Sayre and H. N. Chapman, "X-ray microscopy," Acta Crystallographica Section A **51**, 237 (1995).

[9] K. Tamasaku, K. Sawada, E. Nishibori, and T. Ishikawa, "Visualizing the local optical response to extreme-ultraviolet radiation with a resolution of $\lambda/380$," Nature Physics **7**, 705 (2011).

[10] H. Mimura, S. Handa, T. Kimura, H. Yumoto, D. Yamakawa, H. Yokoyama, S. Matsuyama, K. Inagaki, K. Yamamura, Y. Sano *et al.*, "Breaking the 10 nm barrier in hard-X-ray focusing," Nature Physics **6**, 122 (2010).

[11] X. Huang, H. Yan, E. Nazaretski, R. Conley, N. Bouet, J. Zhou, K. Lauer, L. Li, D. Eom, D. Legnini *et al.*, "11 nm hard X-ray focus from a large-aperture multilayer Laue lens," Scientific Reports **3**, 3562 (2013).

[12] D. A. Shapiro, Y.-S. Yu, T. Tyliszczak, J. Cabana, R. Celestre, W. Chao, K. Kaznatcheev, A. D. Kilcoyne, F. Maia, S. Marchesini *et al.*, "Chemical composition mapping with nanometre resolution by soft X-ray microscopy," Nature Photonics (2014).

[13] G. C. Baldwin and J. C. Solem, "Recoilless gamma-ray lasers," Rev. Mod. Phys. **69**, 1085 (1997).

[14] D. H. Bilderback, P. Elleaume, and E. Weckert, "Review of third and next generation synchrotron light sources," Journal of Physics B: Atomic, Molecular and Optical Physics **38**, S773 (2005).

[15] B. W. McNeil and N. R. Thompson, "X-ray free-electron lasers," Nature photonics **4**, 814 (2010).

[16] P. Emma, R. Akre, J. Arthur, R. Bionta, C. Bostedt, J. Bozek, A. Brachmann, P. Bucksbaum, R. Coffee, F.-J. Decker, Y. Ding, D. Dowell, S. Edstrom, A. Fisher, J. Frisch, S. Gilevich, J. Hastings, G. Hays, P. Hering, Z. Huang, R. Iverson, H. Loos, M. Messerschmidt, A. Miahnahri, S. Moeller, H.-D. Nuhn, G. Pile, D. Ratner, J. Rzepiela, D. Schultz, T. Smith, P. Stefan, H. Tompkins, J. Turner, J. Welch, W. White, J. Wu, G. Yocky, and J. Galayda, "First lasing and operation of an angstrom-wavelength free-electron laser," Nature Photon. **4**, 641 (2010).

[17] T. Ishikawa, H. Aoyagi, T. Asaka, Y. Asano, N. Azumi, T. Bizen, H. Ego, K. Fukami, T. Fukui, Y. Furukawa, S. Goto, H. Hanaki, T. Hara, T. Hasegawa, T. Hatsui, A. Higashiya, T. Hirono, N. Hosoda, M. Ishii, T. Inagaki, Y. Inubushi, T. Itoga, Y. Joti, M. Kago, T. Kameshima, H. Kimura, Y. Kirihara, A. Kiyomichi, T. Kobayashi, C. Kondo, T. Kudo, H. Maesaka, X. M. Marechal, T. Masuda, S. Matsubara, T. Matsumoto, T. Matsushita, S. Matsui, M. Nagasono, N. Nariyama, H. Ohashi, T. Ohata, T. Ohshima, S. Ono, Y. Otake, C. Saji, T. Sakurai, T. Sato, K. Sawada, T. Seike, K. Shirasawa, T. Sugimoto, S. Suzuki, S. Takahashi, H. Takebe, K. Takeshita, K. Tamasaku, H. Tanaka, R. Tanaka, T. Tanaka, T. Togashi, K. Togawa, A. Tokuhisa, H. Tomizawa, K. Tono, S. Wu, M. Yabashi, M. Yamaga, A. Yamashita, K. Yanagida, C. Zhang, T. Shintake, H. Kitamura, and N. Kumagai, "A compact X-ray free-electron laser emitting in the sub-angstrom region," Nature Photon. **6**, 540 (2012).

[18] M. Altarelli, R. Brinkmann, M. Chergui, W. Decking, B. Dobson, S. Düsterer, G. Grübel, W. Graeff, H. Graafsma, J. Hajdu, J. Marangos, J. Pflüger, H. Redlin, D. Riley, I. Robinson, J. Rossbach, A. Schwarz, K. Tiedtke, T. Tschentscher, I. Vartaniants, H. Wabnitz, H. Weise, R. Wichmann, K. Witte, A. Wolf, M. Wulff, and M. Yurkov, "The European X-Ray Free Electron Laser. Technical Design Report," Tech. rep., DESY, Hamburg (2007).

[19] R. Ganter, "SwissFEL - Conceptual design report," Tech. rep., Paul Scherrer Institute (PSI), Villigen (Switzerland) (2010).

[20] Matter-Radiation Interactions in Extremes - MaRIE (2015). http://www.lanl.gov/science-innovation/science-facilities/marie/.

[21] J. Feldhaus, E. Saldin, J. Schneider, E. Schneidmiller, and M. Yurkov, "Possible application of X-ray optical elements for reducing the spectral bandwidth of an X-ray SASE FEL ," Optics Commun. **140**, 341 (1997).

[22] E. Saldin, E. Schneidmiller, Y. Shvyd'ko, and M. Yurkov, "X-ray FEL with a meV bandwidth," Nucl. Instrum. Meth. A **475**, 357 (2001).

[23] G. Geloni, V. Kocharyan, and E. Saldin, “Extension of self-seeding to hard X-rays > 10 keV as a way to increase user access at the European XFEL,” Tech. rep., DESY, Hamburg (2011).

[24] K.-J. Kim, Y. Shvyd’ko, and S. Reiche, “A Proposal for an X-Ray Free-Electron Laser Oscillator with an Energy-Recovery Linac,” Phys. Rev. Lett. **100**, 244802 (2008).

[25] R. R. Lindberg, K.-J. Kim, Y. Shvyd’ko, and W. M. Fawley, “Performance of the x-ray free-electron laser oscillator with crystal cavity,” Phys. Rev. ST Accel. Beams **14**, 010701 (2011).

[26] Y. Shvyd’ko, *X-ray Optics: High-energy-resolution Applications*, vol. 98 (Springer, 2013).

[27] Y. Shvyd’ko, S. Stoupin, V. Blank, and S. Terentyev, “Near-100% Bragg reflectivity of X-rays,” Nature Photon. **5**, 539 (2011).

[28] D. Ratner, R. Abela, J. Amann, C. Behrens, D. Bohler, G. Bouchard, C. Bostedt, M. Boyes, K. Chow, D. Cocco, F. J. Decker, Y. Ding, C. Eckman, P. Emma, D. Fairley, Y. Feng, C. Field, U. Flechsig, G. Gassner, J. Hastings, P. Heimann, Z. Huang, N. Kelez, J. Krzywinski, H. Loos, A. Lutman, A. Marinelli, G. Marcus, T. Maxwell, P. Montanez, S. Moeller, D. Morton, H. D. Nuhn, N. Rodes, W. Schlotter, S. Serkez, T. Stevens, J. Turner, D. Walz, J. Welch, and J. Wu, “Experimental Demonstration of a Soft X-Ray Self-Seeded Free-Electron Laser,” Phys. Rev. Lett. **114**, 054801 (2015).

[29] J. Amann, W. Berg, V. Blank, F.-J. Decker, Y. Ding, P. Emma, Y. Feng, J. Frisch, D. Fritz, J. Hastings, Z. Huang, J. Krzywinski, R. Lindberg, H. Loos, A. Lutman, H.-D. Nuhn, D. Ratner, J. Rzepiela, D. Shu, Y. Shvyd’ko, S. Spampinati, S. Stoupin, S. Terentyev, E. Trakhtenberg, D. Walz, J. Welch, J. Wu, A. Zholents, and D. Zhu, “Demonstration of self-seeding in a hard-X-ray free-electron laser,” Nature Photonics **6**, 693 (2012).

[30] T. Hara, Y. Inubushi, T. Katayama, T. Sato, H. Tanaka, T. Tanaka, T. Togashi, K. Togawa, K. Tono, M. Yabashi *et al.*, “Two-colour hard X-ray free-electron laser with wide tunability,” Nature communications **4** (2013).

[31] A. Marinelli, D. Ratner, A. Lutman, J. Turner, J. Welch, F.-J. Decker, H. Loos, C. Behrens, S. Gilevich, A. Miahnahri *et al.*, “High-intensity double-pulse X-ray free-electron laser,” Nature communications **6** (2015).

[32] T. Pfeifer, Y. Jiang, S. Düsterer, R. Moshammer, and J. Ullrich, “Partial-coherence method to model experimental free-electron laser pulse statistics,” Opt. Lett. **35**, 3441 (2010).

[33] P. Beiersdorfer, A. L. Osterheld, J. H. Scofield, J. R. Crespo López-Urrutia, and K. Widmann, “Measurement of QED and Hyperfine Splitting in the $2s_{1/2}$- $2p_{3/2}$ X-Ray Transition in Li-like $^{209}Bi^{80+}$,” Phys. Rev. Lett. **80**, 3022 (1998).

[34] S. Bernitt, G. Brown, J. K. Rudolph, R. Steinbrügge, A. Graf, M. Leutenegger, S. Epp, S. Eberle, K. Kubivcek, V. Mäckel *et al.*, “An unexpectedly low oscillator strength as the origin of the Fe XVII emission problem,” Nature **492**, 225 (2012).

[35] S. M. Cavaletto, C. Buth, Z. Harman, E. P. Kanter, S. H. Southworth, L. Young, and C. H. Keitel, “Resonance fluorescence in ultrafast and intense x-ray free-electron-laser pulses,” Phys. Rev. A **86**, 033402 (2012).

[36] S. M. Cavaletto, Z. Harman, C. Buth, and C. H. Keitel, “X-ray frequency combs from optically controlled resonance fluorescence,” Phys. Rev. A **88**, 063402 (2013).

[37] S. M. Cavaletto, Z. Harman, C. Ott, C. Buth, T. Pfeifer, and C. H. Keitel, “Broadband high-resolution X-ray frequency combs,” Nature Photonics **8**, 520 (2014).

[38] Z. Liu, C. Ott, S. M. Cavaletto, Z. Harman, C. H. Keitel, and T. Pfeifer, “Generation of high-frequency combs locked to atomic resonances by quantum phase modulation,” New Journal of Physics **16**, 093005 (2014).

[39] T. J. Bürvenich, J. Evers, and C. H. Keitel, “Nuclear Quantum Optics with X-Ray Laser Pulses,” Phys. Rev. Lett. **96**, 142501 (2006).

[40] A. Pálffy, “A systematic study of nuclear photoexcitation with X-ray laser fields,” Journal of Modern Optics **55**, 2603 (2008).

[41] K. P. Heeg, H.-C. Wille, K. Schlage, T. Guryeva, D. Schumacher, I. Uschmann, K. S. Schulze, B. Marx, T. Kämpfer, G. G. Paulus *et al.*, “Vacuum-assisted generation and control of atomic coherences at x-ray energies,” Phys. Rev. Lett. **111**, 073601 (2013).

[42] S. Matinyan, “Lasers as a bridge between atomic and nuclear physics,” Physics Reports **298**, 199 (1998).

[43] P. Walker and G. Dracoulis, “Energy traps in atomic nuclei,” Nature **399**, 35 (1999).

[44] A. Aprahamian and Y. Sun, “Nuclear physics: Long live isomer research,” Nature Phys. **1**, 81 (2005).

[45] C. B. Collins, F. Davanloo, M. C. Iosif, R. Dussart, J. M. Hicks, S. A. Karamian, C. A. Ur, I. I. Popescu, V. I. Kirischuk, J. J. Carroll, H. E. Roberts, P. McDaniel, and C. E. Crist, “Accelerated Emission of Gamma Rays from the 31-yr Isomer of ^{178}Hf Induced by X-Ray Irradiation,” Phys. Rev. Lett. **82**, 695 (1999).

[46] J. J. Carroll, “An experimental perspective on triggered gamma emission from nuclear isomers,” Laser Phys. Lett. **1**, 275 (2004).

[47] A. Pálffy, J. Evers, and C. H. Keitel, “Isomer Triggering via Nuclear Excitation by Electron Capture,” Phys. Rev. Lett. **99**, 172502 (2007).

[48] D. Belic, C. Arlandini, J. Besserer, J. de Boer, J. J. Carroll, J. Enders, T. Hartmann, F. Käppeler, H. Kaiser, U. Kneissl, M. Loewe, H. J. Maier, H. Maser, P. Mohr, P. von Neumann-Cosel, A. Nord, H. H. Pitz, A. Richter, M. Schumann, S. Volz, and A. Zilges, “Photoactivation of $^{180}\mathrm{Ta}^{m}$ and Its Implications for the Nucleosynthesis of Nature’s Rarest Naturally Occurring Isotope,” Phys. Rev. Lett. **83**, 5242 (1999).

[49] D. Belic, C. Arlandini, J. Besserer, J. de Boer, J. J. Carroll, J. Enders, T. Hartmann, F. Käppeler, H. Kaiser, U. Kneissl, E. Kolbe, K. Langanke, M. Loewe, H. J. Maier, H. Maser, P. Mohr, P. von Neumann-Cosel, A. Nord, H. H. Pitz, A. Richter, M. Schumann, F.-K. Thielemann, S. Volz, and A. Zilges, “Photo-induced depopulation of the $^{180}\mathrm{Ta}^{m}$ isomer via low-lying intermediate states: Structure and astrophysical implications,” Phys. Rev. C **65**, 035801 (2002).

[50] A. I. Chumakov, A. Q. R. Baron, I. Sergeev, C. Strohm, O. Leupold, Y. Shvyd’ko, G. V. Smirnov, R. Rüffer, Y. Inubushi, M. Yabashi, K. Tono, T. Kudo, and T. Ishikawa, “Multiple coherent excitations of a nuclear ensemble by an X-ray laser,” Talk presented at the International Conference on the Applications of the Mössbauer Effect (ICAME), Hamburg, Germany (2015).

[51] I. Wong, A. Grigoriu, J. Roslund, T.-S. Ho, and H. Rabitz, “Laser-driven direct quantum control of nuclear excitations,” Phys. Rev. A **84**, 053429 (2011).

[52] W.-T. Liao, A. Pálffy, and C. H. Keitel, “Nuclear coherent population transfer with X-ray laser pulses,” Physics Letters B **705**, 134 (2011).

[53] W.-T. Liao, A. Pálffy, and C. H. Keitel, “Three-beam setup for coherently controlling nuclear-state population,” Phys. Rev. C **87**, 054609 (2013).

[54] S. P. Hau-Riege, *High-Intensity X-rays – Interaction with Matter* (WILEY-VCH, Weinheim, 2011).

[55] R. Neutze, R. Wouts, D. van der Spoel, E. Weckert, and J. Hajdu, “Potential for biomolecular imaging with femtosecond X-ray pulses,” Nature **406**, 752 (2000).

[56] M. M. Seibert, T. Ekeberg, F. R. Maia, M. Svenda, J. Andreasson, O. Jönsson, D. Odić, B. Iwan, A. Rocker, D. Westphal *et al.*, “Single mimivirus particles intercepted and imaged with an X-ray laser,” Nature **470**, 78 (2011).

[57] T. Kimura, Y. Joti, A. Shibuya, C. Song, S. Kim, K. Tono, M. Yabashi, M. Tamakoshi, T. Moriya, T. Oshima *et al.*, “Imaging live cell in micro-liquid enclosure by X-ray laser diffraction,” Nature communications **5** (2014).

[58] H. N. Chapman, P. Fromme, A. Barty, T. A. White, R. A. Kirian, A. Aquila, M. S. Hunter, J. Schulz, D. P. DePonte, U. Weierstall *et al.*, “Femtosecond X-ray protein nanocrystallography,” Nature **470**, 73 (2011).

[59] A. Barty, C. Caleman, A. Aquila, N. Timneanu, L. Lomb, T. A. White, J. Andreasson, D. Arnlund, S. Bajt, T. R. Barends *et al.*, “Self-terminating diffraction

gates femtosecond X-ray nanocrystallography measurements," Nature Photonics **6**, 35 (2012).

[60] K. H. Kim, J. G. Kim, S. Nozawa, T. Sato, K. Y. Oang, T. W. Kim, H. Ki, J. Jo, S. Park, C. Song *et al.*, "Direct observation of bond formation in solution with femtosecond X-ray scattering," Nature **518**, 385 (2015).

[61] J. Kern, R. Alonso-Mori, R. Tran, J. Hattne, R. J. Gildea, N. Echols, C. Glöckner, J. Hellmich, H. Laksmono, R. G. Sierra, B. Lassalle-Kaiser, S. Koroidov, A. Lampe, G. Han, S. Gul, D. DiFiore, D. Milathianaki, A. R. Fry, A. Miahnahri, D. W. Schafer, M. Messerschmidt, M. M. Seibert, J. E. Koglin, D. Sokaras, T.-C. Weng, J. Sellberg, M. J. Latimer, R. W. Grosse-Kunstleve, P. H. Zwart, W. E. White, P. Glatzel, P. D. Adams, M. J. Bogan, G. J. Williams, S. Boutet, J. Messinger, A. Zouni, N. K. Sauter, V. K. Yachandra, U. Bergmann, and J. Yano, "Simultaneous Femtosecond X-ray Spectroscopy and Diffraction of Photosystem II at Room Temperature," Science **340**, 491 (2013).

[62] C. Kupitz, S. Basu, I. Grotjohann, R. Fromme, N. A. Zatsepin, K. N. Rendek, M. S. Hunter, R. L. Shoeman, T. A. White, D. Wang *et al.*, "Serial time-resolved crystallography of photosystem II using a femtosecond X-ray laser," Nature (2014).

[63] M. Suga, F. Akita, K. Hirata, G. Ueno, H. Murakami, Y. Nakajima, T. Shimizu, K. Yamashita, M. Yamamoto, H. Ago *et al.*, "Native structure of photosystem II at 1.95 A resolution viewed by femtosecond X-ray pulses," Nature (2014).

[64] N. Berrah, L. Fang, B. Murphy, T. Osipov, K. Ueda, E. Kukk, R. Feifel, P. van der Meulen, P. Salen, H. T. Schmidt *et al.*, "Double-core-hole spectroscopy for chemical analysis with an intense X-ray femtosecond laser," Proceedings of the National Academy of Sciences **108**, 16912 (2011).

[65] K. Tamasaku, M. Nagasono, H. Iwayama, E. Shigemasa, Y. Inubushi, T. Tanaka, K. Tono, T. Togashi, T. Sato, T. Katayama, T. Kameshima, T. Hatsui, M. Yabashi, and T. Ishikawa, "Double Core-Hole Creation by Sequential Attosecond Photoionization," Phys. Rev. Lett. **111**, 043001 (2013).

[66] K. Tamasaku, E. Shigemasa, Y. Inubushi, T. Katayama, K. Sawada, H. Yumoto, H. Ohashi, H. Mimura, M. Yabashi, K. Yamauchi *et al.*, "X-ray two-photon absorption competing against single and sequential multiphoton processes," Nature Photonics **8**, 313 (2014).

[67] T. Glover, D. Fritz, M. Cammarata, T. Allison, S. Coh, J. Feldkamp, H. Lemke, D. Zhu, Y. Feng, R. Coffee *et al.*, "X-ray and optical wave mixing," Nature **488**, 603 (2012).

[68] T. Glover, M. Hertlein, S. Southworth, T. Allison, J. van Tilborg, E. Kanter, B. Krässig, H. Varma, B. Rude, R. Santra *et al.*, "Controlling X-rays with light," Nature Physics **6**, 69 (2010).

[69] M. Beye, S. Schreck, F. Sorgenfrei, C. Trabant, N. Pontius, C. Schüßler-Langeheine, W. Wurth, and A. Föhlisch, “Stimulated X-ray emission for materials science,” Nature **501**, 191 (2013).

[70] N. Rohringer, D. Ryan, R. A. London, M. Purvis, F. Albert, J. Dunn, J. D. Bozek, C. Bostedt, A. Graf, R. Hill, S. P. Hau-Riege, and J. Rocca, “Atomic inner-shell X-ray laser at 1.46 nanometres pumped by an X-ray free-electron laser,” Nature **481**, 488 (2012).

[71] H. Yoneda, Y. Inubushi, K. Nagamine, Y. Michine, H. Ohashi, H. Yumoto, K. Yamauchi, H. Mimura, H. Kitamura, T. Katayama *et al.*, “Atomic inner-shell laser at 1.5-angstrom wavelength pumped by an X-ray free-electron laser,” Nature **524**, 446 (2015).

[72] N. Rohringer and R. Santra, “X-ray nonlinear optical processes using a self-amplified spontaneous emission free-electron laser,” Phys. Rev. A **76**, 033416 (2007).

[73] B. Nagler, U. Zastrau, R. R. Fäustlin, S. M. Vinko, T. Whitcher, A. Nelson, R. Sobierajski, J. Krzywinski, J. Chalupsky, E. Abreu *et al.*, “Turning solid aluminium transparent by intense soft X-ray photoionization,” Nature Physics **5**, 693 (2009).

[74] L. Young, E. P. Kanter, B. Krässig, Y. Li, A. M. March, S. T. Pratt, R. Santra, S. H. Southworth, N. Rohringer, L. F. DiMauro, G. Doumy, C. A. Roedig, N. Berrah, L. Fang, M. Hoener, P. H. Bucksbaum, J. P. Cryan, S. Ghimire, J. M. Glownia, D. A. Reis, J. D. Bozek, C. Bostedt, and M. Messerschmidt, “Femtosecond electronic response of atoms to ultra-intense X-rays,” Nature **466**, 56 (2010).

[75] O. Ciricosta, H.-K. Chung, R. W. Lee, and J. S. Wark, “Simulations of neon irradiated by intense X-ray laser radiation,” High Energy Density Physics **7**, 111 (2011).

[76] B. Rudek, S.-K. Son, L. Foucar, S. W. Epp, B. Erk, R. Hartmann, M. Adolph, R. Andritschke, A. Aquila, N. Berrah *et al.*, “Ultra-efficient ionization of heavy atoms by intense X-ray free-electron laser pulses,” Nature photonics **6**, 858 (2012).

[77] S. M. Vinko, O. Ciricosta, B. I. Cho, K. Engelhorn, H.-K. Chung, C. R. D. Brown, T. Burian, J. Chalupsky, R. W. Falcone, C. Graves, V. Hajkova, A. Higginbotham, L. Juha, J. Krzywinski, H. J. Lee, M. Messerschmidt, C. D. Murphy, Y. Ping, A. Scherz, W. Schlotter, S. Toleikis, J. J. Turner, L. Vysin, T. Wang, B. Wu, U. Zastrau, D. Zhu, R. W. Lee, P. A. Heimann, B. Nagler, and J. S. Wark, “Creation and diagnosis of a solid-density plasma with an X-ray free-electron laser,” Nature **482**, 59 (2012).

[78] O. Ciricosta, S. M. Vinko, H.-K. Chung, B.-I. Cho, C. R. D. Brown, T. Burian, J. Chalupský, K. Engelhorn, R. W. Falcone, C. Graves, V. Hájková, A. Higginbotham, L. Juha, J. Krzywinski, H. J. Lee, M. Messerschmidt, C. D. Murphy, Y. Ping, D. S. Rackstraw, A. Scherz, W. Schlotter, S. Toleikis, J. J. Turner,

L. Vysin, T. Wang, B. Wu, U. Zastrau, D. Zhu, R. W. Lee, P. Heimann, B. Nagler, and J. S. Wark, "Direct Measurements of the Ionization Potential Depression in a Dense Plasma," Phys. Rev. Lett. **109**, 065002 (2012).

[79] S.-K. Son and R. Santra, "Monte Carlo calculation of ion, electron, and photon spectra of xenon atoms in x-ray free-electron laser pulses," Phys. Rev. A **85**, 063415 (2012).

[80] R. W. Lee, S. J. Moon, H.-K. Chung, W. Rozmus, H. A. Baldis, G. Gregori, R. C. Cauble, O. L. Landen, J. S. Wark, A. Ng, S. J. Rose, C. L. Lewis, D. Riley, J.-C. Gauthier, and P. Audebert, "Finite temperature dense matter studies on next-generation light sources," J. Opt. Soc. Am. B **20**, 770 (2003).

[81] A. Pálffy, W. Scheid, and Z. Harman, "Theory of nuclear excitation by electron capture for heavy ions," Phys. Rev. A **73**, 012715 (2006).

[82] G. Gosselin and P. Morel, "Enhanced nuclear level decay in hot dense plasmas," Phys. Rev. C **70**, 064603 (2004).

[83] P. Morel, V. Méot, G. Gosselin, D. Gogny, and W. Younes, "Evaluation of nuclear excitation by electronic transition in ^{235}U plasma at local thermodynamic equilibrium," Phys. Rev. A **69**, 063414 (2004).

[84] G. Gosselin, V. Méot, and P. Morel, "Modified nuclear level lifetime in hot dense plasmas," Phys. Rev. C **76**, 044611 (2007).

[85] P. Morel, V. Méot, G. Gosselin, G. Faussurier, and C. Blancard, "Calculations of nuclear excitation by electron capture (NEET) in nonlocal thermodynamic equilibrium plasmas," Phys. Rev. C **81**, 034609 (2010).

[86] S. Helmrich, K. Spenneberg, and A. Pálffy, "Coupling highly excited nuclei to the atomic shell in dense astrophysical plasmas," Phys. Rev. C **90**, 015802 (2014).

[87] M. R. Harston and J. F. Chemin, "Mechanisms of nuclear excitation in plasmas," Phys. Rev. C **59**, 2462 (1999).

[88] K. W. D. Ledingham, I. Spencer, T. McCanny, R. P. Singhal, M. I. K. Santala, E. Clark, I. Watts, F. N. Beg, M. Zepf, K. Krushelnick, M. Tatarakis, A. E. Dangor, P. A. Norreys, R. Allott, D. Neely, R. J. Clark, A. C. Machacek, J. S. Wark, A. J. Cresswell, D. C. W. Sanderson, and J. Magill, "Photonuclear Physics when a Multiterawatt Laser Pulse Interacts with Solid Targets," Phys. Rev. Lett. **84**, 899 (2000).

[89] T. E. Cowan, A. W. Hunt, T. W. Phillips, S. C. Wilks, M. D. Perry, C. Brown, W. Fountain, S. Hatchett, J. Johnson, M. H. Key, T. Parnell, D. M. Pennington, R. A. Snavely, and Y. Takahashi, "Photonuclear Fission from High Energy Electrons from Ultraintense Laser-Solid Interactions," Phys. Rev. Lett. **84**, 903 (2000).

[90] P. Gibbon, *Short Pulse Laser Interactions with Matter. An Introduction* (Imperial College Press, London, 2005).

[91] K. M. Spohr, M. Shaw, W. Galster, K. W. D. Ledingham, J. M. Robson, L. amd Yang, P. McKenna, T. McCanny, J. J. Melone, K.-U. Amthor, F. Ewald, B. Liesfeld, H. Schwoerer, and R. Sauerbrey, "Study of photo-proton reactions driven by bremsstrahlung radiation of high-intensity laser generated electrons," New J. Phys. **10**, 043037 (2008).

[92] G. Mourou and T. Tajima, "More Intense, Shorter Pulses," Science **331**, 41 (2011).

[93] V. P. Krainov and M. B. Smirnov, "Cluster beams in the super-intense femtosecond laser pulse," Phys. Rep. **370**, 237 (2002).

[94] T. Ditmire, T. Donnelly, A. M. Rubenchik, R. W. Falcone, and M. D. Perry, "Interaction of intense laser pulses with atomic clusters," Phys. Rev. A **53**, 3379 (1996).

[95] H.-K. Chung, M. Chen, W. Morgan, Y. Ralchenko, and R. Lee, "FLYCHK: Generalized population kinetics and spectral model for rapid spectroscopic analysis for all elements," High Energy Density Phys. **1**, 3 (2005).

[96] Y. V. Shvyd'ko, T. Hertrich, U. van Bürck, E. Gerdau, O. Leupold, J. Metge, H. D. Rüter, S. Schwendy, G. V. Smirnov, W. Potzel, and P. Schindelmann, "Storage of Nuclear Excitation Energy through Magnetic Switching," Phys. Rev. Lett. **77**, 3232 (1996).

[97] P. Helistö, I. Tittonen, M. Lippmaa, and T. Katila, "Gamma echo," Phys. Rev. Lett. **66**, 2037 (1991).

[98] R. N. Shakhmuratov, F. Vagizov, and O. Kocharovskaya, "Radiation burst from a single γ-photon field," Phys. Rev. A **84**, 043820 (2011).

[99] R. N. Shakhmuratov, F. Vagizov, J. Odeurs, and O. Kocharovskaya, "Slow γ photon with a doublet structure: Time delay via a transition from destructive to constructive interference of collectively scattered radiation with the incoming photon," Phys. Rev. A **80**, 063805 (2009).

[100] F. Vagizov, V. Antonov, Y. Radeonychev, R. Shakhmuratov, and O. Kocharovskaya, "Coherent control of the waveforms of recoilless γ-ray photons," Nature **508**, 80 (2014).

[101] R. Mössbauer, "Kernresonanzfluoreszenz von Gammastrahlung in Ir191," Zeitschrift für Physik **151**, 124 (1958).

[102] R. Mössbauer, "Kernresonanzabsorption von Gammastrahlung in Ir191," Naturwissenschaften **45**, 538 (1958).

[103] J. Hannon and G. Trammell, "Coherent γ-ray optics," Hyperfine Interact. **123-124**, 127 (1999).

[104] R. Röhlsberger, *Nuclear Condensed Matter Physics With Synchrotron Radiation: Basic Principles, Methodology and Applications* (Springer Verlag, Berlin, 2004).

[105] K. P. Heeg and J. Evers, “X-ray quantum optics with Mössbauer nuclei embedded in thin-film cavities,” Phys. Rev. A **88**, 043828 (2013).

[106] R. Röhlsberger, K. Schlage, B. Sahoo, S. Couet, and R. Rüffer, “Collective Lamb Shift in Single-Photon Superradiance,” Science **328**, 1248 (2010).

[107] R. Röhlsberger, H.-C. Wille, K. Schlage, and B. Sahoo, “Electromagnetically induced transparency with resonant nuclei in a cavity,” Nature **482**, 199 (2012).

[108] K. P. Heeg, J. Haber, D. Schumacher, L. Bocklage, H.-C. Wille, K. S. Schulze, R. Loetzsch, I. Uschmann, G. G. Paulus, R. Rüffer, R. Röhlsberger, and J. Evers, “Tunable Subluminal Propagation of Narrow-band X-Ray Pulses,” Phys. Rev. Lett. **114**, 203601 (2015).

[109] K. P. Heeg, C. Ott, D. Schumacher, H.-C. Wille, R. Röhlsberger, T. Pfeifer, and J. Evers, “Interferometric phase detection at x-ray energies via Fano resonance control,” Phys. Rev. Lett. **114**, 207401 (2015).

[110] W.-T. Liao, A. Pálffy, and C. H. Keitel, “Coherent Storage and Phase Modulation of Single Hard-X-Ray Photons Using Nuclear Excitons,” Phys. Rev. Lett. **109**, 197403 (2012).

[111] X. Kong, W.-T. Liao, and A. Pálffy, “Field control of single x-ray photons in nuclear forward scattering,” New Journal of Physics **16**, 013049 (2014).

[112] A. Pálffy, C. H. Keitel, and J. Evers, “Single-Photon Entanglement in the keV Regime via Coherent Control of Nuclear Forward Scattering,” Phys. Rev. Lett. **103**, 017401 (2009).

[113] W.-T. Liao and A. Pálffy, “Proposed Entanglement of X-ray Nuclear Polaritons as a Potential Method for Probing Matter at the Subatomic Scale,” Phys. Rev. Lett. **112**, 057401 (2014).

[114] W.-T. Liao, C. H. Keitel, and A. Pálffy, “Magnetic quantum-phase control between two entangled macroscopic nuclear ensembles,” arXiv:1407.3292 (2014).

[115] Y. V. Shvyd’ko, M. Lerche, H.-C. Wille, E. Gerdau, M. Lucht, H. D. Rüter, E. E. Alp, and R. Khachatryan, “X-Ray Interferometry with Microelectronvolt Resolution,” Phys. Rev. Lett. **90**, 013904 (2003).

[116] S.-L. Chang, Y. P. Stetsko, M.-T. Tang, Y.-R. Lee, W.-H. Sun, M. Yabashi, and T. Ishikawa, “X-Ray Resonance in Crystal Cavities: Realization of Fabry-Perot Resonator for Hard X Rays,” Phys. Rev. Lett. **94**, 174801 (2005).

[117] S.-Y. Chen, H.-H. Wu, Y.-Y. Chang, Y.-R. Lee, W.-H. Sun, S.-L. Chang, Y. P. Stetsko, M.-T. Tang, M. Yabashi, and T. Ishikawa, “Coherent trapping of x-ray photons in crystal cavities in the picosecond regime,” Applied Physics Letters **93**, 141105 (2008).

[118] Y. V. Shvyd'ko, S. Stoupin, A. Cunsolo, A. H. Said, and X. Huang, "High-reflectivity high-resolution X-ray crystal optics with diamonds," Nature Phys. **6**, 196 (2010).

[119] T. Osaka, M. Yabashi, Y. Sano, K. Tono, Y. Inubushi, T. Sato, S. Matsuyama, T. Ishikawa, and K. Yamauchi, "A Bragg beam splitter for hard x-ray free-electron lasers," Opt. Express **21**, 2823 (2013).

[120] F. Pfeiffer, C. David, M. Burghammer, C. Riekel, and T. Salditt, "Two-Dimensional X-ray Waveguides and Point Sources," Science **297**, 230 (2002).

[121] A. Jarre, C. Fuhse, C. Ollinger, J. Seeger, R. Tucoulou, and T. Salditt, "Two-Dimensional Hard X-Ray Beam Compression by Combined Focusing and Waveguide Optics," Phys. Rev. Lett. **94**, 074801 (2005).

[122] T. Salditt, S. P. Krüger, C. Fuhse, and C. Bähtz, "High-Transmission Planar X-Ray Waveguides," Phys. Rev. Lett. **100**, 184801 (2008).

[123] K. Okamoto, T. Noma, A. Komoto, W. Kubo, M. Takahashi, A. Iida, and H. Miyata, "X-ray waveguide mode in resonance with a periodic structure," Phys. Rev. Lett. **109**, 233907 (2012).

[124] S. P. Krüger, H. Neubauer, M. Bartels, S. Kalbfleisch, K. Giewekemeyer, P. J. Wilbrandt, M. Sprung, and T. Salditt, "Sub-10nm beam confinement by X-ray waveguides: design, fabrication and characterization of optical properties," Journal of Synchrotron Radiation **19**, 227 (2012).

[125] M. A. Nielsen and I. L. Chuang, *Quantum Computation and Quantum Information* (Cambridge University Press, Cambridge, 2000).

[126] F. Döring, A. Robisch, C. Eberl, M. Osterhoff, A. Ruhlandt, T. Liese, F. Schlenkrich, S. Hoffmann, M. Bartels, T. Salditt, and H. Krebs, "Sub-5 nm hard x-ray point focusing by a combined Kirkpatrick-Baez mirror and multilayer zone plate," Opt. Express **21**, 19311 (2013).

[127] P. Kok, W. J. Munro, K. Nemoto, T. C. Ralph, J. P. Dowling, and G. J. Milburn, "Linear optical quantum computing with photonic qubits," Rev. Mod. Phys. **79**, 135 (2007).

[128] S. Kocsis, G.-Y. Xiang, T. C. Ralph, and G. J. Pryde, "Heralded noiseless amplification of a photon polarization qubit," Nature Physics **9**, 23 (2013).

[129] A. Crespi, R. Ramponi, R. Osellame, L. Sansoni, I. Bongioanni, F. Sciarrino, G. Vallone, and P. Mataloni, "Integrated photonic quantum gates for polarization qubits," Nature communications **2**, 566 (2011).

[130] J. L. O'Brien, G. J. Pryde, A. G. White, T. C. Ralph, and D. Branning, "Demonstration of an all-optical quantum controlled-NOT gate," Nature **426**, 264 (2003).

[131] S. Tashenov, T. Bäck, R. Barday, B. Cederwall, J. Enders, A. Khaplanov, Y. Poltoratska, K.-U. Schässburger, and A. Surzhykov, "Measurement of the Correlation between Electron Spin and Photon Linear Polarization in Atomic-Field Bremsstrahlung," Phys. Rev. Lett. **107**, 173201 (2011).

[132] S. Tashenov, T. Bäck, R. Barday, B. Cederwall, J. Enders, A. Khaplanov, Y. Fritzsche, K.-U. Schässburger, A. Surzhykov, V. A. Yerokhin, and D. Jakubassa-Amundsen, "Bremsstrahlung polarization correlations and their application for polarimetry of electron beams," Phys. Rev. A **87**, 022707 (2013).

[133] T. S. Toellner, E. E. Alp, W. Sturhahn, T. M. Mooney, X. Zhang, M. Ando, Y. Yoda, and S. Kikuta, "Polarizer/analyzer filter for nuclear resonant scattering of synchrotron radiation," Applied Physics Letters **67**, 1993 (1995).

[134] B. Marx, I. Uschmann, S. Höfer, R. Lötzsch, O. Wehrhan, E. Förster, M. Kaluza, T. Stöhlker, H. Gies, C. Detlefs, T. Roth, J. Härtwig, and G. Paulus, "Determination of high-purity polarization state of X-rays," Optics Communications **284**, 915 (2011).

[135] N. Bohr, "Das Quantenpostulat und die neuere Entwicklung der Atomistik," Naturwissenschaften **16**, 245 (1928).

[136] M. O. Scully and K. Drühl, "Quantum eraser: A proposed photon correlation experiment concerning observation and "delayed choice" in quantum mechanics," Phys. Rev. A **25**, 2208 (1982).

[137] T. J. Herzog, P. G. Kwiat, H. Weinfurter, and A. Zeilinger, "Complementarity and the Quantum Eraser," Phys. Rev. Lett. **75**, 3034 (1995).

[138] Z. Y. Ou, L. J. Wang, X. Y. Zou, and L. Mandel, "Evidence for phase memory in two-photon down conversion through entanglement with the vacuum," Phys. Rev. A **41**, 566 (1990).

[139] A. Zajonc, L. Wang, X. Zou, and L. Mandel, "Quantum eraser," Nature **353**, 507 (1991).

[140] P. G. Kwiat, A. M. Steinberg, and R. Y. Chiao, "Observation of a "quantum eraser": A revival of coherence in a two-photon interference experiment," Phys. Rev. A **45**, 7729 (1992).

[141] G. Hackenbroich, B. Rosenow, and H. Weidenmüller, "A mesoscopic quantum eraser," EPL (Europhysics Letters) **44**, 693 (1998).

[142] E. Weisz, H. Choi, I. Sivan, M. Heiblum, Y. Gefen, D. Mahalu, and V. Umansky, "An electronic quantum eraser," science **344**, 1363 (2014).

[143] A. Bramon, G. Garbarino, and B. C. Hiesmayr, "Quantum Marking and Quantum Erasure for Neutral Kaons," Phys. Rev. Lett. **92**, 020405 (2004).

[144] G. Teklemariam, E. M. Fortunato, M. A. Pravia, T. F. Havel, and D. G. Cory, "NMR Analog of the Quantum Disentanglement Eraser," Phys. Rev. Lett. **86**, 5845 (2001).

[145] U. L. Andersen, O. Glöckl, S. Lorenz, G. Leuchs, and R. Filip, "Experimental Demonstration of Continuous Variable Quantum Erasing," Phys. Rev. Lett. **93**, 100403 (2004).

[146] A. Ridolfo, R. Vilardi, O. Di Stefano, S. Portolan, and S. Savasta, "All Optical Switch of Vacuum Rabi Oscillations: The Ultrafast Quantum Eraser," Phys. Rev. Lett. **106**, 013601 (2011).

[147] J. Odeurs, G. Hoy, Y. Rostovtsev, and R. Shakhmuratov, "Towards more relaxed conditions for a gamma-ray laser: Methods to realize induced transparency for nuclear resonant gamma radiation," Laser & Photonics Reviews **4**, 1 (2010).

[148] N. ten Brinke, R. Schützhold, and D. Habs, "Feasibility study of a nuclear exciton laser," Phys. Rev. A **87**, 053814 (2013).

[149] M. Abd-Elmeguid *et al.*, "TESLA Technical Design Report. THE X-RAY FREE ELECTRON LASER," Tech. rep., DESY, Hamburg (2001).

[150] G. Margaritondo and P. Rebernik Ribic, "A simplified description of X-ray free-electron lasers," Journal of Synchrotron Radiation **18**, 101 (2011).

[151] Linac Coherent Light Source - LCLS (2015). http://lcls.slac.stanford.edu.

[152] SPring-8 Angstrom Compact Free Electron Laser - SACLA (2015). http://xfel.riken.jp/eng/sacla/.

[153] J. Arthur *et al.*, "Linac Coherent Light Source (LCLS). Conceptual Design Report," Tech. rep., SLAC, Stanford (2002).

[154] C. Gutt, P. Wochner, B. Fischer, H. Conrad, M. Castro-Colin, S. Lee, F. Lehmkühler, I. Steinke, M. Sprung, W. Roseker, D. Zhu, H. Lemke, S. Bogle, P. H. Fuoss, G. B. Stephenson, M. Cammarata, D. M. Fritz, A. Robert, and G. Grübel, "Single Shot Spatial and Temporal Coherence Properties of the SLAC Linac Coherent Light Source in the Hard X-Ray Regime," Phys. Rev. Lett. **108**, 024801 (2012).

[155] S. Goto *et al.*, "XFEL/SPring-8. Beam Line Technical Design Report," Tech. rep., RIKEN, Japan (2010).

[156] A. Pálffy, J. Evers, and C. H. Keitel, "Electric-dipole-forbidden nuclear transitions driven by super-intense laser fields," Phys. Rev. C **77**, 044602 (2008).

[157] E. Gerdau and H. deWaard (Eds.), "Nuclear resonant scattering of synchrotron radiation," Hyperfine Interact. **123-125**, 1 (1999).

[158] O. Kocharovskaya, R. Kolesov, and Y. Rostovtsev, "Coherent Optical Control of Mössbauer Spectra," Phys. Rev. Lett. **82**, 3593 (1999).

[159] A. Pálffy and J. Evers, “Coherent control of nuclear forward scattering,” Journal of Modern Optics **57**, 1993 (2010).

[160] A. Pálffy, C. H. Keitel, and J. Evers, “Coherent control of the cooperative branching ratio for nuclear x-ray pumping,” Phys. Rev. B **83**, 155103 (2011).

[161] A. Junker, A. Pálffy, and C. H. Keitel, “Cooperative effects in nuclear excitation with coherent x-ray light,” New Journal of Physics **14**, 085025 (2012).

[162] W.-T. Liao, S. Das, C. H. Keitel, and A. Pálffy, “Coherence-Enhanced Optical Determination of the ^{229}Th Isomeric Transition,” Phys. Rev. Lett. **109**, 262502 (2012).

[163] K. P. Heeg and J. Evers, “Collective effects between multiple nuclear ensembles in an x-ray cavity-QED setup,” Phys. Rev. A **91**, 063803 (2015).

[164] R. Coussement, Y. Rostovtsev, J. Odeurs, G. Neyens, H. Muramatsu, S. Gheysen, R. Callens, K. Vyvey, G. Kozyreff, P. Mandel, R. Shakhmuratov, and O. Kocharovskaya, “Controlling Absorption of Gamma Radiation via Nuclear Level Anticrossing,” Phys. Rev. Lett. **89**, 107601 (2002).

[165] E. Peik and C. Tamm, “Nuclear laser spectroscopy of the 3.5 eV transition in Th-229,” EPL (Europhysics Letters) **61**, 181 (2003).

[166] XCOM: Photon Cross Sections Database (2015). http://www.nist.gov/pml/data/xcom/.

[167] J.-J. Niez, “Electronically induced nuclear transitions – temperature dependence and Rabi oscillations,” Comptes Rendus Physique **3**, 1255 (2002).

[168] J.-J. Niez and P. Averbuch, “Electronically induced nuclear transitions: A projection method for analyzing their temperature dependence and possible resonant processes,” Phys. Rev. C **67**, 024611 (2003).

[169] M. E. Rose, *Multipole Fields* (Wiley, New York, 1955).

[170] A. R. Edmonds, *Angular Momentum in Quantum Mechanics* (Princeton University Press, Princeton, 1974), 2nd ed.

[171] P. Ring and P. Schuck, *The Nuclear Many-Body Problem* (Springer Verlag, New York, 1980).

[172] J. M. Blatt and V. F. Weisskopf, *Theoretical Nuclear Physics* (Springer Verlag, New York, 1979).

[173] D. Barb, *Grundlagen und Anwendung der Mössbauerspektroskopie* (Akademieverlag, Berlin, 1980).

[174] Y. V. Shvyd’ko, “Nuclear resonant forward scattering of x rays: Time and space picture,” Phys. Rev. B **59**, 9132 (1999).

[175] V. M. Shabaev, “Quantum electrodynamic theory of recombination of an electron with a highly charged ion,” Phys. Rev. A **50**, 4521 (1994).

[176] M. Zimmermann, N. Grün, and W. Scheid, “Photo recombination on highly charged few-electron uranium ions,” Journal of Physics B: Atomic, Molecular and Optical Physics **30**, 5259 (1997).

[177] A. Pálffy, Z. Harman, and W. Scheid, “Quantum interference between nuclear excitation by electron capture and radiative recombination,” Phys. Rev. A **75**, 012709 (2007).

[178] V. Goldanskii and V. Namiot, “On the excitation of isomeric nuclear levels by laser radiation through inverse internal electron conversion,” Physics Letters B **62**, 393 (1976).

[179] G. Gosselin, P. Morel, and P. Mohr, “Modification of nuclear transitions in stellar plasma by electronic processes: K isomers in ^{176}Lu and ^{180}Ta under s-process conditions,” Phys. Rev. C **81**, 055808 (2010).

[180] N. Cue, J.-C. Poizat, and J. Remillieux, “Exciting the Nucleus by Target Electron Capture into Atomic Orbitals,” EPL (Europhysics Letters) **8**, 19 (1989).

[181] N. Cue, “Nuclear excitation by target electron capture,” Nuclear Instruments and Methods in Physics Research Section B: Beam Interactions with Materials and Atoms **40–41, Part 1**, 25 (1989).

[182] J. Kimball, D. Bittel, and N. Cue, “A comment on “nuclear excitation by target electron capture”,” Physics Letters A **152**, 367 (1991).

[183] Z.-S. Yuan and J. C. Kimball, “First-principles calculation of the cross sections for nuclear excitation by electron capture of channeled nuclei,” Phys. Rev. C **47**, 323 (1993).

[184] *Proposal S003: Exciting the Nucleus by Electron Capture in Axial Channeling* (GSI, Darmstadt, 1989).

[185] D. Dauvergne (Habilitation dissertation, 2006).

[186] S. Kishimoto, Y. Yoda, M. Seto, Y. Kobayashi, S. Kitao, R. Haruki, T. Kawauchi, K. Fukutani, and T. Okano, “Observation of Nuclear Excitation by Electron Transition in ^{197}Au with Synchrotron X Rays and an Avalanche Photodiode,” Phys. Rev. Lett. **85**, 1831 (2000).

[187] T. Carreyre, M. R. Harston, M. Aiche, F. Bourgine, J. F. Chemin, G. Claverie, J. P. Goudour, J. N. Scheurer, F. Attallah, G. Bogaert, J. Kiener, A. Lefebvre, J. Durell, J. P. Grandin, W. E. Meyerhof, and W. Phillips, “First direct proof of internal conversion between bound states,” Phys. Rev. C **62**, 024311 (2000).

[188] A. Pálffy, “Theory of nuclear excitation by electron capture for heavy ions,” Ph.D. thesis, Justus-Liebig-Universität Gießen (2006).

[189] P. Zimmerer, N. Grün, and W. Scheid, “Auger rates for dielectronic recombination cross sections with highly charged relativistic heavy ions,” Physics Letters A **148**, 457 (1990).

[190] P. Zimmerer, “Relativistische Theorie für die Dielektronische Rekombination bei sehr schweren hochgeladenen Ionen,” Ph.D. thesis, Justus-Liebig-Universität Gießen (1992).

[191] S. L. Haan and V. L. Jacobs, “Projection-operator approach to the unified treatment of radiative and dielectronic recombination,” Phys. Rev. A **40**, 80 (1989).

[192] S. K. Arigapudi and A. Pálffy, “Overlapping resonances in nuclei coupling to the atomic shells,” Phys. Rev. A **85**, 012710 (2012).

[193] J. Eichler and T. Stöhlker, “Radiative electron capture in relativistic ion–atom collisions and the photoelectric effect in hydrogen-like high-Z systems,” Physics Reports **439**, 1 (2007).

[194] Nuclear Structure and Decay Databases (2015). http://www.nndc.bnl.gov/.

[195] T. Ditmire, J. W. G. Tisch, E. Springate, M. B. Mason, R. A. S. N. Hay, J. Marangos, and M. H. R. Hutchinson, “High-energy ions produced in explosions of superheated atomic clusters,” Nature **386**, 54 (1997).

[196] T. Ditmire, J. W. G. Tisch, E. Springate, M. B. Mason, N. Hay, J. P. Marangos, and M. H. R. Hutchinson, “High Energy Ion Explosion of Atomic Clusters: Transition from Molecular to Plasma Behavior,” Phys. Rev. Lett. **78**, 2732 (1997).

[197] T. Ditmire, E. Springate, J. W. G. Tisch, Y. L. Shao, M. B. Mason, N. Hay, J. P. Marangos, and M. H. R. Hutchinson, “Explosion of atomic clusters heated by high-intensity femtosecond laser pulses,” Phys. Rev. A **57**, 369 (1998).

[198] M. Lezius, S. Dobosz, D. Normand, and M. Schmidt, “Explosion Dynamics of Rare Gas Clusters in Strong Laser Fields,” Phys. Rev. Lett. **80**, 261 (1998).

[199] H. M. Milchberg, S. J. McNaught, and E. Parra, “Plasma hydrodynamics of the intense laser-cluster interaction,” Phys. Rev. E **64**, 056402 (2001).

[200] K. Y. Kim, I. Alexeev, E. Parra, and H. M. Milchberg, “Time-Resolved Explosion of Intense-Laser-Heated Clusters,” Phys. Rev. Lett. **90**, 023401 (2003).

[201] F. Peano, R. A. Fonseca, and L. O. Silva, “Dynamics and Control of Shock Shells in the Coulomb Explosion of Very Large Deuterium Clusters,” Phys. Rev. Lett. **94**, 033401 (2005).

[202] E. Skopalová, Y. C. El-Taha, A. Zaïr, M. Hohenberger, E. Springate, J. W. G. Tisch, R. A. Smith, and J. P. Marangos, “Pulse-Length Dependence of the Anisotropy of Laser-Driven Cluster Explosions: Transition to the Impulsive Regime for Pulses Approaching the Few-Cycle Limit,” Phys. Rev. Lett. **104**, 203401 (2010).

[203] D. D. Hickstein, F. Dollar, J. A. Gaffney, M. E. Foord, G. M. Petrov, B. B. Palm, K. E. Keister, J. L. Ellis, C. Ding, S. B. Libby, J. L. Jimenez, H. C. Kapteyn, M. M. Murnane, and W. Xiong, “Observation and Control of Shock Waves in Individual Nanoplasmas,” Phys. Rev. Lett. **112**, 115004 (2014).

[204] F. Peano, F. Peinetti, R. Mulas, G. Coppa, and L. O. Silva, “Kinetics of the Collisionless Expansion of Spherical Nanoplasmas,” Phys. Rev. Lett. **96**, 175002 (2006).

[205] F. Peano, G. Coppa, F. Peinetti, R. Mulas, and L. O. Silva, “Ergodic model for the expansion of spherical nanoplasmas,” Phys. Rev. E **75**, 066403 (2007).

[206] Experimental Nuclear Reaction Data - EXFOR (2015). http://www-nds.iaea.org/exfor/exfor.htm/.

[207] J. Gunst, Y. A. Litvinov, C. H. Keitel, and A. Pálffy, “Dominant Secondary Nuclear Photoexcitation with the X-Ray Free-Electron Laser,” Phys. Rev. Lett. **112**, 082501 (2014).

[208] Gesellschaft für Schwerionenforschung GSI Darmstadt (2015). http://www.gsi.de.

[209] Proton Linac for FAIR at GSI (2015). https://www.gsi.de/fs2/C/start/beschleuniger/fachabteilungen/linac/projects/proton_linac_for_fair.htm.

[210] J. Gunst, Y. Wu, N. Kumar, C. H. Keitel, and A. Pálffy, “Direct and secondary nuclear excitation with x-ray free-electron lasers,” arXiv:1508.07264 (2015).

[211] K. Dyall, I. Grant, C. Johnson, F. Parpia, and E. Plummer, “GRASP: A general-purpose relativistic atomic structure program,” Comput. Phys. Commun. **55**, 425 (1989).

[212] B. Henke, E. Gullikson, and J. Davis, “X-Ray Interactions: Photoabsorption, Scattering, Transmission, and Reflection at E = 50-30,000 eV, Z = 1-92 ,” At. Data Nucl. Data Tabl. **54**, 181 (1993).

[213] H.-K. Chung, M. Chen, and R. Lee, “Extension of atomic configuration sets of the Non-LTE model in the application to the Kα diagnostics of hot dense matter,” High Energy Density Physics **3**, 57 (2007). Radiative Properties of Hot Dense Matter.

[214] A. Kemp and J. M. ter Vehn, “An equation of state code for hot dense matter, based on the {QEOS} description,” Nuclear Instruments and Methods in Physics Research Section A: Accelerators, Spectrometers, Detectors and Associated Equipment **415**, 674 (1998).

[215] J. C. Stewart and K. D. J. Pyatt, “Lowering of Ionization Potentials in Plasmas,” Astrophys. J. **144**, 1203 (1966).

[216] R. L. Mössbauer, “Kernresonanzabsorption von γ-Strahlung in Ir191,” Zeitschrift für Naturforschung A **14**, 211 (1959).

[217] S. L. Ruby, “Mössbauer experiments without conventional sources,” J. Phys. Colloques **35**, C6 (1974).

[218] R. L. Cohen, G. L. Miller, and K. W. West, “Nuclear Resonance Excitation by Synchrotron Radiation,” Phys. Rev. Lett. **41**, 381 (1978).

[219] G. Shenoy, “Scientific legacy of Stanley Ruby,” Hyperfine Interactions **170**, 5 (2006).

[220] G. Smirnov, “General properties of nuclear resonant scattering,” Hyperfine Interactions **123-124**, 31 (1999).

[221] Y. Kagan, “Theory of coherent phenomena and fundamentals in nuclear resonant scattering,” Hyperfine Interactions **123-124**, 83 (1999).

[222] W. Sturhahn, “Nuclear resonant spectroscopy,” J. Phys.: Condens. Matter **16**, S497 (2004).

[223] E. Gerdau, R. Rüffer, H. Winkler, W. Tolksdorf, C. P. Klages, and J. P. Hannon, “Nuclear Bragg diffraction of synchrotron radiation in yttrium iron garnet,” Phys. Rev. Lett. **54**, 835 (1985).

[224] J. Hastings, D. Siddons, U. Van Bürck, R. Hollatz, and U. Bergmann, “Mössbauer spectroscopy using synchrotron radiation,” Physical review letters **66**, 770 (1991).

[225] M. O. Scully, E. S. Fry, C. H. R. Ooi, and K. Wódkiewicz, “Directed Spontaneous Emission from an Extended Ensemble of N Atoms: Timing Is Everything,” Phys. Rev. Lett. **96**, 010501 (2006).

[226] M. Scully, “Correlated spontaneous emission on the Volga,” Laser Physics **17**, 635 (2007).

[227] W.-T. Liao, *Coherent Control of Nuclei and X-rays* (Springer Science & Business Media, 2013).

[228] Y. V. Shvyd’ko, “Coherent nuclear resonant scattering of X-rays: Time and space picture,” Hyperfine Interactions **123-124**, 275 (1999).

[229] Y. Kagan, A. M. Afanas’ev, and V. G. Kohn, “On excitation of isomeric nuclear states in a crystal by synchrotron radiation,” Journal of Physics C: Solid State Physics **12**, 615 (1979).

[230] G. T. Trammell and J. P. Hannon, “Quantum beats from nuclei excited by synchrotron pulses,” Phys. Rev. B **18**, 165 (1978).

[231] G. T. Trammell and J. P. Hannon, “Erratum: Quantum beats from nuclei excited by synchrotron pulses,” Phys. Rev. B **19**, 3835 (1979).

[232] G. R. Hoy, J. Odeurs, and R. Coussement, “Coherent-path model for nuclear resonant scattering of gamma radiation from nuclei excited by synchrotron radiation,” Phys. Rev. B **63**, 184435 (2001).

[233] V. G. Kohn and G. V. Smirnov, “On the theory of nuclear resonant forward scattering of synchrotron radiation,” Phys. Rev. B **76**, 104438 (2007).

[234] Y. V. Shvyd’ko, “MOTIF: Evaluation of time spectra for nuclear forward scattering,” Hyperfine Interactions **125**, 173 (2000).

[235] Y. V. Shvyd’ko and G. V. Smirnov, “Enhanced yield into the radiative channel in Raman nuclear resonant forward scattering,” Journal of Physics: Condensed Matter **4**, 2663 (1992).

[236] Y. V. Shvyd’ko, S. L. Popov, and G. V. Smirnov, “Coherent re-emission of gamma -quanta in the forward direction after a stepwise change of the energy of nuclear excitation,” Journal of Physics: Condensed Matter **5**, 1557 (1993).

[237] V. G. Kohn and Y. V. Shvyd’ko, “Coherent scattering of a synchrotron radiation pulse by nuclei in vibrating crystals,” Journal of Physics: Condensed Matter **7**, 7589 (1995).

[238] G. V. Smirnov, U. van Bürck, W. Potzel, P. Schindelmann, S. L. Popov, E. Gerdau, Y. V. Shvyd’ko, H. D. Rüter, and O. Leupold, “Propagation of nuclear polaritons through a two-target system: Effect of inversion of targets,” Phys. Rev. A **71**, 023804 (2005).

[239] Y. V. Shvyd’ko, “Perturbed nuclear scattering of synchrotron radiation,” Hyperfine Interactions **90**, 287 (1994).

[240] Y. V. Shvyd’ko, A. I. Chumakov, G. V. Smirnov, V. G. Kohn, T. Hertrich, U. van Bürck, E. Gerdau, H. D. Rüter, J. Metge, and O. Leupold, “Nuclear Bragg Diffraction of Synchrotron Radiation in the Presence of Acoustic Vibrations,” EPL (Europhysics Letters) **22**, 305 (1993).

[241] G. Smirnov and W. Potzel, “Perturbation of nuclear excitons by ultrasound,” Hyperfine Interactions **123-124**, 633 (1999).

[242] D. Siddons, U. Bergmann, and J. Hastings, “Polarization effects in resonant nuclear scattering,” Hyperfine Interactions **123-124**, 681 (1999).

[243] G. E. Moore *et al.*, “Cramming more components onto integrated circuits,” Proceedings of the IEEE **86**, 82 (1998).

[244] G. Smirnov, “Synchrotron Mössbauer source of ^{57}Fe radiation,” Hyperfine Interactions **125**, 91 (2000).

[245] Y. V. Shvyd’ko, A. I. Chumakov, G. V. Smirnov, T. Hertrich, U. van Bürck, H. D. Rüter, O. Leupold, J. Metge, and E. Gerdau, “Fast Switching of Nuclear Bragg Scattering of Synchrotron Radiation by a Pulsed Magnetic Field,” EPL (Europhysics Letters) **26**, 215 (1994).

[246] H.-W. Lee and J. Kim, “Quantum teleportation and Bell’s inequality using single-particle entanglement,” Phys. Rev. A **63**, 012305 (2000).

[247] D. Jaksch, J. I. Cirac, P. Zoller, S. L. Rolston, R. Côté, and M. D. Lukin, “Fast Quantum Gates for Neutral Atoms,” Phys. Rev. Lett. **85**, 2208 (2000).

[248] T. Calarco, E. A. Hinds, D. Jaksch, J. Schmiedmayer, J. I. Cirac, and P. Zoller, “Quantum gates with neutral atoms: Controlling collisional interactions in time-dependent traps,” Phys. Rev. A **61**, 022304 (2000).

[249] T. Calarco, A. Datta, P. Fedichev, E. Pazy, and P. Zoller, “Spin-based all-optical quantum computation with quantum dots: Understanding and suppressing decoherence,” Phys. Rev. A **68**, 012310 (2003).

[250] K. Hammerer, A. S. Sørensen, and E. S. Polzik, “Quantum interface between light and atomic ensembles,” Rev. Mod. Phys. **82**, 1041 (2010).

[251] F. Beil, T. Halfmann, F. Remacle, and R. D. Levine, “Logic operations in a doped solid driven by stimulated Raman adiabatic passage,” Phys. Rev. A **83**, 033421 (2011).

[252] D. G. Cory, A. F. Fahmy, and T. F. Havel, “Ensemble quantum computing by NMR spectroscopy,” Proceedings of the National Academy of Sciences **94**, 1634 (1997).

[253] N. A. Gershenfeld and I. L. Chuang, “Bulk Spin-Resonance Quantum Computation,” Science **275**, 350 (1997).

[254] F. Mintert and C. Wunderlich, “Ion-Trap Quantum Logic Using Long-Wavelength Radiation,” Phys. Rev. Lett. **87**, 257904 (2001).

[255] N. Timoney, I. Baumgart, M. Johanning, A. Varón, M. Plenio, A. Retzker, and C. Wunderlich, “Quantum gates and memory using microwave-dressed states,” Nature **476**, 185 (2011).

[256] J. Gunst, C. H. Keitel, and A. Pálffy, “Logical operations with single x-ray photons via dynamically-controlled nuclear resonances,” arXiv:1506.00517 (2015).

[257] U. van Bürck, R. L. Mössbauer, E. Gerdau, R. Rüffer, R. Hollatz, G. V. Smirnov, and J. P. Hannon, “Nuclear Bragg scattering of synchrotron radiation with strong speedup of coherent decay, measured on antiferromagnetic ^{57}FeBO$_3$,” Phys. Rev. Lett. **59**, 355 (1987).

[258] G. V. Smirnov, Y. V. Shvyd’ko, O. S. Kolotov, and V. A. Pogozhev, “Nanosecond modulation of Fe^{57} Mössbauer radiation,” Sov. Phys. JETP **59**, 875 (1984).

[259] S. Roling, L. Samoylova, B. Siemer, H. Sinn, F. Siewert, F. Wahlert, M. Wöstmann, and H. Zacharias, “ Design of an x-ray split- and delay-unit for the European XFEL ,” Proc. SPIE **8504**, 850407 (2012).

[260] T. Osaka, T. Hirano, M. Yabashi, Y. Sano, K. Tono, Y. Inubushi, T. Sato, K. Ogawa, S. Matsuyama, T. Ishikawa, and K. Yamauchi, “ Development of split-delay x-ray optics using Si(220) crystals at SACLA ,” Proc. SPIE **9210**, 921009 (2014).

[261] B. Marx, K. S. Schulze, I. Uschmann, T. Kämpfer, R. Lötzsch, O. Wehrhan, W. Wagner, C. Detlefs, T. Roth, J. Härtwig, E. Förster, T. Stöhlker, and G. G. Paulus, "High-Precision X-Ray Polarimetry," Phys. Rev. Lett. **110**, 254801 (2013).

[262] W. Roseker, H. Franz, H. Schulte-Schrepping, A. Ehnes, O. Leupold, F. Zontone, S. Lee, A. Robert, and G. Grübel, "Development of a hard X-ray delay line for X-ray photon correlation spectroscopy and jitter-free pump–probe experiments at X-ray free-electron laser sources," Journal of Synchrotron Radiation **18**, 481 (2011).

[263] W. Roseker, S. Lee, M. Walther, H. Schulte-Schrepping, H. Franz, A. Gray, M. Sikorski, P. H. Fuoss, G. B. Stephenson, A. Robert, and G. Grübel, " Hard x-ray delay line for x-ray photon correlation spectroscopy and jitter-free pump-probe experiments at LCLS ," Proc. SPIE **8504**, 85040I (2012).

[264] T. Pittman, "It's a Good Time for Time-Bin Qubits," Physics **6**, 110 (2013).

[265] P. C. Humphreys, B. J. Metcalf, J. B. Spring, M. Moore, X.-M. Jin, M. Barbieri, W. S. Kolthammer, and I. A. Walmsley, "Linear Optical Quantum Computing in a Single Spatial Mode," Phys. Rev. Lett. **111**, 150501 (2013).

[266] J. M. Donohue, M. Agnew, J. Lavoie, and K. J. Resch, "Coherent Ultrafast Measurement of Time-Bin Encoded Photons," Phys. Rev. Lett. **111**, 153602 (2013).

[267] T. B. Pittman, B. C. Jacobs, and J. D. Franson, "Probabilistic quantum logic operations using polarizing beam splitters," Phys. Rev. A **64**, 062311 (2001).

[268] T. B. Pittman, B. C. Jacobs, and J. D. Franson, "Demonstration of Nondeterministic Quantum Logic Operations Using Linear Optical Elements," Phys. Rev. Lett. **88**, 257902 (2002).

[269] J. L. O'Brien, "Optical quantum computing," Science **318**, 1567 (2007).

[270] C. K. Hong, Z. Y. Ou, and L. Mandel, "Measurement of subpicosecond time intervals between two photons by interference," Phys. Rev. Lett. **59**, 2044 (1987).

[271] J. F. Seely, C. N. Boyer, G. E. Holland, and J. L. Weaver, "X-ray absolute calibration of the time response of a silicon photodiode," Appl. Opt. **41**, 5209 (2002).

[272] J. Keister, J. Smedley, E. Muller, J. Bohon, R. Garrett, I. Gentle, K. Nugent, and S. Wilkins, "Responsivity of diamond X-ray photodiodes calibrated at NSLS," Aip Conference Proceedings **1234**, 93 (2010).

[273] N. B. in, *Albert Einstein: Philosopher-Scientist* (edited by P. A. Schilpp (Library of Living Philosphers, Evanston, 1949).

[274] Y.-H. Kim, R. Yu, S. P. Kulik, Y. Shih, and M. O. Scully, "Delayed "Choice" Quantum Eraser," Phys. Rev. Lett. **84**, 1 (2000).

[275] T. Peng, H. Chen, Y. Shih, and M. O. Scully, "Delayed-Choice Quantum Eraser with Thermal Light," Phys. Rev. Lett. **112**, 180401 (2014).

[276] W. Heisenberg, “Über den anschaulichen Inhalt der quantentheoretischen Kinematik und Mechanik,” Zeitschrift für Physik **43**, 172 (1927).

[277] R. Feynman, R. Leighton, and M. Sands, *The Feynman Lectures on Physics* (Addison Wesley, Reading, 1965).

[278] M. O. Scully, B.-G. Englert, and H. Walther, “Quantum optical tests of complementarity,” Nature **351**, 111 (1991).

[279] P. Storey, S. Tan, M. Collett, and D. Walls, “Path detection and the uncertainty principle,” Nature **367**, 626 (1994).

[280] B.-G. Englert, M. O. Scully, and H. Walther, “Complementarity and uncertainty,” Nature **375**, 367 (1995).

[281] E. P. Storey, S. M. Tan, M. J. Collett, and D. F. Walls, “Complementarity and uncertainty,” Nature **375**, 368 (1995).

[282] H. Wiseman and F. Harrison, “Uncertainty over complementarity?” Nature **377**, 584 (1995).

[283] U. Eichmann, J. C. Bergquist, J. J. Bollinger, J. M. Gilligan, W. M. Itano, D. J. Wineland, and M. G. Raizen, “Young’s interference experiment with light scattered from two atoms,” Phys. Rev. Lett. **70**, 2359 (1993).

[284] S. Dürr, T. Nonn, and G. Rempe, “Origin of quantum-mechanical complementarity probed by a ‘which-way’ experiment in an atom interferometer,” Nature **395**, 33 (1998).

[285] R. Mir, J. S. Lundeen, M. W. Mitchell, A. M. Steinberg, J. L. Garretson, and H. M. Wiseman, “A double-slit ’which-way’ experiment on the complementarity–uncertainty debate,” New Journal of Physics **9**, 287 (2007).

[286] Y. Aharonov and D. Bohm, “Time in the Quantum Theory and the Uncertainty Relation for Time and Energy,” Phys. Rev. **122**, 1649 (1961).

[287] J. Kijowski, “On the time operator in quantum mechanics and the heisenberg uncertainty relation for energy and time,” Reports on Mathematical Physics **6**, 361 (1974).

[288] J. Muga and C. Leavens, “Arrival time in quantum mechanics,” Physics Reports **338**, 353 (2000).

[289] N. Vona, G. Hinrichs, and D. Dürr, “What Does One Measure When One Measures the Arrival Time of a Quantum Particle?” Phys. Rev. Lett. **111**, 220404 (2013).

[290] F. Lindner, M. G. Schätzel, H. Walther, A. Baltuvska, E. Goulielmakis, F. Krausz, D. B. Milovsević, D. Bauer, W. Becker, and G. G. Paulus, “Attosecond Double-Slit Experiment,” Phys. Rev. Lett. **95**, 040401 (2005).

[291] D. G. Arbó, E. Persson, and J. Burgdörfer, “Time double-slit interferences in strong-field tunneling ionization,” Phys. Rev. A **74**, 063407 (2006).

[292] K. L. Ishikawa, “Temporal Young’s interference experiment by attosecond double and triple soft-x-ray pulses,” Phys. Rev. A **74**, 023806 (2006).

[293] M. Richter, M. Kunitski, M. Schöffler, T. Jahnke, L. P. H. Schmidt, M. Li, Y. Liu, and R. Dörner, “Streaking Temporal Double-Slit Interference by an Orthogonal Two-Color Laser Field,” Phys. Rev. Lett. **114**, 143001 (2015).

[294] M. Kiffner, J. Evers, and C. H. Keitel, “Quantum Interference Enforced by Time-Energy Complementarity,” Phys. Rev. Lett. **96**, 100403 (2006).

[295] E. K. Akhmedov, J. Kopp, and M. Lindner, “Comment on ’Time–energy uncertainty relations for neutrino oscillations and the Mössbauer neutrino experiment’,” Journal of Physics G: Nuclear and Particle Physics **36**, 078001 (2009).

[296] M. O. Scully, “Collective Lamb Shift in Single Photon Dicke Superradiance,” Phys. Rev. Lett. **102**, 143601 (2009).

[297] T. Toellner, E. Alp, T. Graber, R. Henning, S. Shastri, G. Shenoy, and W. Sturhahn, “Synchrotron Mössbauer spectroscopy using high-speed shutters,” Journal of Synchrotron Radiation **18**, 183 (2011).

[298] D. M. Brink and G. R. Satchler, *Angular Momentum* (Clarendon Press, Oxford, 1968), 2nd ed.

[299] J. P. Blazer, F. Boehm, P. Marmier, and P. Scherrer, “Anregungsfunktionen und Wirkungsquerschnitte der ((p,n)-Reaktion (II)*),” Helvetica Physica Acta **24**, 441 (1951).

[300] B. G. Kiselev and N. R. Fajzrakhmanova, “Cross-sections of (p, n)-,(p, pn)-and (p, αn)-reactions on the 93 Nb nuclei,” 24th Conf. in Nucl. Spectr. and Nucl. Struct., Kharkov p. 356 (1974).

[301] V. N. Levkovskij, *Activation cross-sections by protons and alphas* (Moscow, 1991).

[302] B. Singh, M. K. Sharma, M. Musthafa, H. Bhardwaj, and R. Prasad, “A study of pre-equilibrium emission in some proton- and alpha-induced reactions,” Nuclear Instruments and Methods in Physics Research Section A: Accelerators, Spectrometers, Detectors and Associated Equipment **562**, 717 (2006). Proceedings of the 7th International Conference on Accelerator ApplicationsAccApp057th International Conference on Accelerator Applications.

[303] M. Avila-Rodriguez, J. Wilson, M. Schueller, and S. McQuarrie, “Measurement of the activation cross section for the (p,xn) reactions in niobium with potential applications as monitor reactions,” Nuclear Instruments and Methods in Physics Research Section B: Beam Interactions with Materials and Atoms **266**, 3353 (2008).

[304] F. Ditrói, S. Takács, F. Tárkányi, M. Baba, E. Corniani, and Y. Shubin, "Study of proton induced reactions on niobium targets up to 70 MeV," Nuclear Instruments and Methods in Physics Research Section B: Beam Interactions with Materials and Atoms **266**, 5087 (2008).

[305] F. Ditrói, A. Hermanne, E. Corniani, S. Takács, F. Tárkányi, J. Csikai, and Y. N. Shubin, "Investigation of proton induced reactions on niobium at low and medium energies," Nuclear Instruments and Methods in Physics Research Section B: Beam Interactions with Materials and Atoms **267**, 3364 (2009).

[306] ATIMA (2015). http://web-docs.gsi.de/~weick/atima/.

[307] iba-cyclotron-solutions (2015). http://www.iba-cyclotron-solutions.com/sites/default/files/ressources/CBR_Cyclone30_R01.pdf.

Acknowledgements

Es ist an der Zeit mich bei den vielen Menschen zu bedanken, ohne dessen Unterstützung diese Arbeit nicht möglich gewesen wäre.

Zuerst, möchte ich ein großes Dankeschön an meinen Doktorvater Prof. Christoph H. Keitel richten, dafür dass er mir es ermöglichte Teil seiner Arbeitsgruppe am Max-Planck-Institut für Kernphysik zu werden. Ich habe sehr profitiert von dem kollegialen und inspirierenden Arbeitsumfeld über die Jahre meiner Promotion. Ich bin sehr dankbar, dass er mir mit seinem breiten Erfahrungsschatz immer helfend zur Seite stand, mich immer wieder ermutigte und förderte neue Ideen und Ansätze zu verfolgen, und ich sein vollstes Vertrauen während meiner Promotion genießen durfte.

Meiner Betreuerin Adriana Pálffy möchte ich meinen ganz besonderen Dank aussprechen. Ich konnte jederzeit und in allen Belangen ihren Rat erfragen, sie hatte immer, auch kurzfristig für mich Zeit. Ich habe die konstruktive und freundschaftliche Zusammenarbeit mit ihr während meiner Promotion sehr genossen. In unseren vielen Diskussionen stand sie mir nicht nur mit ihrem Wissen fachlich zur Seite, sondern durch ihren Optimismus und ihre Energie konnte sie mich auch in schwierigen Phasen immer wieder neu motivieren und antreiben. Sie hatte maßgeblichen Anteil an der Entwicklung und Ausreifung neuer Ideen, die letztendlich den Inhalt dieser Arbeit ausmachen. Mulțumesc frumos!

Ich möchte mich auch bei Prof. Jörg Jäckel bedanken, dafür dass er sich bereiterklärt hat, das Zweitgutachten für meine Dissertation zu erstellen.

Many thanks go to Naveen Kumar and Yuanbin Wu for their cooperation in the plasma project. I really enjoyed the collaboration and the many productive discussions.

I want to thank Dr. Yuri Litvinov for his estimates and ideas about the molybdenum isomer production directly embedded in solid state niobium foils.

I am indebted to Dr. R. Ramis Abril for providing us with the EOS tables for iron, niobium and molybdenum.

I would like to thank Dr. Stanislav Tashenov who has been reachable for any questions and discussions about x-ray polarization concerns.

Many thanks go to the proofreaders of my thesis, Jiri Danek, Kilian Heeg, Xiangjin Kong, Sebastian Meuren, Niklas Michel, Nicolas Teeny and Lida Zhang whose remarks significantly improved the manuscript.

During the last years, I very much enjoyed the fruitful discussions about nuclear quantum optics with my colleagues and friends Kilian Heeg, Xiangjin Kong and Wen-Te Liao.

Desweiteren bedanke ich mich recht herzlich bei der Sektretärin unserer Abteilung, Sibel Babacan, und bei den Systemadministratoren, Carsten Pinnow und Julian König, für ihre Hilfe in administrativen und technischen Angelegenheiten während meiner Promotion.

Special thanks go to all my officemates with whom I enjoyed my working days at the Max-Planck Institute for Nuclear Physics over the last years, in particular, Shikha Bhadoria, Jiri Danek, Niklas Michel, David Schönleber, Nicolas Teeny and Anton Wöllert.

Besonderer Dank gilt auch meiner Familie, die mich stets bedingungslos unterstützt und voll hinter mir steht.

Aus tiefstem Herzen bedanke ich mich bei meiner Verlobten Anja Geweniger, die mir besonders in stressigen und schwierigen Zeiten während meiner Promotion immer unterstützend und aufmunternd zur Seite stand und mir den Rücken frei hielt. Sie ist immer für mich da, wenn ich sie brauche.